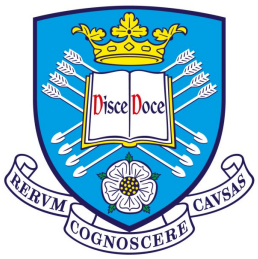

The University Of Sheffield.

Department of Mechanical Engineering

Ultrasonic Viscosity Sensors to Measure Degradation and Contamination in a Dielectric Battery Coolant

David **Fort**

March 2022

Prof. Rob Dwyer-Joyce

Thesis submitted to the Department of Mechanical Engineering, University of Sheffield in fulfilment of the requirements for the degree of PhD.

[Page intentionally left blank]

Abstract

To meet the current demands to reduce pollution, electric vehicles are becoming more powerful and are utilising faster charging. This puts the battery cells into heavy and demanding usage causing heat generation. Also, as electric vehicles become more popular and are used in more extreme conditions, batteries require pre-heating in some cold environments. To meet these demands, electrically non-conductive liquids can be used in direct contact with immersed power electronics to provide cooling, heating, and health maintenance capabilities. These liquids are commonly known as dielectric fluids.

Just like any other oil, dielectric fluids deteriorate throughout their service life due to chemical, electrical, and thermal stresses. Oil degradation is a very complex and unique phenomenon to each environment and application. The main cause of oil deterioration is oxidation, and the rate at which the oil oxidises can be increased with particle and moisture contamination. Each individual degradation feature such as oxidation, particle contamination and water contamination can decrease the electrical insulation of a dielectric fluid. Due to the complex nature of oxidation, this project investigates whether particle and water contamination can be monitored in order to preserve the flow, cooling and electrical insulation properties of the dielectric oil.

Viscosity is a property that changes with oil degradation, and is measured ex-situ using conventional viscometry methods. An available non-invasive technology that can be used to measure the viscosity is ultrasound. This measurement technique has many advantages including low cost, intrinsically high shear rates, small installation area, capable of working in harsh environments, and requires no moving parts. The use of ultrasonic shear waves in a three layered system (a transducer propagating sound through three dissimilar layers such as aluminium, polyimide and oil) has been previously utilised to measure the viscosity of oils in-situ. In order to illustrate ultrasound's potential to monitor a dielectric oil's degradation, water and copper were used to simulate contamination in static conditions without the presence of air bubbles. Hence by using the three layered ultrasonic viscometer to measure their impact on viscosity, a potential in-situ condition sensor could be established.

In this thesis a viscosity investigation was conducted using frequencies of 1.79, 2.98, 10.1 and 13.86 MHz. Water contaminated mixtures consisted of 3, 10 and 20 % volumes. This high and relatively large percentage range was chosen as in many electronic environments, cellulose is also used to increase insulation. It can hold as much as 20 % water. Copper contamination consisted of 0.1, 0.5 and 1 % volumes, which were low in comparison to water. This was because most electronic cooling environments would not typically produce more than 1 % copper from erosion and chemical reactions during their service life.

Analytical and numerical models were developed in order to interpret the measured ultrasonic data. Modelling the physical aspects of acoustic shear wave motion throughout three layers provided a link between theory and experiment. To validate the models, calibration oils were measured and variations between theory and experimental data were justified and accounted for.

The measured ultrasonic viscosity of the pure coolant fluid showed Newtonian behaviour at low frequencies that aligned well with conventional viscometer results. However at high frequencies the viscosity was much lower, which appeared as shear thinning behaviour between two Newtonian plateaus. A similar shear thinning behaviour between high and low ultrasonic measurements was also seen in contaminated fluids, which further supported the proposed shear thinning behaviour. With the addition of copper there was little effect on the viscosity, which was due to such low fractions of contamination. Water contamination showed distinguishable viscosity data with increasing dispersed phase volume across all frequencies. The results did not match the conventional rheometer data but they did illustrate shear thinning, which appeared more drastic with an increasing shear rate.

Based on the ultrasonic viscosity results, shear transducers show the potential to be used to measure the condition of battery coolants similar to the fluid tested in this thesis. A combination of low and high frequencies can provide viscosity results similar to conventional methods and at shear rates potentially within a transition zone. Finally, it was a promising investigation as to whether water and copper could be detected in a dielectric oil based on their impact on viscosity.

Acknowledgements

First and foremost I am extremely grateful to my supervisor, Prof. Rob Dwyer-Joyce for his invaluable advice, continuous support, and patience during my PhD study. I would also like to thank him for introducing me to the exciting engineering area of acoustic tribological sensors and for all the opportunities he provided. Additionally, I would like to express gratitude to Dr Rocco Potenza, Dr Giles Prentice, Mr Jason Wong, Dr Marc Payne and Miss Rachel Fort for their knowledge, plentiful experience and support throughout this entire process.

I would also like to thank the University of Sheffield, the CDT and BP, Castrol for the financial assistance and training to enable this research to be completed, with an additional thank you to Ms Kim Matthews-Hyde for her support.

Thank you to Mr Dave Butcher for his technical genius and guidance on all things mechanical, and thanks to Dr Andrew Hunter for all his hardware and software support.

I would like to thank my friends, lab mates, colleagues and research team for a cherished time spent together in the lab, and in social settings. A special mention goes out to Mr João Lucas Novo, Mr Richard Okhiria, Mr Rasmus Wagner, Mr Jack Rooke, Dr Tomos Brenchley, Mr Sushil Simkhada, Mr Thomas Butcher, Dr Xiangwei Li, Dr Georgios Tyreas and all the cohorts.

Finally and most importantly, I would like to say a huge thank you to Gail (mother), Paul, John and Freya who have been, and will always be, supporting me through any and all challenging times. Their support throughout this entire process has been second to none, and without their tremendous understanding and encouragement in the past few years, it would have been impossible for me to complete my study.

Contents

1 Introduction **1**
- 1.1 Statement of the Problem . . . 1
- 1.2 Novelty Statements . . . 4
- 1.3 Aims and Objectives . . . 5
  - 1.3.1 Objectives: . . . 5
- 1.4 Thesis Chapters . . . 6

2 Literature Review 1: Fundamentals of Dielectric Oils **9**
- 2.1 Introduction . . . 9
- 2.2 Composition . . . 10
  - 2.2.1 Petroleum-base Oils . . . 10
  - 2.2.2 Synthetic-base Oils . . . 11
  - 2.2.3 Additives . . . 12
- 2.3 Physical Properties . . . 14
  - 2.3.1 Viscosity . . . 14
  - 2.3.2 Thermal Properties . . . 23
  - 2.3.3 Surface and Interfacial Tension . . . 24
  - 2.3.4 Flash Point . . . 24
  - 2.3.5 Pour Point . . . 25
- 2.4 Electrical Properties . . . 25
  - 2.4.1 Dielectric Strength . . . 25
  - 2.4.2 Specific Resistance . . . 25
  - 2.4.3 Dielectric Dissipation Factor . . . 26
- 2.5 Chemical Properties . . . 26
  - 2.5.1 Water Content . . . 26
  - 2.5.2 Acidity . . . 27
- 2.6 Testing Properties of Dielectric Fluids . . . 27
  - 2.6.1 Capillary Viscometer . . . 27
  - 2.6.2 Rotational Rheometers . . . 28
  - 2.6.3 Water Content Measurement . . . 31
  - 2.6.4 Electrical Property Testing . . . 31
- 2.7 Dielectric Oil Degradation . . . 32
  - 2.7.1 Water Contamination . . . 35
  - 2.7.2 Particle Contamination . . . 38
- 2.8 Rheology of Emulsions and Suspensions . . . 41
  - 2.8.1 Breaking of Emulsions and Suspensions . . . 41
  - 2.8.2 Dilute and Concentrated Contamination . . . 43
  - 2.8.3 Impacting Factors on the Rheology of Mixtures . . . 46
- 2.9 Conclusion . . . 51

3 Literature Review 2: Ultrasound to Measure Viscosity 54
3.1 Introduction . . . 54
3.2 Wave Modes . . . 55
3.3 Propagation in Materials . . . 56
3.3.1 Speed of Sound . . . 56
3.3.2 Acoustic Impedance . . . 57
3.3.3 Attenuation . . . 58
3.3.4 Wave Propagation Distance in Fluids . . . 60
3.3.5 Interference . . . 62
3.4 Wave Interaction with Boundaries . . . 63
3.4.1 Two Layered System . . . 64
3.4.2 Three layered system . . . 65
3.4.3 Comparison of a Two and Three Layered System . . . 66
3.5 Ultrasonic Transducers . . . 68
3.5.1 Piezoelectric Effect . . . 68
3.5.2 Piezoelectric Element . . . 69
3.5.3 Commercial Transducers . . . 69
3.5.4 Coupling . . . 70
3.5.5 Near Field Effect . . . 71
3.5.6 Beam Spread . . . 71
3.5.7 Transducer Arrangements . . . 72
3.6 Pulsing and Receiving Instruments . . . 73
3.7 Ultrasonic Signal Characteristics . . . 75
3.7.1 Sensor Waveform Excitation Modes . . . 75
3.7.2 Frequency Domain . . . 76
3.8 Combining Rheology with Acoustics . . . 78
3.9 Ultrasonic Shear Rheology . . . 79
3.9.1 Early Developments . . . 80
3.9.2 The Matching Layer Viscometer . . . 81
3.9.3 Mathematical Model . . . 83
3.9.4 Ultrasonic Viscometer Excitation . . . 84
3.9.5 Shear Rate of an Ultrasonic Viscometer . . . 85
3.10 Conclusion . . . 88

4 Rotational Viscometry 91
4.1 Rheology Instrument . . . 91
4.2 Pure Coolant Characteristic Expectations . . . 92
4.3 Geometry Selection . . . 94
4.4 Experimental Procedure . . . 98
4.5 Characterising Pure Coolant . . . 99
4.6 Viscosity Predictions for Coolant Mixtures . . . 102
4.7 Characterising Behaviour of Coolant Mixtures . . . 105
4.8 Conclusion . . . 110

5 Analytical and Numerical Models to Predict Ultrasonic Shear Viscosity 111
5.1 Introduction . . . 111
5.2 Analytical Study . . . 112
5.2.1 Reflection Coefficient in a Three Layered System . . . 112
5.2.2 Newtonian Model For Shear Viscosity . . . 117
5.2.3 Reflection Coefficient From a Newtonian Fluid Layer . . . 120
5.3 Numerical Study . . . 123
5.3.1 Numerical Model . . . 123
5.3.2 Numerical Implementation . . . 125
5.3.3 Initial Wave Design . . . 126
5.3.4 Numerical Parameters . . . 127
5.3.5 Numerical Simulation Method . . . 129
5.3.6 Numerical Simulation . . . 131
5.3.7 Analysis Method . . . 133
5.3.8 Reflection Coefficient From a Newtonian Fluid Layer . . . 134
5.4 Comparison Between Numerical and Analytical Models . . . 135
5.5 Conclusion . . . 137

6 Methodology for Ultrasonic Shear Viscometry 139
6.1 Matching Layer Methodology Outline . . . 139
6.2 Apparatus . . . 141
6.2.1 Ultrasonic Viscometer Rig . . . 141
6.2.2 Matching Layers . . . 143
6.2.3 Transducers . . . 144
6.2.4 Instrumentation . . . 148
6.3 Procedure . . . 149
6.4 Transducer Excitation Setting . . . 150
6.5 Signal Processing . . . 152
6.6 Experimental Protocol . . . 156
6.7 Evaluation with Calibration Oils . . . 157
6.7.1 Model Tuning . . . 159
6.8 Conclusion . . . 160

7 Ultrasonic Shear Viscometry to Detect Contamination 163
7.1 Introduction . . . 163
7.2 Evaluation of Pure Coolant . . . 164
7.3 Evaluation of the Effect of Water Contamination . . . 165
7.4 Evaluation of the Effect of Copper Contamination . . . 167
7.5 Shear Rate Effects on the Flow Behaviour . . . 169
7.5.1 Calculating Shear Rate . . . 170
7.5.2 Evaluating the Flow Behaviour . . . 174
7.6 Discussion . . . 177
7.7 Conclusion . . . 181

8 Conclusion **183**
8.1 Further Directions 185
8.1.1 Ultrasonic Measurement in a Battery Coolant System 187

Bibliography **188**

Appendices **201**

A Shear Analytical Model **203**

B Shear Numerical Model **205**

C Signal Processing **211**

D Sensor Block for a Battery Cooling System **215**

List of Figures

1.1 Diagram of an electric vehicle with a direct immersion method of cooling, [5]. 2
1.2 Immersion cooling of batteries in electric vehicles, [7]. 3

2.1 Petroleum-based oil composition, [24]. 10
2.2 Synthetic-based oil composition, [31]. 12
2.3 Viscosity two plates model under laminar flow conditions, where the bottom plate is fixed and the top plate is forced into motion. 15
2.4 Shear stress and viscosity behaviour of Newtonian and non-Newtonian fluids. 1) Newtonian, 2) Shear thinning, 3) Shear thickening, 4) Plastic, 5) Thixotropic, 6) Rheopectic, [40]. 17
2.5 Shear thinning behaviour of polymer chains, droplets and particles, [41]. . . 18
2.6 Steady and oscillatory shear. 19
2.7 Argand diagram for the shear modulus relationship. 21
2.8 Illustration of the phase angle changes for a material under oscillatory shear, [43]. 21
2.9 Illustration of the 3 zones for the viscosity behaviour with high shear rates for complex oils, [16]. 22
2.10 Carreau-Yasuda Model, [16]. 23
2.11 The dielectric dissipation factor (tan δ) where an ideal oil with high insulation has a current leading the voltage by 90°. Any losses in insulation reduce this lead by angle, δ, [50]. 26
2.12 Capillary viscometer, [16]. 28
2.13 Common rotational rheometers. Top left: Cone on plate. Bottom left: Parallel plates. Right: Concentric cylinder, [40]. 29
2.14 Karl Fischer moisture test, [56]. 31
2.15 Typical set-up of a test cell used to measure the dielectric breakdown voltage of an oil, [57]. 32
2.16 Graph showing the oxidation effects of an oil with anti-oxidant additives as it degrades over time. Viscosity and acidity remain relatively unchanged with the help of anti-oxidants until they have been depleted. After this point, viscosity and acidity increase, [59]. 33
2.17 Wu's, [63], synthetic ester oil oxidation results over 60 hours at 150°C. . . 34
2.18 Saturation point changes with temperature, [31]. 36
2.19 Example of a polar ester linkage attracting a polar water molecule, [31]. . . 37
2.20 Water in oil states. 37
2.21 Copper in oil states. 38
2.22 Metallic particle contamination effects on a petroleum-based oil as it oxidises over time. a) Solubility of each metal in oil, b) The effect of each particulate on the viscosity, and c) The effect of each particulate on the acid content, [75]. 40

2.23 Illustration of how the dispersed phase breaks from the continuous phase. This illustration was created for emulsions, however flocculation and sedimentation occur for particulate suspensions without the coalescence, [77]. . 42
2.24 Ostwald ripening occurring over time, where a smaller droplet dissolves and eventually feeds into a larger a droplet, [80]. 43
2.25 The change of rheological behaviour of mixtures with the increase of dispersed phase volume fraction, where ϕ_G is the glass transition volume fraction, ϕ_{RCP} is the randomly close pack volume fraction and ϕ_{FCC} is the‘ face-concentrated cubic volume fraction, [76]. 44
2.26 The viscosity of mixtures as the dispersed phase volume fraction increases. The viscosity can be described by Einstein's equation for dilute systems, Equation 2.23, however for a concentrated system a more effective mathematical equation is required. Therefore the effective medium line was created using Equation 2.23, [76]. 46
2.27 Behaviour of an emulsion or suspension with increased dispersed phase volume fraction over shear rate. 47
2.28 Dispersed phase volume effects on the rheological behaviour and how it increases viscosity of the continuous phase. (a) Dilute mixture showing Newtonian behaviour. (b) Semi-dilute mixture showing Newtonian behaviour with an increase in viscosity. (c) Concentrated mixture illustrating non-Newtonian shear thinning behaviour. (d) Highly concentrated mixture showing shear thinning behaviour after its newly developed yield stress. (e) Highest concentrated mixture showing Newtonian behaviour after it has yielded, [89]. 48
2.29 Illustration of the viscosity behaviour with shear rate for a continuous phase with the same dispersed phase volume fraction but varying particle/droplet sizes, [88]. 50

3.1 Acoustic waves differentiated by frequency, [16]. 54
3.2 Illustration of an elastic particle undergoing shear and longitudinal wave motion, [107]. 55
3.3 Comparison between an un-attenuated and an attenuated sound wave inside a metal block. 59
3.4 The penetration depth of longitudinal and shear waves for different viscosities over the ultrasonic range of frequencies. 61
3.5 Illustration of constructive and destructive wave interference. 62
3.6 A schematic diagram of the behaviour of a wave in a quarter wavelength thick, $\lambda/4$, matching layer, [17]. 63
3.7 Normal incident wave for a two layered system. 65
3.8 Normal incident wave at two boundaries. 66
3.9 Comparison between a two (Equations 3.19) and three layered (Equation 3.20) system using the reflection coefficient with respect to frequency, where the matching layer thickness corresponded with 2 MHz. The two layered system was a metal - oil and the three layered system was a metal - polymer - oil set-up. 67

3.10 Piezoelectric effect [17]. 68
3.11 Piezoelectric element [120]. 69
3.12 Exploded diagram of the internals of an ultrasonic commercial transducer [109]. 70
3.13 Forming of a fully constructed waveform in the near field range. 71
3.14 Beam spread and beam divergence of a wave inside a metal block. 72
3.15 Transducer pulsing and receiving arrangements. 72
3.16 Schematic of a typical ultrasonic pulsing system, [122]. 73
3.17 Ultrasonic pulsing and data acquisition instruments used with ultrasonic transducers. 74
3.18 Excitation modes consisting of impulse/spike, square and sine waveforms, [123]. 75
3.19 Linear and exponential chirp excitation types, [123]. 76
3.20 Ultrasonic signal characteristics of a frequency domain signal, [126]. 77
3.21 Transducer time and frequency response for a damped signal, [123]. 77
3.22 Transducer time and frequency response for an un-damped signal, [123]. . . 77
3.23 Mason's ultrasonic viscometer and signal analysis, [131]. 79
3.24 Sketch of a) simple metal - fluid two layered viscometer, and b) Schirru's newly developed matching layer viscometer, [142]. 81
3.25 Schirru's matching layer sensitivity results showing dips in the reflection coefficient where the matching layer creates resonance. In comparison to reflection coefficient values without a matching layer, this was a good development, [15]. 82
3.26 Schirru's calibration curve used to predict viscosity using a measured reflection coefficient, [14]. 83
3.27 A comparison of viscosity results completed using a matching layer ultrasonic viscometer and predicted values from a mathematical model, [16]. . . 84
3.28 Shows the reflection coefficient differences between sine and chirp wave forms at a low 1 MHz and high 10 MHz frequency [16]. 85
3.29 Schirru's ultrasonic spectroscopy results using a matching layer viscometer, [14]. 86
3.30 Brenchley's measurements for the shear thinning behaviour of PAO oil blends mixed with a viscosity modifier, [16]. 86
3.31 Sketch of how the frequency of an oscillator can be directly related to the frequency of the test fluid using the Coz-Merz rule, Equation 2.7. a) Plate is directly applying the shear stress to the fluid. b) Acoustic shear stress applied through a plate and into the fluid, therefore the Cox-Merz rule can not be used. 87
3.32 Brenchley's velocity and shear rate data for a 1 and 2 MHz sensor as the excitation voltage is increased, [16]. 88

4.1 Rheometer utilised throughout this chapter. The rheometer itself was controlled by its own computer unit, which connected to an external PC. The plates were cooled / heated using a temperature control device that was also connected to the rheometers computer. 92

4.2 BP, Castrol's pure dielectric coolant with a clear appearance. 93
4.3 Parallel plate analytical torsional flow diagram used to depict the link between geometric values with measured values. 94
4.4 Effects of changing the gap size between parallel plates on viscosity with an applied shear rate of 0 - 2000 s^{-1} at 30°C. Gap sizes consisted of 1000 μm, 800 μm and 500 μm. 95
4.5 Surface tension effects on steady shear rotational viscometry and the ideal set-up to reduce these effects, where r is the radius of the contact line and ϕ is the surface tension angle created by being situated between two plates. 96
4.6 TA Instruments comparing shear viscosity data for water, using three different spindles, and an oil sample. Blue Triangle: Parallel plate results for water. Blue square: Cone on plate results for water. Blue circle: Standard concentric cylinder results for water. Red crosses: Cone on plate results for oil. Cone and parallel plates both had gaps of 1 mm, [55]. 97
4.7 Fluid loading gap illustration. Left: gap unloaded. Centre: Loaded gap. Right: Correct sample loading. In accordance with rheological testing guidance [55, 148], and backed up by research, Johnston et al, [149]. 99
4.8 Pure coolant comparison between measured dynamic viscosity using the rheometer and the data sheet dynamic viscosity from Table 4.1. Temperature ramp of 20 - 60°C at a constant shear rate of 1000 s^{-1}. Error bars are plotted after conducting the same measurement 3 times. The Vogel equation was used to fit each data set. 100
4.9 Characterising the behaviour of pure coolant under an applied shear rate of 0 - 3500 s^{-1} at 23 °C. Data analysis disregards shear rate data below 400 s^{-1}. 102
4.10 Contaminated coolant mixtures. Reading from left to right and top to bottom: Pure coolant, 3, 10 and 20 % distilled water contamination fractions, and 0.1, 0.5 and 1 % copper fractions. 103
4.11 Contaminated viscosity predictions based on a pure coolant viscosity of 6.01 $mPas$ at 23 °C. Prediction 1 is Equation 4.3, Prediction 2 is Equation 4.4, and Prediction 3 is Equation 4.5. 104
4.12 Characterising the behaviour of water contaminated coolant under an applied shear rate of 0 - 3500 s^{-1} at 23 °C. 106
4.13 Characterising the behaviour of copper contaminated coolant under an applied shear rate of 0 - 3500 s^{-1} at 23 °C. 106
4.14 Sketch illustrating the cause of the initial shear thinning behaviour, beyond the discarded region, where aggregates begin to form towards a phase separation. With increasing shear rate, these aggregates are broken down. . 107
4.15 Measured viscometry data in comparison to predicted viscosity for pure coolant, and water and copper contamination fractions. The contaminated viscosity predictions were based on a pure coolant viscosity of 6.01 $mPas$ at 23 °C. Prediction 1 is Equation 4.3, Prediction 2 is Equation 4.4, and Prediction 3 is Equation 4.5. 108

4.16 Measured viscometry data in comparison to predicted viscosity for pure coolant, and water and copper contamination fractions. The contaminated viscosity predictions were based on a pure coolant viscosity of 6.01 $mPas$ at 23 °C. Prediction 1 is Equation 4.3, Prediction 2 is Equation 4.4, and Prediction 3 is Equation 4.5. 108

5.1 Three layered shear analytical diagram illustrating sound interaction at boundaries. Here pressure, P, and acoustic impedance, Z are used. For a three layered ultrasonic viscometer, the intermediate material, layer 2, is an impedance matching layer between layers 1 and 3. 113
5.2 Reflection coefficient with respect to frequency showing different acoustic impedance and thickness values (t1 and t2) of the intermediate medium using Equation 5.10. 116
5.3 Reflection coefficient with respect to frequency showing a comparison between Equation 5.10 and 5.11, where resonant dips were created at a matching layer thickness corresponded to 10 MHz for two different viscosity fluids, Equation 5.11 117
5.4 Illustration of both spring and viscous models while subject to stress. . . . 118
5.5 Argand diagram for the shear modulus relationship. Where G^* is the complex shear modulus, G' is the storage modulus, G'' is the loss modulus and δ is the phase angle. 119
5.6 Reflection coefficient with respect to frequency for a Newtonian model comparing values from Equations 5.10 and 5.11. 122
5.7 A comparison of the minimum reflection coefficient at resonance with respect to frequency for a Newtonian three-layer system, for different viscosity fluids. 122
5.8 Shear numerical diagram illustrating sound propagation specifically for the numerical model. Here pressure, P, is replaced with amplitude, A, layer thicknesses, x, are applied, and speed of sound, c replaces impedance, Z. . 124
5.9 Space and time discretisation for a one-dimensional acoustic system. 125
5.10 Initial wave design showing progression from a harmonic sine wave through to a Gaussian distributed chirp wave. 127
5.11 Numerical Simulation Method. 130
5.12 Representation of layer locations within the simulation. At each boundary a speed of sound change occurs which creates a reflection. 131
5.13 Numerical solution example of an ultrasonic wave striking a fluid interface in a three layered model. 132
5.14 Signal voltage amplitude observation with respect to time at $x = 0$ 133
5.15 Numerical model time domain response at 10 MHz centre frequency for a range of different viscosity fluids and a reference simulation. 134
5.16 Numerical model frequency domain response at 10 MHz centre frequency for a range of different viscosity fluids. 135
5.17 Comparison of the reflection coefficient data obtained using both analytical and numerical solutions for a 10 MHz centre frequency. The analytical model uses Equation 5.18. 136

5.18 Comparison of the reflection coefficient with respect to viscosity. Numerical data points were plotted and fitted with the analytical model, Equation 5.18, which provided a perfect correlation. Results were obtained using a 10 MHz frequency. 137

6.1 Sketch of the ultrasonic viscometer set-up. 140
6.2 Illustration of how a pulsed wave propagates throughout a matching layered viscometer. 140
6.3 Ultrasonic viscometer with a range of matching layers and transducers, where only four of the layers were used. The frequencies shown are the resonant frequencies that relate to the thicknesses of the matching layer. . 142
6.4 Sketch of the ultrasonic viscometer with a range of frequency sensors and corresponding matching layers. 142
6.5 Optimum matching layer impedance 143
6.6 Simulated and measured data of resonance created at 13.86 MHz using a 10 MHz centre frequency piezoelectric element (14 MHz transducer) paired with a matching layer thickness that corresponded to a 5 MHz transducer. 145
6.7 Near field range and beam spread of sound waves inside the matching layer viscometer. 146
6.8 Ultrasonic viscometry fluid measurement radius on the solid - liquid interface for each transducer frequency. Based on the near field range and the beam divergence (half of the beam spread), the additional radius measured due to the sensor size and frequency was calculated. Green is for the 2 MHz transducer, red is for 3 MHz transducer, dark blue is for the 10 MHz transducers and the 14 MHz transducer is simply the radius. 147
6.9 Data acquisition instruments consisting of the PicoScope, TC08, coaxial cables, ultrasonic viscometer and the LabVIEW DAQ VI open on the laptop.148
6.10 Schematic of the experimental configuration, where Tx is the transmitted electronic signal and Rx is the received electronic signal. 150
6.11 Selection of the number of cycles for the ultrasonic waveform. 151
6.12 Averaged full time domain signal using a 10 MHz sensor on the ultrasonic viscometer. 152
6.13 The trimmed first reflection from the measurement interface. 153
6.14 Zero padding added to the trimmed first reflection. 153
6.15 Signal FFT amplitude in the frequency domain. 154
6.16 Reflection coefficient with respect to the frequency. 154
6.17 Indexed reflection coefficient with respect to the frequency, where the indexed frequency for each transducer is shown in Table 6.5. 155
6.18 Untuned evaluation of the analytical (Equation 5.18) and numerical viscosity models with measured data from the standard oils shown in Table 6.6. 158
6.19 Tuned evaluation of the analytical (Equation 5.18) and numerical viscosity models with measured data from the standard oils shown in Table 6.6. . . 160
6.20 Flow chart overview of the signal processing steps required to obtain a functioning ultrasonic viscometer. 162

7.1 Viscosity mean and percentage deviation values of the pure coolant using conventional and ultrasonic viscometry. Figure 7.1a includes the analytical and numerical models compared with the rheometer data for each transducer name. Figure 7.1b compares the percentage deviation of ultrasound and rheometer measurements, where the deviation of the analytical and numerical models are equal. 165
7.2 Water contaminated viscosity comparison between conventional and ultrasonic viscometry for each individual transducer. The black coloured plot is the rheometer data, the green plot is the analytical model and the blue plot is the numerical model. 166
7.3 Copper contaminated viscosity comparison between conventional and ultrasonic viscometry for each individual transducer. The black coloured plot is the rheometer data, the green plot is the analytical model and the blue plot is the numerical model. 168
7.4 Ultrasonic viscosity data with measured frequency for water and copper contaminated mixtures compared with the pure coolant. 170
7.5 Sketch of the ultrasonic wave path and velocity considered by Equation 7.1 and 7.2. 171
7.6 Extrapolating Branchley's, [16], incident velocity with voltage data to obtain velocity values for the frequencies used in this work. 172
7.7 Reading from left to right: A flow diagram showing the method for calculating the shear rate. The analytical viscosity model uses Equation 5.11, the velocity model uses Equation 7.1 and the shear rate model uses Equation 7.2.173
7.8 Ultrasonic viscosity data with calculated shear rate for water and copper contaminated mixtures compared with the pure coolant. 174
7.9 Flow behaviour of pure and contaminated fluid samples, where data from conventional methods for obtaining viscosity is plotted with the corresponding ultrasonic viscosity, over the applied shear rate. The Carreau-Yasuda model (Equation 2.14) was used to fit each sample data set and the values for these fits are presented in Table 7.3. 175
7.10 Measurement area, wavelength and the propagation depth inside the pure coolant for each transducer indexed frequency, Table 6.5. Subscripts 2, 3, 10 and 14 relate to the frequency of the transducers. 178
7.11 Droplets and particles in contact with the measurement interface where the measurement diameter is a small section of the total. 179

D.1 BP's partner rig sensor block. 215
D.2 BP's partner rig sensor block design. 216
D.3 Thermal rig sensor block design. 217
D.4 Shear viscosity sensor plug. 218

List of Tables

2.1 Water solubility of four different dielectric oil compositions at room temperature, [31]. . . . 36
2.2 Petroleum-based oil solubility and viscosity changes with copper contamination over 120 hours of oxidisation, [75]. . . . 40

3.1 Longitudinal and shear SOS values for some common materials, [110, 111]. 57
3.2 Longitudinal acoustic impedance values for some common materials, [110, 112]. . . . 58
3.3 Shear impedance values used in Equations 3.19 and 3.20 to produce Figure 3.9. These values were similar to a metal - oil and a metal - polymer - oil set-up. . . . 67

4.1 Pure coolant density and kinematic viscosity values from the supplied BP data sheet. These values were then used to calculate the dynamic viscosity for each temperature increment. . . . 93
4.2 Measured dynamic viscosity with varying temperatures for pure coolant. . 100
4.3 Predicted viscosity of pure coolant with varying fractions of contamination, calculated using Equation 4.3, 4.5 and 4.4. . . . 105
4.4 Newtonian and Power law parameters used to fit measured data for pure and contaminated coolants. . . . 107

5.1 Initial shear acoustic impedance values for the three layered model used to produce Figure 5.2. Layer 1 has a value similar to that of aluminium, layer 2 has a value similar to a matching layer polymer and layer 3 has values representative of two fluids with different viscosities. . . . 115
5.2 Input variables for the rheological analytical model where parameters for layers 1 and 2 were used with the solid impedance and parameters for layer 3 used the liquid impedance. . . . 120
5.3 Numerical model parameters. . . . 128

6.1 Determining the resonant frequency using different transducer frequencies and corresponding matching layer thicknesses (supplied by polyimide data sheet). Here the actual resonant frequency is created by the polyimide matching layer thickness with the partnered transducer. . . . 144
6.2 Near field and beam spread calculations for each transducer frequency used. 146
6.3 Measurement area for each transducer frequency based on the calculations made in Figure 6.8. . . . 147
6.4 Chirp excitation settings for each frequency using 5 cycles at 4V peak to peak. Here the actual resonant frequency is created by the polyimide matching layer thickness, which is partnered with a transducer of a certain centre frequency. . . . 151

6.5 Indexed frequency values to obtain the reflection coefficient for each transducer. The indexed frequency is the same as the resonant frequency shown in Table 6.4. 156
6.6 Standard calibration oil data from the data sheet, [157, 158]. 157
6.7 Analytical and numerical untuned and tuned materials impedance values used to fit the data in Figures 6.18 and 6.19. 159
6.8 Correlation coefficients for both the analytical and numerical model with respect to measured data. 160

7.1 Low shear rate viscosity of pure coolant with varying fractions of contamination, where the rheometer viscosity was measured in Chapter 4, and the predicted viscosity was calculated using Equation 2.23, 2.25 and 2.24. . . . 164
7.2 Calculated shear rate, in ks^{-1}, for each fluid sample with each transducer. 174
7.3 Carreau-Yasuda model (Equation 2.14) constants used to create fits shown in Figure 7.9. 175

Nomenclature

α	Attenuation Coefficient $(-)$
α_P	Pressure - Viscosity Coefficient $(-)$
β	Numerical Wave Source $(-)$
δ	Oscillatory Shear Phase Shift $(^\circ)$
δ	Wave Displacement (m)
$\dot{\gamma}$	Shear Rate (s^{-1})
η	Dynamic Viscosity (Pas)
η_0	Dynamic Viscosity at Atmospheric Pressure (Pas)
η_0	Zero Viscosity (Pas)
η_∞	Infinite Viscosity (Pas)
η_C	Continuous Phase Viscosity (Pas)
η_D	Dispersed Phase Viscosity (Pas)
η_i	Intrinsic Viscosity (Pas)
η_P	Dynamic Viscosity at Pressure (Pas)
γ	Strain $(-)$
λ	Relaxation Time (s)
λ	Wavelength (m)
λ_r	Ratio of Dispersed to Continuous Phase Viscosity $(-)$
ν	Kinematic Viscosity (m^2s^{-1})
ω	Angular Frequency $(rads^{-1})$
ϕ	Angle of Incidence from the Normal$(^\circ)$
ϕ	Dispersed Phase Volume Fraction $(-)$
ϕ	Surface Tension Angle $(^\circ)$
ϕ	Torsional Flow Angle $(^\circ)$
ϕ_{FCC}	Face-Concentrated Cubic Volume Fraction $(-)$
ϕ_G	Glass Transition Volume Fraction $(-)$
ϕ_p	Maximum Packing Fraction $(-)$
ϕ_{RCP}	Randomly Close Pack Volume Fraction $(-)$
Ψ_l	Liquid-Air Interface Surface Tension (Nm^{-1})
Ψ_{sl}	Solid-Liquid Interface Surface Tension (Nm^{-1})
ρ	Density (Kgm^{-3})
σ	Shear Stress (Pa)
σ^*	Complex Shear Stress (Pa)
σ_0	Initially Applied Stress (Pa)
θ	Acoustic Phase Shift $(^\circ)$
θ	Angle $(^\circ)$
θ	Beam Spread Angle $(^\circ)$
A	Amplitude $(-)$
B	Bulk Modulus (Pa)
c	Speed of Sound (ms^{-1})
c_l	Liquid Speed of Sound (ms^{-1})
c_m	Matching Speed of Sound (ms^{-1})
c_s	Solid Speed of Sound (ms^{-1})
d	Diameter (m)
E	Elastic Modulus (Pa)
F	Force (N)
f	Frequency (Hz)

G	Shear Modulus (Pa)	R	Reflection Coefficient $(-)$
g	Acceleration due to Gravity (ms^{-2})	r	Radius (m)
G^*	Complex Shear Modulus (Pa)	T	Temperature $(°C)$
G''	Shear Storage Modulus (Pa)	T	Torque (Nm)
G'	Shear Loss Modulus (Pa)	T	Transmission Coefficient $(-)$
h	Depth/Thickness/Gap (m)	t	Time (s)
K	Flow Consistency Index $(-)$	t_m	Matching Layer Thickness (m)
k	Spring Stiffness (Nm)	U	Velocity (ms^{-1})
k	Wave Number $(-)$	U_i	Incident Velocity (ms^{-1})
K_γ	Geometric Strain Constant $(-)$	U_r	Reflected Velocity (ms^{-1})
K_σ	Geometric Stress Constant $(-)$	U_t	Transmitted Velocity (ms^{-1})
l	Length (m)	V	Volume (m^3)
P	Pressure (Pa)	x	Space (m)
p	Complex Pressure (Pa)	Z	Acoustic Impedance $(Rayl)$
P_i	Incident Wave Pressure (Pa)	Z_l	Liquid Acoustic Impedance $(Rayl)$
P_r	Reflected Wave Pressure (Pa)	Z_Q	Quartz Acoustic Impedance $(Rayl)$
P_t	Transmitted Wave Pressure (Pa)	Z_s	Solid Acoustic Impedance $(Rayl)$

Chapter 1

Introduction

Current demands to reduce automotive pollution require the need for innovative solutions to meet the demands of their users, such as electrically powered vehicles instead of combustion powered vehicles. Wherever high power is required cooling is necessary, and so, the industry is moving towards dielectric fluids, a tool used previously in transformer technology. Over time, these dielectric fluids degrade, highlighting the need to monitor the health to increase safety and efficiency. This could be achieved using ultrasound.

1.1 Statement of the Problem

Battery cooling fluids are being developed based on previous dielectric fluids used in transformers. Companies like BP Castrol, Shell, Midel and Mivolt are developing dielectric oils that are tailored to a direct (immersion), method for cooling batteries in electric vehicles, Figure 1.1. This is because energy conservation and emissions reduction have become increasingly significant for automobiles due to high energy demand, fuel economy and environmental concerns. Therefore, Electric Vehicles (EV), the most promising solution to emissions reduction, require more power and faster charging to meet user demands [1, 2]. Thus standard cooling methods and fluids are unable to keep up in terms of robustness, heat resistance and cooling capacity. Not only are these fluids essentials for regulating the temperature of the vehicle's battery and power electronics, but they are also needed to lubricate and cool the new types of powertrains and transmissions.

Maintaining battery temperatures between 15-35$°C$ keeps them working at optimum performance [3]. During the charge and discharge cycles, lithium-ion battery cells generate a large amount of heat. The majority of this heat generation happens at charge and discharge extremes, whereas, at a state of charge (SOC) between 20 and 80 percent, there

is usually little heat produced [3]. Also cold batteries cannot be charged quickly, so must be pre-heated. Immersion cooling is a method of thermal management that can keep batteries within their optimum temperature range. Studies have identified immersion cooling as the most efficient and least expensive means of cooling electronics assemblies [4]. Direct contact liquid cooling systems are the simplest and least expensive to build and operate. The drawback to these systems is the large weight increase and so immersed battery modules are spread out underneath the vehicle, Figure 1.1.

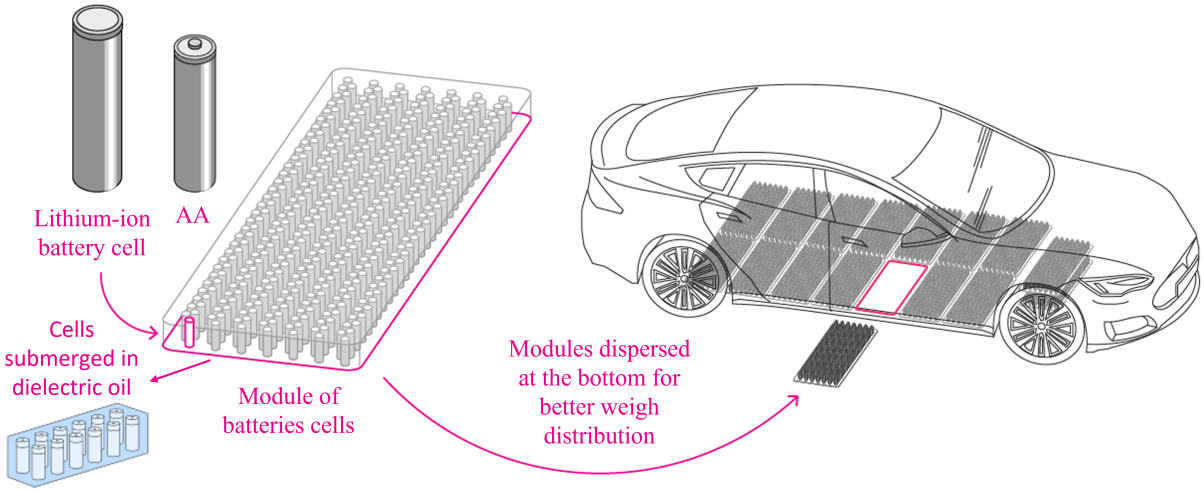

Figure 1.1: Diagram of an electric vehicle with a direct immersion method of cooling, [5].

Harsh conditions can be controlled by an electrically non-conductive liquid that is in direct contact with immersed power electronics. Such liquids are called dielectric oils and have been used in transformer applications for years, as they are compatible with electrical components. These fluids are required to have long lasting dielectric properties in harsh operating conditions such as high temperatures, oxidation, humidity and particle abrasion. In addition, these fluids have excellent thermal properties to cool the high heat generation from high power electronics, and typically have low viscosities to aid heat transfer and pumping efficiency, which is necessary in a cooling system, Figure 1.2. In this situation hydrocarbon oils are used, however synthetic oils are increasing in popularity due to them offering better thermal resistance, cooling properties and having increased

electrical resistance. Examples of good dielectric cooling oils are natural and synthetic esters, [6].

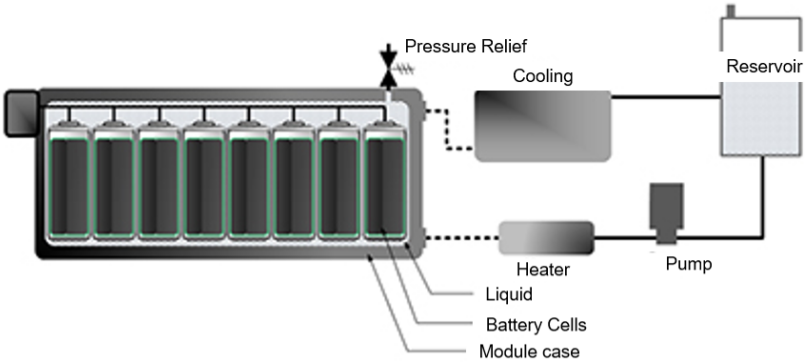

Figure 1.2: Immersion cooling of batteries in electric vehicles, [7].

Dielectric coolants deteriorate throughout their service life due to chemical, electrical and thermal stresses, which stops them functioning as intended. A good example of deterioration is oxidation, which is caused by thermal stress and worsened by contamination. Deterioration can be monitored by measuring the condition of these oils and any additional insulation, such as cellulose to increase thermal management. By monitoring the condition, a timely oil change can be executed and hence a reduction in energy losses and costly system disruptions. During the last two decades a large range of studies have been conducted in developing oil condition sensors which can provide real time and continuous monitoring of health [8]. In general the reasons for oil deterioration are oxidation, wear particle contamination, water contamination, and oil dilution caused by ingress of other fluids [8, 9]. These causes of oil deterioration can be measured through properties such as viscosity, water content, total acid number (TAN), total base number (TBN), particle counting, and flash point, [8, 9], however these are lab based measurements and not in-situ. For in-situ condition monitoring sensors must be able to measure accurately and exhibit a long lifetime while under constant exposure to an aggressive environment inside the engine [10]. They must also be relatively cheap to produce and require little or efficient data processing. The final product should be a system that can accurately determine when the oil is about to reach the end of its life so that it can be replaced. Over time, the data from this product could also be used as a predictive tool to predict the oils end of life. It could

also be used in conjunction with pre existing oil life monitoring (OLM) systems. These systems range in complexity for example, some use a basic miles completed vs mileage interval programmed at the factor, and others use a variety of sensors that measure engine RPM, temperature, pressure, driving habits, climate conditions and more [11, 12, 13].

Non-invasive ultrasonic sensors have shown great promise in harsh operating environments such as journal bearings to measure fluid viscosity at high shear rates using the ultrasonic reflectance technique [14]. An available technology to conduct in-situ high shear measurements is the three layered ultrasonic viscometer. The high ultrasonic shear rates were originally desired to match those produced inside journal bearings, which illustrated the behaviour of the oil and the benefits of its composition under such conditions. It was shown that some oils could exhibit Newtonian behaviour at low shear rates and then shear thinning behaviour at high shear rates from an ultrasonic sensor [15, 16]. The main benefit of this high shear rate is its ability to expose the effects of the oils chemical composition and any additives such as viscosity modifiers. As well as intrinsically high shear rates, this measurement technique has further advantages including low cost, small installation area, capable of working in harsh environments and requires no moving parts. Work carried out using this method has produced reliable results for Newtonian and non-Newtonian fluids and an investigation of accurate shear rate values has recently been conducted with success, [15, 17, 18, 16].

1.2 Novelty Statements

This research thesis utilised the three layered ultrasonic viscometer, developed by Schirru, [15], in a novel application. More specifically, monitoring the health of a dielectric battery coolant with regards to the viscosity changes caused by degradation. The two major catalysts contributing to the degradation of electrical coolants were identified as water and copper contamination. To validate the ultrasonic viscometer a novel numerical model was produced alongside an analytical model to accurately measure the viscosity based on the acoustic theory. Using spectroscopy methods a range of frequencies were utilised to determine the viscometers sensitivity in order to measure a low viscosity oil and to distinguish

between small viscosity changes. By exciting the oil with different transducer frequencies, the fluid is sheared at varying rates, hence the viscosity behaviour with calculated shear rate was observed to understand the impact that contamination had on the dielectrics flow behaviour. Finally the successful use of ultrasound opens up the new possibility to monitor dielectric oil health in-situ. This will have a significant impact as dielectric oils become more widely used in the automotive industry due to the market demands of battery power.

1.3 Aims and Objectives

The aim of this project was to develop ultrasonic viscosity sensors that can measure the quality of a dielectric fluid inside a battery cooling system. It builds on developed technology, which has been used in-situ, that can perform measurements of Newtonian and non-Newtonian fluids at high shear rates. A focus is made on measuring the impact that two major contaminants have on a low viscosity dielectric fluid. These contaminates consist of water and copper, and are most likely to promote oxidation in an automotive battery cooling system. Measurements were completed at a single temperature due to the complexities arising from a large range of temperatures. If contamination could potentially be measured at room temperature, then it would be reasonable to extrapolate that variances can also be observed at higher or lower temperatures. Hence in terms of detection purposes, only one temperature of $23°C$ was used.

1.3.1 Objectives:

- Identify contamination features influencing how a dielectric coolant would degrade in service and highlight how these features will effect the viscosity.
- Produce mixtures of coolant that will best simulate particulate contaminated that will ultimately lead to oxidation and ultimately cause degradation.
- Conduct lab bench measurements using the ultrasonic viscometer to explore the behaviour of the pure coolant and coolant with contamination features, and deduce

whether a change in viscosity with contamination can be monitored.

- Validate measured ultrasonic data with a range of rheological models, acoustic models and standard laboratory rheological testing:
  - Make use of rheological models that can predict the change in viscosity of contaminating features when mixing with the continuous fluid (dielectric oil).
  - Utilise standard rotational rheometer to measure the viscosity of the pure and contaminated coolant mixtures. Evaluate the differences in viscosity between the rotational rheometer data and rheological model predictions.
  - Develop an ultrasonic analytical and numerical model to allow viscosity information to be obtained from the shear ultrasound reflection coefficient by integrating the three layered ultrasonic equation with the Newtonian viscosity equation. This information will then be used to complete a resonant frequency analysis at a range of different frequencies and predict the reflection coefficient for a given viscosity.
  - Validate the analytical and numerical model by comparing with ultrasonic measurements using calibration oils. If necessary, tune both models until a better correlation with measured data is achieved.
- Summarise the effectiveness of the ultrasonic viscometer as a tool to detect contamination which would lead to degradation.

1.4 Thesis Chapters

- **Chapter 2 – Literature Review 1: Fundamentals of Dielectric Oils.**
  This chapter introduces the reader to the composition, physical properties, classification tests of dielectric oils, dielectric oil degradation, and rheology of emulsions and suspensions. The main focus of this chapter is to highlight what a good dielectric oil is composed of, how they degrade and the most influential degradation features. A particular focus is made on the viscosity as this physical property is required to understand the contents in later chapters.

- **Chapter 3 – Literature Review 2: Ultrasound to Measure Viscosity.**
  The main focus of this thesis is to use ultrasonic sensors to measure the viscosity of a coolant with varying degrees of contamination. Therefore, this chapter provides an introduction to the physics of ultrasound. It is structured methodically by starting with a basic definition, advancing to the various wave modes, how they behave inside materials and with boundaries, and how these waves are practically applied and analysed. This chapter concludes by linking rheology with acoustics and exploring the current literature of ultrasonic viscometers.

- **Chapter 4 – Rotational Viscometry.**
  The focus of this chapter is to characterise the pure coolant, followed by coolant-water emulsions and coolant-copper suspensions, which are used throughout this thesis. Characterisation consists of investigating their viscosity behaviour under varying shear rates (Newtonian/non-Newtonian) and measuring the apparent viscosity. To verify the dynamic viscosity, pure coolant is investigated at varying temperatures in order to compare measured values with values attained from its supplied data sheet. Mathematical models described in Chapter 2 are utilised to predict the apparent viscosity of mixtures and are later compared with measured data as an explanation tool. Finally, this chapter provides the feasibility of using shear viscosity to measure contamination in a dielectric coolant and observes its sensitivity for each degree of contamination.

- **Chapter 5 – Analytical and Numerical Models to Predict Ultrasonic Shear Viscosity.**
  This chapter describes an analytical model that is used in conjunction with a numerical model to understand the effects of a shear wave contacting a solid-liquid interface. More specifically, how the reflection coefficient changes with varying liquid viscosity. This enables viscosity predictions of the coolant and contaminated mixtures, which are carried out in Chapter 7.

- **Chapter 6 – Methodology for Ultrasonic Shear Viscometry**
  This chapter outlines the practical measurement methodology of ultrasonic viscome-

tery that is used to measure viscosity changes due to contamination in a dielectric coolant, which is discussed in Chapter 7. It outlines all experimental hardware, procedures and setup in order to conduct measurements. It then discusses the calibration process for a range of sensor frequencies and evaluates their results with the analytical and numerical model from Chapter 5.

- **Chapter 7 – Ultrasonic Shear Viscometry to Detect Contamination.**
  This chapter outlines the practical measurement of ultrasonic viscometry in order to measure viscosity changes caused by contamination in a dielectric coolant. Firstly, the ultrasonic transducers are used to measure the viscosity of the pure coolant fluid and a comparison is made with conventional viscometer tests conducted in Chapter 4. The coolant is then artificially contaminated using distilled water and copper. An evaluation is then made on the measured ultrasonic viscosity and how this compares with viscometer data. Finally the applied shear rate is calculated and the flow behaviour of each fluid is observed in order to determine the negative impact contamination has on their dielectric and cooling properties.

- **Chapter 8 – Conclusions.**
  The key findings of the research conducted in this thesis are presented. It begins by highlighting the novelty and impact, followed by an overview of each segment that lead to the discoveries of this work. Each segment consisted of conventional rheometry testing and comparisons with mixture models, the development of an analytical and numerical model, explaining the methodology and finally, measuring viscosity using a three layered ultrasonic viscometer.

Chapter 2

Literature Review 1: Fundamentals of Dielectric Oils

This chapter introduces the reader to the composition, physical properties, classification testing and the degradation of dielectric oils. The main focus of this chapter is to highlight what a good dielectric oil is composed of, how they degrade and the most influential degradation features. A particular focus is made on the viscosity as this physical property is required to understand the contents in later chapters.

2.1 Introduction

The primary objective of a dielectric oil is to provide effective cooling capability for power electronics, such as batteries, transformers, capacitors and high voltage cables. In order to provide this, they are required to be electrically insulating and suppress unwanted electrical discharge. The viscosity of insulating oil is a principal parameter for characterising its design for heat dissipation and pump forced convection. It is also a very informative parameter for indicating the condition of an oil. The most common degradation feature for dielectric oils is oxidation. With increased oxidation, there is an increase in the viscosity and a decrease in its ability to dissipate electrical discharge, which hinders the oils effectiveness [19, 20]. Oxidation is exacerbated by the ingress of water and particulates, both reportedly cause an increase in viscosity [19, 20]. If monitoring of the viscosity could be achieved in-situ then timely oil changes could aid effective cooling and electric insulation. There is a great variety in the type of oil that can be used as the insulation fluid, and the chemistry, performance and sustainability of these fluids vary greatly.

2.2 Composition

Modern dielectric fluids are formulated from a range of base fluids and chemical additives, where base fluids can be divided into natural and synthetic organic liquids and inorganic liquids, [21]. A base oil is the foundation of a lubricant before additives are added, at which point it is considered a formulated oil.

2.2.1 Petroleum-base Oils

The majority of dielectric base fluids are petroleum-based, and are produced by refining crude oil due to performance, availability and low-cost [21]. Saturated and unsaturated hydrocarbons are the most important classes of refined crude oil, which are predominantly made up of paraffinic (straight and branched alkanes), naphthenic and aromatic, Figure 2.1, [22]. They each have their own characteristics that change the oil performance for a variety of electronic applications [23].

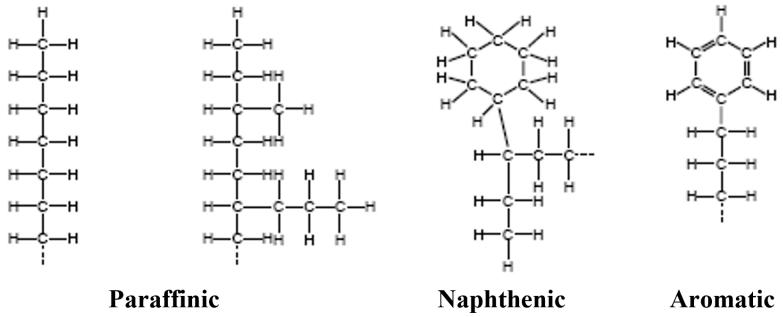

Figure 2.1: Petroleum-based oil composition, [24].

The physical characteristics of petroleum-based oil are determined by the dominant compound of the oil, which is either paraffinic and naphthenic. Paraffinic oil is known for its good thermal and oxidation durability, as it has a high viscosity index, caused by the presence of wax, and the rate of oxydation is lower than naphthenic oils, [25]. Viscosity index (VI) is an arbitrary measure to characterise the change of oil viscosity with temperature variations, where a higher VI indicates less change in viscosity with temperature and vice versa, [18]. Naphthenic dominated petroleum oils do not contain wax, which reduces

the pour point. They also have better heat distribution and a lower viscosity than paraffinic oils and their oxidation by-product (sludge) is soluble, [26]. Aromatic compounds also influence the physical and chemical properties and can maintain thermal properties similar to purely paraffinic or naphthenic oil, [25, 27]. However, retention of aromatic compounds lowers the oxidation resistance and adversely influence their electrical properties, [28].

Petroleum-base oils are an effective dielectric oil, however they are highly flammable, hazardous when in direct contact, and have poor biodegradability, [26]. For these reasons, synthetic-base oils are being explored.

2.2.2 Synthetic-base Oils

Synthetic oils are similarly available for use, and can provide inherent performance improvements over conventional petroleum-based dielectric oils. However, the cost of producing synthetic based oils can be much greater than petroleum-based oils. A large range of potential synthetic-base stocks exist, where the most common are, polyalphaolephins (PAO), silicones, synthetic esters and natural esters, which are illustrated in Figure 2.2, [24, 25, 29].

PAOs are a very common synthetic oil, which have a variety of uses. For liquid dielectrics, they can be manipulated in the polymerisation process to produces oils with a lower pour point and a higher viscosity index. They also have high resistance to oxidation and are not toxic or corrosive, [30]. Synthetic esters are commonly used to replace petroleum oils and are produced by reacting alcohol with acids. They have advantages over petroleum and other synthetic bases, such as less viscosity, higher dielectric strength, low flammability and increased biodegradability. Silicone based oils are less flammable than synthetic esters but they are more expensive and less biodegradable. Vegetable oils are also being used to replace petroleum-based oils in distribution apparatus for environmental reasons. These natural ester compounds are derived from castor, corn, linseed, rapeseed, olive oils, etc. However, some natural esters work poorly in low temperature conditions.

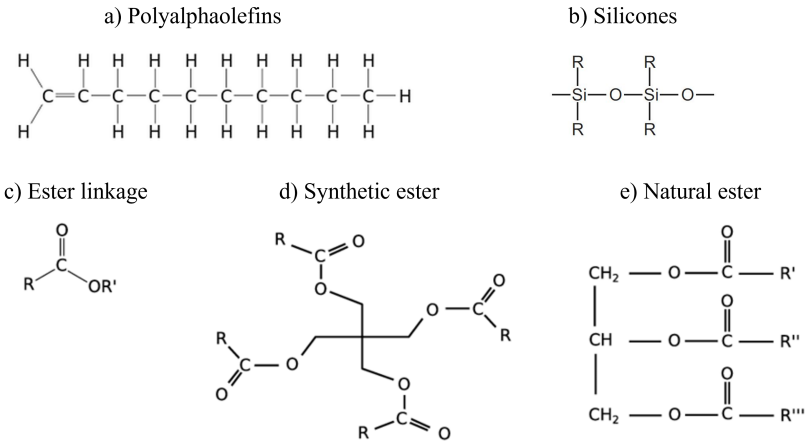

Figure 2.2: Synthetic-based oil composition, [31].

2.2.3 Additives

Petroleum and synthetic base oils have similar problems with regards to their fortification against contamination and degradation, and their ability to withstand varying operation environments. Dielectric oil additives are chemicals that are added to oils in quantities of a few weight percent to ensure greater functionality, long term stability and increase resistance to oxidation. However, additives can change a Newtonian base oil into a non-Newtonian oil, due to their behaviour and interaction with oil molecules while under varying shear rates.

2.2.3.1 Viscosity Improvers

Viscosity improvers are mainly oil soluble polymers or copolymers that work via shape change. When cold the polymer molecules are small and coil-shaped, thus they do not increase the oil's viscosity. With rising temperature, the molecules expand and uncoil, which compensate for the decrease of viscosity that is caused by the higher temperatures. Unfortunately, viscosity additives are sensitive to ageing caused by repeated mechanical shearing, and over time, lose their ability to act as thickener at high temperatures.

2.2.3.2 Pour Point Additives

These additives are used to reduce the pour point value and allow the oil to operate at low temperatures. They are often used to modify low temperature flow characteristics, which allows for a greater choice of base stock selection. Some examples of pour point additives consist of alkylaromatics and aliphatic polymers.

2.2.3.3 Demulsifier additives

Demulsifier additives prevent the formation of a stable oil-water mixture or an emulsion by changing the interfacial tension of the oil so that water will coalesce and separate more readily from the oil, [32].

2.2.3.4 Antioxidants

Dielectric oils inevitably oxidise during service and this causes a gradual rise in the acidity, and eventually the viscosity. When acids are produced they are extremely corrosive and lead to deterioration of non-ferrous metals such as copper. Dielectric oils are therefore added with antioxidants to counteract this phenomenon. Antioxidants stop the formation of acids by acting as a free radical trap, which disrupts the oxidation process, [33]. Any differences in oil oxidation resistance largely depends on these additives.

2.2.3.5 Corrosion Control

Corrosion inhibitors are added for several reasons. Firstly, they mitigate corrosion problems of metal (both ferrous and non-ferrous) components within a cooling system or power electronics. They also act as an indirect antioxidant, as they protect the metal surfaces that promote oxidation, [30]. Finally, they reduce electrostatic charging of an oil during pump forced convection flow through small pipes, [33].

2.2.3.6 Contamination Control

Contaminants of dielectric oils consist of water, ferrous and non-ferrous wear debris, cellulose, etc. To control and prevent the development of these contaminants, detergents

and dispersants are added [34]. Detergents are used to reduce deposits and provide anti-corrosion and anti-rust protection within direct oil cooled electrical systems. They work by neutralising acids formed in the oxidation process. Dispersants are used to suspend the sludge build up as a result of oxidation, and they do this by stopping large particles conglomerating. The drawback when using these is that their high molecular weight causes an increase in viscosity, which hinders its ability as a coolant.

2.3 Physical Properties

Viscosity provides important information about how a fluid flows. Typically a good heat transfer fluid requires a lower viscosity as it designed to be easily pumped around a cooling system. Other properties of a heat transfer fluid are also vital to consider. These properties consist of specific heat, thermal conductivity, thermal diffusivity, surface tension, interfacial tension, flash point and pour point, which are all discussed in the following subsections.

2.3.1 Viscosity

When a force is applied to a liquid comprised of molecules they interact with each other in a sliding motion and cause a resistance to flow. The larger the molecules, the greater the viscosity value. The dynamic viscosity is defined as the ratio of the applied shear stress, σ, to the resulting shear rate, $\dot{\gamma}$. Dynamic viscosity is important as it illustrates a fluid's ability to work effectively in a situation where the fluid is being moved at different rates. Using the two plates model analogy, Figure 2.3, to represent a fluid being sheared, the shear stress and shear rate are defined in Equations 2.1 and 2.2, with units N/m^2 and s^{-1} respectively. Equation 2.1 represents the shear stress produced by an applied force, F to the top plate over an area. Equation 2.2 shows the rate of shear induced by the top plate moving at a velocity, U. As the bottom plate is fixed, a velocity gradient over the distance, h, is created between the two plates. Therefore the shear rate is a differential equation where the change in velocity, δU, is dependent on the change in distance, δy.

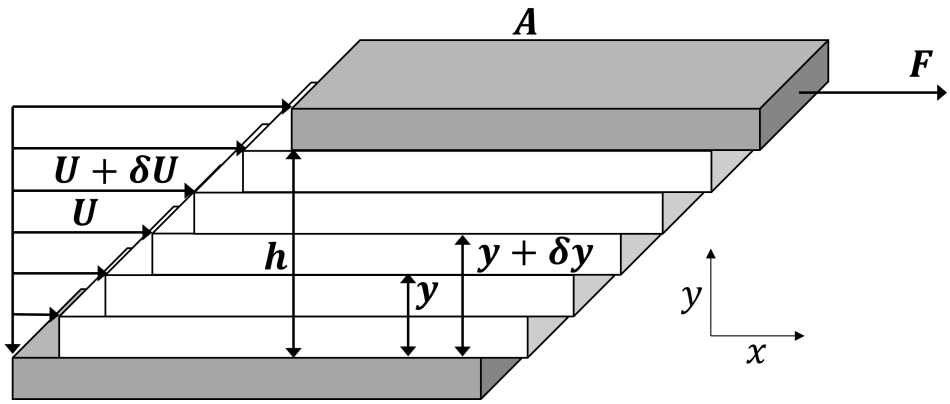

Figure 2.3: Viscosity two plates model under laminar flow conditions, where the bottom plate is fixed and the top plate is forced into motion.

$$\sigma = \frac{F}{A} \tag{2.1}$$

$$\dot{\gamma} = \frac{\delta U}{\delta y} \tag{2.2}$$

The relationship between dynamic viscosity, η, shear stress, σ, and shear rate, $\dot{\gamma}$, is shown in Equation 2.3. According to Newton's law the ratio of shear stress to shear rate is equal to the dynamic viscosity, measured in Pas (Ns/m^2).

$$\sigma = \eta\dot{\gamma} \tag{2.3}$$

Kinematic viscosity is defined as fluid motion under the constant force of gravity, whereas the dynamic viscosity gives information on the force required to make the fluid flow at a certain rate [35]. The benefits for using kinematic viscosity are the simplicity and precision achieved in comparison to dynamic viscosity. Kinematic viscosity, ν, has units, m^2/s, and is related to the dynamic viscosity by the fluid's density, ρ.

$$\nu = \frac{\eta}{\rho} \tag{2.4}$$

2.3.1.1 Viscosity and Temperature

Considering the behaviour of viscosity with temperature is necessary for many engineering applications. As the temperature increases the viscosity will decrease. This is caused by molecules within an oil gaining energy, which produces a reduction in strength between interacting molecular bonds. Measuring the kinematic viscosity of a liquid at several temperatures allows its viscosity-temperature relationship to be determined, which can be used to extrapolate values for unknown viscosities, [36]. If dynamic viscosity is measured at several temperatures an unknown dynamic viscosity can be accurately calculated using the Vogel equation, Equation 2.5, where a, b and c are constants, T is temperature and η is viscosity, [37].

$$\eta = ae^{\frac{b}{T-c}} \tag{2.5}$$

2.3.1.2 Viscosity and Pressure

With increasing pressure, there is an increase in the viscosity as there is less volume for the fluid molecules to occupy. Hence there is a greater resistance to flow. The behaviour between pressure and viscosity is typically expressed using the Barus equation shown in Equation 2.6, where η_P is the viscosity at the concerned pressure, η_0 is the viscosity at atmospheric pressure, α_P is the pressure - viscosity coefficient and P is the pressure concerned, [38].

$$\eta_P = \eta_0 e^{\alpha_P P} \tag{2.6}$$

2.3.1.3 Viscosity and Shear Rate

Fluids have either a Newtonian or non-Newtonian behaviour when a shear rate is applied. Newtonian oils have viscosities that obey Equation 2.3, whereas non-Newtonian fluids have a viscosity which changes with time or an applied shear rate, [39]. There are a number of different behaviour types for a non-Newtonian fluid, some key behaviours consist of plastic, pseudo-plastic (shear thinning), dilatant (shear thickening), thixotropic and rheopectic.

Figure 2.4 shows these examples for when the shear stress and viscosity are non-linear with either shear rate or time. Each behaviour in Figure 2.4 is defined as:

1. Newtonian - Viscosity is not dependant on time or applied shear rate.
2. Pseudo-plastic - Viscosity decreases with an increasing rate of shear.
3. Dilatant - Viscosity increases with an increasing rate of shear.
4. Plastic - Shear stress must reach a minimum value (yield point) before flow begins.
5. Thixotropic - At a constant shear rate the viscosity decreases over time.
6. Rheopectic - At a constant shear rate the viscosity increases over time.

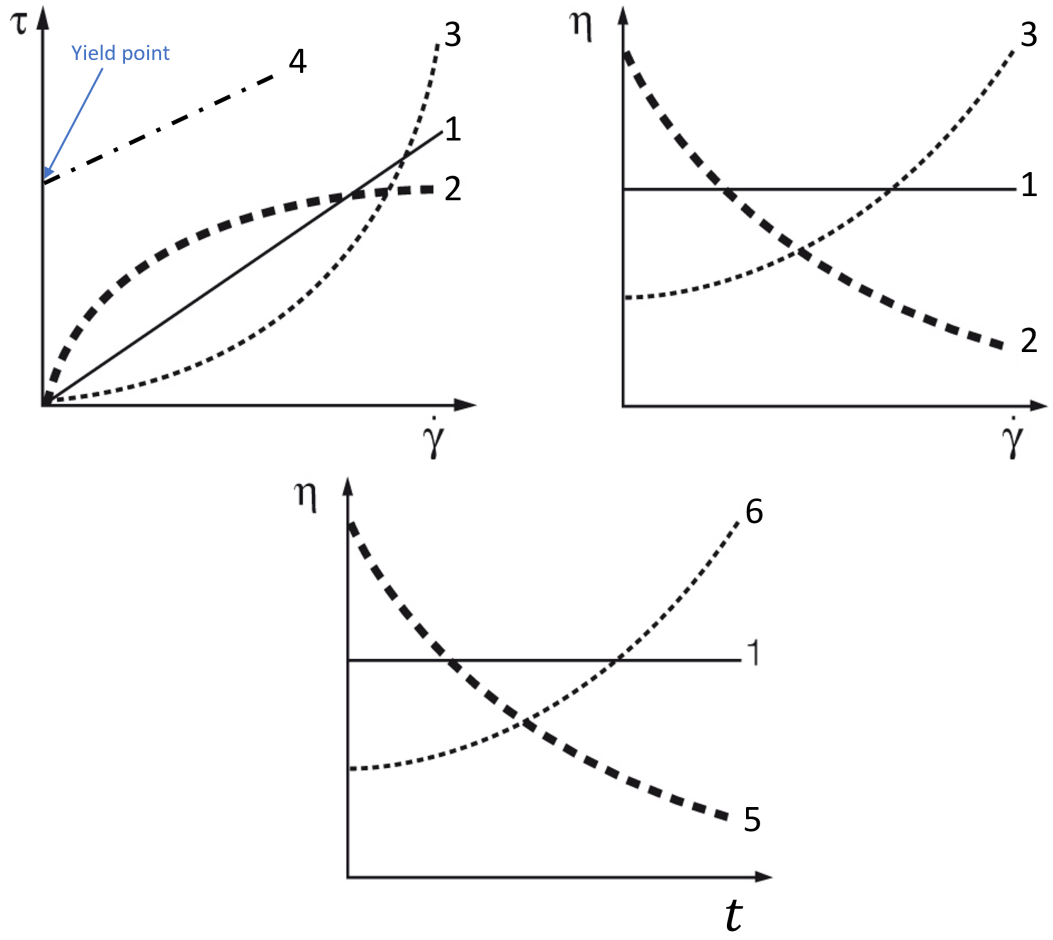

Figure 2.4: Shear stress and viscosity behaviour of Newtonian and non-Newtonian fluids. 1) Newtonian, 2) Shear thinning, 3) Shear thickening, 4) Plastic, 5) Thixotropic, 6) Rheopectic, [40].

To describe shear thinning behaviour, Figure 2.5 illustrates polymer chains, emulsion droplets and particles which are all suspended in a fluid under a shearing motion. As the fluid is sheared the suspended matter align and elongate, which causes a reduced resistance to motion and therefore, viscosity. If the emulsion is water in oil, individual droplets naturally attract each other to form larger droplets, until there are two separate liquid phases. When a shear force is applied to this emulsion, it can causes the water to break up, which produces a progressively smaller resistance to motion and therefore a smaller viscosity. Shear thickening behaviour is far less common than shear thinning, and is mostly undesirable.

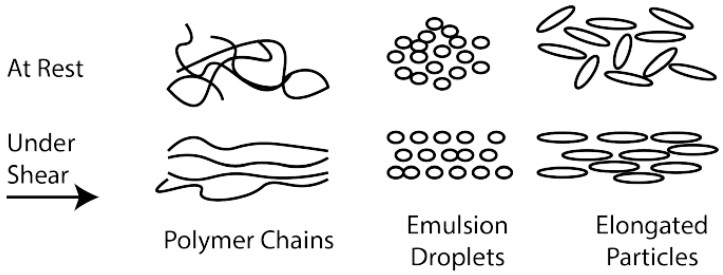

Figure 2.5: Shear thinning behaviour of polymer chains, droplets and particles, [41].

2.3.1.4 Shear Modulus and Non-Newtonian Fluids

Up to this point, only steady shear has been considered, however, shear may be applied by oscillatory motion. Where steady shear operates with a continuous rotation, oscillatory shear operates with a sinusoidal displacement, as shown in Figures 2.6a and 2.6b respectively. The two measurement types are often related by the Cox-Merz rule [42], where $\dot{\gamma}$ is the steady shear rate and ω is the angular velocity, 2.7.

$$\eta\left(\dot{\gamma}\right) = \eta\left(\omega\right) \tag{2.7}$$

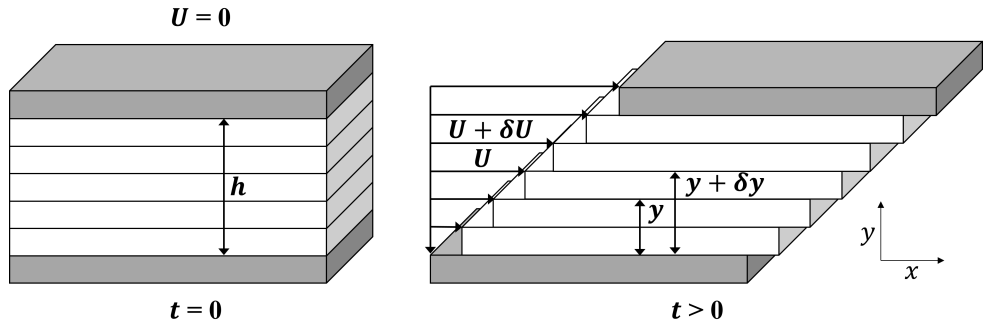

(a) Steady shear.

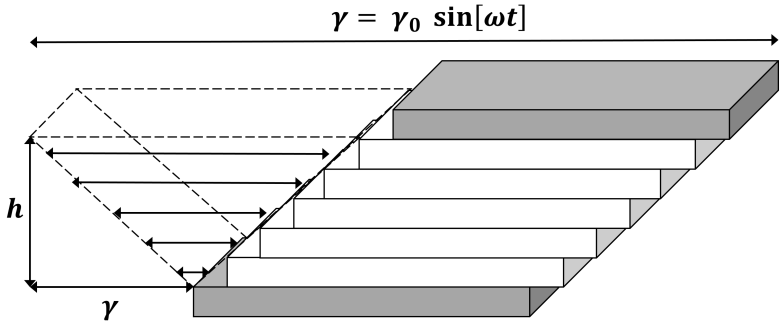

(b) Oscillatory shear.

Figure 2.6: Steady and oscillatory shear.

The shear modulus, G, represents the ratio between the shear stress, σ, and shear strain, γ, and reveals information about whether the material exhibits ideally elastic deformation, Equation 2.8.

$$G = \frac{\sigma}{\gamma} \tag{2.8}$$

Referring to Figure 2.6a, the shear strain is equal to the distance moved in the x direction divided by the distance between the plates, h. The relationship between dynamic viscosity and shear modulus can be derived from Equation 2.3 and Equation 2.8, where ω is equal to the angular velocity, $\omega = 2\pi f$.

$$\eta = \frac{G}{\omega} \tag{2.9}$$

Non-Newtonian fluids display a mixture of viscous and elastic behaviour when under a shear force. In contrast, Newtonian fluids only exhibit viscous behaviour. The complex

shear modulus, G^*, represents both viscous and elastic components of a non-Newtonian fluid under oscillatory shear conditions. Its relationship with the complex shear stress, σ^*, and shear strain, γ, is shown in Equation 2.10.

$$G^* = \frac{\sigma^*}{\gamma} \tag{2.10}$$

To represent both viscous and elastic behaviour, the complex shear modulus is a combination of the storage modulus, G', and the loss modulus, G'', shown in Equation 2.11. The storage modulus is the elastic portion of the viscoelastic behaviour and represents the energy stored in the deformed material, which is used to reform the structure to its original shape. The loss modulus is the viscous part of the viscoelastic behaviour and occurs due to the internal friction, which creates heat that is absorbed by the material.

$$G^* = G' + iG'' \tag{2.11}$$

The relationship between the complex shear modulus, storage modulus and loss modulus can be illustrated using an Argand diagram shown in Figure 2.7 and the two plates model in Figure 2.6b. If the top plate is driven by a force, the bottom plate opposes this with a counter force to remain in an equilibrium state. With respect to time, the stress and strain caused by the applied force and counter force can be represented using sine waves, where any lag between them creates a phase shift, δ. The phase shift is $0°$ for a pure elastic material, $90°$ for a pure viscous material and between $0° - 90°$ for a viscoelastic response. This phase shift is described using the loss factor, $tan\delta$. The relationship between the complex shear modulus, storage modulus, loss modulus, and phase shift is shown in Equation 2.12 and presented in Figures 2.7 and 2.8, [41].

$$tan\delta = \frac{G''}{G'} \qquad G' = \sigma^* cos\delta \qquad G'' = \sigma^* sin\delta \tag{2.12}$$

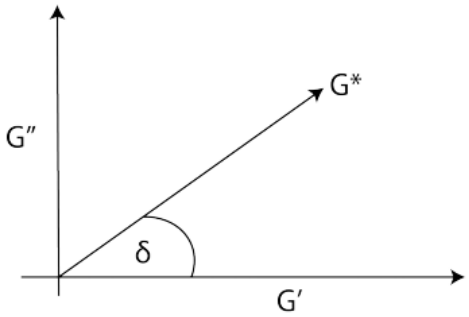

Figure 2.7: Argand diagram for the shear modulus relationship.

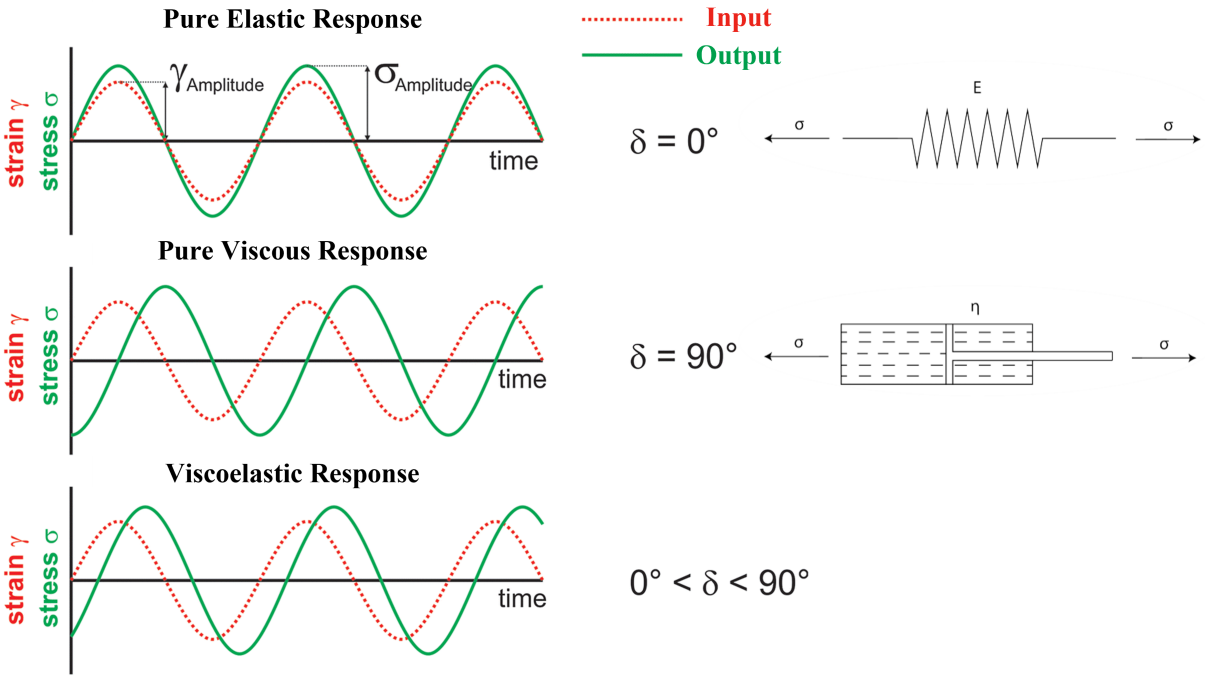

Figure 2.8: Illustration of the phase angle changes for a material under oscillatory shear, [43].

2.3.1.5 High Shear Viscosity of Complex Oils

Base oils are typically considered Newtonian due to their behaviour under an applied shear and their relative structural simplicity. However, fully formulated oil and oil with water and/or particulate contamination can cause non-Newtonian behaviour when a high shear rate is applied, [44, 45]. This is due to the polymer chains, droplets and particles which were discussed in Section 2.3.1.3. The non-Newtonian behaviour occurs within a certain shear rate region, as depicted in Figure 2.9. Figure 2.9 illustrates this behaviour, where 3

significant sections are highlighted.

- Initial Newtonian plateau - Also called the zero viscosity, η_0, the viscosity in this region remains constant as the shear rate increases.
- Transition zone - The viscosity reduces because the high shear rate causes the contamination particles to become aligned and elongated.
- Second Newtonian plateau - Also called the infinite viscosity, η_∞, the viscosity becomes constant again as the contamination particles are fully aligned and elongated.

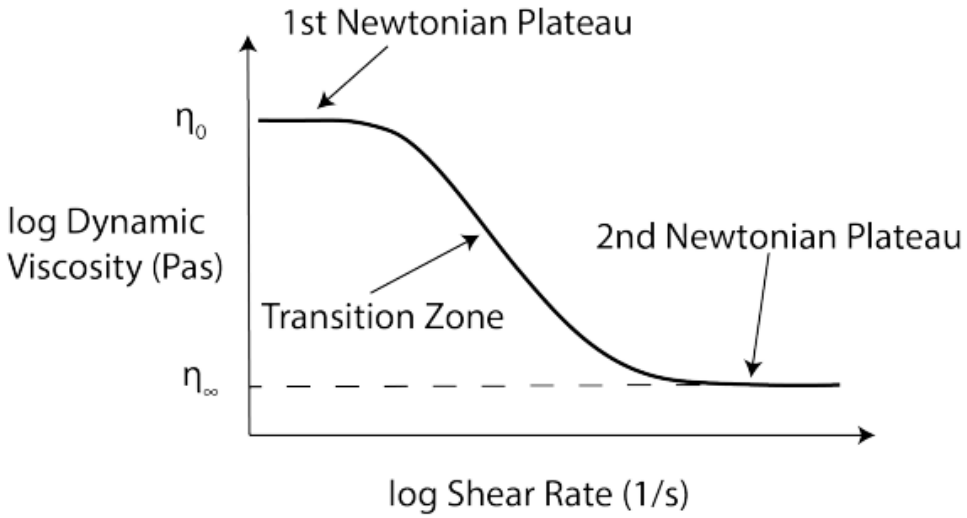

Figure 2.9: Illustration of the 3 zones for the viscosity behaviour with high shear rates for complex oils, [16].

Mathematical models can be used to relate the shear rate with the viscosity for complex oils. The two most popular for high shear rate non-Newtonian behaviour are the Power Law model and the Carreau-Yasuda model, [46]. The Power Law model is used to model the viscosity of shear-thinning fluids where the fluid does not have Newtonian plateau regions. It calculates the viscosity, η, using flow consistency index, K, and the power law constant, n, Equation 2.13. A Newtonian fluid has an n value equal to 1, a shear thinning fluid is less than 1, and shear thickening has a value greater than 1.

$$\eta = K\dot{\gamma}^{n-1} \tag{2.13}$$

The Carreau-Yasuda model is more complex than the Power Law model and is used to model both shear thinning and shear thickening flow for the viscosity as it approaches infinity. The relationship between these models can be seen in Figure 2.10.

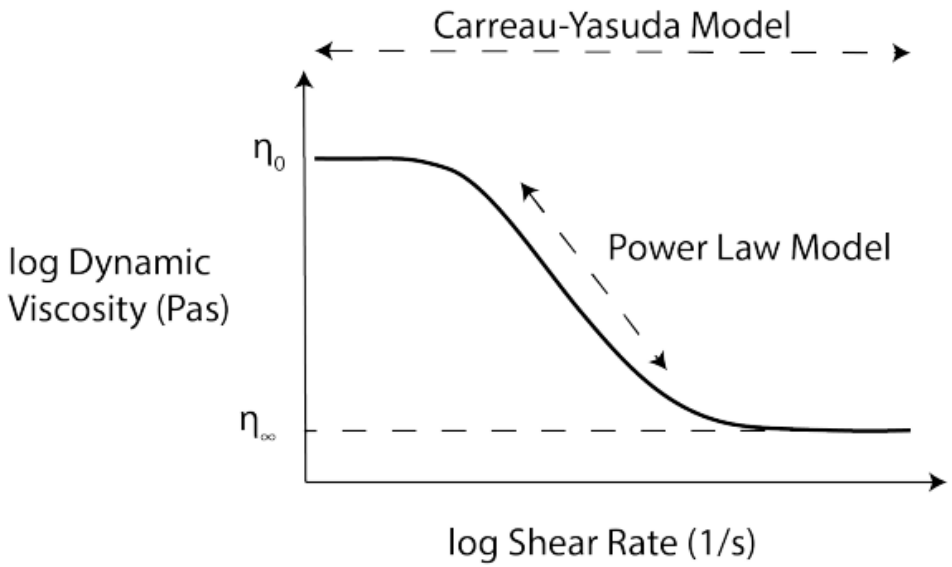

Figure 2.10: Carreau-Yasuda Model, [16].

The Carreau-Yasuda model calculates the viscosity, η, using the viscosity at zero shear rate, η_0, the viscosity at an infinite shear rate, η_∞, the relaxation time of the fluid, λ, the shear rate, $\dot{\gamma}$, the power index, n, and the index controlling the transition from the first Newtonian plateau to the power law region, a. The variables in the Power law and Carreau-Yasuda model are independent of each other.

$$\eta = (\eta_0 - \eta_\infty)\left[\left[1 + (\lambda\dot{\gamma})^a\right]^{\frac{1-n}{a}}\right] + \eta_\infty \tag{2.14}$$

2.3.2 Thermal Properties

The most important thermal properties of oils are specific heat, thermal conductivity, and thermal diffusivity. The specific heat is defined as the amount of heat energy required to raise the temperature of the unit mass of a material. The thermal conductivity is the rate at which heat is transferred through a material, when a temperature gradient occurs. The thermal diffusivity describes how well a material can spread heat. These

parameters are essential for assessing the cooling properties of dielectric oils. Specific heat has a linear relationship with temperature and usually decreases with decreasing hydrogen bonding. For scale, the specific heat of oils are usually half that of water. Thermal conductivity also varies linearly with temperature and decreases with decreasing hydrogen bonding. Temperature characteristics are also important. At high temperatures oils degrade by oxidation, while at low temperatures oils are near solid. Defining an oil's working temperature range is essential before using in a certain application.

2.3.3 Surface and Interfacial Tension

Surface and interfacial tension are directly related to the free energy of a fluids molecules at the surface boundary between a gas or another liquid, respectively. Surface tension is defined as a surface film of minimum area between a liquid and a gas. In this case liquid molecules at the surface form stronger bonds to other neighbouring surface molecules. The interfacial tension is a similar phenomena that occurs between two immiscible liquids such as oil and water. Surface tension for oils is important as it allows the design of better wetting and spreading ability over surfaces, [47]. It is also frequently used with the neutralisation number (total acid number, TAN, and total base number, TBN) to measure deterioration in dielectric oils. Interfacial tension is approximately the difference between surface tension values of two dissimilar fluids. It can also be used to determine the presence of contaminants and oil decay products, where oxidation and contamination causes a lower interfacial tension, [47].

2.3.4 Flash Point

The flash point is the temperature at which an oil gives off enough vapours to produce a flammable mixture with air. It specifies the chances of a fire hazard within high power electrical systems. Therefore, dielectric oils require high flash points to withstand the maximum temperature of the electrical application.

2.3.5 Pour Point

The pour point is the minimum temperature at which oil starts to flow under standard test conditions. Pour point is a valuable property as it could allow the dielectric fluid to operate in cold conditions. If the oil temperature falls below the pour point, the dielectric coolant seizes to flow under pumped convection, and therefore, it would fail to fulfil its purpose.

2.4 Electrical Properties

Dielectric oils are required to provide electrical insulation to power electronics to maintain safety while keeping the temperature in a working range. Therefore, their electrical properties are tested to observe their behaviour under standardised test methods. These properties consist of dielectric strength, resistance and dielectric dissipation, and are discussed in the following subsections, [48].

2.4.1 Dielectric Strength

The dielectric strength, or breakdown voltage (BDV), is the amount of voltage required to produce a spark between two electrodes that are submerged in oil. A low value of BDV indicates a poor dielectric oil or the presence of moisture content and conducting substances in the oil. The minimum BDV an oil can be for use with high power electronics is considered 30 kV, [48].

2.4.2 Specific Resistance

The specific oil resistance is a measure of direct current resistance between two opposite sides of a 1 cm^3 block of oil. With an increase in temperature, the resistivity of oil decreases rapidly. Therefore, a dielectric oil's specific resistance must be high across a full range of temperatures in a specific application. Hence specific resistance of an oil is measured at a low temperature of $27°C$ and a high temperature of $90°C$.

2.4.3 Dielectric Dissipation Factor

The dielectric dissipation factor (tan δ) is measured by placing a dielectric oil between the live part and the grounded part of an electrical circuit, and measuring the flow of leakage current. When a potential difference is created across the oil, the capacitive current will lead the voltage by 90°, Figure 2.11, [49]. If the loss angle is small, a good insulating material with high resistance to current is indicated. As the value of tan δ increases, the specific resistance decreases, therefore, both values are not required for the same oil.

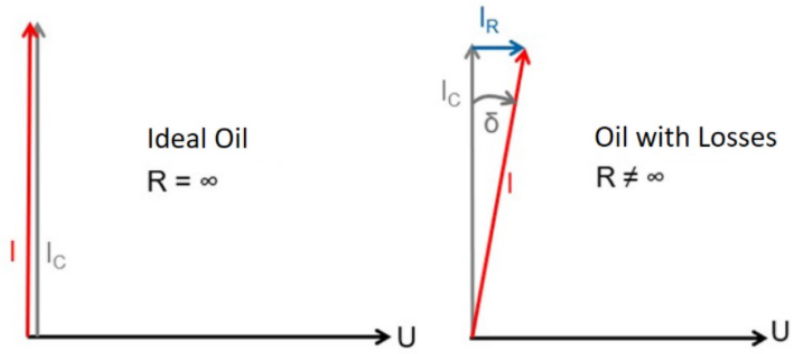

Figure 2.11: The dielectric dissipation factor (tan δ) where an ideal oil with high insulation has a current leading the voltage by 90°. Any losses in insulation reduce this lead by angle, δ, [50].

2.5 Chemical Properties

All oils contain an amount of water and/or acidity level. As they are polar, these chemical properties have a direct impact on the ability of a dielectric oil to provide the necessary insulation to electrical components. Therefore, assessments and removal of an oil's water content, along with neutralisation of acids are completed to an industry standard. These properties are discussed in the following subsections.

2.5.1 Water Content

Water content, measured in parts per million (ppm), in a dielectric oil is highly undesirable as it affects the oil's dielectric properties adversely. According to industry standards, [51],

the recommended water content in a dielectric petroleum-base oil is allowed up to 50 ppm, or 0.005%, whereas a synthetic ester can have up to 2600 ppm for a new oil, [52, 31]. Temperature monitoring is critical when examining the amount of water content, as water in oil solubility increases with increasing temperature, Furthermore, larger temperatures cause oxidation where acids form and further increase the solubility of water in the oil. This is a detrimental sequence of heat, oxidation, acidity and water.

2.5.2 Acidity

As previously stated, increasing acidity results in water becoming more soluble in the oil and causing a knock-on effect that accelerates degradation. The amount of acidity is measured using a neutralisation number, which is the amount of potassium hydroxide per gram of oil required to neutralise the acid levels. Its result is reported as the total acid number (TAN). There is also total base number (TBN), which is the neutralisation of alkaline compounds.

2.6 Testing Properties of Dielectric Fluids

The important properties formerly discussed require standardised methods of testing to ensure effective dielectric oils are created. The following subsections elaborate on a variety of key tests, mainly focusing on viscosity measurement.

2.6.1 Capillary Viscometer

The capillary viscometer, Figure 2.12, measures kinematic viscosity using a fluid in the left side of the tube and allowing it to flow into the right side using surface tension and adhesive forces between the fluid sample and capillary walls. The flow is timed between level A and level B, where this time is directly proportional to the liquid's kinematic viscosity. The simple design, using no moving parts, and ease of use makes this test advantageous to use. However, error can occur with angular misalignment, temperature inaccuracy and oil cross contamination due to the difficulty of cleaning. Equation 2.15 illustrates a common

method for calculating the viscosity using this test, where g is the acceleration due to gravity, h is the height of the capillary, d is the diameter of the capillary, l is the length of the capillary and V is the volume of liquid dispensed, [53].

$$\nu = \frac{\rho g h d^4}{8 l V} \tag{2.15}$$

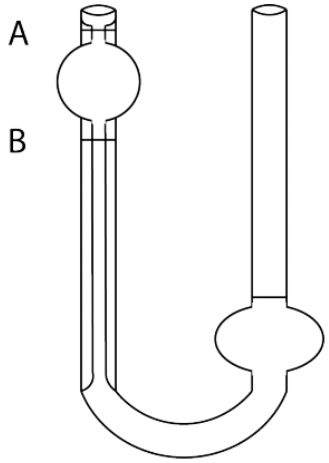

Figure 2.12: Capillary viscometer, [16].

2.6.2 Rotational Rheometers

Rotational rheometers measure the dynamic viscosity of fluids at a specific shear rate value or over a range of shear rates. To shear a fluid it uses a drive motor to rotate the spindle and a force sensor to measure the torque, [54]. The most common types of rotational rheometers are cone on plate, parallel plate, and cylindrical rheometers, whereby the dimensions of their spindles can be manipulated to measure at different shear rates and increase accuracy for a certain fluid. The viscosity, η, is obtained using Equation 2.16, where T is the torque, ω is the angular velocity, and K_σ and K_γ are the stress and strain geometric constants respectively.

$$\eta = \frac{T K_\sigma}{\omega K_\gamma} \tag{2.16}$$

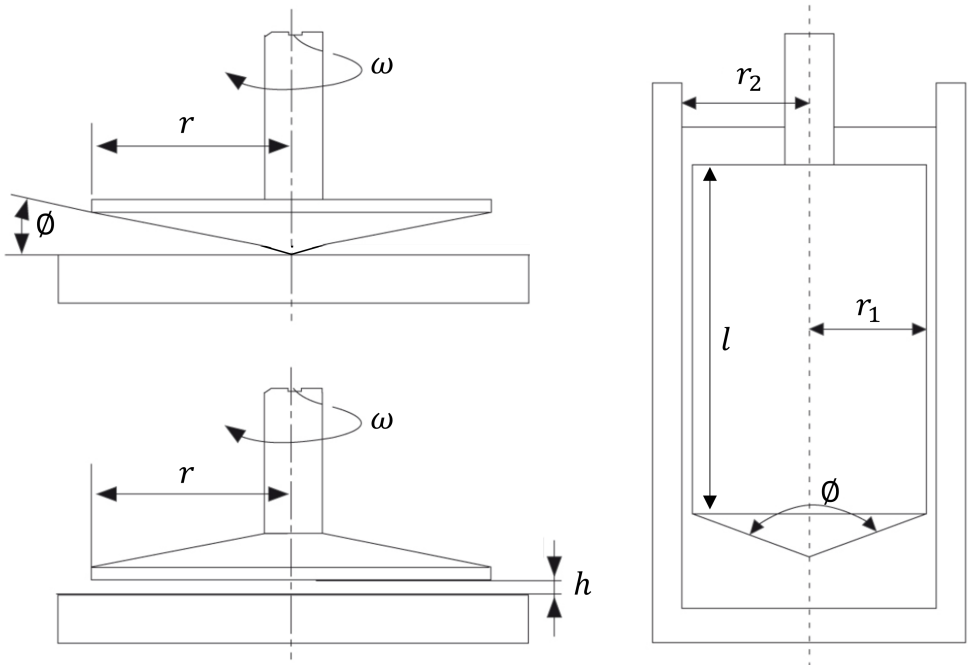

Figure 2.13: Common rotational rheometers. Top left: Cone on plate. Bottom left: Parallel plates. Right: Concentric cylinder, [40].

2.6.2.1 Cone On Plate Rheometer

A cone on plate rheometer uses a cone shaped spindle that rotates parallel to a flat plate, as shown in the top left of Figure 2.13. An angle, θ, is created between the cone and plate, where values are typically small and range from 0.5° - 2°. Introducing fluid between the cone and plate and rotating it with an angular velocity allows the viscosity to be calculated using Equation 2.18, [55]. The main advantage of this rheometer is that it provides homogenous shear conditions since the shear rate is constant inside the entire conical gap, [40].

$$K_\sigma = \frac{3}{2\pi r^3} \qquad K_\gamma = \frac{1}{\theta} \tag{2.17}$$

$$\eta = \frac{3T\theta}{2\pi r^3 \omega} \tag{2.18}$$

2.6.2.2 Parallel Plate Rheometer

A parallel plate rheometer uses two plates positioned parallel to each other, as shown in the bottom left of Figure 2.13. The gap between the top and bottom plate is denoted, h, and changes depending on the fluid being tested. Typical values for this gap are between 1000 and 500 μm. Once fluid is introduced between the plates, the viscosity can be calculated using Equation 2.20, which is obtained using the geometry dependant stress and strain constants, Equation 2.19. Parallel plates are often used to test mixtures and suspensions since their gap is uniform.

$$K_\sigma = \frac{2}{\pi r^3} \qquad K_\gamma = \frac{r}{h} \tag{2.19}$$

$$\eta = \frac{2Th}{\pi r^4 \omega} \tag{2.20}$$

2.6.2.3 Cylindrical Rheometer

This rheometer consists of a cylindrical spindle concentrically positioned in a a cup. A fluid is then placed in the cup, completely submerging the spindle, as shown on the right in Figure 2.13. The viscosity is calculated using Equation 2.22, where T, is the torque, ω is the angular velocity, l, is the length of the spindle, r_1, is the inside radius and r_2 is the outside radius, [55]. The shear rate can be controlled in multiple ways with the most common by changing the velocity of the motor or the dimension of the spindle.

$$K_\sigma = \frac{1}{4\pi l}\left[\frac{r_1^2 + r_2^2}{r_2^2 r_1^2}\right] \qquad K_\gamma = \frac{r_1^2 + r_2^2}{r_2^2 r_1^2} \tag{2.21}$$

$$\eta = \frac{T\left[r_2^2 - r_1^2\right]}{2\pi r_1^2 r_2^2 l \omega} \tag{2.22}$$

2.6.3 Water Content Measurement

The most precise method for detecting the presence of water in a dielectric oil is the coulometric Karl Fischer titration moisture test, Figure 2.14, [56]. It can determine the quantity of water in oil for all states, including free, emulsified and dissolved water and it can measure to as little as 10ppm (0.001%). To measure water content, an oil sample is added to an electrolytic solution consisting of iodide ions, sulphur dioxide, a base, and a solvent. Electrolytic oxidation causes the production of iodine, resulting in an immediate Karl Fischer reaction. Therefore, the water content can be determined immediately from the coulombs required for electrolytic oxidation, [56].

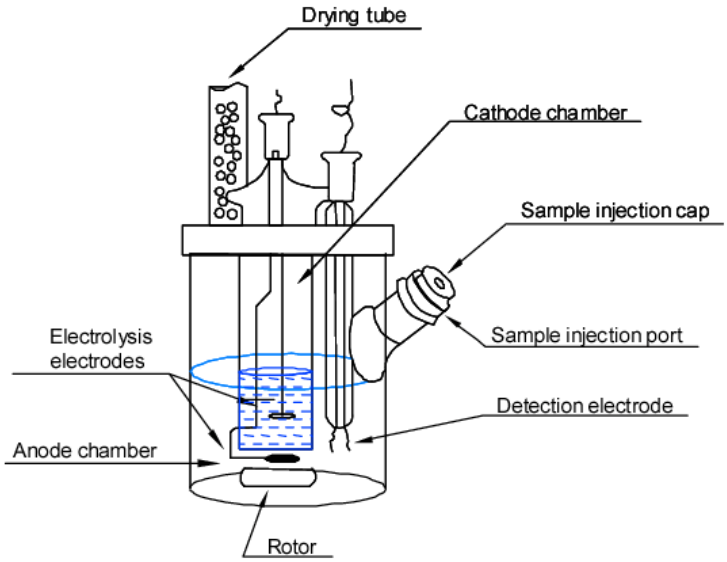

Figure 2.14: Karl Fischer moisture test, [56].

2.6.4 Electrical Property Testing

Breakdown voltage is the primary electrical property parameter used to indicate the health of a dielectric oil. It is measured by applying a potential difference between two electrodes immersed in an oil, which is separated by a specific gap. Starting at 0 V, the voltage is increased at a rate of 2 kV/s until a spark forms between the two electrodes. At that point, the voltage at which the spark is created is recorded as the breakdown voltage. The test is repeated 3-6 times to obtain an average. ASTM D1816, ASTM D877, and IEC

60156 are common standards which specify the procedure and the test cell construction used for testing breakdown voltage. A typical set-up is illustrated in Figure 2.15.

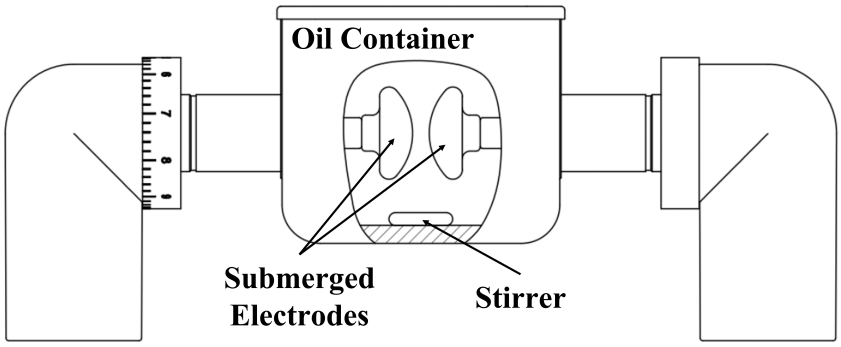

Figure 2.15: Typical set-up of a test cell used to measure the dielectric breakdown voltage of an oil, [57].

2.7 Dielectric Oil Degradation

Oxidation, a permanent chemical alteration process, is the primary way a lubricant permanently degrades over time in service. It normally results in impaired physical, electrical and chemical properties of the base oil and additives. The oxidation process occurs over time and starts by degrading the additives. If this process is left unchanged additives can deplete at a near linear rate. The break point of the oil is reached when the oxidation inhibitors are mostly depleted, at which time the base oil has lost its first line of defence against oxidation, [58]. This is illustrated using Figure 2.16, where oxidation is initially neutralised by the antioxidant additives up to a certain critical point, at which the viscosity and acidity begin to increase due to oxidation. It is important to note that some synthetic base oils are extremely robust and resist oxidation naturally and are thus favourable over petroleum-based oils in some applications, [58].

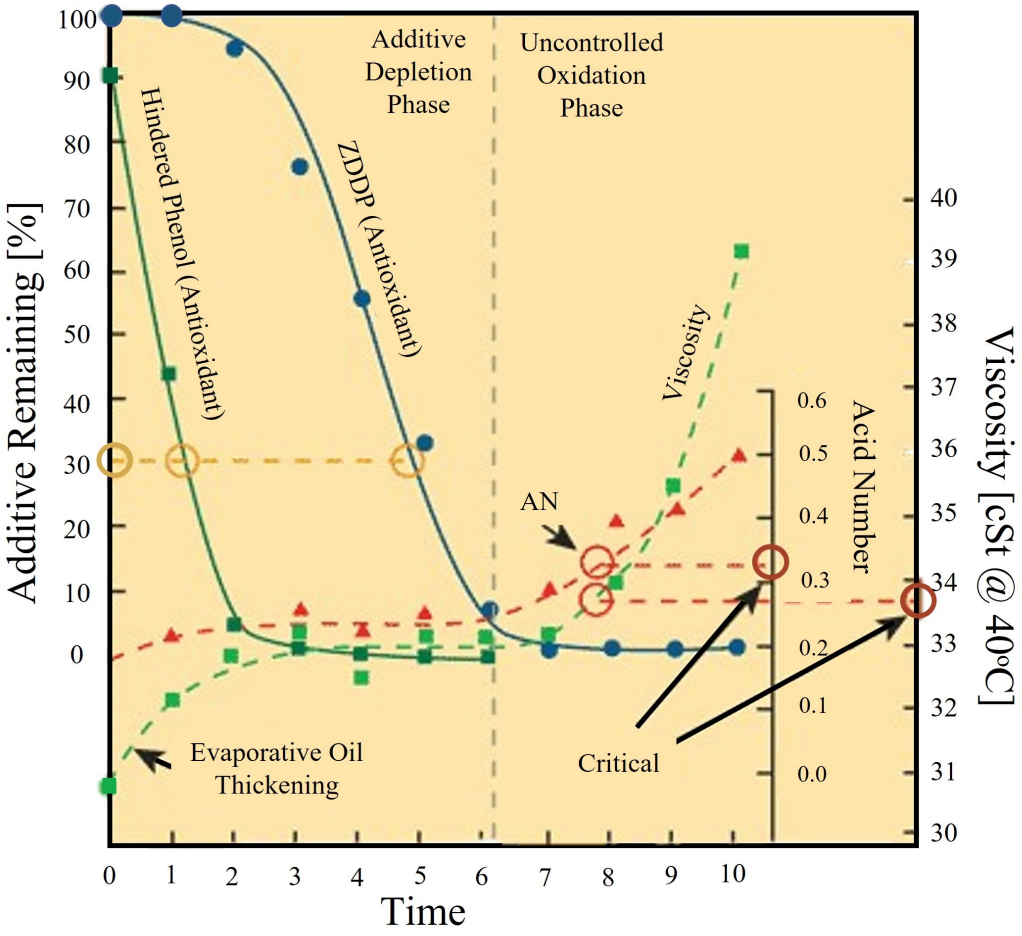

Figure 2.16: Graph showing the oxidation effects of an oil with anti-oxidant additives as it degrades over time. Viscosity and acidity remain relatively unchanged with the help of anti-oxidants until they have been depleted. After this point, viscosity and acidity increase, [59].

There are four pro-oxidants consisting of heat, air, water and metal catalysts. If an oil is exposed to these pro-oxidants to a severe degree, the most robust synthetic oils will oxidise. This oxidation process can occur if the oil is sitting dormant. However the rate correlates to the intensity of pro-oxidants existing within the oil, [60]. Pro-oxidant ramifications include increased oil viscosity and organic acids; the formation of sludge, varnish and deposits; additive depletion; and the loss of other vital base oil performance properties, such as the reduction of volume resistivity and interfacial tension and increased dielectric loss, [61, 60]. Oil analysis often includes an investigation into viscosity and acid number to determine the health of the lubricant, [62].

Wu, [63], oxidised a synthetic ester using a pressurised oxidation reactor at 150°C in order to study the effects on tribological properties. Samples were removed at 5, 10, 15, 20, 30, 40 and 60 hour intervals. The results, Figure 2.17, showed a colour change and a clear increase in the acidity using the TAN representation. However, the kinematic viscosity showed a very small change, which was slightly more drastic at the lower 40°C temperature. Clark [64] and Yao [65], demonstrated that the addition of heterogeneous copper and iron oxidising catalyst accelerated the deterioration of lubricating oil and this produced greater changes in viscosity.

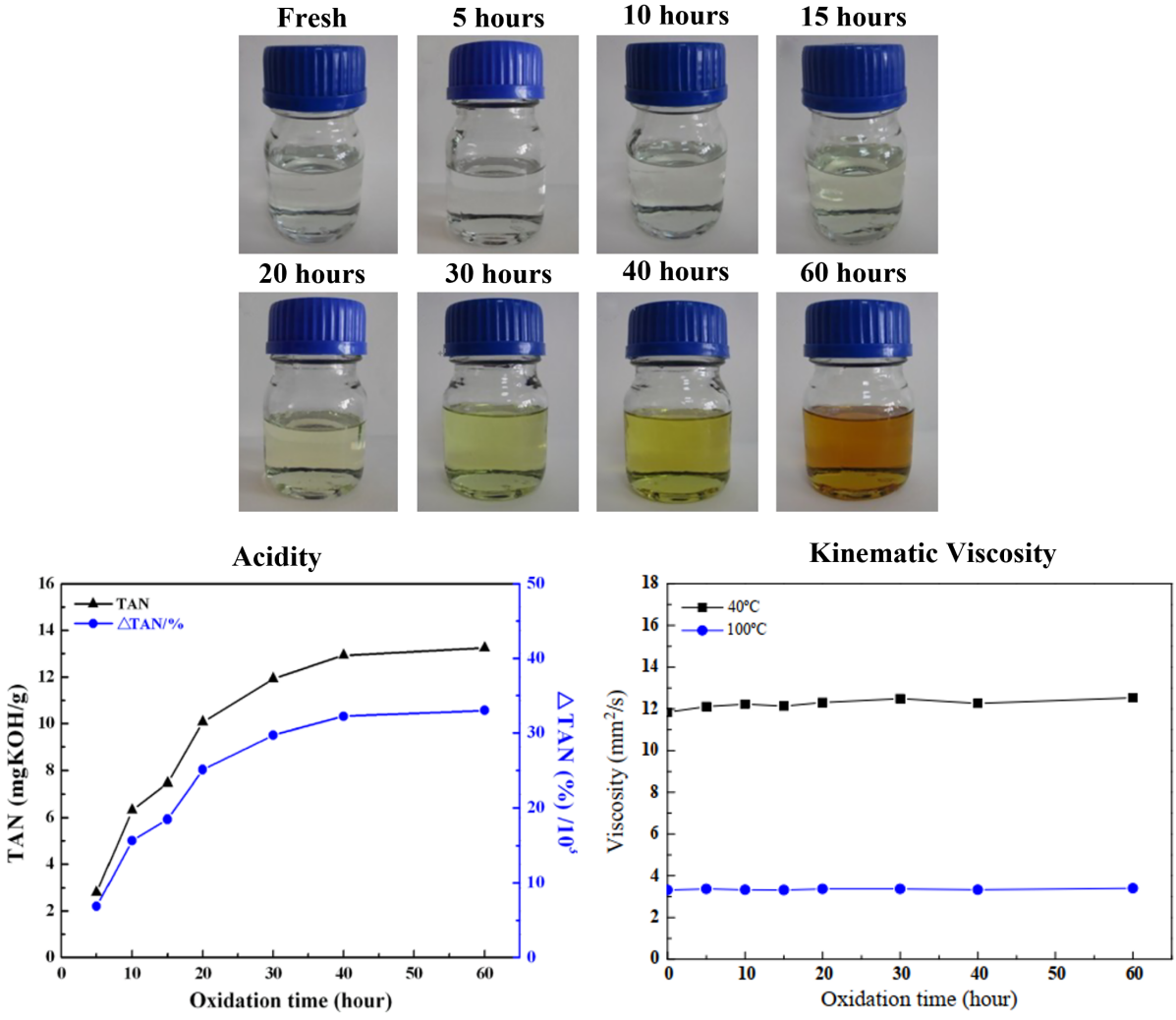

Figure 2.17: Wu's, [63], synthetic ester oil oxidation results over 60 hours at 150°C.

These investigations outlined the difficulty of simulating oxidation effects due to constant exposure to elevated temperature over an extended time period. Augusta, [66], also

attempted to study the effects of oxidation but similarly provided evidence for the difficulties of oxidising fluids in a laboratory environment, as Augusta oxidised 3 oils at 6 different temperatures, where each temperature was held for a week. Its important to note that Augusta's oxidised oils were not clearly illustrated in comparison to Wu's, [63], who provided visual changes, Figure 2.17.

The research also highlights the importance of an oils oxidation dependence on its application and environment. Therefore tests and simulations investigating oxidation would provide more impactful data if conducted in-situ or with regards to its specific application. A more practical lab investigation would be to detect the presence of foreign particles that would ultimately lead to oxidation. In fact, a significant quantity of foreign particles is a key determinant to the characteristics in a dielectric oil. Cellulose, water, copper and iron particles are commonly found in electrical transformer dielectric oil, [67]. Water can already be present in a fresh oil or it can find its way into an oil from its surrounding environment. Iron and copper particles can be generated by degradation of the conductors, system pipes, and container walls, [68]. Cellulose is released by insulating paper found in transformer oils. It is also worth noting that the insulating paper can hold more water content than oil, with respect to the saturation point of the oil.

2.7.1 Water Contamination

One major cause of electronic insulation failure, component failure and poor machine reliability is water. Therefore it is imperative to recognise its existence and control or eliminate the source of water ingression. Furthermore, water levels should be kept as low as possible and not exceed the saturation limit, which is described as the first of three states in which water can exist in oil.

Dissolved water, the first state, is characterised by individual water molecules that are dispersed throughout the oil. An oil can contain a significant concentration of dissolved water with no visible indication of its presence. The amount of dissolved water an oil can absorb depends on the composition, temperature and age of the oil, where aged oils have the capacity to hold notably more water in the dissolved state than new oil. Table 2.1 illustrates the amount of water soluble in four common types of dielectric oils at $23°C$.

Figure 2.18 shows how the saturation point changes with temperature.

Table 2.1: Water solubility of four different dielectric oil compositions at room temperature, [31].

Dielectric Oil Type	Water Content at $23°C$ (ppm)
Mineral	55
Silicone	220
Natural ester	1100
Synthetic ester	2600

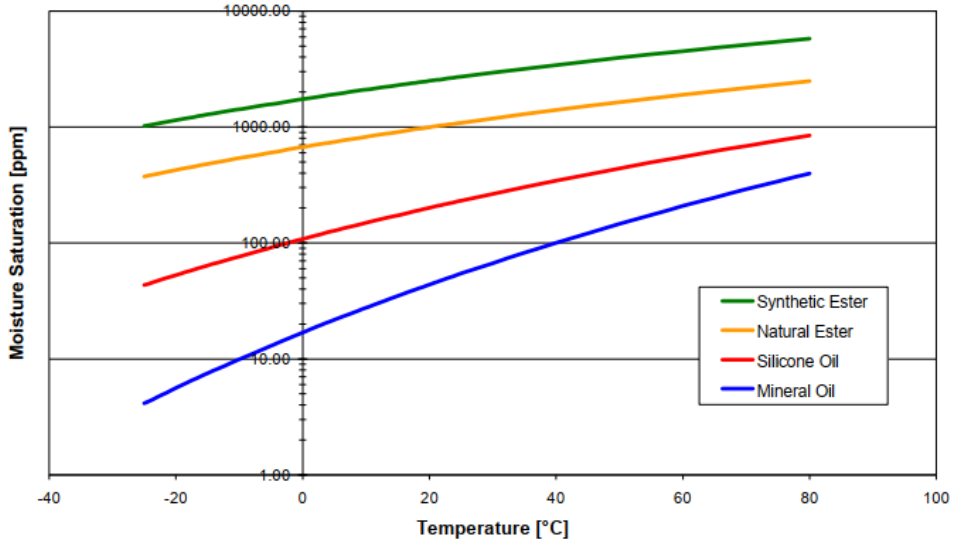

Figure 2.18: Saturation point changes with temperature, [31].

Esters have higher saturation points due to their ester linkages, which are polar in nature. This polarity allows the ester linkages to attract very polar water molecules, however the overall polarity of esters are low, Figure 2.19. The term polar refers to areas of a substance with different attractions, like the poles of a magnet. The more ester linkages available the higher the saturation point becomes. Mineral and silicone oils are not as polar as esters and so their saturation values are much lower.

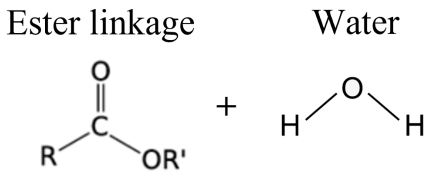

Figure 2.19: Example of a polar ester linkage attracting a polar water molecule, [31].

The oil is saturated when the amount of water exceeds the maximum level for it to remain dissolved. On reaching this point, microscopic droplets of water are suspended in the oil, becoming an emulsion. At this point the resulting suspension of small droplets of moisture makes the oil appear cloudy. With the addition of more water, phase separation begins. This results in a layer of free water and free oil. For oils whose specific gravity is less than 1, this free water layer is found on the bottom of tanks and sumps, [69]. The states just described are illustrated in Figure 2.20.

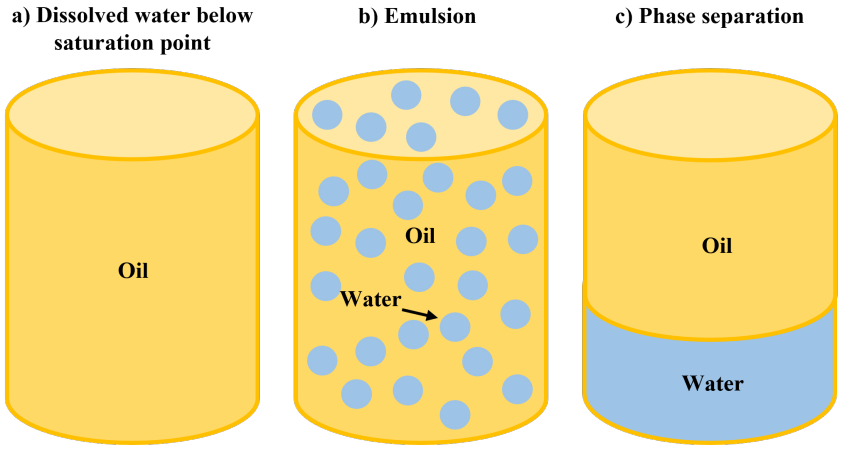

Figure 2.20: Water in oil states.

Free and emulsified water are the two most harmful phases, therefore it is essential to make sure that the water content remains below the point of saturation. However a significant level of damage can still occur at these quantities. The presence of water in a lubricating oil causes the progress of oxidation to increase, resulting in premature ageing of the oil, particularly in the presence of catalytic metals such as copper.

Detrimental values of water content vary as the oil is highly dependent on the oils chemistry, temperature, oil condition and impurities. However for a transformer mineral

oil, used samples contain water only in the lower ppm range (above 55 ppm). This is because water is barely soluble in oil and prefers to reside in the cellulose insulation, where the range for water is usually in the area of 0.3 % to 6 % but can be as high as 20 %.

2.7.2 Particle Contamination

Particulates can exist in four forms within a fluid consisting of a solution, suspension, slurry and sedimentation. A solution is the dissolving of solid particles into a bulk fluid. A suspension is where solid particles are suspended throughout a fluid, which creates a heterogeneous mixture, [44]. A slurry forms when a suspension is travelling at a velocity, and finally, sedimentation occurs when a suspension settles out and forms up separate to the bulk fluid.

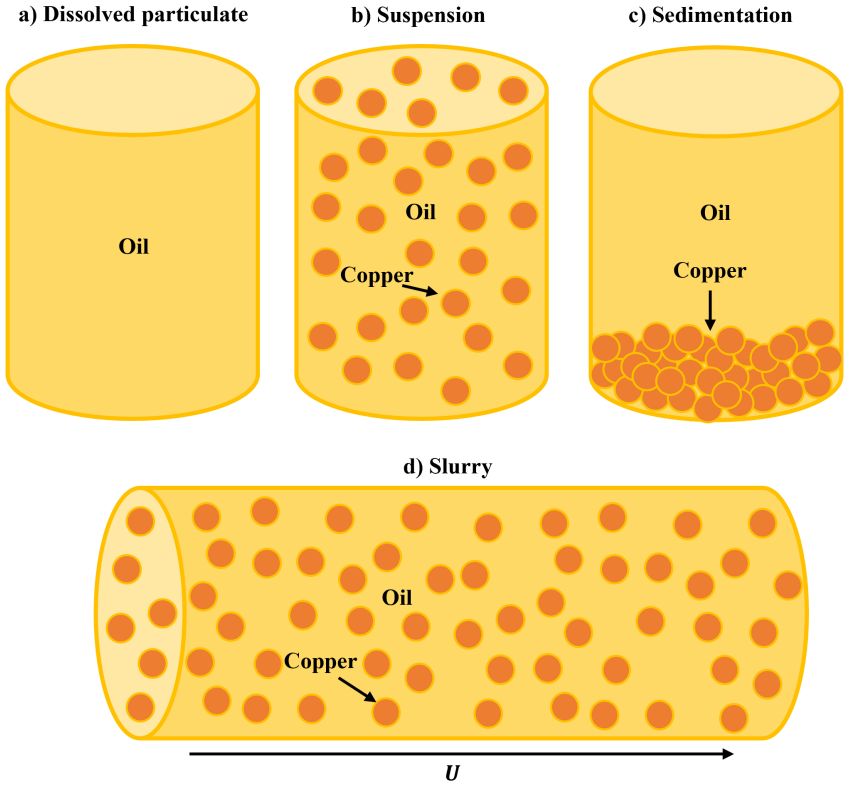

Figure 2.21: Copper in oil states.

Metallic particulates are major catalysts for accelerating oxidation of oil and are aggra-

vated by oxygen and high temperatures. They become present due to abrasion, mechanical working, erosion and/or corrosion, [65]. Most cooling systems utilise copper piping due to it being non-permeable, highly resistant to corrosion, non-toxic, relatively cheap and recyclable. Unfortunately, this copper tubing is susceptible to wear, driven by two different phenomena; physical erosion of the copper tubing due to fluid flow, and chemical corrosion due to chemical reactions between the fluid and copper tubing, [70]. Controlling the copper tubing wear due to fluid flow can be done by controlling flow rates, whereas chemical corrosion is not as simple. Copper particulates can have a detrimental effect on components such as hydraulic valves, pumps, and bearings, and can also cause a reduction in the electrical insulation of a dielectric oil.

Copper particulate in oil can cause damage to occur through reacting with dissolved oxygen (or air), [71, 72], or corrosive sulphur, [73, 74]. As most dielectric oil is petroleum-based, sulphur-containing compounds are often present within the fluid. This sulphur, combined with heat generated, are the principle contributors to deposition of copper sulphide, which accumulate on surfaces, reducing the dielectric strength [72]. Copper sulphide suspended within the bulk fluid can also cause electrical discharges between leads and the grounded system. The total removal of sulphur from petroleum-based oil is difficult, so corrosion inhibitors are used to mitigate the detrimental effects by binding to the copper.

Welbourn, [72], reports that there has been little work carried out into the corrosion behaviour of copper in oil and the work that has cannot necessarily be applied to the wide range of oil chemistries in varied applications. Nevertheless Abou, [75], conducted research into the effects of oxidation caused by worn metals in a petroleum-based oil. Abou investigated changes in dissolved metal contents, viscosity and acidity after oxidation in the presence of copper, iron, nickle chromium (Ni-Cr) and aluminium. Figure 2.22 illustrates the findings, where copper increased the oils oxidation rate substantially and was attributed to it being a heterogeneous oxidising catalyst, which resulted in the high oil deterioration. Figure 2.22a shows that copper is highly soluble in oil and increases in solubility as oxidation increases. Abou attributed this to the high tendency of copper ions to dissolve in the acids that form due to oxidation. Figures 2.22b and 2.22c show the increase in viscosity and acidity, respectively, where viscosity values are illustrated in

Table 2.2. From this data Abou concluded that the presence of copper as an oxidation catalyst resulted in a great increase in the viscosity and acidity of the oil and that such changes occurred at higher rates than with the other metals.

Table 2.2: Petroleum-based oil solubility and viscosity changes with copper contamination over 120 hours of oxidisation, [75].

Oxidation time (hours)	Solubility content (ppm)	Viscosity $40°C$ (cSt)
0	-	185
24	18	192
48	160	212
72	250	232
96	470	300
120	680	475

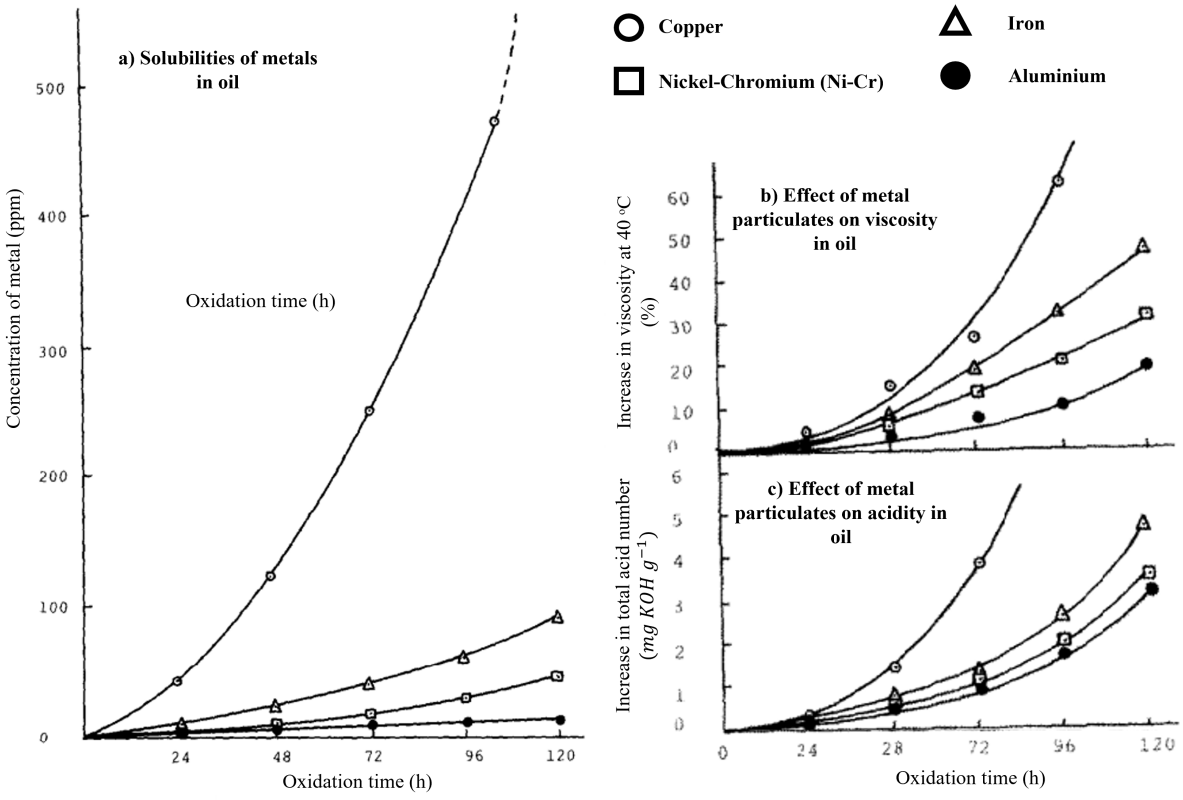

Figure 2.22: Metallic particle contamination effects on a petroleum-based oil as it oxidises over time. a) Solubility of each metal in oil, b) The effect of each particulate on the viscosity, and c) The effect of each particulate on the acid content, [75].

Copper from wear debris will typically produce concentrations of 10 ppm to 20 ppm.

However, wear debris is not the only contributing factor to copper contamination. As mentioned previously in this section, copper sulphides form on the copper cooler tubes and cast off into the oil, leading to a rising copper concentration that can reach well over 300 ppm, with recorded heights of up to 1000 ppm.

2.8 Rheology of Emulsions and Suspensions

Rheology characterises the flow of materials that show a combination of elastic, viscous, and plastic behaviour by properly combining elasticity and fluid mechanics. It also predicts behaviour based on the structure of the material, for example the particle size distribution in a solid suspension. Materials with fluid characteristics flow when subjected to a stress. This stress can be shear, torsional, and extensional, with materials responding differently under each type. Some of the main methods of shear rheological testing have been discussed in Section 2.6.2. Immiscible fluid particles in an emulsion and solid particles in a suspension are classed depending on their volume percent concentration, and consist of dilute and concentrated, [76].

2.8.1 Breaking of Emulsions and Suspensions

Before discussing the concentration, it is important to highlight how emulsions and suspensions break from a fluid. The breaking mechanisms that exist for mixtures consist of creaming, sedimentation, and aggregation. Droplets in an emulsion may aggregate due to coalescence, partial coalescence, flocculation, and Ostwald ripening, [77, 78, 79]. For suspensions, however, only flocculation occurs.

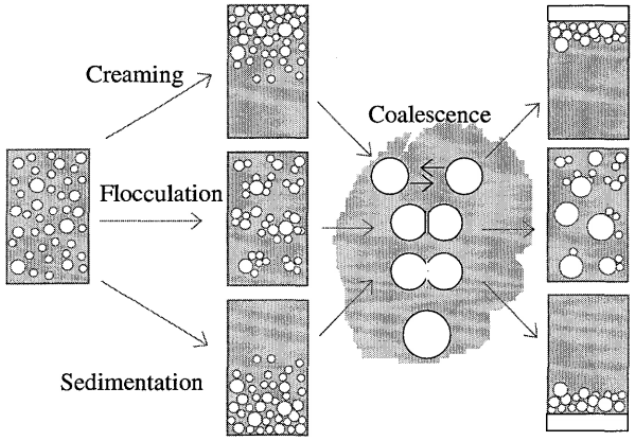

Figure 2.23: Illustration of how the dispersed phase breaks from the continuous phase. This illustration was created for emulsions, however flocculation and sedimentation occur for particulate suspensions without the coalescence, [77].

- Coalescence is when a larger droplet is formed due to smaller droplets merging together. This is because droplets contact each another, causing the interfacial film to rupture. Partial coalescence occurs when two droplets partially penetrate each other and form an irregular shape clump.

- Mixtures typically contain two dissimilar materials that have different densities. It is this difference in density between the continuous and dispersed phases, which causes either creaming or sedimentation. When the density of the dispersed phase is larger than the continuous phase, sedimentation occurs and vice-versa. For an emulsion, coalescence occurs which produces complete separation between the two phases. Creaming or sedimentation can be prevented by having a high viscosity continuous phase.

- Flocculation manifests when particles and/or droplets remain individual but interact with one another. Brownian motion can produce flocculation of a mixture, as random collisions between the dispersed and continuous phases causes continuous movement of particles, which aggregate. Flocculation may lead to very high viscosities at low shear rates, whereas at higher rates of shear the floc size is reduced, thus releasing continuous phase, and the viscosity decreases, [77].

- In a polydisperse mixture, where different sized particles or droplets are present, a

process called Ostwald ripening may take place. Most dispersed phases are soluble to some finite extent within the continuous phase. The chemical potential for small droplets is higher than that of large droplets, therefore the local concentration of dissolved disperse phase molecules will be higher around smaller droplets than around larger ones, Figure 2.24. Thus there is a growth in the number of larger droplets at the expense of the small ones.

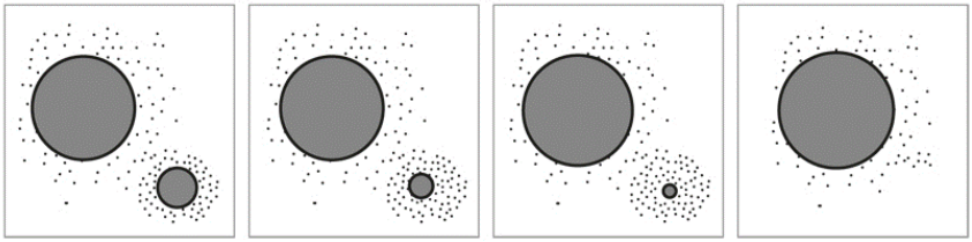

Figure 2.24: Ostwald ripening occurring over time, where a smaller droplet dissolves and eventually feeds into a larger a droplet, [80].

2.8.2 Dilute and Concentrated Contamination

A dilute mixture is a disperse phase volume fraction below 0.03 (3%), [81]. The interactions between the emulsion droplets are relatively weak under these conditions because they are so distant, Figure 2.25. Consequently, the flow pattern experienced by another droplet is not influenced by the ability of one droplet to disrupt the flow pattern of the continuous phase. Rheological properties of the continuous phase therefore dominate the apparent viscosity of dilute emulsions.

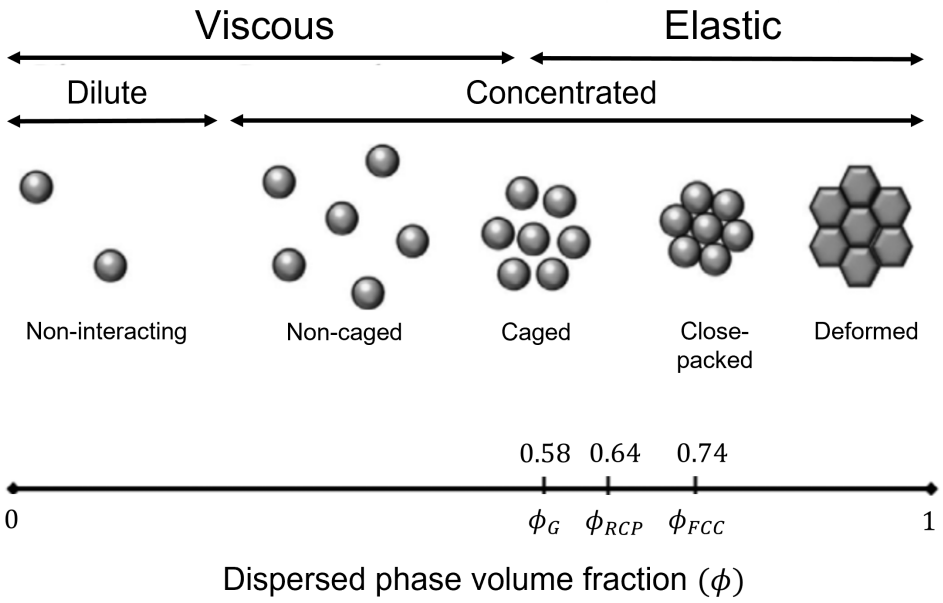

Figure 2.25: The change of rheological behaviour of mixtures with the increase of dispersed phase volume fraction, where ϕ_G is the glass transition volume fraction, ϕ_{RCP} is the randomly close pack volume fraction and ϕ_{FCC} is the‘ face-concentrated cubic volume fraction, [76].

The theoretical and experimental characteristics for the flow behaviour of dilute mixtures have been studied extensively. Albert Einstein first derived the classic equation for describing the dependence of the apparent viscosity of dilute suspensions on particle concentration, [82]. The Einstein equation, Equation 2.23, resulted from the mathematical analysis of the frictional losses occurring when an ideal fluid flows past an isolated rigid sphere. Considering Equation 2.23, η is the viscosity of the mixture, η_C is the viscosity of the continuous phase, and ϕ is the volume fraction of the disperse phase.

$$\eta = \eta_C \left(1 + 2.5\phi\right) \tag{2.23}$$

Equation 2.23 is only applicable to dilute suspensions containing rigid isolated spherical particles. Therefore a number of researchers such as Frohlich, [83], and Taylor, [84], have expanded this equation to also include droplet fluidity, interfacial properties, and droplet aggregation. For instance, Equation 2.24 recognises that the droplets in an emulsion are fluid, [81].

$$\eta = \eta_C \left(1 + \frac{2 + 5\lambda_r}{2\,(1 + \lambda_r)}\phi\right) \tag{2.24}$$

In Equation 2.24, λ_r represents the proportion of the dispersed to continuous phase viscosities (η_C/η_D). As this ratio increases, the viscosity of the emulsion should increase. Equation 2.24 also assumes that the applied shear force does not cause droplet deformation [81].

Beyond 3 % contamination the mixture is considered concentrated. For a concentrated system, droplet-droplet interactions are important, as a disturbance in the flow caused by one droplet impacts the flow around another, Figure 2.25. It was found that the apparent viscosity of concentrated mixtures were greater than predictions from the Einstein equation, due to the degree of energy dissipation being larger than expected. Therefore the viscosity of concentrated mixtures can be expressed by Equation 2.25, [76, 85].

$$\eta = \eta_C \left[1 - \left(\frac{\phi}{\phi_p}\right)\right]^{-\eta_i \phi_p} \tag{2.25}$$

Where, η_i represents the intrinsic viscosity, which is equal to 2.5 for rigid spheres, and ϕ_p represents the maximum packing fraction, which is equal to 0.64 for randomly packed monodisperse rigid spheres. In practice, for emulsions, the value of ϕ_p depends on the polydispersity, interactions, and deformability of the droplets, [79]. For this reason, it may be either higher or lower than the value of 0.64.

Figure 2.26 presents Equations 2.23 and 2.25 for the viscosity with increasing dispersed phase volume fraction. The result of the Einstein equation shows that the viscosity of a mixture will increase linearly with an increased disperse phase volume. However Equation 2.25 shows an apparent linear trend for dilute and initial semi-dilute phases when particles and/or droplets do not interact. With increased dispersed phase volume, the viscosity increases steeply. This is due to increased particle/droplet interactions which disrupts the flow and increases the viscosity.

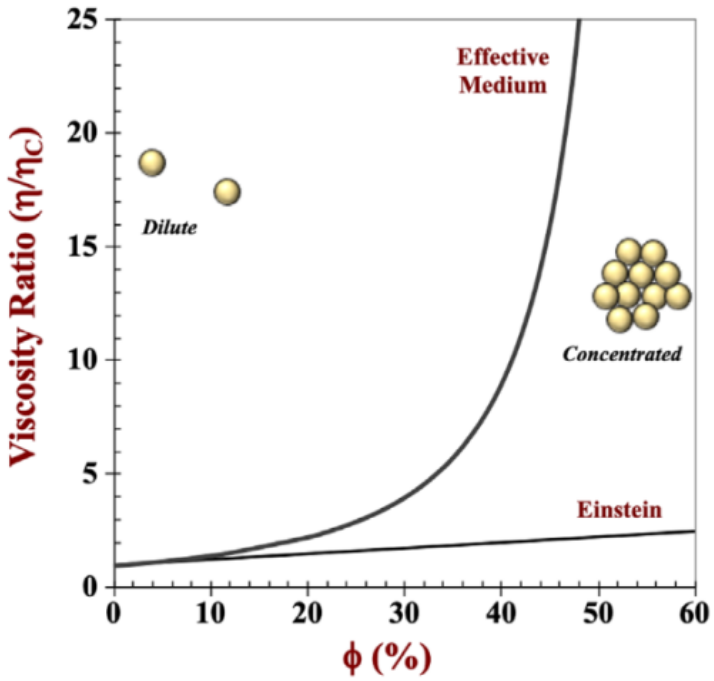

Figure 2.26: The viscosity of mixtures as the dispersed phase volume fraction increases. The viscosity can be described by Einstein's equation for dilute systems, Equation 2.23, however for a concentrated system a more effective mathematical equation is required. Therefore the effective medium line was created using Equation 2.23, [76].

2.8.3 Impacting Factors on the Rheology of Mixtures

The continuous phase is considered more dominant with regards to the viscosity, hence any changes in its properties can impact the rheology of the entire mixture, [79]. Furthermore, factors such as the disperse phase particle size and distribution, volume fraction, particle aggregation and particle interactions have an impact on the rheology of mixtures, [86]. Mixtures may display Newtonian and/or non-Newtonian behaviours due to the nature of the particles and/or droplets they contain. Additionally, these behaviours can be determined by particle deformability, interactions with other particles, and aggregation state.

2.8.3.1 Dispersed Phase Volume Fraction

The rheological properties of a dispersion are related to their dispersed phase volume fraction, [87]. At a low dispersed phase Brownian motion is the primary force acting on

particles. However with increasing dispersed phase volume, hydrodynamic interactions and droplet-droplet collisions are more influential on the rheological properties. Mixtures displaying non-Newtonian behaviour can be explained by the flow-induced movement from a random distribution of particles at rest to an ordered distribution at higher shear rate, Figure 2.27a. Hence the application of a shear motion to a mixture may initiate the orientation of particles into the shear flow direction, and may also instigate the breaking up of agglomerates or change the shape of particles. Therefore the forces caused by interactions between the particles is reduced, which produces a shear thinning behaviour, Figure 2.27b.

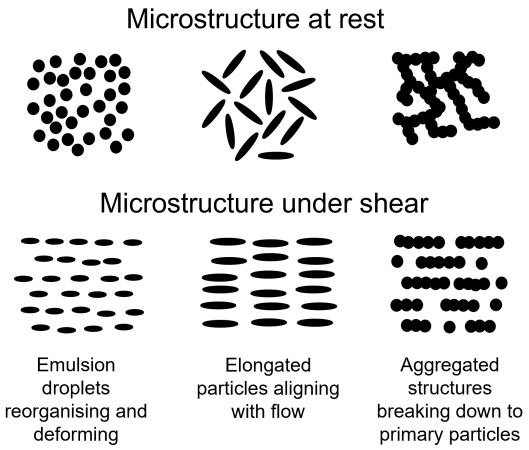

(a) Dispersed phase particle behaviour under shear.

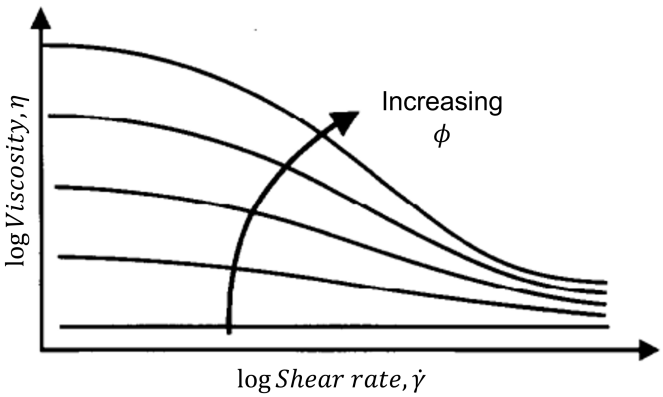

(b) Overall viscosity increase with increasing dispersed phase, while showing shear thinning behaviour, [88].

Figure 2.27: Behaviour of an emulsion or suspension with increased dispersed phase volume fraction over shear rate.

To understand how the viscosity increases and its behaviour becomes non-Newtonian when the addition of the dispersed phase is increased, Figure 2.28 was created by Mueller, [89].

(a) In dilute mixtures, $\phi < 3\%$, the suspended particles are sufficiently well separated that there are negligible interactions between them. A viscosity increase is caused by the fluid having to do more work to flow around them. The rheological behaviour is Newtonian and the monotonically increasing viscosity is linear with increased particle volume fraction, Figure 2.28(a).

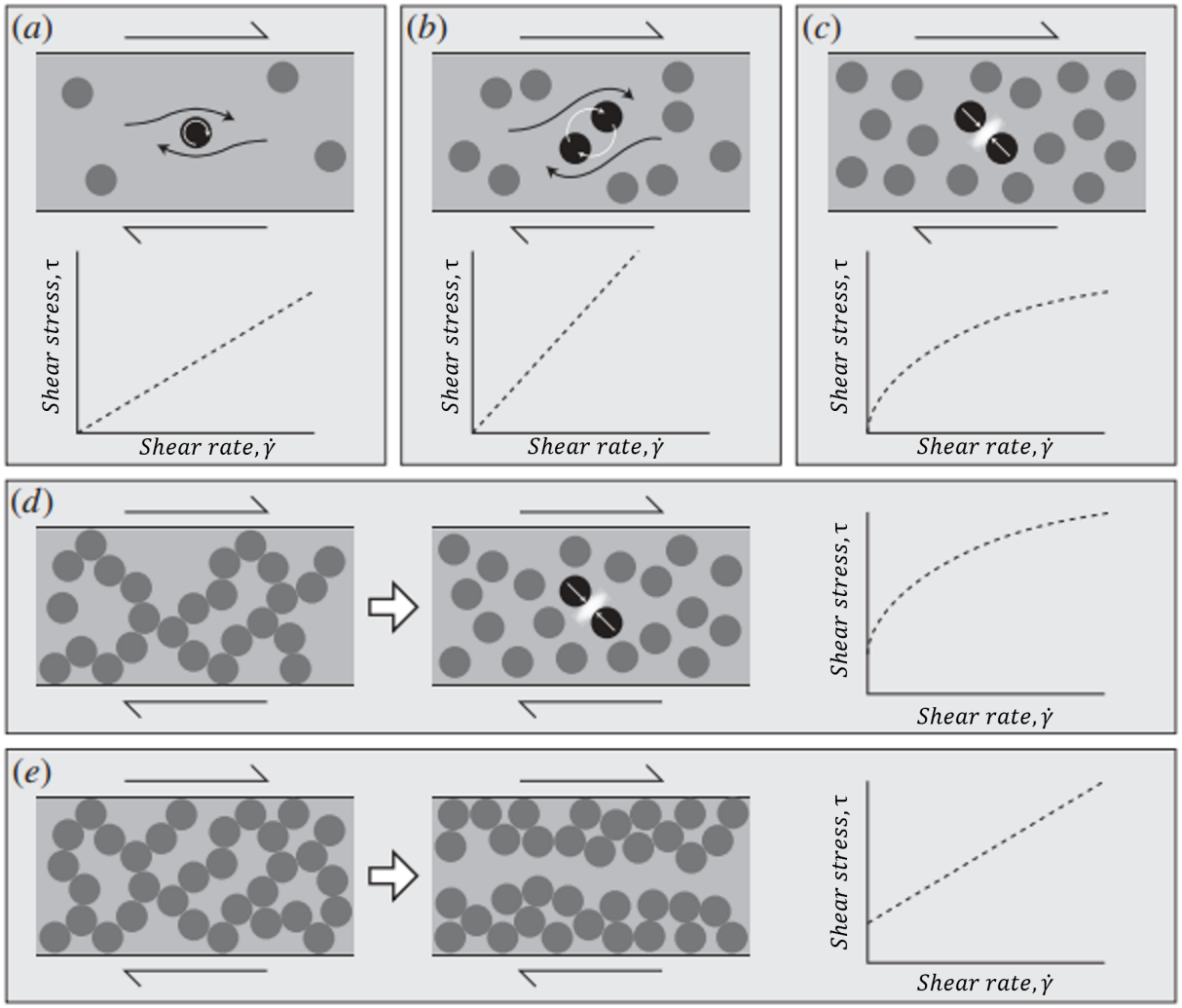

Figure 2.28: Dispersed phase volume effects on the rheological behaviour and how it increases viscosity of the continuous phase. (a) Dilute mixture showing Newtonian behaviour. (b) Semi-dilute mixture showing Newtonian behaviour with an increase in viscosity. (c) Concentrated mixture illustrating non-Newtonian shear thinning behaviour. (d) Highly concentrated mixture showing shear thinning behaviour after its newly developed yield stress. (e) Highest concentrated mixture showing Newtonian behaviour after it has yielded, [89].

(b) At a semi-dilute stage, $3\% < \phi < 25\%$, the behaviour is still Newtonian but the viscosity now increases non-linearly with ϕ, Figure 2.28(b). In this stage, particles interact hydrodynamically as they are more tightly packed. They therefore produce a high viscosity as they begin to aggregate and rotate together, which enhances the work done by the fluid to move around them.

(c) As the volume fraction increases to concentrated, $25\% < \phi < 50\%$, shear-thinning is observed, Figure 2.28(c). Here particles are much more tightly packed that the work to flow between the small gaps increases. However over time, gaps between particles become lubricated, creating a preferred path of flow, and particles become more aligned, which leads to a decrease in viscosity at high shear rates.

(d) A yield stress is apparent at $50\% < \phi$, Figure 2.28(d), and is a result of particle chains and networks forming. These formations can elastically withstand the applied stress until they break down (point of yield) and shear-thinning is observed. The magnitude of the yield stress is likely to be a function of particle size and the coefficient of friction between particles, [89].

(e) At near maximum volume fractions, after the yield point is reached, the relationship between shear stress and shear rate is approximately linear, Figure 2.28(c). Muller's, [89], explanation for this is that the networks do not break down fully, but particle-free shear planes develop containing only the Newtonian continuous phase, which accommodate the bulk of the strain.

2.8.3.2 Particle/Droplet Size

Alteration of size and distribution of the particle/droplet have a direct affect on the rheology of a mixture, as it alters how particles interact. The diameter size distribution of water in oil emulsions typically ranges from 1-100 μm, [90, 91, 92, 93]. Droplet size also plays a significant role in droplet coagulation, as increased coagulation results in the formation of larger droplets, thus a change in rheology, [79]. For dilute mixtures droplet size has negligible effects on the viscosity, providing that there are no interactions between the droplets, [85, 94]. Concentrated mixtures are affected by the average droplet size and polydispersity degree, [95, 96]. There are also Brownian or osmotic effects which can be explained using three emulsions of monodispersed particles with the same phase volume. The movement required to order random particles is resisted for longer by smaller particles than by large ones, Figure 2.29.

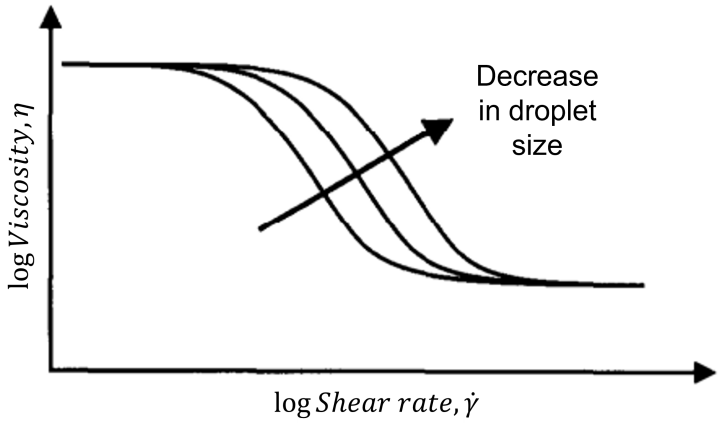

Figure 2.29: Illustration of the viscosity behaviour with shear rate for a continuous phase with the same dispersed phase volume fraction but varying particle/droplet sizes, [88].

Controlling solid particle sizes is much easier than controlling emulsion droplet sizes. However Mason, [87], reports a number of different methods for making mono-dispersed emulsions exist. The most achievable method being controlled shear rupturing, which involves breaking up singular and/or flocculated droplets at a steady shear rate until a constant droplet size is achieved, [87, 97, 98]. However as the droplets break down and flow induced collisions occur there is a change in the viscosity with time of shearing as opposed to the rate of shearing, [99]. This suggests that the emulsion is thixotropic, whereby the microstructure is brought to a new equilibrium. The process is reversible as when the flow ceases, the Brownian motion slowly rebuilds the structure. Thixotropy is dependent on both time and the applied shear rate, hence it cannot be properly accounted for if both of these variables are simultaneously changing.

2.8.3.3 Particle/Droplet Interactions

The interactions between particles/droplets are a challenge for determining rheological behaviour. High level structural information and mechanical property knowledge is needed to clearly understand the relationship between particle/droplet interactions, [79]. The interactions between the droplets consist of attractive (van der Waals and hydrophobic) and repulsive (mostly electrostatic, and thermal fluctuation) forces. The relative magnitude of these interactions dictates the rheological properties of a mixture.

2.8.3.4 Solid Particle Shape

Up to this point in the thesis, emulsion droplets and suspension particles have been considered spherical in shape. This is true for emulsion droplets as it is thermodynamically efficient to form spheres. However, many solid particulates are not spherical in shape, which also impacts the mixture viscosity. A lot research, [100, 101, 102, 103], has focused on suspensions of spheres, and therefore additional effects of non-spherical particles have been neglected, which have been highlighted in literature, [89, 104, 105]. Firstly, the contribution to suspension viscosity of non-spherical particles is different from spherical particles due to the local flow around a non-spherical particle and its orientation. Secondly, particle interactions are strongly affected by particle shape. At the same particle volume fraction, the degree of interaction among non-spherical particles will be greater than among spherical particles, [89].

Research on particle suspensions has been centred on establishing a relationship between apparent viscosity and particle volume fraction. However, there are two previously reviewed, [89, 101, 102], issues in this research:

1. The focus on apparent viscosity means that non-Newtonian behaviour typically receives only a qualitative description.

2. Experiments lack constraints, which involve mixtures with a wide range of particle size distributions.

As a consequence, results for the relationship between apparent viscosity and particle volume fraction may vary by an order of magnitude between different workers.

2.9 Conclusion

The following conclusions are drawn from this chapter:

- Dielectric fluids are specially engineered using a base oil and additives in order to meet the requirements for good electrical insulation and heat transfer with the key properties being:

  - High dielectric strength - The oil's ability to not conduct electricity.
  - Low viscosity - Required to be circulated efficiently around a battery cooling system.
  - Low pour point - The oil can function as a fluid at low temperatures (cold operating environments)

- Oxidation can have a negative impact on these properties, specifically the viscosity, and is exacerbated by the ingress of water and particulates.
- The viscosity behaviour of dielectric fluids is formulated to be Newtonian due to the pump forced convection used to circulate the oil over high powered electronics.
- With the ingress of water and particulates causing oxidation and deterioration of the fluid, the viscosity behaviour could change. Therefore it is vital to conduct viscosity measurements over a range of shear rates.
- Standard rotational viscometers can be used to measure the viscosity, however these measurements are at a relatively low shear rate in comparison to ultrasonic viscometry. Furthermore rotational viscometers are typically utilised in a laboratory environment and are difficult to adapt for in-situ purposes.
- Nevertheless, both in-situ and ex-situ can be used together to formulate conclusive evidence as to whether viscosity can be used to monitor changes in a dielectric oils health, and illustrate the viscosity behaviour with varying increments of contamination.
- Oil degradation is a very complex and unique phenomenon to each individual environment, and therefore lab-bench measurements are predicted to be vastly different to reality. Also the ability to create such degraded samples is difficult to achieve.
- Based on the findings of this literature review regarding oxidation time and its affects on viscosity with temperature, a more feasible investigation was drawn. This would be to detect contaminants, such as water and copper, that lead to such degradation levels and compromise the oils health.

- Rheological testing can illustrate important details regarding the mixture properties. These consist of the strength of the interactions between the droplets/particles, the aggregation state and the morphology of any flocs.

- Rheometers with high sensitivity are required to observe the rheological characteristics of dilute mixtures, which is the most common state for dielectric isolation oil. This is due to the lack of particle interactions between the dispersed phase throughout the bulk fluid, hence the continuous phase dictates the apparent viscosity.

Chapter 3

Literature Review 2: Ultrasound to Measure Viscosity

The main focus of this thesis is to use ultrasonic sensors to measure the viscosity of a coolant with varying degrees of contamination. Therefore, this chapter provides an introduction to the physics of ultrasound. It is structured methodically by starting with a basic definition, advancing to the various wave modes and how they behave inside materials and with boundaries. Finally it highlights how these acoustic waves are practically applied and how they are theoretically linked to the rheology of fluids they propagate within.

3.1 Introduction

Ultrasound, a section of acoustics, is the study of sound frequencies beyond 20 kHz, Figure 3.1. All materials are composed of atoms, which may be forced out of their equilibrium positions and into vibrational motion, therefore they are considered an elastic medium. Providing these atoms are stressed within their elastic limit, a mechanical oscillatory wave will be formed. These waves are made up of a series of compressions and rarefactions, which are representative of the applied stress.

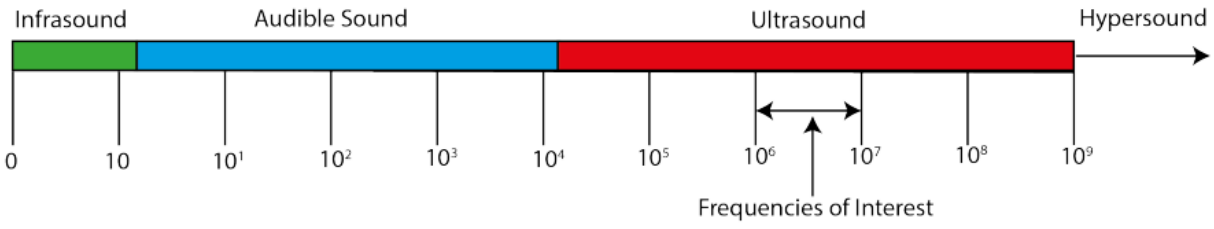

Figure 3.1: Acoustic waves differentiated by frequency, [16].

3.2 Wave Modes

Ultrasonic wave motion occurs by transferring energy from one particle to the next in the the direction of propagation. Using Figure 3.2, if that particle, and surrounding particles above and below it, was excited in unison using a sinusoidal oscillation, all particles in the plane would oscillate at the same amplitude and frequency, [106]. This would result in a wave of deformation that is dependant on the stiffness of the host medium. Sound can propagate as a longitudinal wave or a shear wave, Figure 3.2.

Longitudinal waves are oscillations that occur in the direction of sound propagation as a series of compressions and rarefactions. Due to the longitudinal method of travel, these waves are effective in both solid and fluid media.

Shear waves, or transverse waves, oscillate perpendicular to the direction of propagation and prefer solids as a host medium. They can propagate in liquids and gasses but it is usually an extremely small distance, as perpendicular motion in less dense materials is not easily supported.

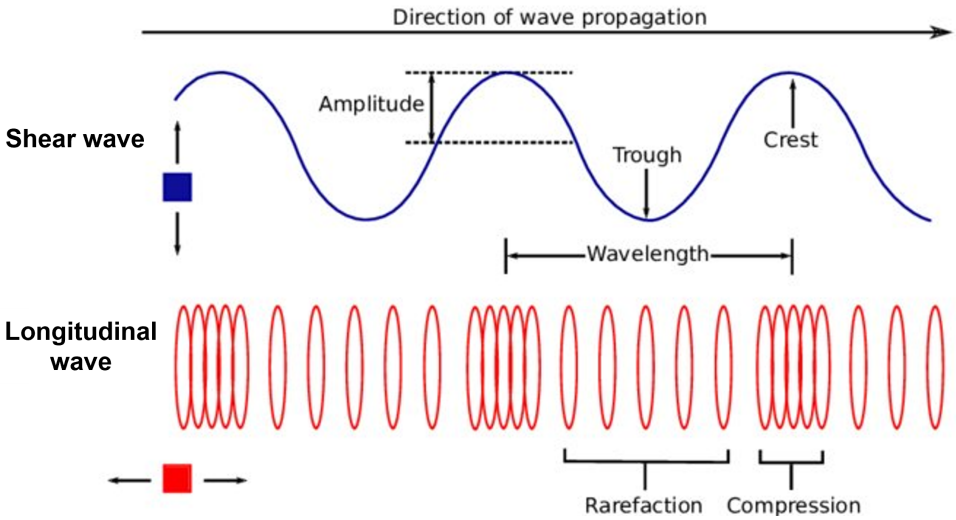

Figure 3.2: Illustration of an elastic particle undergoing shear and longitudinal wave motion, [107].

3.3 Propagation in Materials

Acoustic wave propagation is reliant on the material that it is travelling within. A variety of different characteristics influence this wave motion, including the speed of sound, acoustic impedance and attenuation. Furthermore, depending on the size and shape of the material, interference can occur. These influencing factors are discussed in the following subsections.

3.3.1 Speed of Sound

The speed of sound (SOS) for various host media can be explained using material properties. For a longitudinal wave the SOS in a solid, c_s, and a liquid, c_l, are defined in Equation 3.1, where, E, is the elastic modulus, B, is the bulk modulus, and ρ, is the density. The SOS for a shear wave in both a solid and a liquid, $c_{s,l}$, is defined as Equation 3.2, where, G, is the shear modulus. Equation 3.1 and 3.2 include subscripts s and l which represent solid and liquid respectively.

$$c_s = \sqrt{\frac{E}{\rho}} \qquad\qquad c_l = \sqrt{\frac{B}{\rho}} \tag{3.1}$$

$$c_{s,l} = \sqrt{\frac{G}{\rho}} \tag{3.2}$$

Equations 3.1 and 3.2 show how the SOS is independent of frequency, which indicates a non dispersive wave, [108]. Any phenomenon that effects the density of a material such as an applied stress or temperature will have an effect on the SOS. SOS gets faster with an increase in temperature as each particle has more energy. Also, if a material is isotropic and homogeneous, SOS can be considered to be uniform in all directions and at every point. If a material is deemed non-isotropic and/or non-homogeneous, SOS will most likely change with direction and location within the material, [109]. Table 3.1 shows some common materials and their SOS values. Notice that shear SOS values are not represented for liquids due to the difficulty to measure them. This is a result of their extremely short

propagation lengths.

Table 3.1: Longitudinal and shear SOS values for some common materials, [110, 111].

Material	Longitudinal SOS (m/s)	Shear SOS (m/s)
Aluminium	6420	3100
Nylon 6/6	2600	1070
Transformer Oil	1390	-
Water at 20°C	1480	-

3.3.2 Acoustic Impedance

The acoustic impedance, Z, is a parameter used to describe the resistance that a sound wave is subject to whilst travelling throughout a material, and is defined as the ratio of acoustic pressure, P, and the particle displacement velocity, U, Equation 3.3.

$$Z = \frac{P}{U} \tag{3.3}$$

It is also used to determine the quantity of energy that is transmitted and reflected at a boundary between two materials having an impedance mismatch. The longitudinal and shear acoustic impedance of a solid, Z_s is related to the density, ρ_s, and the speed of sound, Equation 3.4. However the value for the longitudinal impedance is different to the shear impedance as the longitudinal and shear SOS is different.

$$Z_s = \rho_s c_s \tag{3.4}$$

The longitudinal acoustic impedance of a liquid is similarly given by Equation 3.4. In contrast the shear acoustic impedance of a liquid, Z_l is a combination of the liquid's density and the liquids complex shear modulus, G, which was defined in Chapter 2.

$$Z_l = \sqrt{\rho_l G} \tag{3.5}$$

Table 3.2 shows some common material impedance values as an illustration of how impedance varies depending on the material. The consideration of a material's impedance when designing an ultrasonic system is extremely important. For example, when designing

an ultrasonic transducer, sound is emitted from a source, which could be enhanced in signal to noise ratio, intensity, or controlled in one direction by selecting specific materials with varying impedances.

Table 3.2: Longitudinal acoustic impedance values for some common materials, [110, 112].

Material	Impedance ($MRayl$)
Aluminium	17.33
Nylon 6/6	2.9
Transformer Oil	1.28
Water at 20°C	1.48

3.3.3 Attenuation

Sound energy diminishes over distance as it travels through a material. Equation 3.6 explains this diminishing effect using the initial energy amplitude, A_0, which travels a distance, x and is reduced by a frequency dependent attenuation coefficient, α, which varies with material. The effect of attenuation on a sound wave is illustrated by comparing an un-attenuated sound wave with an attenuated one, Figure 3.3.

$$A = A_0 e^{-\alpha x} \tag{3.6}$$

The attenuation coefficient determines how quickly the pressure amplitude decays with distance due to various dissipative effects, including radiation, absorption and scattering [106]. Radiation is simply the spreading of the wave from the point of source. Scattering is the reflection of the sound in directions other than its original direction of propagation, and absorption is the conversion of the sound energy to other forms of energy such as heat. The severity of the attenuation increases with increasing frequency, as shorter wavelengths are more effected by minute material property variances. The units of the attenuation coefficient requires taking the logarithm of the ratio of pressures at different distances. Therefore either nepers per metre, Np/m or decibels, dB can be used to characterise the pressure decay.

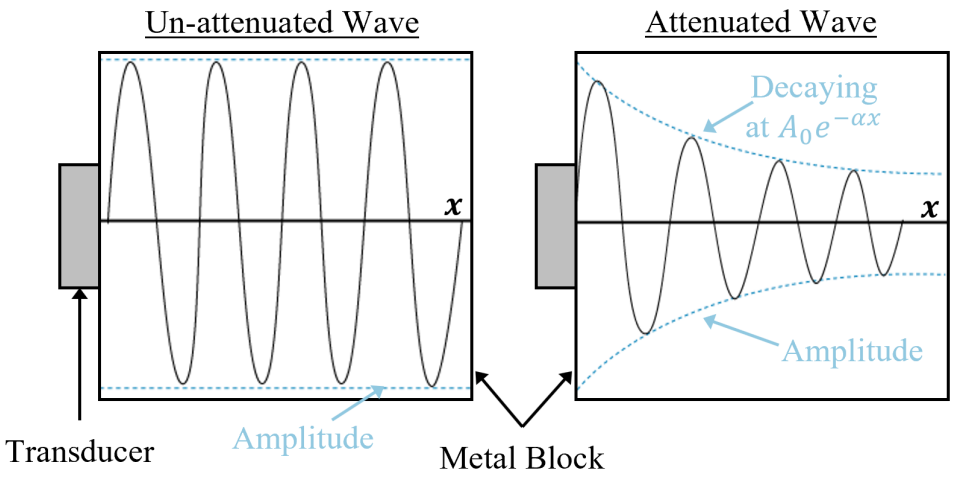

Figure 3.3: Comparison between an un-attenuated and an attenuated sound wave inside a metal block.

In emulsions and suspensions, scattering is the result of the boundaries created between the continuous phase and suspended particles. For this explanation, it assumed that each of these particles are spherical and far apart, so that the scattering from multiple particles does not interact. In this case the scattering characteristic length is given by the dimensionless number in Equation 3.7, [112].

$$ka << 1 \tag{3.7}$$

Where $k = \frac{2\pi}{\lambda}$ is the wavenumber and a is the particle radius. This equation is known as the Rayleigh limit can be written in terms of wavelength as shown in Equation 3.8.

$$\frac{2\pi a}{\lambda} < \frac{1}{10} \tag{3.8}$$

An important theory arising from Rayleigh's work was that the attenuation is inversely proportional to the square of the frequency, shown in Equation 3.9. This theory was later improved and advanced on by Epstein and Carhart, and Allegra and Hawley, [113, 114], to include thermal and visco-inertial effects.

$$a \propto f^2 \tag{3.9}$$

Scattering of acoustic waves by obstacles are relatively easy to present for the case where the wavelength is either much greater or much less than the characteristic dimension of the particle, [115]. When the particle size is much larger than the wavelength of the sound wave, $ka >> 1$, the particle acts like a complete reflector of acoustics. Therefore, the scattering cross section is independent of frequency, which is equal to the geometric cross sectional area. Rayleigh scattering is when the particle size is much smaller than the wavelength of the sound wave, $ka << 1$. Most acoustic measurements on the particle size and volume are investigated in this region. For this type of scattering, the scattering cross section is independent of the particle shape, dependent on the volume and acoustic frequency, [115].

When the particle size is similar to the wavelength of the sound wave, $ka \approx 1$, the interaction between the sound wave and the particle is complicated. The scatted wave is critically dependent upon the dimensions, shape and acoustic properties of the particle. Scattering results are of a periodic nature as its value increases and decreases due to the interference from the reverberation inside the particle and the incident wave, [115]. No matter whether the particle is solid, liquid or gas phase, this type of behaviour is always present.

3.3.4 Wave Propagation Distance in Fluids

Another method for showing the effects of attenuation is by using the penetration depth. The penetration depth is the distance an acoustic wave travels through a material before it is completely attenuated. Equation 3.10 illustrates that the penetration depth is inversely proportional to the attenuation.

$$\delta = \frac{1}{\alpha} \tag{3.10}$$

In fluids, longitudinal waves can travel much greater distances than shear waves, The penetration depth for a longitudinal and shear wave is given by Equation 3.11 and 3.12, respectively.

$$\delta = \frac{\rho_l c^3}{\omega \eta} \tag{3.11}$$

$$\delta = \sqrt{\frac{2\eta}{\rho_l \omega}} \tag{3.12}$$

Using Equation 3.11 and 3.12, values such as a density of 800 kg/m^3, longitudinal SOS of 1400 m/s, and varying viscosities were evaluated across the ultrasonic frequency range, Figure 3.1. The result in Figure 3.4 shows that liquids do not support shear waves very well, which means that the penetration depth is significantly shorter than longitudinal depths. Furthermore longitudinal waves attenuate more with increasing viscosity, whereas shear waves travel further distances with increasing viscosity.

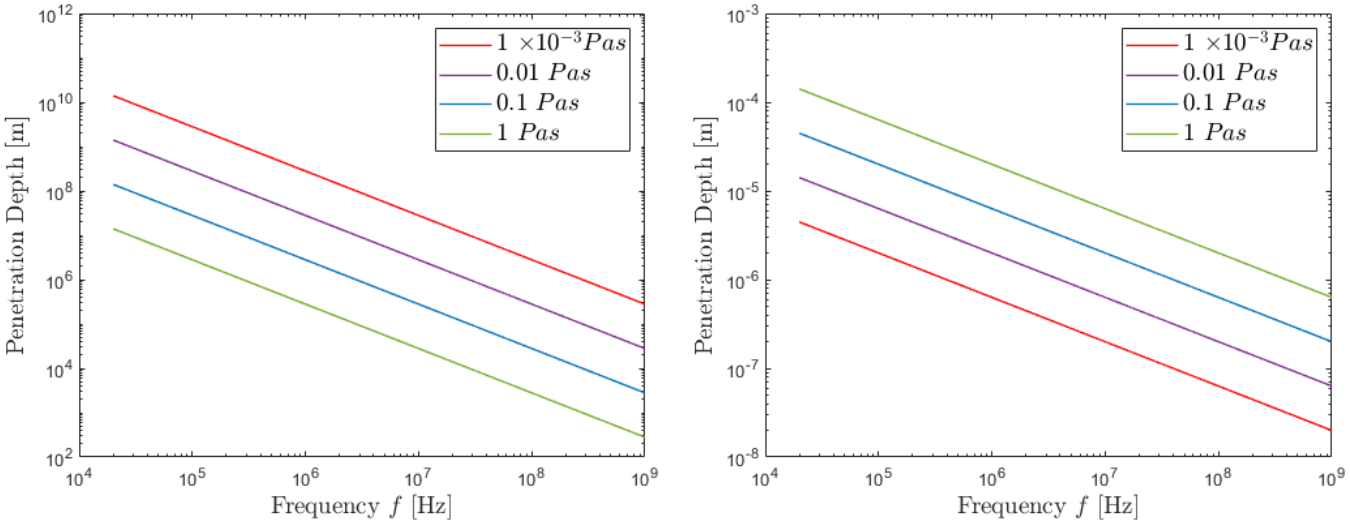

(a) Longitudinal penetration depth.

(b) Shear penetration depth.

Figure 3.4: The penetration depth of longitudinal and shear waves for different viscosities over the ultrasonic range of frequencies.

3.3.5 Interference

When two waves of the same frequency come into contact, the sum of their amplitudes creates a new wave form. If the two waves are in phase, constructive interfere will occur. Whereas if the two waves are $\pi/2$ radians out of the phase, there will be destructive interference, and the resultant wave is zero, Figure 3.5. The phase, θ, is typically used to describe the change between two waves at the same frequency and is measured in radians.

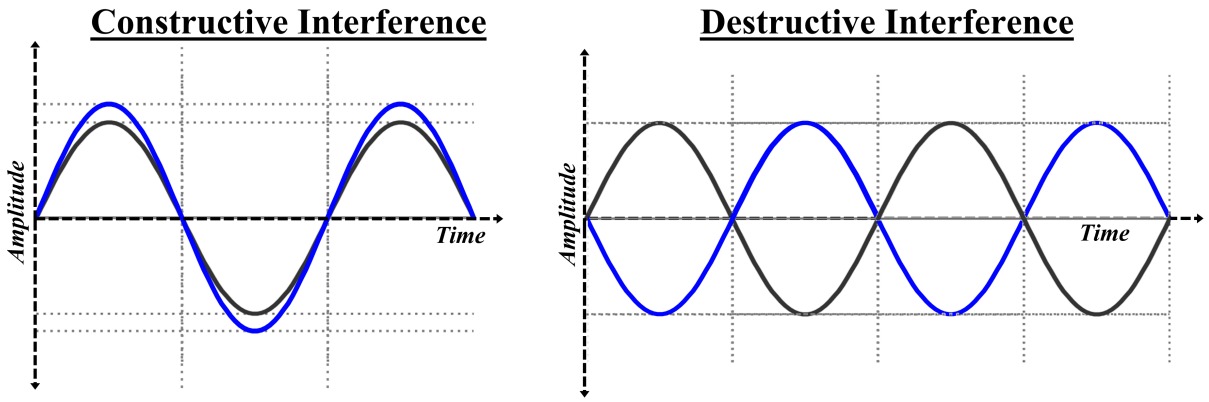

Figure 3.5: Illustration of constructive and destructive wave interference.

Interference can be used to control an ultrasonic system to achieve a more desired result. Figure 3.6 shows a schematic of a three layered system, where the intermediate medium is a matching layer that is a quarter thickness of the frequency wavelength, $\lambda/4$. The matching layer thickness is calculated using Equation 3.13. Destructive interference is created using reflections from an initial wave at boundaries x_1 and x_2. The reflected waves from these boundaries are 180 degrees, or $\pi/2$, out of phase and so the resultant reflected wave is zero. This is commonly employed when creating ultrasonic transducers and using ultrasonic shear sensors to measure viscosity, [15].

$$t_m = \frac{c_m}{4f} \tag{3.13}$$

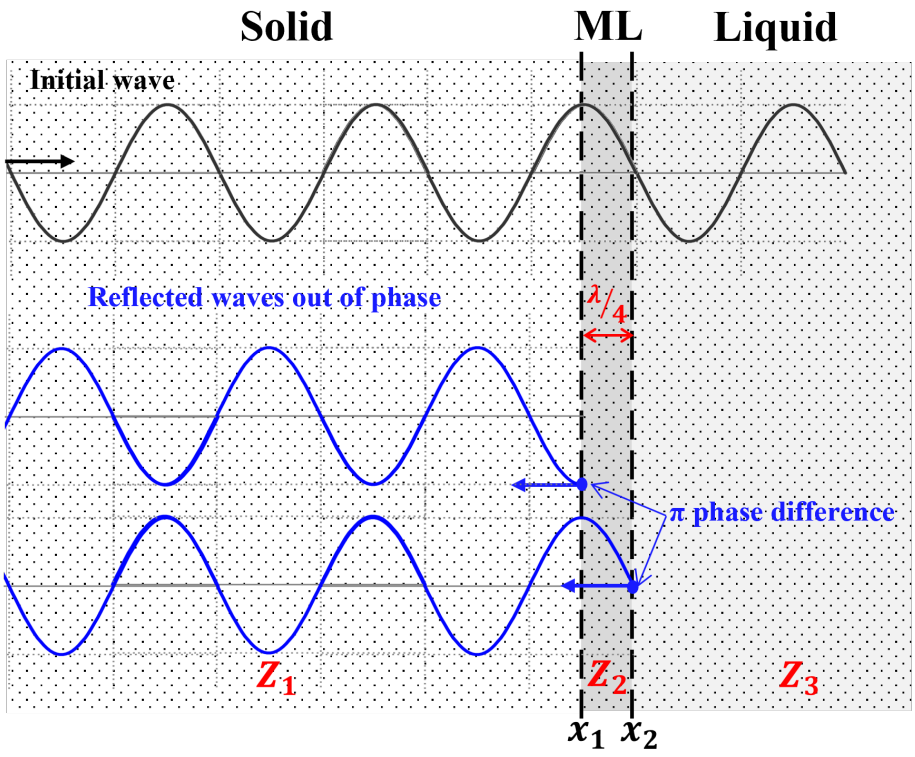

Figure 3.6: A schematic diagram of the behaviour of a wave in a quarter wavelength thick, $\lambda/4$, matching layer, [17].

3.4 Wave Interaction with Boundaries

The reflection coefficient, R, is the ratio between the reflected and the incident acoustic pressure, whereas the transmission coefficient, T, is the transmitted divided by the initial acoustic pressure. Since the incident wave energy is split between the reflected energy and the transmitted energy, the transmission coefficient can be calculated by simply subtracting the reflection coefficient from one, [116]. Equation 3.14 shows the solutions for the reflection and transmission coefficients.

$$R = \frac{P_r}{P_i} \qquad T = \frac{P_t}{P_i} \qquad T = 1 - R \tag{3.14}$$

3.4.1 Two Layered System

Figure 3.7 shows two dissimilar materials that are completely bound together forming an interface at x_1, where the subscripts i, r and t, refer to the incident, reflected and transmitted energy, respectively. When a propagating sound wave of a certain pressure and velocity contacts that interface at a normal incidence, a quantity is reflected and transmitted. This is caused by the acoustic impedance mismatch between the two materials, where a large impedance mismatch results in a reduction in transmitted energy, [117]. To establish the portion of energy reflected in terms of material impedance values, Equation 3.19 is derived. Equation 3.15 is produced by continuity of pressure and velocity at the boundary x_1. This is then rearranged to get Equation 3.16.

$$P_i + P_r = P_t \qquad\qquad U_i + U_r = U_t \tag{3.15}$$

$$\frac{P_i + P_r}{U_i + U_r} = \frac{P_t}{U_t} \tag{3.16}$$

Using the definition of impedance in Equation 3.3, Equation 3.17 is produced, where a negative impedance value indicates the sound direction of travel in Figure 3.7.

$$\frac{P_i}{U_i} = Z_1 \qquad\qquad \frac{P_r}{U_r} = -Z_1 \qquad\qquad \frac{P_t}{U_t} = Z_2 \tag{3.17}$$

Therefore the ratio of pressure to velocity on the right side of Equation 3.16 is the impedance of layer 2. For the left side of Equation 3.16, the velocity terms are written in terms of impedance and pressure by rearranging Equation 3.17 to become $U = P/Z$. This produces Equation 3.18.

$$Z_1 \frac{P_i + P_r}{P_i - P_r} = Z_2 \tag{3.18}$$

Finally Equation 3.19 is obtained by combining the reflection coefficient in Equation

3.14 with Equation 3.18. This allows the reflection coefficient to be calculated in terms of the layer impedance values.

$$R = \frac{Z_2 - Z_1}{Z_2 + Z_1} \tag{3.19}$$

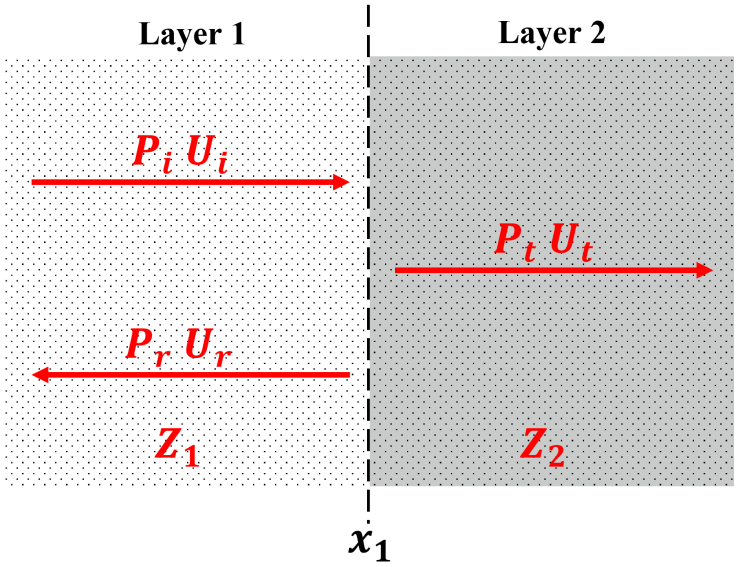

Figure 3.7: Normal incident wave for a two layered system.

3.4.2 Three layered system

As discussed previously for a two layered system, whenever a wave reaches a boundary, a portion will be reflected and another portion transmitted. For a three layered system, Figure 3.8, the same process will occur, however the transmitted wave from the first boundary will be the initial wave acting on the second boundary. This provides a progressively weaker sound wave with each boundary added. However as mentioned in Section 3.3.5, this intermediate layer could be optimised to benefit an application, for example, through use of a quarter wavelength, $\lambda/4$, matching layer in an ultrasonic viscometer.

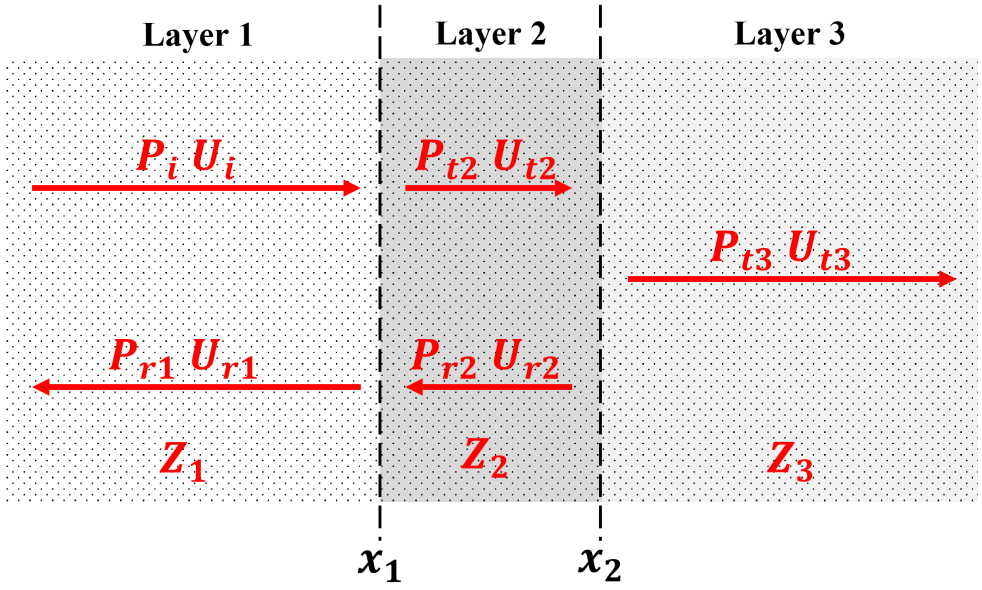

Figure 3.8: Normal incident wave at two boundaries.

To establish the portion of energy that is reflected, Equation 3.19 is given. This equation was derived by Kinsler, [116], which is reproduced later in Chapter 5. The wave number, k, describes the number of waves per distance in the intermediate layer, $k = \frac{2\pi}{\lambda}$.

$$R = \frac{(1 - Z_1/Z_3)\cos(k_2 x) + j(Z_2/Z_3 - Z_1 Z_2)\sin(k_2 x)}{(1 + Z_1/Z_3)\cos(k_2 x) + j(Z_2/Z_3 + Z_1/Z_2)\sin(k_2 x)} \tag{3.20}$$

3.4.3 Comparison of a Two and Three Layered System

Figure 3.9 illustrates the difference between the reflection coefficient of a two and three layered system, using Equations 3.19 and 3.20 respectively. Table 3.3 shows the shear impedance values used in both equations. The thickness of layer two in Equation 3.20 was set to be a quarter of the wavelength of a 2 MHz frequency. The impedance values mimic a metal - oil and a metal - polymer - oil set-up, for example, aluminium - oil or aluminium - polyimide - oil.

Table 3.3: Shear impedance values used in Equations 3.19 and 3.20 to produce Figure 3.9. These values were similar to a metal - oil and a metal - polymer - oil set-up.

Acoustic Impedance	
Layer 1	8.52 $MRayl$
Layer 2	1.1 $MRayl$
Layer 3	0.01 $MRayl$

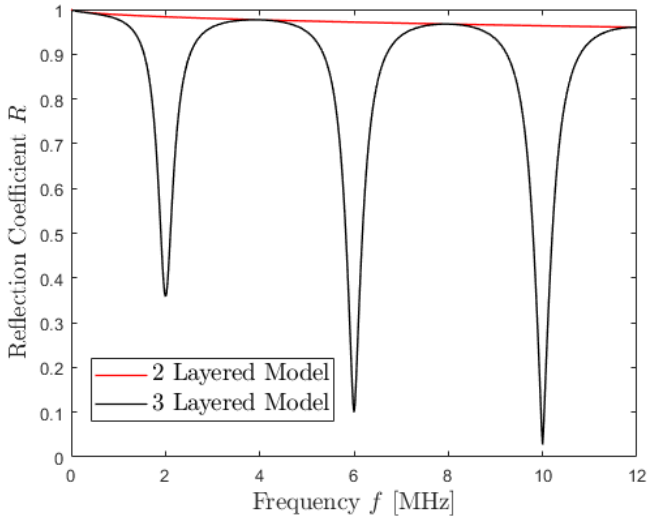

Figure 3.9: Comparison between a two (Equations 3.19) and three layered (Equation 3.20) system using the reflection coefficient with respect to frequency, where the matching layer thickness corresponded with 2 MHz. The two layered system was a metal - oil and the three layered system was a metal - polymer - oil set-up.

As the shear acoustic impedance of a liquid is dependant on the frequency, Equation 3.5, both systems show a decrease in reflection coefficient as the frequency increases. However, the three layered system has dips in the reflection coefficient at frequencies corresponding to 2 MHz. This is due to layer 2 being a quarter of the wavelength of the frequency at the minimum dip point. Hence more energy is transmitted into the fluid layer. Using Equation 3.13 and multiplying it by an odd integer, for example from 1-5, multiple resonant frequencies are highlighted at 2, 6 and 10 MHz. These are the odd harmonics created by the destructive interference of layer 2. The two layered system has an almost complete reflection coefficient (R = 1). This is due to such a large impedance mismatch between the metal and oil. In contrast, the three layered system has an impedance matching layer, which acts as a step down between a high impedance material to a low

one. The three layered system is modelled and discussed in more detail later in Chapter 5.

3.5 Ultrasonic Transducers

This section introduces the phenomenon of the piezoelectric effect and how sound is created. It then introduces the different ultrasonic sensors capable of producing sound in numerous non-destructive testing and evaluating applications.

3.5.1 Piezoelectric Effect

The piezoelectric effect is the phenomenon that describes the creation of electric charge when a ceramic piezoelectric material undergoes an applied mechanical stress. Figure 3.10 shows a typical piezoelectric material at rest, and directly and indirectly effected by vibrational energy. Indirectly effected piezoelectric materials are electrically charged by applying a potential difference across them. Directly effected piezoelectric materials are electrically charged by a series of compressions and extensions (waveform). In other words, piezoelectric materials can produce and receive acoustic signals.

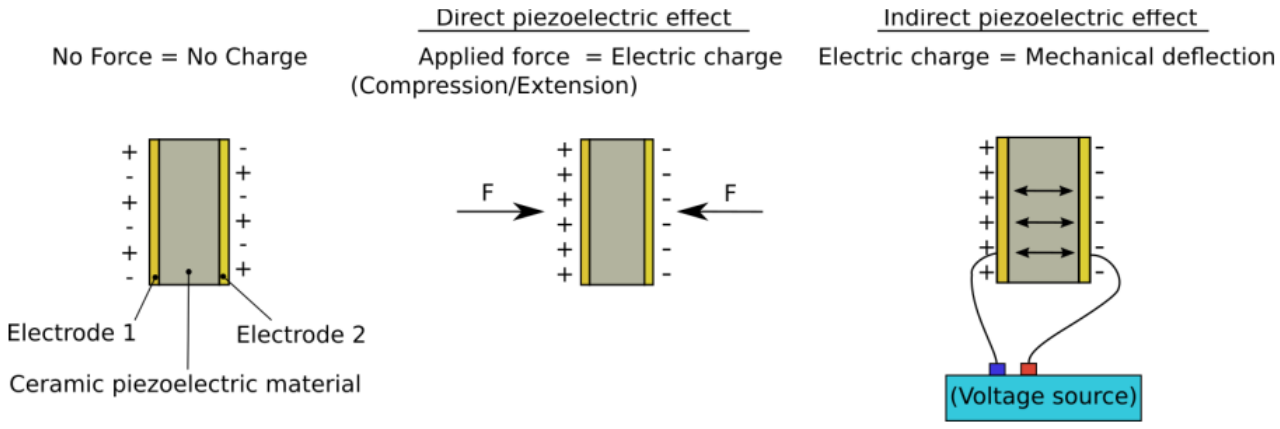

Figure 3.10: Piezoelectric effect [17].

3.5.2 Piezoelectric Element

Piezoelectric elements are categorised by the polarisation direction and the frequency. The polarisation determines the wave mode produced by the element, where shear modes are created with polarisation perpendicular to the propagation direction. To polarise an element, it is heated beyond its Curie temperature and then cooled in the appropriate electrical field, [118]. The resonant frequency is determined by the element's geometry, permittivity and surroundings. When exciting a piezoelectric element at the resonant frequency, the amplitude oscillation is at its maximum. The element can also be forced to oscillate at other frequencies, however, the further away the pulsing frequency is from the transducer frequency, the smaller the resulting amplitude.

Piezoelectric elements are typically made using materials such as, quartz, lead meta-niobate, barium titinate and most commonly, lead zirconate-titonate (PZT), [119]. PZT is most popular due to its functionality as examination and evaluation transducers, though more importantly, its fabrication potential. Figure 3.11 shows piezoelectric elements made in a variety of different shapes and sizes for varying applications.

Figure 3.11: Piezoelectric element [120].

3.5.3 Commercial Transducers

Commercial transducers are designed with more than just the bare piezoelectric element. They also consist of a backing material offering high damping effects, electronic cabling, a protective front face layer and a robust casing, [121]. The damping material is typically attenuative and highly dense, to dissipate ultrasound that originates at the top surface

of the piezoelectric element [112]. Furthermore, it suppresses the undesired reverberation of the oscillations produced by the element, and mechanically protects the piezoelectric element from external interference. A matching layer is used to maximise the energy output. In front of the matching layer is a protective front face that provides wear and corrosion resistance, which helps the transducer function in harsh conditions for increased longevity.

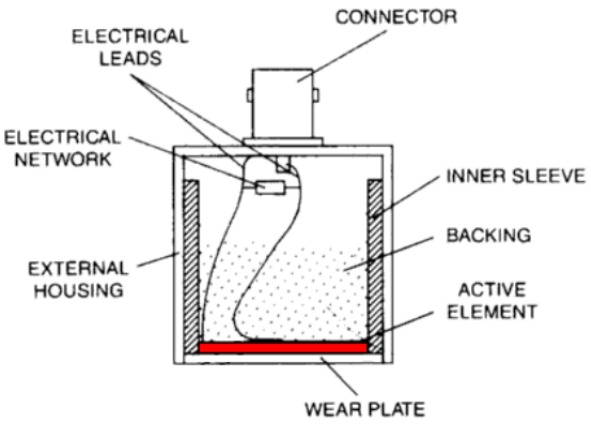

Figure 3.12: Exploded diagram of the internals of an ultrasonic commercial transducer [109].

3.5.4 Coupling

As mentioned in Section 3.4, when sound interacts with a boundary energy loses occur. When a transducer is used in contact with a material boundary, it requires a coupling material to facilitate energy transmission. Without this coupling, most ultrasonic waves would be transmitted due to a thin gap of air between the piezoelectric element and inspection surface. A couplant material greatly reduces air between the sensor and host material, creating a constant path of elastic particles capable of hosting a pressure wave. Coupling can reduce the excitation amplitude and can produce some interfering waves, which may alter the shape of a initial and/or reflected signal. For piezoelectric elements that are bonded to a material surface using an epoxy, the resonant frequency can also be slightly changed, as there is an increased resistance to vibration and a slight thickness increase. Despite this, the benefits of coupling outweigh the drawbacks.

3.5.5 Near Field Effect

Sound propagating from a transducer initially fluctuates in amplitude and phase, as the vibrations are generated from many points across the surface of the piezoelectric element. After a certain distance, the numerous waveforms construct and destruct to form a desired waveform. Figure 3.13 shows the near field range, where fluctuating amplitudes and phase occur, and the far field range, where a stable waveform is achieved. It is important to test in an optimum range outside of the near field, as testing too far into the far field reduces the amplitude of the initial wave. The near field range, N_d, expressed in metres, is calculated using equation 3.21, where d is the active element diameter.

$$N_d = \frac{d^2 f}{4c} \tag{3.21}$$

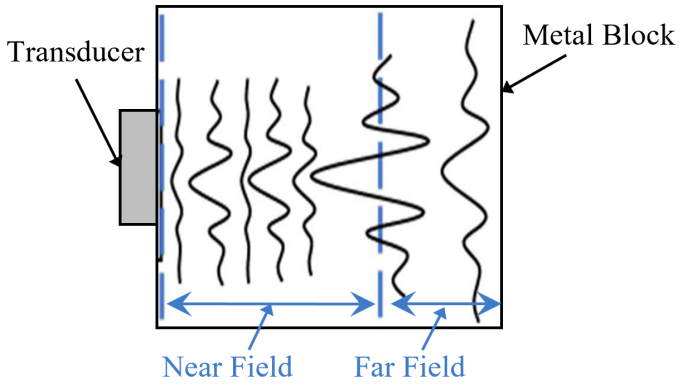

Figure 3.13: Forming of a fully constructed waveform in the near field range.

3.5.6 Beam Spread

As a sound wave propagates from its source, it diverts from a central axis line, where divergence increases with distance. The greater the sound wave spreads, the larger the measurement area. Beam spread occurs because particles are not directly aligned in the direction of wave propagation, hence, some of the energy will get transferred off at an angle, [109]. The effects of beam spread are an increased measurement area and progressively weaker wave. The beam spread angle, θ, is calculated using Equation 3.22, where, c, is the speed of sound in the material, d, is the diameter of the transducer and, f, is the

frequency. Beam divergence can also be used to quantify sound spread, which is equal to $\frac{\theta}{2}$.

$$\sin(\theta) = 1.2\frac{c}{df} \tag{3.22}$$

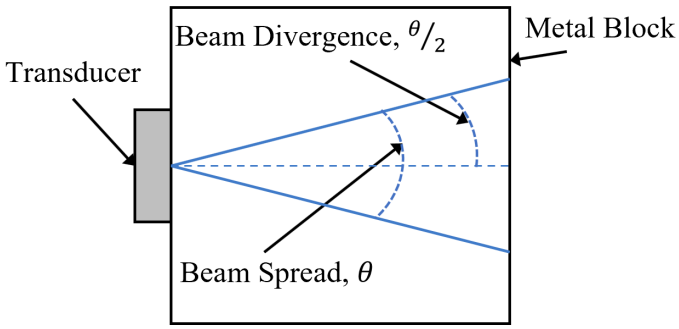

Figure 3.14: Beam spread and beam divergence of a wave inside a metal block.

3.5.7 Transducer Arrangements

There are different transducer arrangements in order to pulse and receive signals. Figure 3.15 shows the pulse-echo, pitch-catch and through transmission configurations. Pitch-catch and through transmission utilise two sensors, where one pulses and the other receives. The difference is that the pitch-catch transducers are adjacent to each other on the same interface, whereas through transmission transducers are opposite on different interfaces. Pulse-echo uses one transducer as a transmitter and the other as a receiver. This type of arrangement is most popular as it only requires one surface of mounted transducers, allowing it to be installed more easily to engineering applications.

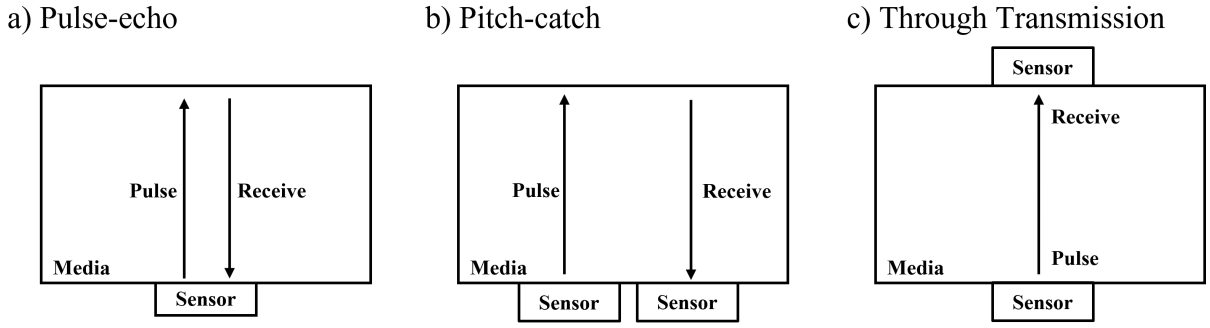

Figure 3.15: Transducer pulsing and receiving arrangements.

3.6 Pulsing and Receiving Instruments

In order to excite a transducer a function generator is used. This generates a waveform as a digital signal which is then converted to an analogue signal before passing into the transducer. When the analogue signal reaches the transducer an ultrasonic pressure wave is created. The reflected pressure wave is then recorded by the transducer in analogue form and then digitised back into an electrical signal. This entire process is illustrated by Figure 3.16. To view this signal, an oscilloscope or digitiser - external PC with the relevant software can be used.

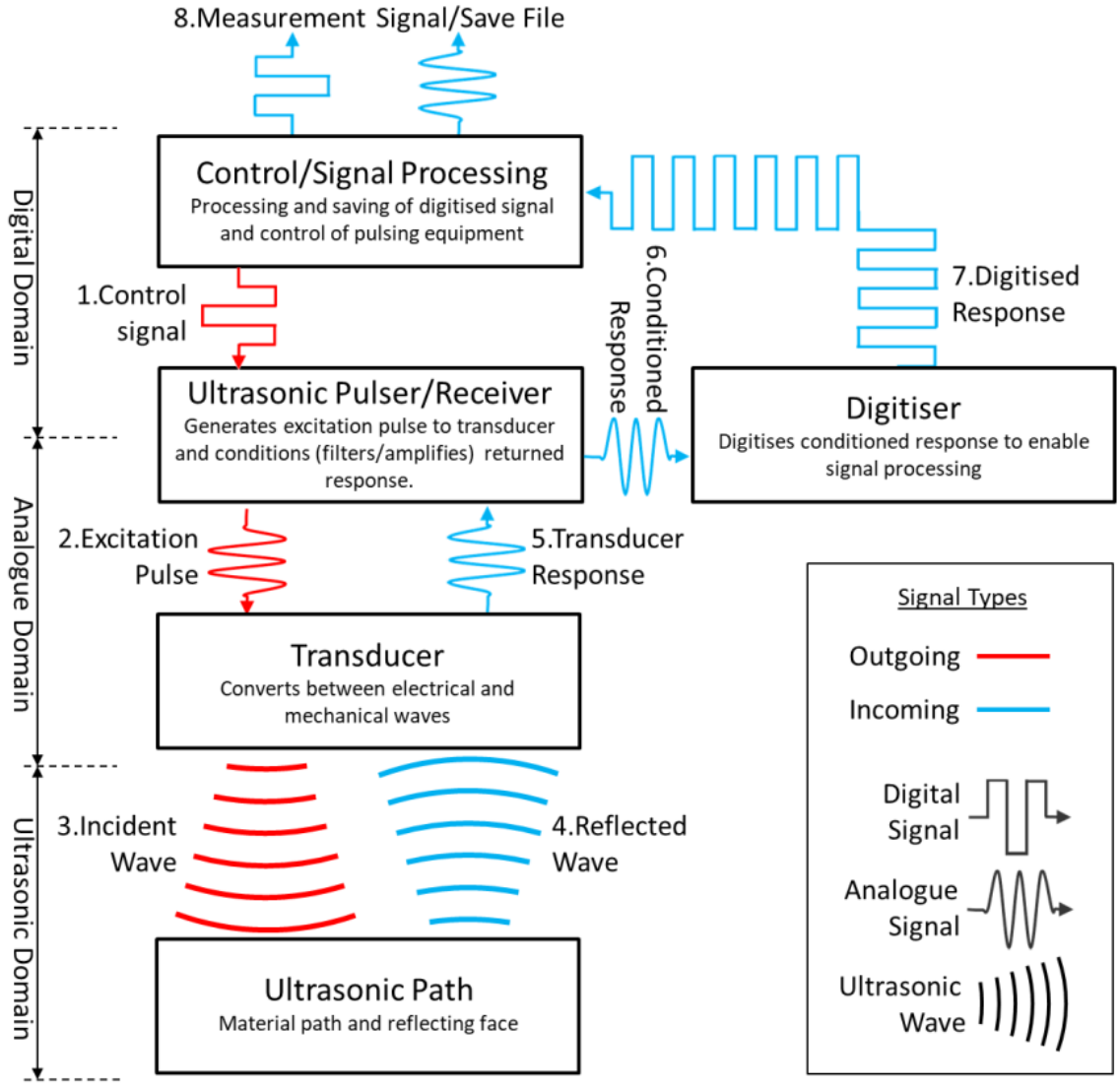

Figure 3.16: Schematic of a typical ultrasonic pulsing system, [122].

Figure 3.17 shows a typical waveform generator, oscilloscope and a PicoScope. The PicoScope is a waveform generator with an on board digitiser capable of working with LabVIEW software. The difference between an oscilloscope and digitiser is that an oscilloscope is a stand alone device. Whereas a digitiser acquires and stores an electrical voltage waveform and displays it on an external device, for example a PC. Defining factors for a good digitiser are its sampling rate, amplitude resolution, bandwidth and the number of channels it is required to convert.

(a) Function generator.

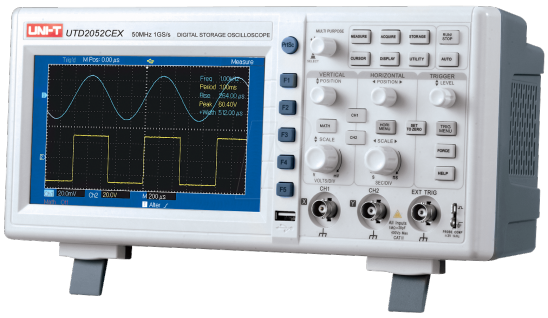

(b) Oscilloscope.

(c) PicoScope waveform generator and digitiser.

Figure 3.17: Ultrasonic pulsing and data acquisition instruments used with ultrasonic transducers.

3.7 Ultrasonic Signal Characteristics

Ultrasonic equipment such as a combined waveform generator and oscilloscope are capable of exciting transducers and recording the received data. This data can be represented in a number of ways, however throughout this thesis the initial raw data is represented as an A-scan. An A-scan presents the amount of received ultrasonic amplitude energy as a function of time. It is also convenient for Fast Fourier Transform (FFT) analysis to view a signal with respect to its frequency components.

3.7.1 Sensor Waveform Excitation Modes

Waveform function generators are capable of producing a variety of waveforms. The most common types of waveforms are shown in Figure 3.18 and consist of a spike wave, square wave and sine wave. Spike pulses have fast rise times and short durations, therefore they are often used to pulse at high voltages. They also have broad spectral excitation, which allows them to work well with probes of all frequencies. Square waveforms are extremely stable when exciting a wide range of sensors as their circuitry has extremely low output impedance. Their pulse duration can also be adapted to excite a signal with a base frequency that matches the center frequency of the transducer. Sine waves are great for frequency efficiency and precision when exciting transducers at their resonant frequency. They are capable of being amplified, however it is difficult to create sine waves at such high frequencies and voltages.

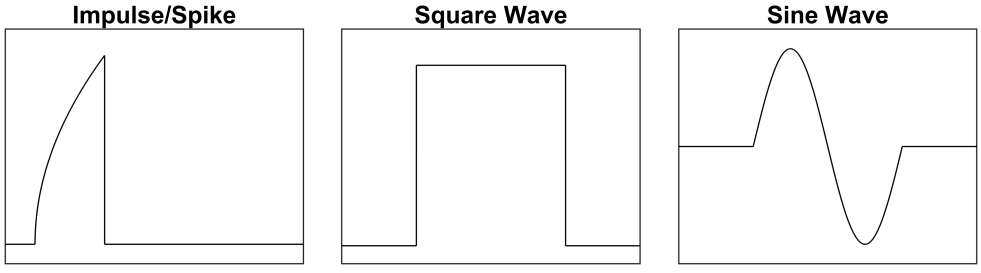

Figure 3.18: Excitation modes consisting of impulse/spike, square and sine waveforms, [123].

Another type of waveform is a linear and exponential chirp, Figure 3.19. A chirp is

a sinusoidal signal that is pulsed over a range frequencies. The difference between these chirps is the frequency sweep style, where one changes frequency linearly and the other one exponentially. The main difference is that linear chirps excite a frequency range with the same energy, while logarithmic chirps do not. Chirps have been used to determine the direct and harmonic responses of variety of systems. For example, Schirru, [15], found the exact resonant frequency for a matching layer in ultrasonic viscometry. Chirps have also been used to address the need to both test at multiple frequencies and achieve a high signal-to-noise ratio. This was done by Michaels, [124], who used deconvolution to extract multiple narrowband responses from a broadband chirp.

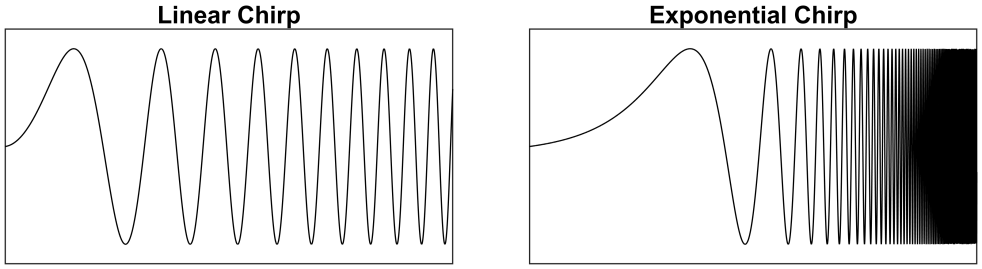

Figure 3.19: Linear and exponential chirp excitation types, [123].

The shape of the initial excitation depends on the desired or expected result in a system, as its characteristics, such as material properties and reflecting features could be accentuated, [106].

3.7.2 Frequency Domain

To obtain the frequency components of a time domain signal, a Fast Fourier Transform is used. Figure 3.20 illustrates a typical FFT response of a time domain wave, where each key characteristic is annotated. The frequency-domain response has several significant characteristics defined by ASTM and ISO standards, [125, 126]. The bandwidth of a transducer is characterised as 50% (or $-6dB$) of the peak frequency value. This creates the upper and lower cut-of frequencies. The centre frequency is not always the peak frequency, hence they are shown as different variables.

Key	Description
X	Frequency
Y	Amplitude
1	Peak Frequency
2	Upper Cut-Off Frequency
3	Lower Cut-Off Frequency
4	Centre Frequency
5	Bandwidth at Specified Amplitude Drop
6	Peak Amplitude
7	Specified Amplitude Drop

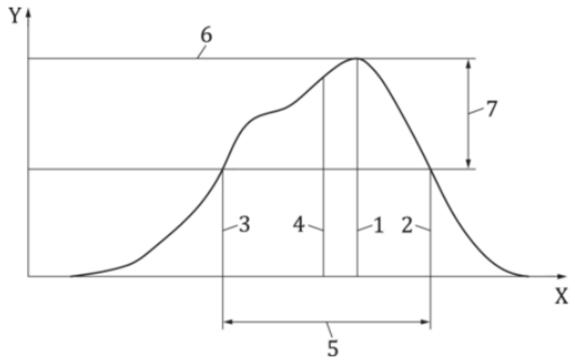

Figure 3.20: Ultrasonic signal characteristics of a frequency domain signal, [126].

Despite standardised signal characteristics, some transducers can have drastically different responses, making them better or worse in a specific scenario. A highly damped transducer will result in a very short pulse and a broadband signal, Figure 3.21, whereas an un-damped transducer will result in a wide pulse with a narrowband signal, Figure 3.22.

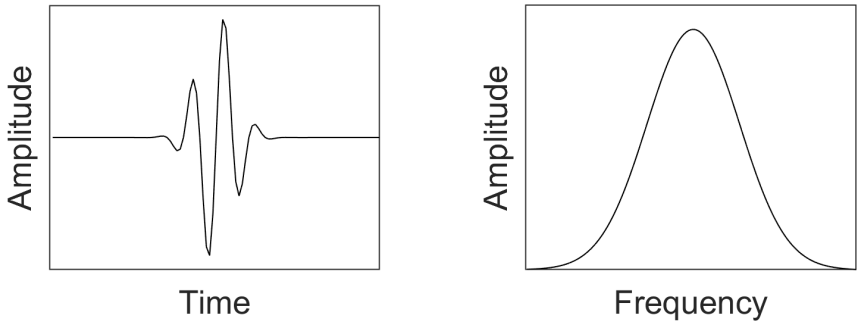

Figure 3.21: Transducer time and frequency response for a damped signal, [123].

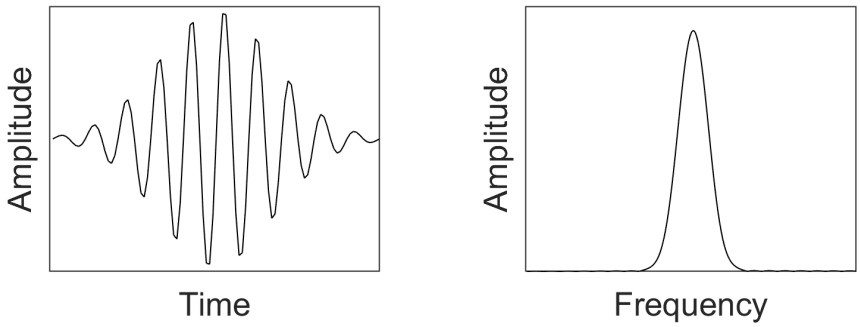

Figure 3.22: Transducer time and frequency response for an un-damped signal, [123].

3.8 Combining Rheology with Acoustics

Shear and extensional stress can be applied to a liquid to study its rheology, [99]. Shear stress is when the applied stress is tangential to the liquid surface, which causes a relative sliding motion of the liquid layers. When this type of stress is oscillated it is called shear rheology. Conversely, extensional stress is when the applied stress is normal to the liquid surface. When the extensional stress varies with time a volume change occurs inside the liquid, thus the fluid under investigation cannot be considered incompressible, [127]. This type of rheology is called longitudinal rheology. Litovitz and Davis [128, 129, 130], present in parallel both shear and longitudinal rheological theories with acoustics, however, here only shear is considered.

If a low frequency oscillation is applied to a liquid in a two plates system, where one is fixed and another is in motion, the displacement caused by the sliding motion has enough time to fill the entire liquid in the first half of the oscillation cycle. Therefore the liquid displaces in one direction. However in a high frequency oscillation, the plate providing the shear motion would change direction before the displacement from the first half of the cycle would fill the entire liquid. Hence, areas in the liquid will have opposite displacements, which creates a wave of displacement. If the oscillation wavelength is much shorter in comparison to the size of the system, then the subjects of rheology and acoustics merge, [127]. These oscillations can be generated in multiple different ways: rotating cylinders, shaking plates and piezoelectric materials. The latter is the focus of this thesis.

3.9 Ultrasonic Shear Rheology

The first written evidence providing a method to measure the viscosity of liquids using ultrasonic shear wave was published by Mason et al, [131]. The investigation comprised of achieving high shear rates to determine whether a shear elastic and viscous effect was exhibited by fluids. The ultrasonic viscometer, Figure 3.23a, was boned together using silver paste and included a crystal and quartz rod, where the measurement interface was at the free end of the quartz rod. The reflection coefficient and the phase, θ, was calculated by comparing a frequency domain signal with liquid to one without liquid, Figure 3.23b.

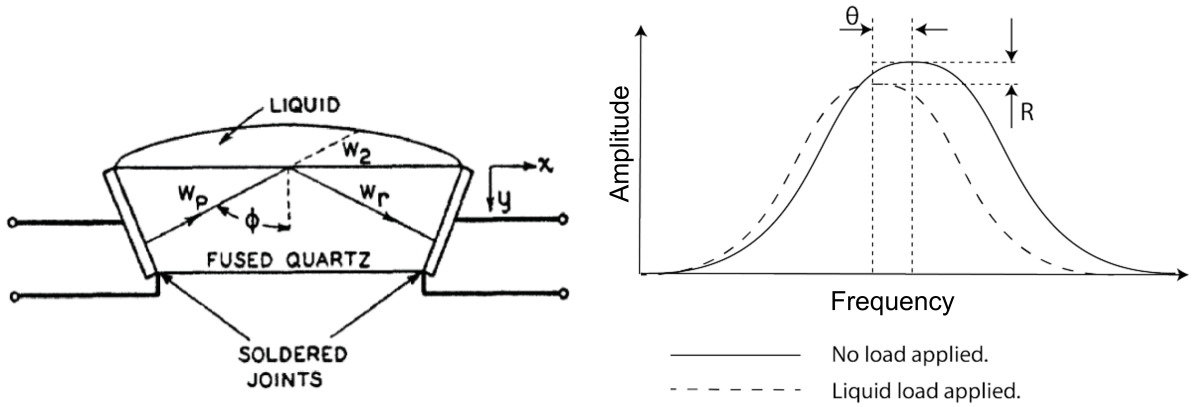

(a) Ultrasonic viscometer.

(b) Signal analysis.

Figure 3.23: Mason's ultrasonic viscometer and signal analysis, [131].

Shear waves were pulsed at 4.5 MHz, 14 MHz and 24 MHz to measure the resistance and reactance for different samples over a temperatures range of $10°C$ - $50°C$. The acoustic impedance of the liquid, Z_l, was then calculated using Equation 3.23 with measured reflection coefficient values, where the fluid was considered Newtonian by combining Equation 3.5 and 2.9. In Equation 3.23 Z_Q is the impedance of the quartz and ϕ is the angle of incidence from the normal.

$$Z_l = cos(\phi) Z_Q \frac{1 - R^2 + 2jRsin(\theta)}{1 + R^2 + 2jRcos(\theta)} \tag{3.23}$$

3.9.1 Early Developments

Since Mason's initial research into measuring the viscosity of fluids using a quarts crystal there has been many novel developments and applications. Roth and Rich, [132], developed this method in order for it to be used in-situ. The main differences from Mason's investigation was that the transducer was boned onto an alloy, which was then submerged in the test fluid and the damped shear vibrations were related to the viscosity. With this apparatus, Roth measured at 30 kHz with an accuracy of ± 5%.

Barlow, [133], produced the first research that included ultrasonic spectroscopy. Barlow did this by obtaining the viscosity at a range of frequencies in order to measure the viscoelastic behaviour of lubricating oil at high shear rates. Using Mason's viscometer, Barlow improved the range and magnitude of the ultrasonic frequency by adapting the electrical apparatus. Following this, the transducer then produced a large range of frequencies as it was excited at its resonant frequency, 6 MHz, and then at odd harmonics up to 78 MHz.

Cohen-Tenoudji et al., [134], adapted Mason's ultrasonic apparatus to obtain the viscosity at high temperatures using sensors that, for the first time, were not in contact with the fluid. Instead, the transducer was distanced from the test fluid using a buffer system. It was then used to measure the viscosity of epoxy over a range of temperatures. The behaviour of the result was comparable to rheometer data taken at 10 Hz, however the absolute value from the rheometer was higher than the ultrasonic measurements.

A major flaw associated with ultrasonic testing was the time-consuming signal analysis. This was a result of the manipulation process that transformed a time domain signal into a frequency domain, which was completed by hand. Alig et al., [135], automated this process using digitisation, where measurements were completed utilising two different pulsing methods, consisting of a single frequency pulse technique and an ultrasonic spectroscopy technique.

These breakthroughs led to further advancements using the ultrasonic viscometers such as measuring the density and viscosity using a combination of shear and longitudinal waves, [136], measuring the viscosity of foodstuffs, [137], wave mode conversion to convert

a longitudinal wave into a shear wave, [138], and additional measurements of the viscosity of oils, [139]. To measure oil viscosity Saggin, [139], utilised a steel - oil set up where the reflection coefficient was above 0.94 for an oil with viscosity of 100 Pas. This showed that the ultrasonic system was very insensitive to low viscosity fluids. Kasolang et al., [140, 141], measured the viscosity of thin oil films inside journal bearings, and showed that if the first layer of their set-up was perspex, a decreased reflection coefficient was attainable. However journal bearings are made from steel and so their reflection coefficient values were similarly high with respect to Saggin's results, [139].

3.9.2 The Matching Layer Viscometer

To eliminate sensitivity issues Schirru, [15], dramatically increased the sensitivity of the ultrasonic viscometer. He accomplished this by employing a matching layer to the interface between the metal and oil, Figure 3.24. This improved the signal to noise ratio and produced reflection coefficient resonant dips at frequencies related to the thickness of the matching layer, Figure 3.25. The result allowed more accurate measurement of low viscosity oils.

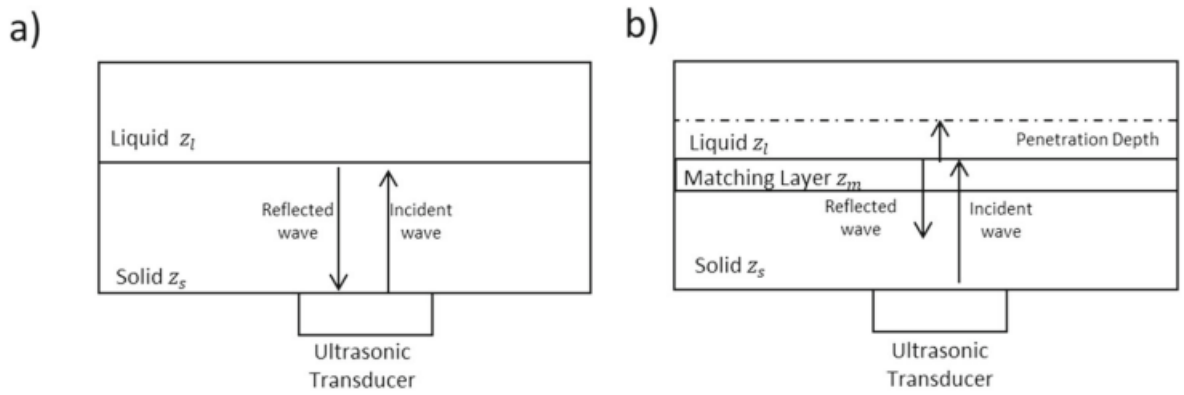

Figure 3.24: Sketch of a) simple metal - fluid two layered viscometer, and b) Schirru's newly developed matching layer viscometer, [142].

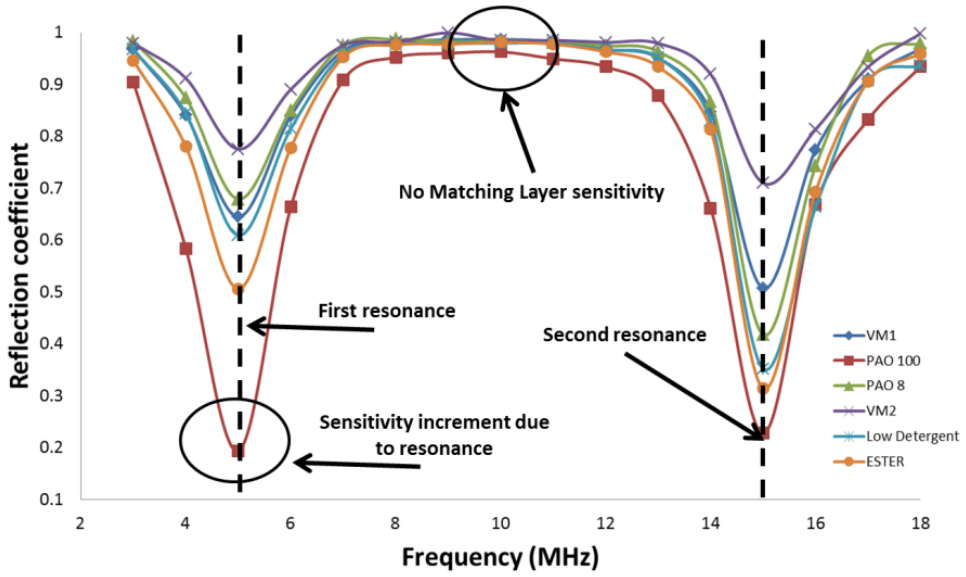

Figure 3.25: Schirru's matching layer sensitivity results showing dips in the reflection coefficient where the matching layer creates resonance. In comparison to reflection coefficient values without a matching layer, this was a good development, [15].

Since the late 1970s the matching layer technique has been utilised in ultrasonic development. Desilets, [143], applied the quarter wavelength concept to ultrasonics, and illustrated that by changing the acoustic impedance of the matching layer the transmission coefficient increased. It was later used by Xiang, [144], in biomedical ultrasound to increase transmission from the ultrasonic transducer into human tissue. It is important to note that the quarter wavelength theory had previously been used in electronics and optics to increase energy transmission in a number of scenarios. This investigation provided the groundwork for acoustic quarter wavelength technology, which resulted in all commercial transducers being designed with a matching layer. Schirru, [14], successfully installed a matching layer on a journal bearing rig with a 5MHz shear transducer and a 50 μm matching layer. The analysis consisted of using a calibration curve, Figure 3.26, which was a best fit curve applied to measured reflection coefficient data of known standard viscosity oils.

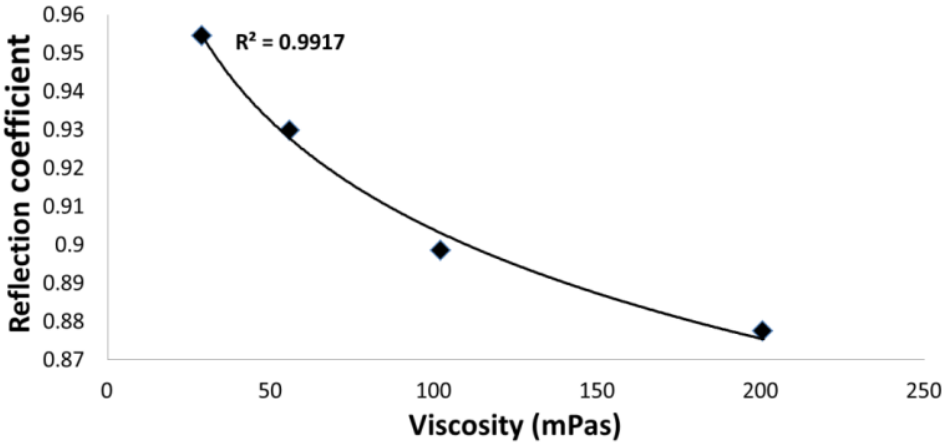

Figure 3.26: Schirru's calibration curve used to predict viscosity using a measured reflection coefficient, [14].

3.9.3 Mathematical Model

Although a calibration curve allowed Schirru to measure the viscosity, its method lacked evidence as to why a calibration method was required. In acoustics the data analysis can be challenging as ultrasonic propagation in heterogeneous materials is complex, therefore, good mathematical models are necessary for accurate data interpretation, [145]. Schirru, [146], later produced an analytical model for the matching layered viscometer using theory provided by Kinsler, [116]. However Brenchley, [16], noticed slight errors and made improvements to obtain the pressure reflection coefficient. Brenchley then incorporated "tuning" which had been done previously by Manfredi, [17], using standing waves in a matching layer viscometer. Tuning accounted for ultrasonic energy losses due to bonding the transducers and matching layers to the aluminium using an epoxy adhesive.

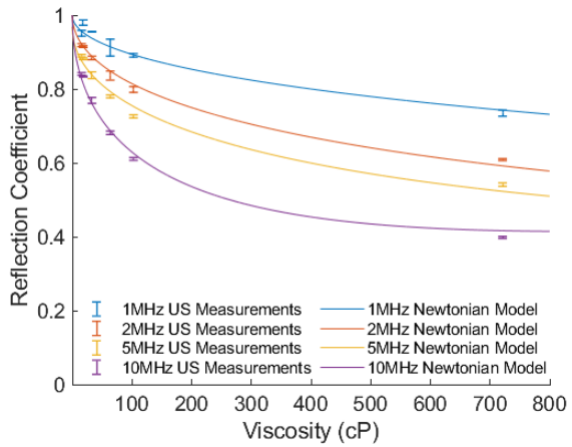

(a) A comparison of viscometer results with the Newtonian model.

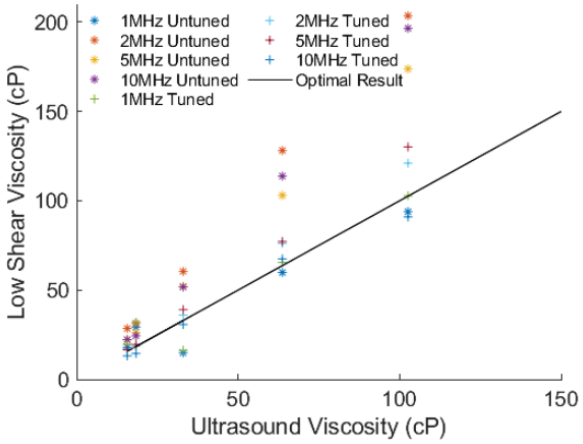

(b) A comparison between untuned and tuned measurements, and a low shear Couette viscometer.

Figure 3.27: A comparison of viscosity results completed using a matching layer ultrasonic viscometer and predicted values from a mathematical model, [16].

3.9.4 Ultrasonic Viscometer Excitation

Considerations regarding the excitation of ultrasonic sensors to measure viscosity were made formally by Brenchley who showed that using a single frequency sine wave could similarly produce required viscosity data with negligible differences in comparison with a chirp wave, Figure 3.28. This was after Schirru, [15], utilised a chirp wave to measure the viscosity of oils.

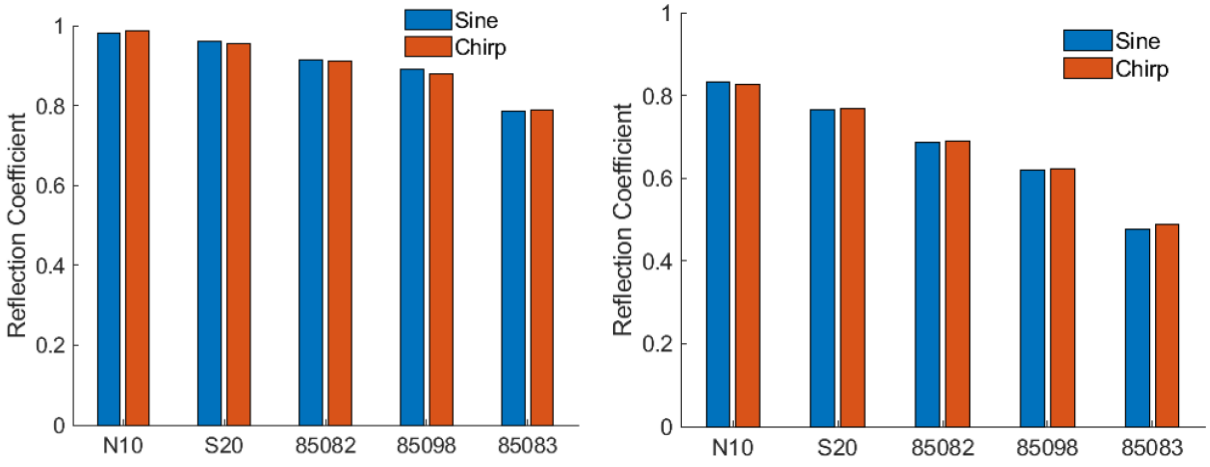

(a) 1MHz shear sensor.

(b) 10MHz shear sensor.

Figure 3.28: Shows the reflection coefficient differences between sine and chirp wave forms at a low 1 MHz and high 10 MHz frequency [16].

The main benefit of using a chirp wave was that the resonant frequency created by the matching layer was accurately found. This was extremely important as after bonding both the matching layer and sensors to the aluminium, slight deviations in sensor resonant frequency and matching layer thickness occurred. Chirp excitation requires more sophisticated hardware to produce wave form sweeping in frequency that is maintained at a desired voltage. Brenchley's work explored effects of high voltage with viscosity measurement in an attempt to conduct a shear amplitude sweep. Therefore pulsing at high voltages while maintaining a complex wave form such as a chirp was difficult. Thus Brenchley used a sine wave form and pulsed at the centre frequency.

3.9.5 Shear Rate of an Ultrasonic Viscometer

Using a chirp wave Schirru conducted measurements at three frequencies using two transducers: a 1 MHz transducer and a 4.5 MHz transducer. The 4.5 Mhz was excited using a large frequency chirp in order to excite the transducer at its first and second harmonics. These three test frequencies allowed schirru to test a series of oil such as PAO 100 and PAO 40 at high shear rates (calculated using the Cox-Merz rule, Equation 2.7), Figure 3.29.

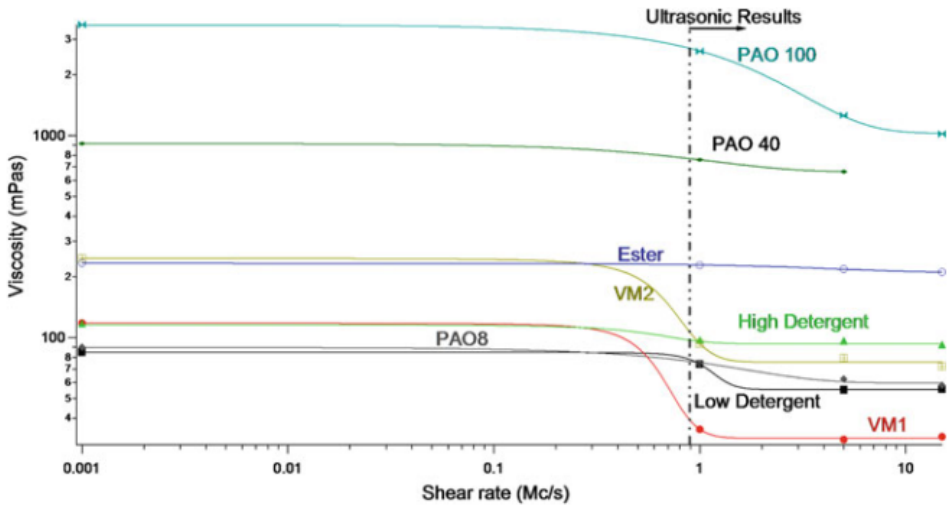

Figure 3.29: Schirru's ultrasonic spectroscopy results using a matching layer viscometer, [14].

Brenchley conducted similar measurements using four ultrasonic testing frequencies for PAO 40 and PAO 100 with different quantities of a viscosity modifier called DMA. Brenchley's presentation of his results, Figure 3.30, illustrates changes in viscosity that are similarly observed Schirru's results, Figure 3.29. However, Brenchley maintains the ultrasonic frequency rather than displaying a shear rate, as the Cox-Merz rule is not valid in an ultrasonic matching layer viscometer.

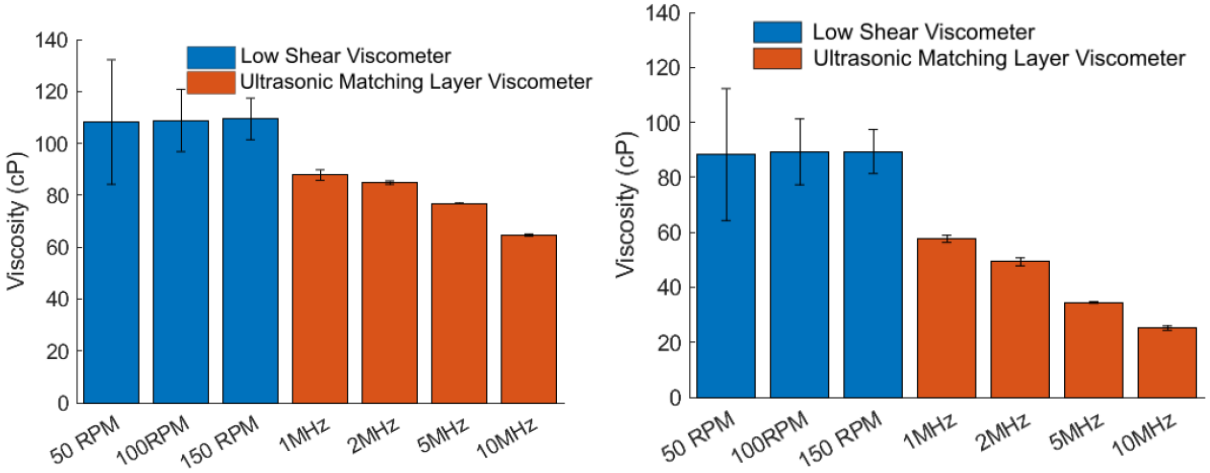

(a) 70% PAO 40 + 30% DMA.

(b) 50% PAO 100 + 50% DMA.

Figure 3.30: Brenchley's measurements for the shear thinning behaviour of PAO oil blends mixed with a viscosity modifier, [16].

Shear rate is the ratio of velocity over a distance. Figure 3.31a illustrates a single plate model where the Cox-Merz rule is applicable. If the plate vibrates in a shearing motion at a certain frequency, the fluid in contact with that plate can be considered to be shearing at a near equal rate. However, for a shear transducer in the scenario shown in Figure 3.31, a shearing motion at a certain frequency must travel through the plate and into the liquid. Therefore the frequency of the transducer does not equal the shear frequency of the fluid due to a change in velocity and distance.

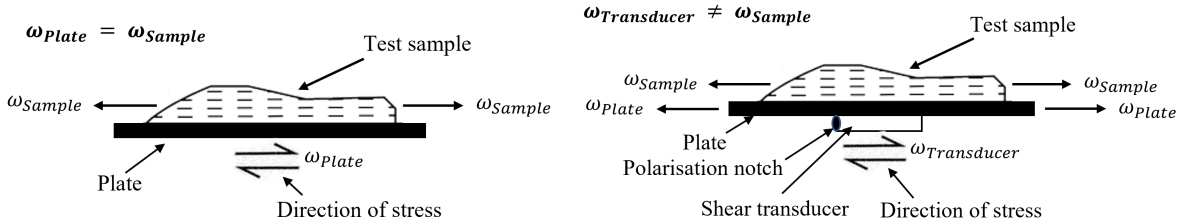

(a) Cox-Merz rule is applicable.

(b) Cox-Merz rule is not applicable.

Figure 3.31: Sketch of how the frequency of an oscillator can be directly related to the frequency of the test fluid using the Coz-Merz rule, Equation 2.7. a) Plate is directly applying the shear stress to the fluid. b) Acoustic shear stress applied through a plate and into the fluid, therefore the Cox-Merz rule can not be used.

This leads to the main focus of Brenchley's work; calculating the true shear rate of ultrasonic viscometry. This was done using a laser vibrometer to measure the velocity of the shear motion on the matching layer - fluid interface. To calculate the velocity of the ultrasonic wave shear motion through a three layered system Equation 3.24 is used, where U_i, is the shear velocity of the incident wave, and U_t, is the shear velocity in the fluid.

$$U_t = \frac{Z_1}{Z_3} U_i \left(R + 1\right) \tag{3.24}$$

To obtain the true shear rate within the fluid, the relationship shown in Equation 3.25 was used, which has similarly been used in a previous investigation to measure the shear rate of ultrasonic shear waves, [147]. This equation illustrates the shear rates dependence on the kinematic viscosity, ν, of the fluid.

$$\dot{\gamma} = U_t \sqrt{\frac{\omega}{\nu}} \tag{3.25}$$

The shear rate shown in Figure 3.32b was calculated using Equation 3.25, which uses the velocity information measured in Figure 3.32a and air as a fluid, with a viscosity of 18.6 μPas and a density of 1.225 kgm^{-3}, [16]. The results show how there is an increase in velocity and shear rate within the fluid as excitation voltage (displacement) is increased for a 1 and 2 MHz transducer. Therefore, a 1 MHz transducer would be able to measure the viscosity of a fluid that has similar properties to air over a shear rate range of 1,200 - 12000 s^{-1}.

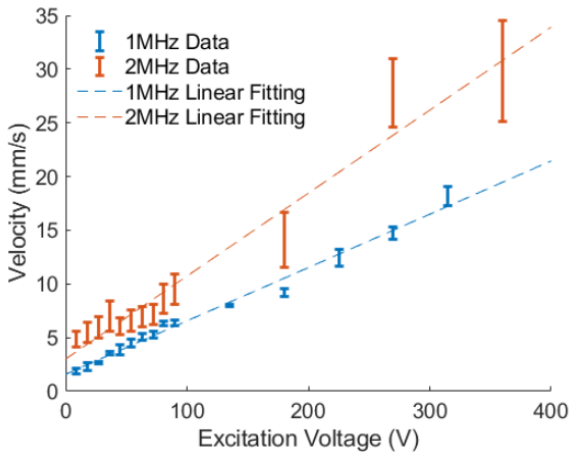

(a) Velocity of the surface of an aluminium plate when excited by shear waves produced by a piezoelectric transducer where the excitation voltage is varied.

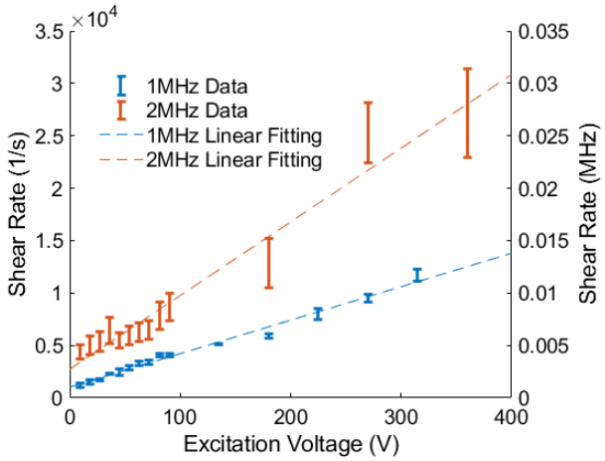

(b) Shear rate calculation for air using velocity information from Figure 3.32a.

Figure 3.32: Brenchley's velocity and shear rate data for a 1 and 2 MHz sensor as the excitation voltage is increased, [16].

3.10 Conclusion

An introduction into ultrasound has been presented and indicates that the ultrasonic technique offers a method to measure the viscosity of a fluid using shear ultrasonic waves. This forms the basis of the viscosity measurements put forward in this thesis. From this chapter the following conclusions were reached:

- Using material properties that effect ultrasound propagation through different material layers, the reflection coefficient can be predicted.

- The reflection coefficient can also be measured by comparing the pressure amplitude of the reflected wave with the incident wave. This quantity can then be directly correlated to the fluid viscosity.

- How sound travels through materials and interacts with boundaries is important to consider when designing transducers to measure viscosity inside a battery cooling system. Theory regarding the three layered system in Section 3.4.2 is explored in greater detail in Chapter 5, where an analytical and numerical model link the reflection coefficient with the viscosity.

- The accuracy of ultrasonic measurement is dependent on good knowledge of the layer material properties. This is highlighted in Chapter 5 when the analytical and numerical model are evaluated with measured reflection coefficient values.

- Constructing transducers using bare piezoelectric elements offers a more adjustable, non-invasive method for an applied application. For example, creating small sensors to take measurements of an otherwise inaccessible interface.

- The pulse-echo transducer arrangement allows the reflection coefficient to be obtained, yet it utilises the least amount of ultrasonic components. This is achieved without sacrificing any quality in the measured signal.

- Ultrasonic shear waves to measure viscosity is advantageous over the more conventional methods. This is because:

  - The shear rate applied to the fluid is very high, which reflects the transducers ultrasonic frequency, however, measuring the exact shear rate requires a laser vibrometer that is sensitive enough to measure the frequency being used.

  - It can be used in-situ due to it requiring a small installation area, having no moving parts and being able to operate in close proximity to harsh environments.

  - When it is used in a three layered set-up, where the intermediate layer is a matching layer, high reflection coefficient sensitivity is achieved. This allows

increased accuracy and differentiation between reflection values, resulting in lower viscosity fluids being measured, and potentially mixtures with dilute contamination.

- A good ultrasonic viscosity mathematical model is required for accurate data interpretation, which has been produced analytically, however a numerical model could improve accuracy between real and predicted data.
- To date, no evidence or literature has been found on the viscosity measurement of emulsions and/or suspensions in oil, using an ultrasonic matching layer viscometer.

Chapter 4

Rotational Viscometry

The focus of this chapter is to characterise the pure coolant, followed by coolant-water emulsions and coolant-copper suspensions, which are used throughout this thesis. Characterisation consists of investigating their viscosity behaviour under varying shear rates (Newtonian/non-Newtonian) and measuring the apparent viscosity. To verify the dynamic viscosity, pure coolant is investigated at varying temperatures in order to compare measured values with values attained from its supplied data sheet. Mathematical models described in Chapter 2 are utilised to predict the apparent viscosity of mixtures and are later compared with measured data as an explanation tool. Finally, this chapter provides the feasibility of using shear viscosity to measure contamination in a dielectric coolant and observes its sensitivity for each degree of contamination.

The measured data will be used in future chapters as a validation tool to observe the accuracy of the ultrasonic viscosity measurements, and as part of a shear rate study in conjunction with the ultrasonic viscosity data.

4.1 Rheology Instrument

A TA Instruments Discovery HR-10, shown in Figure 4.1, was used to conduct the viscosity measurements and was capable of measuring low torque values due to its improved sensitivity over other viscometers. This allowed measurement of lower viscosities, weaker inter-molecular structures and utilised lower sample volumes, while continuing to measure reliable and accurate data. It achieved this by using a magnetic thrust bearing coupled with a drag cup motor, which reduced basic system friction. The motor applied the torque (stress) and measured the rotation (strain) using a displacement sensor. It could apply 5 $nN.m$ - 200 $mN.m$ of torque with a resolution of 0.1 $nN.m$, a 0 - 300 rad/s range of

angular velocity, and had a displacement detection resolution of 10 *nrad*, [54].

The HR-10 functioned with a software called Trios, which allowed the user to control the rheometer, create and execute tests, visualise real-time recording data, compare data with other tests, conduct data analysis and export in a variety of formats.

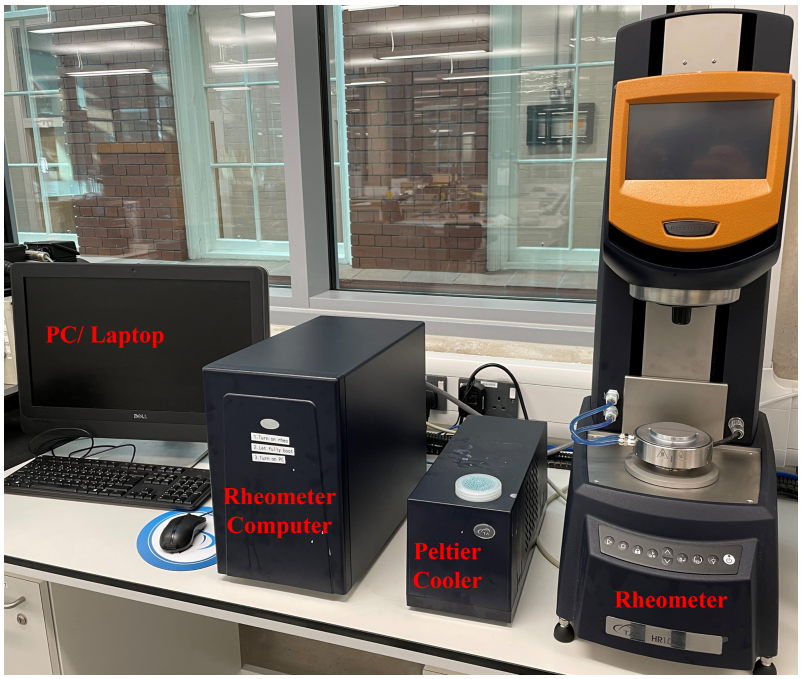

Figure 4.1: Rheometer utilised throughout this chapter. The rheometer itself was controlled by its own computer unit, which connected to an external PC. The plates were cooled / heated using a temperature control device that was also connected to the rheometers computer.

4.2 Pure Coolant Characteristic Expectations

The dielectric coolant supplied by BP, Castrol, was a clear fluid, Figure 4.2, with density and viscosity values shown in Table 4.1. Only the density and kinematic viscosity values across a temperature range were supplied by BP. Therefore, the dynamic viscosity was calculated using Equation 2.4, which will be referred to as the data sheet viscosity. The coolant was considered Newtonian, hence its viscosity does not depend on the shear rate. The main reason for this behaviour was due to its intended use in a cooling system. If the coolant was being pumped, a low viscosity Newtonian oil is preferred due to the effect on the power required to pump at desired flow rates across a range of temperatures. For that

reason the viscosity in Table 4.1 should be very similar to values measured in this chapter.

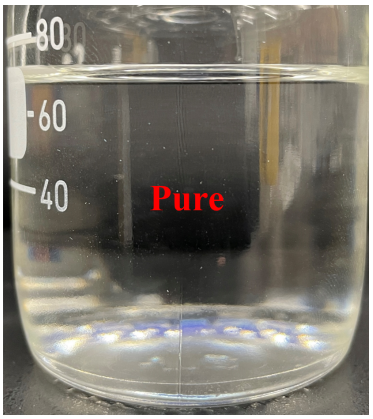

Figure 4.2: BP, Castrol's pure dielectric coolant with a clear appearance.

Table 4.1: Pure coolant density and kinematic viscosity values from the supplied BP data sheet. These values were then used to calculate the dynamic viscosity for each temperature increment.

Temperature ($°C$)	Density (gml^{-1})	Kinematic Viscosity (mm^2s^{-1})	Data Sheet Dynamic Viscosity ($mPas$)
0	0.808	19.83	16.03
10	0.802	13.22	10.6
20	0.795	9.25	7.35
30	0.789	6.79	5.35
40	0.782	5.18	4.05
50	0.775	4.09	3.17
60	0.769	3.3	2.54

It was previously discussed in Chapter 2 how viscosity behaves and how well documented viscosity changes are with temperature. It was also mentioned in Chapter 3, that temperature changes while using an ultrasonic viscometer are hard to monitor due to temperature gradients across multiple layers. Consequently, throughout this and later chapters, unless otherwise stated, tests were conducted at room temperature, $23°C$. The viscosity for pure coolant at $23°C$ is 7.35 $mPas$. This value was obtained using the data in Table 4.1 and the Vogel equation, Equation 2.5.

4.3 Geometry Selection

For low-viscosity liquids it was preferable to use a larger diameter spindle showing a greater shear area [148], which could provide the biggest applied shear rate range. The largest spindle the rheometer could operate had a diameter of 60 mm, which was in the range of standard spindle sizes recorded in Mezger [148]. It was mentioned in Chapter 2 that the main advantage for using a cone spindle was its ability to apply a constant shear rate across the entire conical gap. However, cone spindles should only be used for samples which contain particles up to a limited maximum size. This is because there would not be enough free space available between the particles when in motion, which would influence the deformation and flow behavior. In this case a greater number of particles would directly touch the surfaces of the cone spindle, falsifying the test result due to increased friction forces. The gap, h, can range from 500 μm to 3000 μm. For a cone, however, this gap setting applied to the outer radius, thus providing a smaller gap towards the centre. For a parallel plate spindle, the gap was uniform across the entire radius and was therefore preferred when measuring low viscosity emulsions and suspensions.

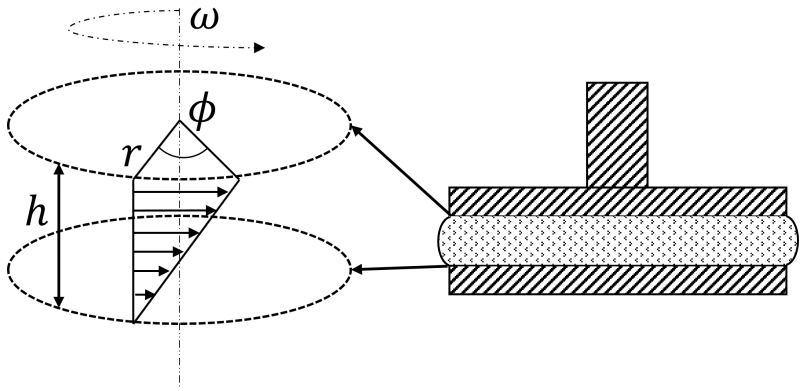

Figure 4.3: Parallel plate analytical torsional flow diagram used to depict the link between geometric values with measured values.

Equation 4.1 shows the relationship between stress, strain and shear rate with geometric values, which are devised using Figure 4.3. These equations show that shear stress increases with increasing spindle diameter and shear rate increases with decreasing gap height.

$$\sigma = \frac{2}{\pi r^3} T \qquad \gamma = \frac{r}{h}\phi \qquad \dot{\gamma} = \frac{r}{h}\omega \tag{4.1}$$

Three flow shear ramp tests were conducted using a pure coolant at 30°C from an initial zero shear rate to a maximum value of 2000 s^{-1}. Three gap heights were tested at 1000, 800 and 500 μm, Figure 4.4. Initially, at low steady shear rates there was an apparent viscous shear thinning behaviour, Figure 4.4a. In actual fact, this behaviour was a symptom of surface tension torque.

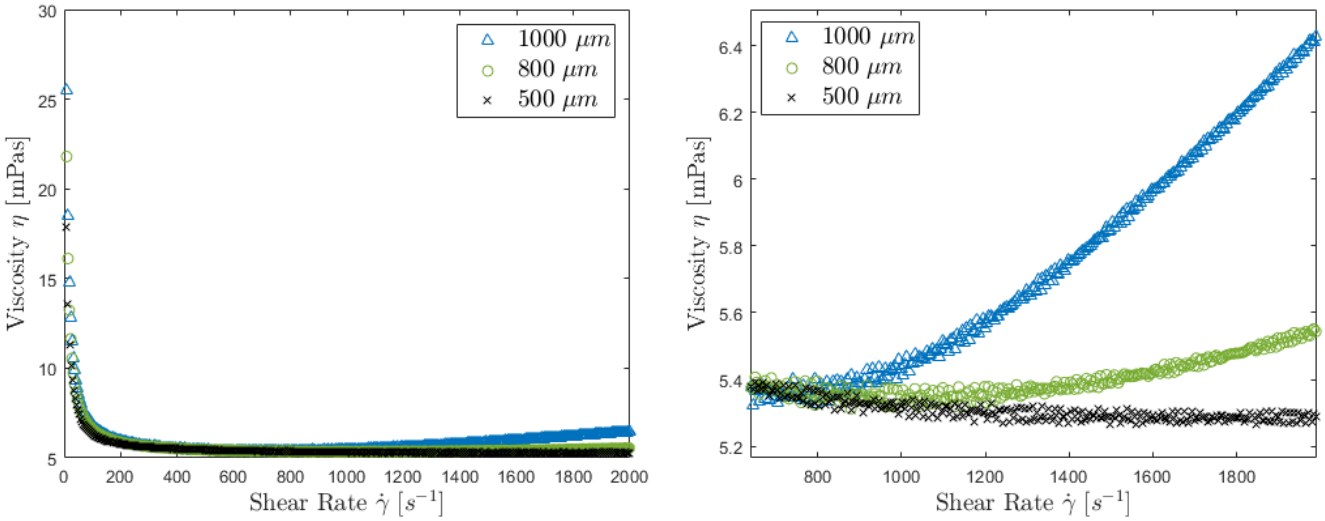

(a) Full viscosity with shear rate.

(b) Focused on high shear rate.

Figure 4.4: Effects of changing the gap size between parallel plates on viscosity with an applied shear rate of 0 - 2000 s^{-1} at 30°C. Gap sizes consisted of 1000 μm, 800 μm and 500 μm.

Surface tension influences the measurement of shear stress and is a significant experimental challenge for measuring low viscosity fluids with relatively high surface tensions. It is the property of a liquid, by which its free surface at rest behaves like an elastic membrane, Figure 4.5a. In viscometry, surface tension causes traction forces around a material contact line, which increases the measured torque values, Figure 4.5b. It occurs at low shear rates because the fluid starts to shear from a resting state until the elastic membrane yields. Traction forces are increased with broken rotational symmetry, which consists of

a non-constant contacting line and angle, ϕ, Figure 4.5b. The symmetry is easy to break due to small deviations in equipment tolerances or over-filling and under-filling the sample. This allows surface tension to directly effect the torque value. Hence measurements at low shear-rates and for low viscosity fluids, a much higher viscosity result is initially observed. The effect is highly variable due to sample loading, wetting conditions, and contact line asymmetries and cannot be corrected in experimental measurements, therefore it raises the lower bound of the instrument low-torque limit, [149].

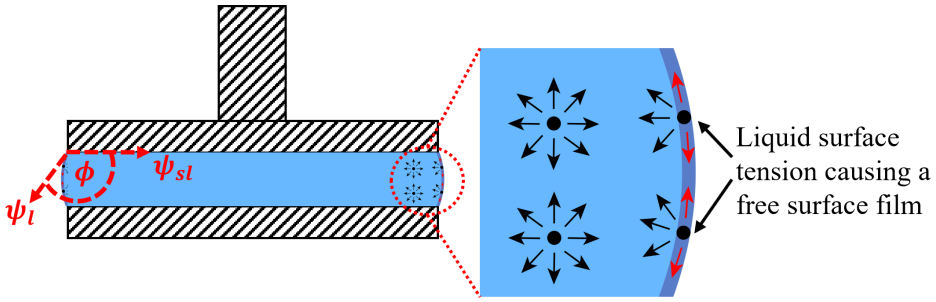

(a) Cohesion of molecules causing surface tension at a liquid-air interface with vector Ψ_l and solid-liquid interface with vector Ψ_{sl}. The term 'surface tension' in the text refers to the liquid-air interface vector Ψ_l.

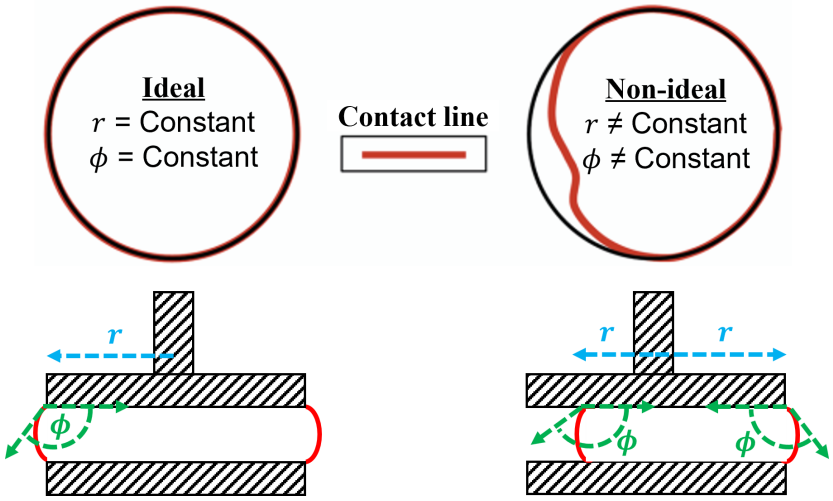

(b) Effects of rotational symmetry contact line within a viscometer, [149].

Figure 4.5: Surface tension effects on steady shear rotational viscometry and the ideal set-up to reduce these effects, where r is the radius of the contact line and ϕ is the surface tension angle created by being situated between two plates.

Considering Figure 4.4b again, at high shear rates there was an increase in viscosity for both 1000 μm and 800 μm. This increase indicated shear thickening behaviour, however, the decrease in gap height reduces the gradient at which viscosity increases. At 500 μm,

the viscosity change with shear rate was visibly more Newtonian. In this situation an increased viscosity at high shear rate indicates hydrodynamic flow instabilities such as secondary flow effects and turbulent flow behaviour, [150, 151]. This was the result of centrifugal forces that push the low-viscosity sample from the inner radius towards the outer one. In this case, flow and viscosity curves would display higher shear stress and viscosity values as well as higher curve gradient values compared to curves measured at laminar flow conditions. Shortly after turbulent flow and centrifugal forces occurred the liquid began to flow out of the gap and an extremely low value of viscosity was recorded.

To support these behavioural observations Figure 4.6 is presented which was created by TA Instruments for a water test sample using varying spindles and an oil sample for comparison, [55]. It illustrates increased torque due to surface tension at low shear rates and flow instabilities at high shear rates for for all spindle types, where cone and parallel plates have a gap of 1000 μm. This is common and difficult to avoid for low viscosity aqueous fluids, especially at cooler temperatures where the surface tension is higher.

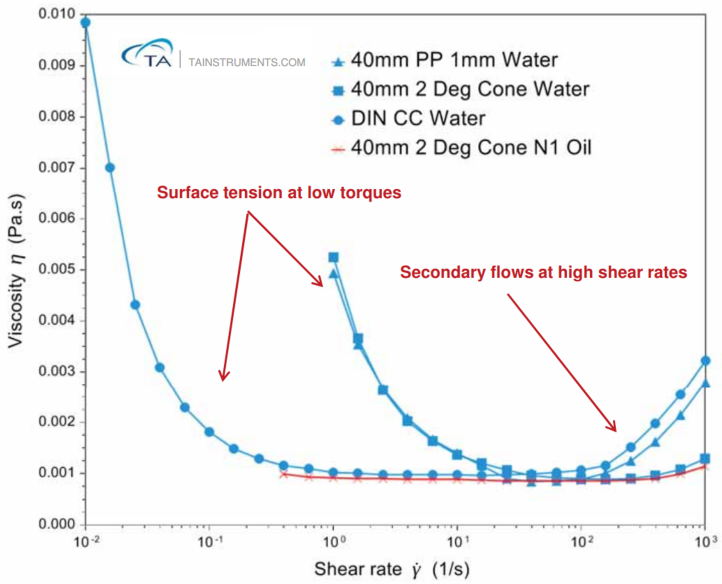

Figure 4.6: TA Instruments comparing shear viscosity data for water, using three different spindles, and an oil sample. Blue Triangle: Parallel plate results for water. Blue square: Cone on plate results for water. Blue circle: Standard concentric cylinder results for water. Red crosses: Cone on plate results for oil. Cone and parallel plates both had gaps of 1 mm, [55].

Although the minimum measurable shear rate of the rheometer was below 400 s^{-1},

due to the effects of surface tension the viscosity recorded below this value were dismissed as unreliable. A 500 μm gap was chosen as it allowed a larger shear rate range to be measured and it was 10 times larger than the 50 μm copper particles used.

4.4 Experimental Procedure

The rheometer was capable of conducting a range of flow and oscillatory tests and could be changed depending on the result required. However the methodology up to the point of loading the sample was kept constant to assure reliable results and align with the guidelines suggested by TA Instruments, [55]. The required spindle was fixed in the correct orientation, ensuring that the motor was locked. By locking the motor, damage was reduced due to the rotating motion when fixing the spindle. Prior to any testing a calibration was executed for the required spindle. This was important as it allowed the motor to establish a baseline for torque and displacement readings at a desired temperature range.

The following test procedure was carried out for each fluid every time a new test was conducted:

- The 60 mm parallel plate spindle and bottom plate were cleaned using Isopropanol.
- A test was set-up on the TA instruments software (Trios).
- The spindle and bottom plate temperature were set to the desired or initial testing temperature.
- The spindle was sent to the zero gap. This step aided the motor to re-establish a datum point between spindle torque, speed, temperature and height before executing the test.
- Spindle was sent to geometry gap. At this point, the spindle could have been sent to the loading gap. However TA Instruments advise that fluids with viscosity less than that of Ketchup ($\approx$ 50 - 100 Pas) are loaded into the geometry gap at a angular velocity between $10^1 - 10^2$, hence this method was used.
- Ensured that the geometry gap was fully filled, using a pipette, according to TA Instrument guidance [55] and a rheological testing handbook [148], Figure 4.7. Cor-

rect loading of samples into the viscometer ensured that surface tension torque was reduced by maximizing rotational symmetry of the contact line and minimizing the migration of the contact line.

- Executed the test and repeated for each fluid sample.

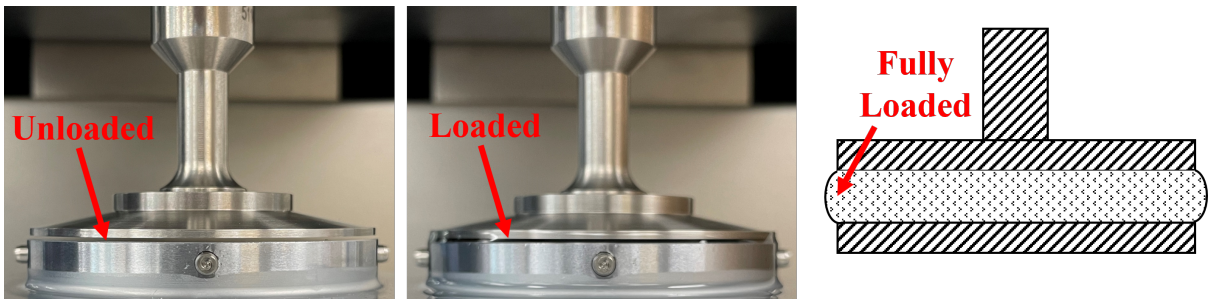

Figure 4.7: Fluid loading gap illustration. Left: gap unloaded. Centre: Loaded gap. Right: Correct sample loading. In accordance with rheological testing guidance [55, 148], and backed up by research, Johnston et al, [149].

4.5 Characterising Pure Coolant

The behaviour of the coolant's viscosity with temperature is shown in Figure 4.8. This Figure was the result of a flow temperature ramp from 20 - 60°C at a constant shear rate of 1000 s^{-1}. This temperature range was selected to mimic the range at which a typical battery coolant would operate between. Before the test began a 180 second soak time allowed the fluid sample to reach the desired start temperature of 20°C. The test was repeated 3 times in order to achieve the standard deviation from an average measurement. The results were compared with the data sheet viscosity values supplied by BP, Castrol in Table 4.1. To better understand the behaviour of each viscosity data set, the Vogel equation, Equation 2.5, was used as a fit.

The discrepancy between data sheet and measured dynamic viscosity becomes increasingly less with increased temperature. One theory for this could be surface tension effects when measuring the kinematic viscosity, in Table 4.1, at lower temperatures where surface tension is higher. However, the overall discrepancy is most likely due to the Table 4.1 values being converted from kinematic viscosity, which is a measure of velocity through a capillary tube, rather than an applied shear force.

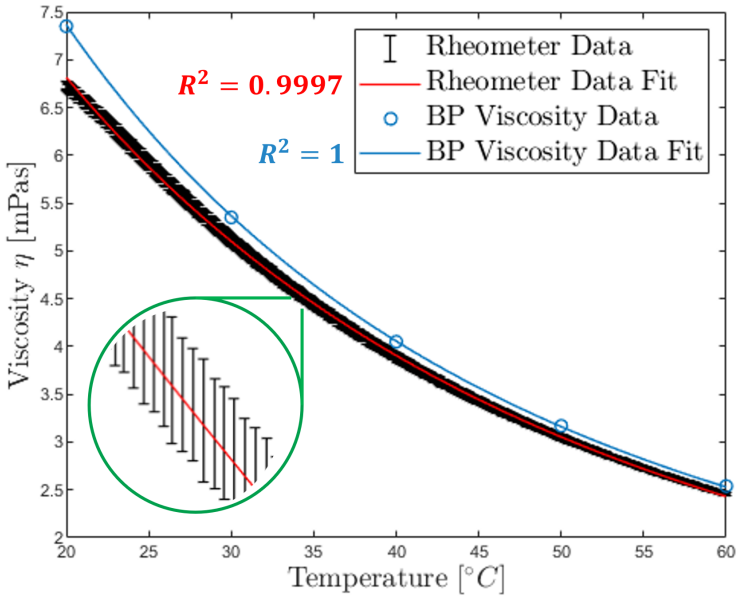

Figure 4.8: Pure coolant comparison between measured dynamic viscosity using the rheometer and the data sheet dynamic viscosity from Table 4.1. Temperature ramp of 20 - 60°C at a constant shear rate of 1000 s^{-1}. Error bars are plotted after conducting the same measurement 3 times. The Vogel equation was used to fit each data set.

Table 4.2 shows the measured average dynamic viscosity and error values. As the dynamic values in Table 4.1 were calculated from the density and kinematic viscosity at different temperatures, it being an accurate dynamic viscosity is unlikely. Therefore, the dynamic viscosity measured here is considered accurate and repeatable, and it is used as a viscosity-temperature reference from here on.

Table 4.2: Measured dynamic viscosity with varying temperatures for pure coolant.

Temperature $^\circ C$	Measured Dynamic Viscosity ($mPas$)	Standard Deviation
20	6.72	0.0459
30	5.11	0.0564
40	3.88	0.0409
50	3.04	0.0274
60	2.46	0.0166

A flow shear sweep test was conducted to observe the behaviour of the coolant without any contamination, Figure 4.9. The test was held at a constant temperature of 23°C while a shear rate was applied from 0 - 3500 s^{-1}. Similarly to the previous test a 180 second soak time allowed the fluid sample to reach the desired temperature. For each ramp step it took 5 seconds for the shear rate to increase, followed by an averaged viscosity value taken over a 30 second period. The test was repeated 3 times.

The most effective way to determine whether a fluid is Newtonian is to plot stress against shear rate and observe the apparent viscosity, Figure 4.9a. The Newtonian model was fitted to ensure observed Newtonian behaviour, Equation 2.3. The model fit with an R^2 value of 1, indicating perfect correlation with measured data, thus showing Newtonian behaviour. Finding the gradient of the fit provided an apparent viscosity (viscosity irrelevant of shear rate) of 6.01 $mPas$ at 23 °C. Figure 4.9b showed how the viscosity behaved with applied shear rate. As discussed previously the initial high viscosity at low shear rates disregarded due to surface tension effects, hence values less than 400 s^{-1} were not considered. A linear equation was applied here, where the y-intercept is the viscosity value from the stress-shear rate gradient. This linear fit displayed an extremely small gradient, m, which could be assumed 0, proving Newtonian behaviour. Furthermore, the Power Law was used to fit the stress-shear rate data, shown in Equation 4.2. The result was a n value of 0.99 and a fit correlation of $R^2 = 1$. As this n value was almost equal to 1, it similarly indicated that the fluid was Newtonian.

$$\sigma = K\dot{\gamma}^n \tag{4.2}$$

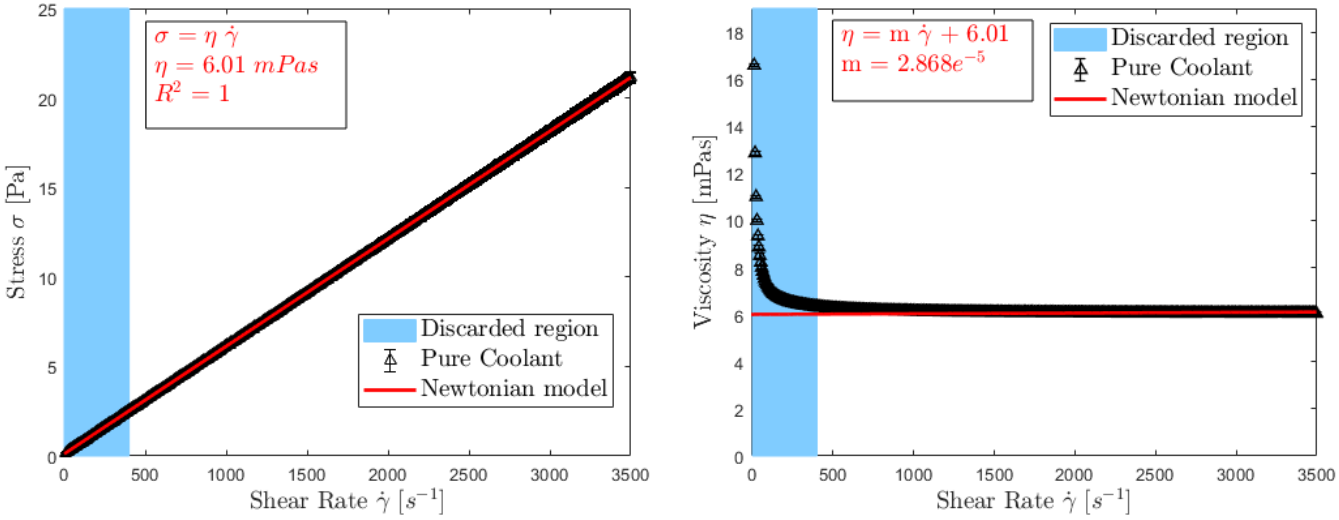

(a) Stress with shear rate.

(b) Viscosity with shear rate.

Figure 4.9: Characterising the behaviour of pure coolant under an applied shear rate of 0 - 3500 s^{-1} at 23 °C. Data analysis disregards shear rate data below 400 s^{-1}.

4.6 Viscosity Predictions for Coolant Mixtures

Despite the behaviour of pure coolant, when contamination such as water and copper are added (Figure 4.10) its viscosity will change with shear rate, as previously highlighted in the literature review, Chapter 2. It is also important to note that distilled water was used to contaminate the coolant due to the detailed physical properties, and yet it could still have a negative impact on the coolants electrical insulation. Furthermore, a 50μm copper powder was used as the solid contaminant which simulates contamination from copper pipes used in cooling systems.

Since the apparent viscosity of pure coolant was measured, predictions for the viscosity with varying degrees of dispersed phase volume fraction could then be made. For water contaminated mixtures 3, 10 and 20 % volumes were chosen. This high and relatively large percentage range was chosen as a way to clearly identify how much of an impact water would have on the viscosity. Furthermore in many electrical insulation environments, paper is also used to increase insulation effects. This paper can hold a much greater amount of water. Hence the total amount of contamination inside a cooling system could

be as large as 20 %. Copper contamination consisted of 0.1, 0.5 and 1 % volumes, which were low in comparison to water. The reason for this, as stated in Chapter 2, is that most electronic cooling environments would not typically produce more than 1 % copper from erosion and chemical reactions during its service life. Before reaching over this value, the oil would most likely be deteriorated from oxidation as a whole. Finally, these water and copper mixtures would indicate how sensitive standardised rotational viscosity measurements are at quantifying each level of contamination. It was observed that all mixtures would remain in suspension for the duration of the rheometer test, providing that the mixture had just been affectively mixed.

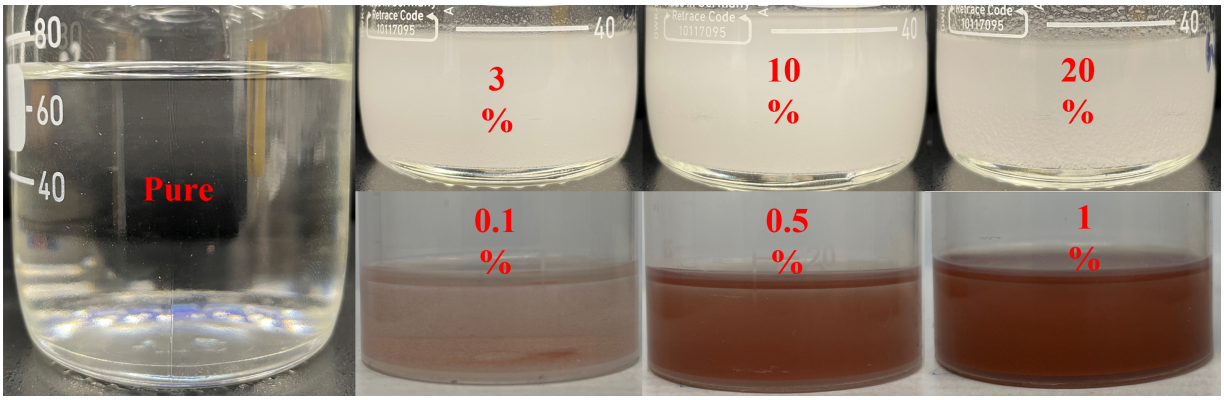

Figure 4.10: Contaminated coolant mixtures. Reading from left to right and top to bottom: Pure coolant, 3, 10 and 20 % distilled water contamination fractions, and 0.1, 0.5 and 1 % copper fractions.

For each coolant mixture the viscosity was calculated using equations from Chapter 2, which are reproduced again for convenience. Copper mixtures with dispersed volume fractions less than 1 % are considered dilute suspensions and therefore Equation 4.3 was used to calculate viscosity.

$$\eta = \eta_C \left(1 + 2.5\phi\right) \tag{4.3}$$

The water mixture at 3 % is considered a dilute dispersed fluid phase, hence Equation 4.4 was used.

$$\eta = \eta_C \left(1 + \frac{2 + 5\lambda}{2\left(1 + \lambda\right)}\phi\right) \tag{4.4}$$

Finally, for water mixture at 10 and 20 %, a concentrated dispersed fluid phase, Equation 4.5 was used, where η_i is equal to 2.5 for rigid spheres, and ϕ_p is equal to 0.64 for randomly packed monodisperse rigid spheres.

$$\eta = \eta_C \left[1 - \left(\frac{\phi}{\phi_p}\right)\right]^{-[\eta]\phi_p} \tag{4.5}$$

The predicted values for each percentage contamination are illustrated in Table 4.3. However to illustrate the differences between each equation, Figure 4.11 is produced. Each equation shows monotonic behaviour which is increasing much faster for the concentrated equation, Equation 4.5. However the differences are smaller between Equations 4.3 and 4.4, where the latter equation increases at a slower rate.

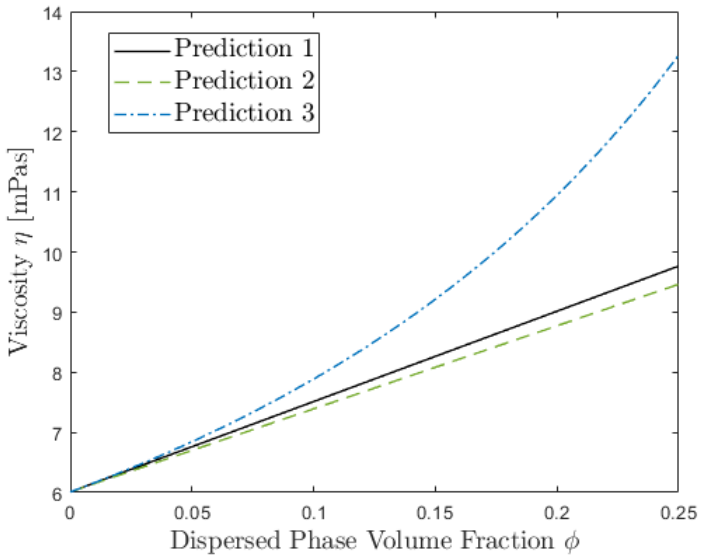

Figure 4.11: Contaminated viscosity predictions based on a pure coolant viscosity of 6.01 $mPas$ at 23 °C. Prediction 1 is Equation 4.3, Prediction 2 is Equation 4.4, and Prediction 3 is Equation 4.5.

Table 4.3: Predicted viscosity of pure coolant with varying fractions of contamination, calculated using Equation 4.3, 4.5 and 4.4.

Oil		Predicted Viscosity at $23°C$ $(mPas)$
Pure Coolant		6.01
Water	3 %	6.42
	10 %	7.89
	20 %	10.95
Copper	0.1 %	6.03
	0.5 %	6.09
	1 %	6.16

4.7 Characterising Behaviour of Coolant Mixtures

The same shear rate flow sweep test completed in Figure 4.9 was carried out for contaminated mixtures. The main difference was the soak time, which was reduced to 10 seconds, as the emulsions/suspensions homogeneous dispersion were time dependant and begin to separate into two phases. To observe error in the acquired data, 3 tests were completed for each fluid. Figure 4.12 illustrated coolant-water emulsions of 3, 10 and 20% fractions, and Figure 4.13 illustrated coolant-copper suspensions of 0.1, 0.5 and 1 % fractions. Both sets of figures are not accompanied with fitted lines, instead Table 4.4 shows the key parameters produced by the Newtonian and Power law models to fit the data.

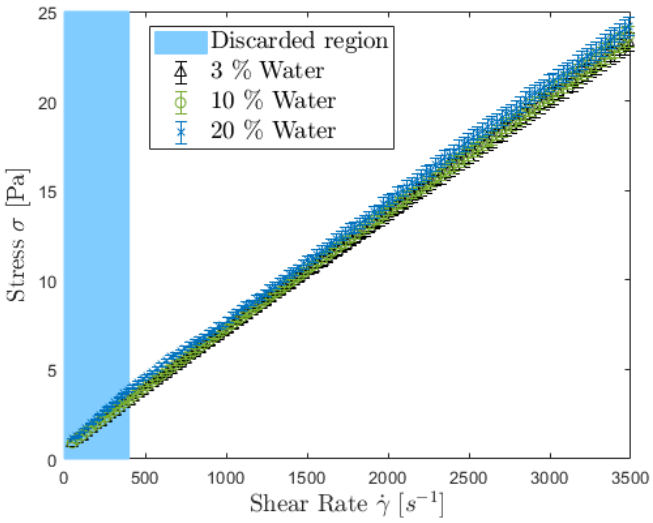

(a) Stress vs shear rate.

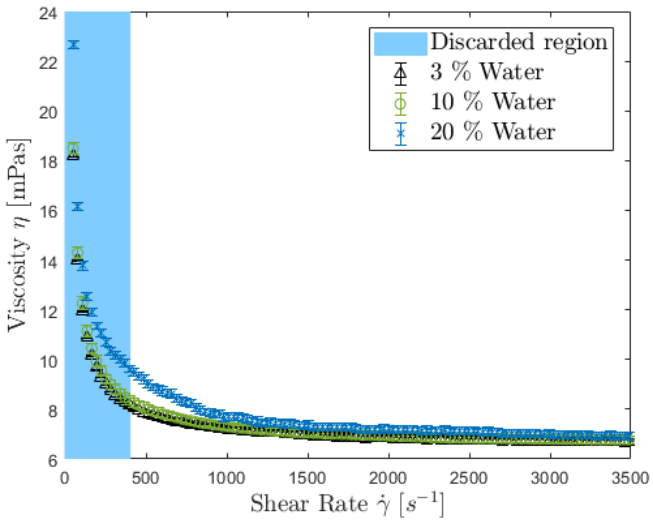

(b) Viscosity vs shear rate.

Figure 4.12: Characterising the behaviour of water contaminated coolant under an applied shear rate of 0 - 3500 s^{-1} at 23 °C.

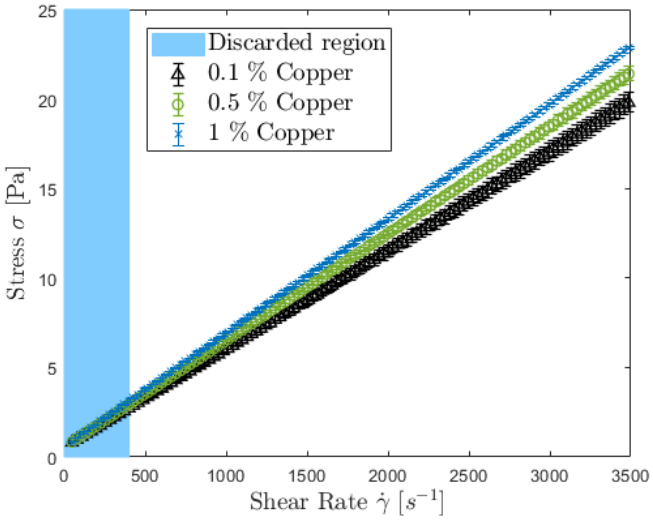

(a) Stress vs shear rate.

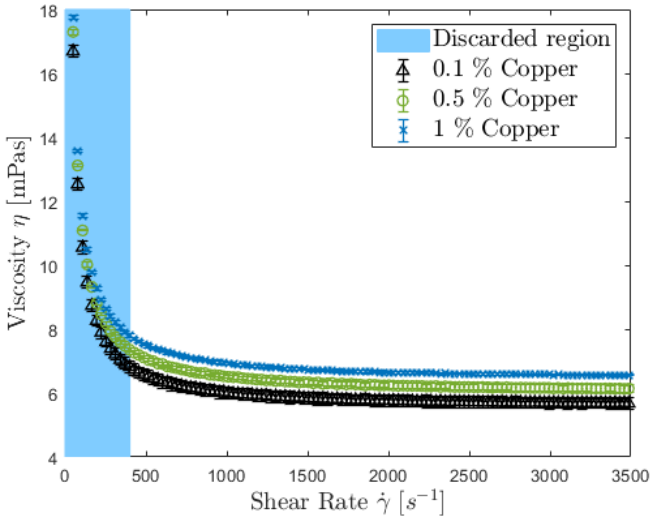

(b) Viscosity vs shear rate.

Figure 4.13: Characterising the behaviour of copper contaminated coolant under an applied shear rate of 0 - 3500 s^{-1} at 23 °C.

The initial viscosity (after discarded region) for 20 % water shows shear thinning behaviour. Based on theory presented in Chapter 2, higher dispersed volume fractions will begin to aggregate and separate into two phases quicker than lower volume fractions,

Figure 4.14. However, as the shear rate increases, aggregates are broken down into smaller droplets, which causes a reduction in the viscosity until the line converges towards a single value.

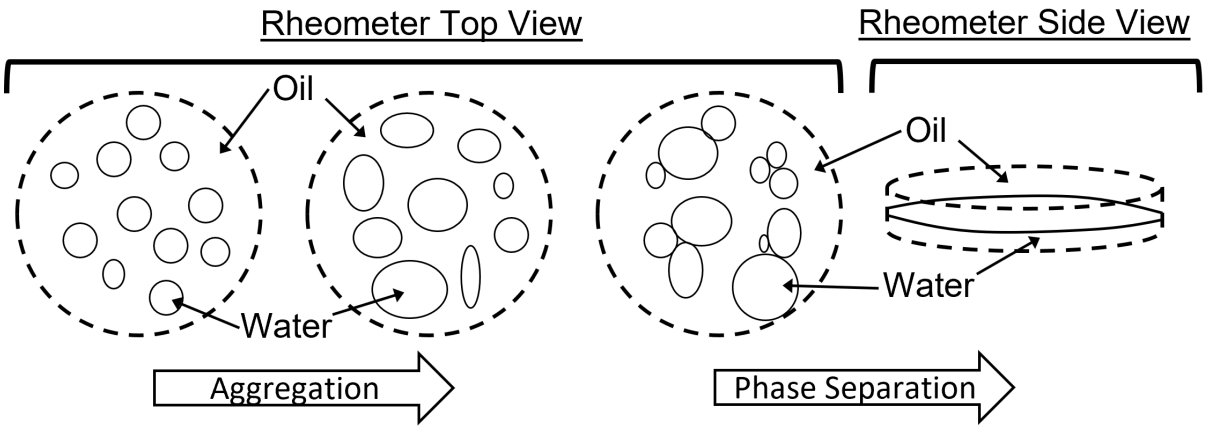

Figure 4.14: Sketch illustrating the cause of the initial shear thinning behaviour, beyond the discarded region, where aggregates begin to form towards a phase separation. With increasing shear rate, these aggregates are broken down.

Further inspection of Figures 4.12 and 4.13 suggested that with more contamination there was an increase in stress gradient, thus an increase in viscosity. To confirm this, Table 4.4 outlines the Newtonian and Power Law model values fitted to each fluid, accompanied by Figure 4.15, which shows the measured viscosity in comparison with predicted viscosity lines.

Table 4.4: Newtonian and Power law parameters used to fit measured data for pure and contaminated coolants.

		Newtonian		Power Law	
Contaminant		R^2	η	R^2	n
Pure Coolant		1	6.01	1	0.99
Water	3 %	0.997	6.782	0.999	0.934
	10 %	0.997	6.871	0.999	0.932
	20 %	0.993	7.106	0.999	0.899
Copper	0.1 %	0.998	5.735	0.999	0.948
	0.5 %	0.998	6.206	0.999	0.945
	1 %	0.998	6.595	0.999	0.949

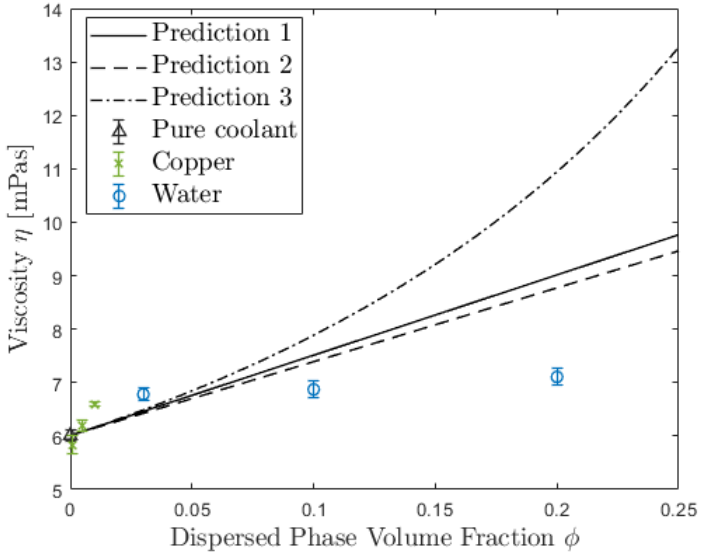

Figure 4.15: Measured viscometry data in comparison to predicted viscosity for pure coolant, and water and copper contamination fractions. The contaminated viscosity predictions were based on a pure coolant viscosity of 6.01 $mPas$ at 23 °C. Prediction 1 is Equation 4.3, Prediction 2 is Equation 4.4, and Prediction 3 is Equation 4.5.

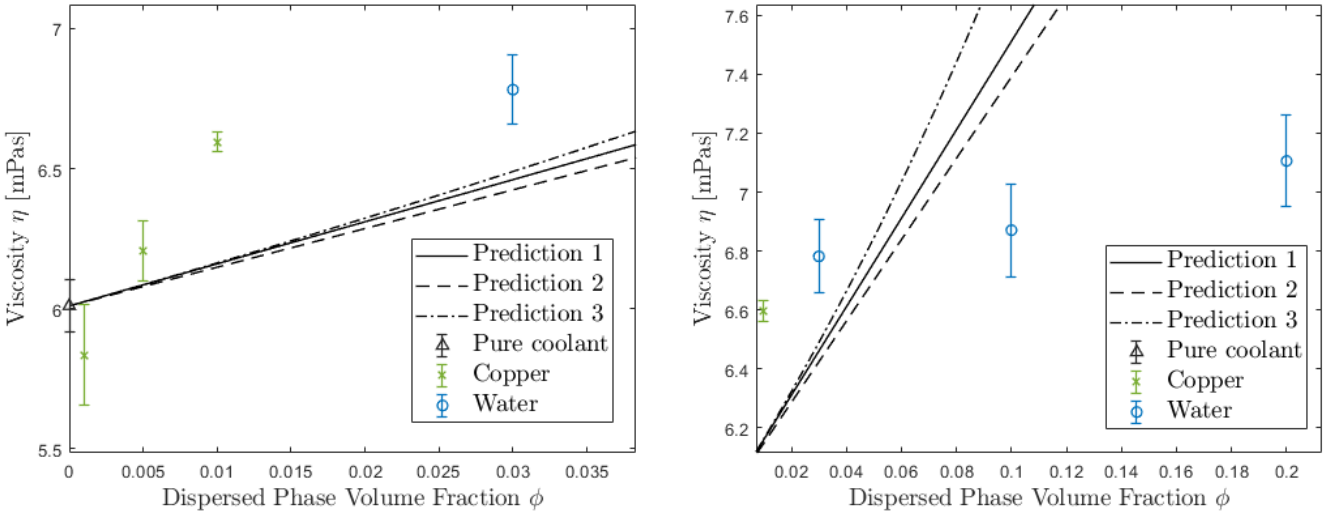

(a) Lower viscosity and volume fraction section.

(b) Higher viscosity and volume fraction section.

Figure 4.16: Measured viscometry data in comparison to predicted viscosity for pure coolant, and water and copper contamination fractions. The contaminated viscosity predictions were based on a pure coolant viscosity of 6.01 $mPas$ at 23 °C. Prediction 1 is Equation 4.3, Prediction 2 is Equation 4.4, and Prediction 3 is Equation 4.5.

Mixture viscosity values in Table 4.4 showed a clear increase from a pure coolant, if 0.1

% copper is disregarded. The average value for 0.1 % copper is lower, however its error suggests that there is not a definitive change from pure coolant. If both pure coolant and 0.1 % copper were tested many more times, the differences between them is considered to be immeasurably minute. Furthermore, although sample preparation for this small quantity of copper is achievable, there is a strong probability that loading the sample using a pipette would not contain a homogeneous dispersion, especially for extremely dilute mixtures such as 0.1 % copper.

Considering the n value from the Power Law, the behaviour for each mixture was more non-Newtonian than the pure coolant, especially the 20 % oil-water emulsion. This behaviour of emulsions was similarly reported by Otsubo, [152], who showed that for some 20 % water in oil fractions, shear thinning occurred. The cause of shear thinning is due to the increased resistance to flow induced by droplets/particulates, especially at low shear rates. As the shear rate increases, droplets/particulates break down and/or become aligned in the direction of flow.

The predictions for the viscosity of the mixtures made in Section 4.6 were compared with measured data shown in Figure 4.15. Prediction 1 and 2, better illustrated in Figure 4.16a, under-state the values measured for copper and 3 % water contaminated mixtures, respectively. Where as prediction 3 under-states 10 and 20 % water contamination values, Figure 4.15. An explanation for this, which has previously been mentioned for lower dispersed fractions, is that with each pipette used to load the rheometer, a evenly distributed amount of dispersed to continuous phase volumes is difficult to achieve. It is also important to mention that each predictive model does not account for the applied shear rate. Thus the measured apparent viscosity obtained using the gradient from a stress-shear rate graph may not be truly represented by each prediction.

The disparity between each mean value in Figure 4.16 is sufficient enough to indicate a change in contamination with respect to viscosity. However considering the error, it cannot be repeatedly distinguished, as it is apparent that the sensitivity of the rheometer is not adequate enough to detect contamination changes.

4.8 Conclusion

Through use of a conventional parallel plate rheometer, the viscosity of pure and contaminated coolant mixtures were measured with the following conclusions:

- To verify the dynamic viscosity, pure coolant was investigated at 20 - 60°C and compared with values attained from its supplied data sheet. The measured data was considered more reliable as the Table 4.1 values were converted from kinematic viscosity.
- Pure coolant was established as a Newtonian fluid due to its behaviour under varying shear rates and its apparent viscosity was measured.
- Mathematical models were used, with the measured viscosity value of pure coolant, to predict the apparent viscosity of mixtures. However, they did not appear to accurately predict measured data, which was highlighted as an issue with the models due to not considering viscosity with shear rate and how droplets/particles interact under shear.
- For coolant-water emulsions and coolant-copper suspensions it was found that there was a general increase in the non-Newtonian behaviour as the contamination dispersed fraction increased. This behaviour was particularly noticeable for concentrated mixtures.
- The drop in viscosity for 0.1 % copper was summarised as difficulties with sensitivity due such a low dilute mixture.
- With regards to the measured mean values, the feasibility of using shear viscosity to measure contamination in a dielectric coolant is good. However, the apparent error illustrates issues with sensitivity when distinguishing between contamination fractions.

Despite the behaviour, variances between measured and predicted data and sensitivity of the rheometer, the viscosity values measured in this chapter will be used in the proceeding chapters.

Chapter 5

Analytical and Numerical Models to Predict Ultrasonic Shear Viscosity

This chapter describes an analytical model that is used in conjunction with a numerical model to understand the effects of an acoustic shear wave when contacting a solid-liquid interface, and how the reflection coefficient changes with varying liquid viscosity. Chapter 3 evaluated the developments of ultrasonic viscosity measurement and found that a three layered viscometer offered the greatest sensitivity to measure low viscosity fluids. Using this information, the analytical and numerical models are produced using acoustic theory through multiple boundaries and different materials. This enables viscosity predictions of the coolant and contaminated mixtures, which are carried out in Chapter 7.

5.1 Introduction

An ultrasonic viscosity model was required for understanding the physical phenomena and accurately interpreting between real and predicted data. Analytically linking the reflection coefficient to the viscosity of a test sample, using a three layered viscometer, has been the focus of a number of previous research publications. Schirru, [15], was the first to produce such a model, which was later improved by Brenchley, [16], by relating the viscosity of a fluid with the pressure reflection coefficient for a two and three-layered system. This was done using Equations 3.19 and 3.20, which are reproduced here for the readers convenience, Equations 5.1 and 5.10, respectively. Furthermore, this model was not limited to Newtonian fluids as it also attempted to predict the viscosity of non-Newtonian fluids by incorporating the Maxwell model with values for oil relaxation times. The analytical model, used by Brenchley, to predict the change in reflection coefficient

with frequency was reproduced in this chapter.

$$R = \frac{Z_2 - Z_1}{Z_2 + Z_1} \tag{5.1}$$

Although no previous publications were found for a numerical model predicting the viscosity using a three layered viscometer, other ultrasonic work attempted to incorporate such tools into predicting values and simulating wave behaviour. For example, Li, [153], utilised a simple numerical finite difference model to understand the behaviour of high power ultrasonic shear waves in contact with an interface under a frictional force. The result was a model that could predict the interaction between the two phenomena and validate measured data based on ultrasonic theory. The numerical model produced by Li, was redeveloped in order to achieve a novel viscosity numerical model, which was then used to predict the pressure reflection coefficient for a corresponding fluid viscosity at varying ultrasonic specifications. The benefit of this type of model is that it mimics real ultrasonic data acquisition parameters (voltage, frequency and wave type variables) that potentially offer a more accurate validation tool for measured data.

5.2 Analytical Study

Throughout this section an analytical study for a three-layered ultrasonic viscometer was reproduced. This study only considers the Newtonian rheological model to illustrate an analytical viscosity prediction, as the non-Newtonian model lacked data for the relaxation times of oils, Brenchley, [16]. Furthermore, if ultrasonic spectroscopy was used (creating ultrasonic waves at multiple frequencies), non-Newtonian behaviour could then be illustrated by viscosity data at varying shear rates.

5.2.1 Reflection Coefficient in a Three Layered System

As discussed in Section 3.4, whenever a wave reaches a boundary, a portion of the amplitude will be reflected and another portion transmitted. For a three layered system, Figure 5.1, the same process will occur. However, the initial wave acting on the second bound-

ary will be the transmitted wave from the first boundary. This provides a progressively weaker sound wave with each boundary added. Despite this, by carefully selecting the intermediate layer's (layer 2) impedance and thickness, an impedance step down from layer 1 to layer 3 increases the amplitude of the transmitted wave into layer 3. In addition to impedance matching, there is also acoustic resonance that similarly increases transmission. The result is much more desirable than that of a two layered system, similarly discussed in Section 3.4.

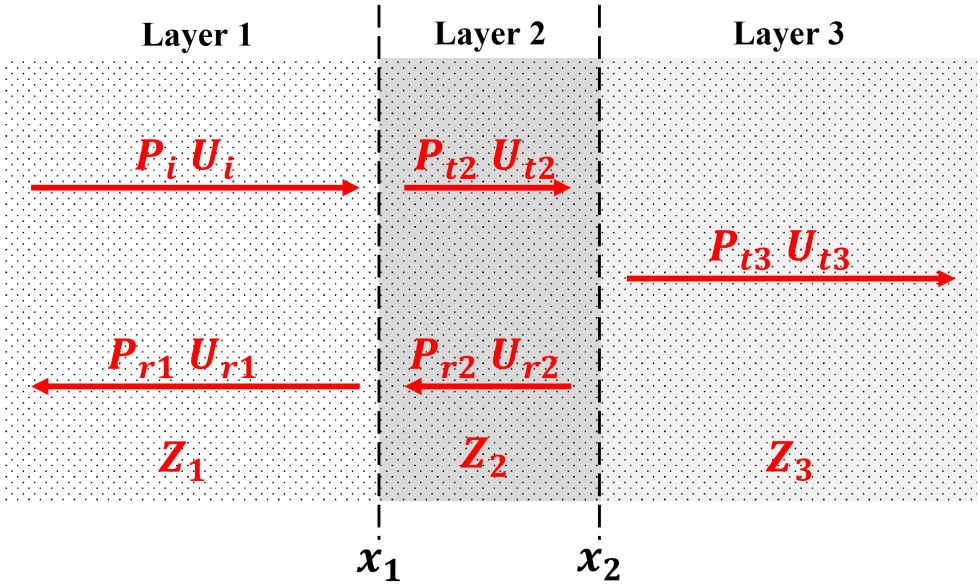

Figure 5.1: Three layered shear analytical diagram illustrating sound interaction at boundaries. Here pressure, P, and acoustic impedance, Z are used. For a three layered ultrasonic viscometer, the intermediate material, layer 2, is an impedance matching layer between layers 1 and 3.

The one dimensional wave equation is given in Equation 5.2, where δ is displacement, x is space, t is time, and c speed of sound. This is derived in David and Cheeke, [112], using transverse vibrational motion along a string fixed at one end. This equation describes the motion of a wave, and is the starting equation to build an analytical model.

$$\frac{\partial^2 \delta}{\partial x^2} = \frac{1}{c^2}\frac{\partial^2 \delta}{\partial t^2} \tag{5.2}$$

This has the general solution, known as d'Alembert formula, Equation 5.3.

$$\delta = A_1 f(x - c_0 t) + A_1 f(x + c_0 t) \tag{5.3}$$

For a wave with angular frequency, this can be reduced further to Equation 5.4.

$$\delta = A sin f(kx - \omega t) \tag{5.4}$$

Equation 5.4 can then be expressed in a more convenient complex exponential form using Euler's identity (i.e $e^{\pm\theta} = \cos\theta \pm i\sin\theta$), Equation 5.5

$$\delta = A e^{j(\omega t - k_i x)} \tag{5.5}$$

Analysing the three layered system required the consideration of the complex pressure, p. The wave number, k, describes the number of waves per distance in the intermediate layer, $k = \frac{2\pi}{\lambda}$. This relationship was expanded using a sinusoidal sound wave in equation 5.6, where p is a constant.

$$P_i = p_i e^{j(\omega t - k_i x)} \tag{5.6}$$

Applying Equation 5.6 at the first boundary, where $x = x_1$, the displacement boundary condition becomes.

$$p_i e^{j(\omega t_i x)} + p_r e^{j(\omega t - k_r x)} = p_{t2} e^{j(\omega t_{t2} x)} + p_{r2} e^{j(\omega t - k_{r2} x)} \tag{5.7}$$

Since the first boundary is considered to equal zero ($x_1 = 0$), equation 5.7 becomes equation 5.8, which is the continuity of the normal specific acoustic impedance at the first boundary.

$$\frac{p_i + p_r}{p_i - p_r} = \frac{Z_2}{Z_1} \frac{p_{t2} + p_{r2}}{p_{t2} - p_{r2}} \tag{5.8}$$

At the second boundary ($x = x_2$), where $x_2 \neq 0$.

$$\frac{p_{t2} e^{(-jk_2 x)} + p_{r2} e^{(jk_2 x)}}{p_{t2} e^{(-jk_2 x)} - p_{r2} e^{(jk_2 x)}} = \frac{Z_3}{Z_2} \tag{5.9}$$

Finally, algebraic manipulation and replacing exponential terms with sine and cosine using Euler's equation (i.e $e^{\pm\theta} = \cos\theta \pm i\sin\theta$), provides Equation 5.10. These derivations are conducted in depth by Kinsler, [116].

$$R = \frac{(1 - Z_1/Z_3)\cos(k_2 x) + j(Z_2/Z_3 - Z_1 Z_2)\sin(k_2 x)}{(1 + Z_1/Z_3)\cos(k_2 x) + j(Z_2/Z_3 + Z_1/Z_2)\sin(k_2 x)} \tag{5.10}$$

To illustrate the relationship that the reflection coefficient has with frequency, Figure 5.2 was plotted using Equation 5.10, where different fluid layer impedance values and matching layer thickness values were used. The model input values are illustrated in Table 5.1, where layer 1 has a value similar to that of aluminium, layer 2 has a value similar to a matching layer polymer, and layer 3 has values representative of two fluids with different viscosities. The reason for impedance matching with these materials was due the typical set-up of an ultrasonic viscometer, which consists of aluminium-polyimide-fluid. The results show a decrease in the reflection coefficient as the fluid layer impedance increases, Figure 5.2. This is because the mismatch between the layers was reduced, hence there is more energy transmission into the fluid.

Table 5.1: Initial shear acoustic impedance values for the three layered model used to produce Figure 5.2. Layer 1 has a value similar to that of aluminium, layer 2 has a value similar to a matching layer polymer and layer 3 has values representative of two fluids with different viscosities.

Acoustic Impedance	
Layer 1	8.52 $MRayl$
Layer 2	1.1 $MRayl$
Layer 3	0.01 $MRayl$
	0.1 $MRayl$

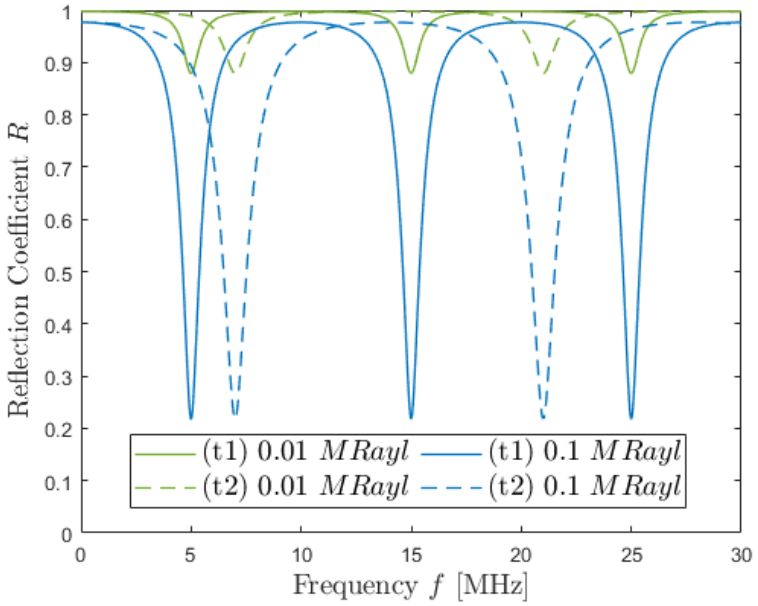

Figure 5.2: Reflection coefficient with respect to frequency showing different acoustic impedance and thickness values (t1 and t2) of the intermediate medium using Equation 5.10.

Furthermore, Figure 5.2 shows resonant dips at specific frequency values. These dips occurred when the thickness of the intermediate layer was a quarter of the frequency wavelength. Considering Figure 5.1, when the wavelength was a quarter thickness of the intermediate layer, the reflection at the interface, x_2, becomes π out of phase with the reflection from the interface, x_1. This induced destructive interference is illustrated by Figure 3.6 and comprehensively reported in Section 3.3.5). At the points of maximum resonance, Equation 5.10 reduces to Equation 5.11.

$$R_{Res} = \frac{Z_2^2 - Z_3 Z_1}{Z_2^2 + Z_3 Z_1} \tag{5.11}$$

Figure 5.2 also shows that the resonant dip bandwidth increased as the acoustic impedance of the fluid tended to that of the matching layer. Again, this behaviour occurred because the acoustic mismatch between the intermediate layer and the fluid was reduced. This would continue until the impedances were equal, at which stage the wave would be completely transmitted, $Z_2 = Z_3$. Beyond this point, when $Z_2 < Z_3$, the reflection coefficient would increase again, however, this would indicate a poor intermediate

layer selection. To obtain maximum sensitivity of the reflection coefficient, the frequency selection was important with regards to the acoustic mismatch. The more dissimilar the mismatch was, the greater the frequency had to be. Moreover, through changing the thickness of the intermediate layer, the resonant dip shifted in frequency. This permitted the capability of adjusting the system by altering the thickness and thereby creating resonance at different frequencies. Thus allowing more sensitive measurements to be achieved.

In the following and future work, the thickness of the intermediate layer was considered a quarter of the wavelength of the frequency. For example, Figure 5.3 illustrates resonant dips that correspond to a frequency of 10 MHz.

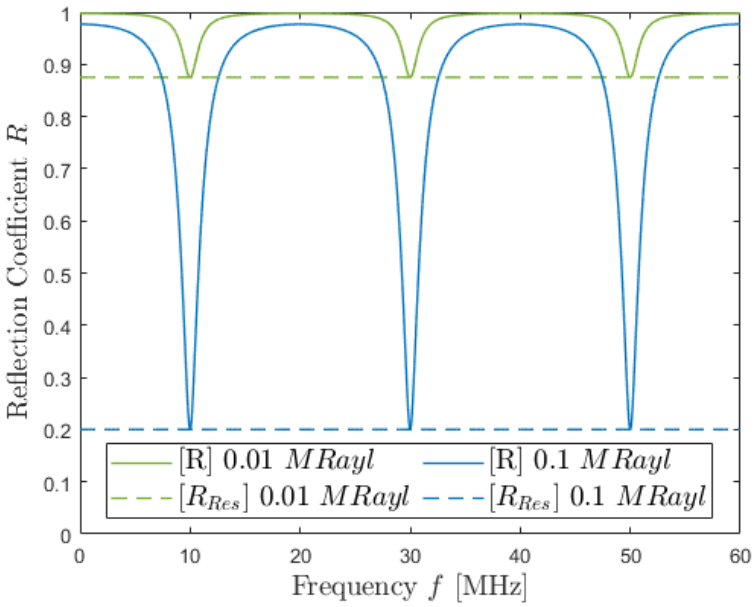

Figure 5.3: Reflection coefficient with respect to frequency showing a comparison between Equation 5.10 and 5.11, where resonant dips were created at a matching layer thickness corresponded to 10 MHz for two different viscosity fluids, Equation 5.11

5.2.2 Newtonian Model For Shear Viscosity

Rheological models were described in Chapter 2 and were implemented in Chapter 4 to explain the characteristics of tested fluids. For clarity, the Newtonian model is reproduced here to outline the behaviour considered by the ultrasonic viscosity model. Fluids can show either viscous or a combination of viscous and elastic behaviour. Therefore, they

are mathematically illustrated using a linear viscous dashpot or a combination of linear elastic spring and viscous dashpot. These models are shown separately in Figure 5.4.

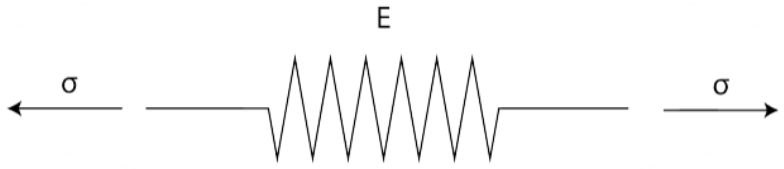

(a) Linear elastic spring model.

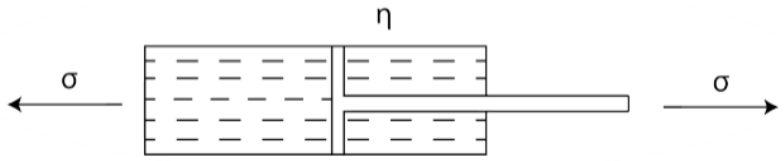

(b) Linear viscous dashpot model.

Figure 5.4: Illustration of both spring and viscous models while subject to stress.

A linear elastic spring is modelled using Equation 5.12, where, E, is stiffness, σ, is stress and, γ, is strain. When under a constant stress, the spring undergoes straining, as it instantly deforms and endures said deformation until the stress is removed. Once removed, deformation immediately reduces and the spring moves back to a its original position. Hence, an ideally elastic material returns to the initial state.

$$\gamma = \frac{1}{E}\sigma \tag{5.12}$$

The viscous dashpot analogy is a piston-cylinder damper set-up where the cylinder is filled with a viscous fluid with viscosity, η. This is modelled using Equation 5.13. Under a constant stress, the fluid is flowing with a constant deformation rate, or strain rate, $\dot{\gamma}$. After the stress is removed, the deformation of the fluid remains. Hence, an ideally viscous fluid completely remains in the deformed state.

$$\dot{\gamma} = \frac{1}{\eta}\sigma \tag{5.13}$$

Combining the spring and viscous models with the shear stress and shear strain relation, the shear modulus could be acquired. The shear modulus is composed of two terms

named the storage modulus, G', and the loss modulus, G'', and were interlinked by the phase angle, δ, illustrated by Figure 5.5. The material behaviour was indicated by the phase angle using the following guidelines:

- Viscous behaviour - An entirely viscous Newtonian fluid is indicated when the phase angle is 0°.
- Elastic behaviour - An elastic solid is indicated when the phase angle is 90°.
- Visco-elastic behaviour - A non-Newtonian material is indicated when the phase angle is between 0° and 90°.

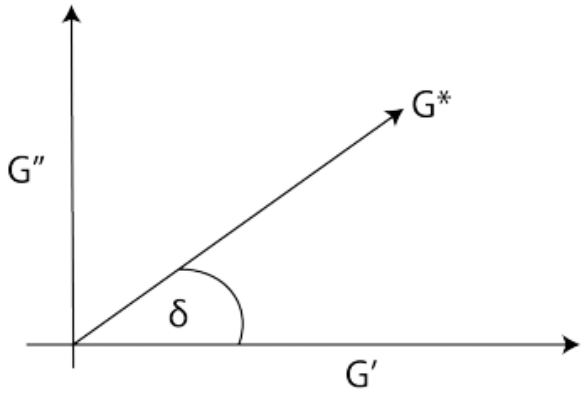

Figure 5.5: Argand diagram for the shear modulus relationship. Where G^* is the complex shear modulus, G' is the storage modulus, G'' is the loss modulus and δ is the phase angle.

As mentioned previously, for a Newtonian fluid, the viscosity does not vary with an applied shear rate. Assuming that the fluid is in-compressible, the mechanical damper in Figure 5.4b represents the final Newtonian model illustration. By integrating Equation 5.13 with respect to time, Equation 5.14 is provided. This equation represents the strain when the stress is initially applied.

$$\gamma = \frac{\sigma_0}{\eta} t \tag{5.14}$$

Combining Equation 5.14 with Equation 2.8, the shear modulus was found.

$$G = G' + iG'' \tag{5.15}$$

Considering a Newtonian fluid, the storage component was equal to zero, $G' = 0$, therefore the shear modulus was equal to the loss modulus.

$$G = iG'' = i\omega\eta \tag{5.16}$$

5.2.3 Reflection Coefficient From a Newtonian Fluid Layer

Section 5.2.2 provided the necessary equations to determine the relationship between the reflection coefficient and viscosity using a Newtonian model. However, as the reflection coefficient is complex, the absolute value is used for all figures and displayed as R. Furthermore, up to this point, simulations have been made using impedance values that are similar to an actual three layered ultrasonic viscometer. Nevertheless from this point on and unless otherwise stated, specific material properties for each layer were used. The three layered ultrasonic viscometer utilised in this work (comprehensively described in Chapter 7) consisted of aluminium as layer 1, polyimide as layer 2 (matching layer) and a fluid as layer 3. It is important to note that the thickness of the matching layer, calculated using Equation 3.13, was dependent on the input frequency. Rather than using an extremely large impedance value, a combination of smaller values for density and speed of sound were evaluated. This increases the accuracy of the calculated impedance and thereafter the simulated results. The values used for each layer are listed in Table 5.2.

Table 5.2: Input variables for the rheological analytical model where parameters for layers 1 and 2 were used with the solid impedance and parameters for layer 3 used the liquid impedance.

Parameter	Layer	Value
Density	1	2700 kg/m^3
	2	1400 kg/m^3
	3	800 kg/m^3
Speed of Sound	1	3158 m/s
	2	780 m/s
Viscosity	3	$1\times10^{-3} Pas$
	3	0.01 Pas
	3	0.1 Pas
	3	1 Pas

Layers 1 and 2 were solids, therefore their impedance values were calculated using Equation 3.4. In order to find the acoustic impedance of a fluid, Equation 3.5 was combined with 5.16 to achieve Equation 5.17.

$$Z_l = \sqrt{\rho i \omega \eta} \tag{5.17}$$

To better represent this process, Equation 3.4 and 5.17 were combined with the acoustic model for a three-layered system, Equation 5.11. The result is shown in Equation 5.18, where the viscosity of a fluid in layer 3 produces a corresponding reflection coefficient value within a three-layered system

$$R_{Res} = \frac{(\rho_2 c_2)^2 - \sqrt{i\rho_3\omega\eta}\rho_1 c_1}{(\rho_2 c_2)^2 + \sqrt{i\rho_3\omega\eta}\rho_1 c_1} \tag{5.18}$$

To illustrate the difference between the reflection coefficient from Equation 5.10 and 5.11, Figure 5.6 was created. The viscosity was programmed to be 0.1 Pas, the matching layer thickness represented a frequency of 2 MHz, and the other parameters were detailed in Table 5.2. Figure 5.6 depicts the frequency dependence the fluid acoustic impedance has on the reflection coefficient, as a decrease in frequency shows a reduced reflection coefficient. This behaviour occurred for both Equation 5.10 and 5.11.

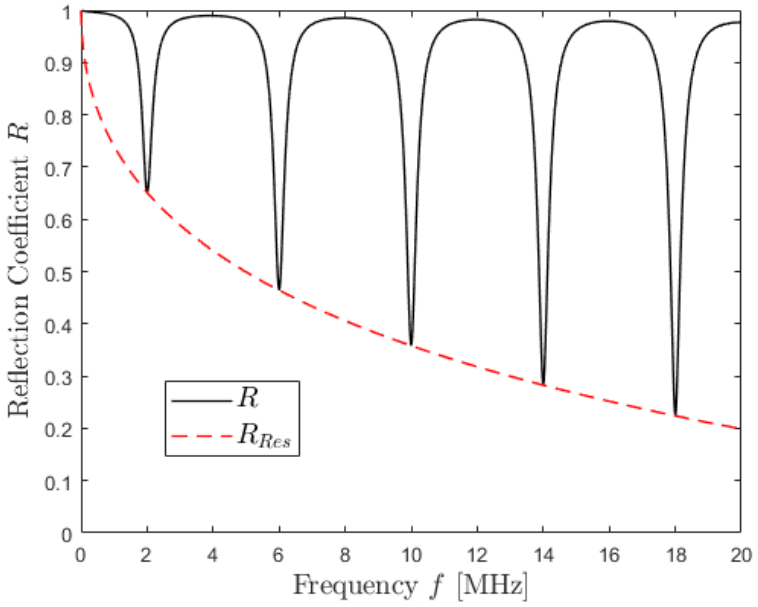

Figure 5.6: Reflection coefficient with respect to frequency for a Newtonian model comparing values from Equations 5.10 and 5.11.

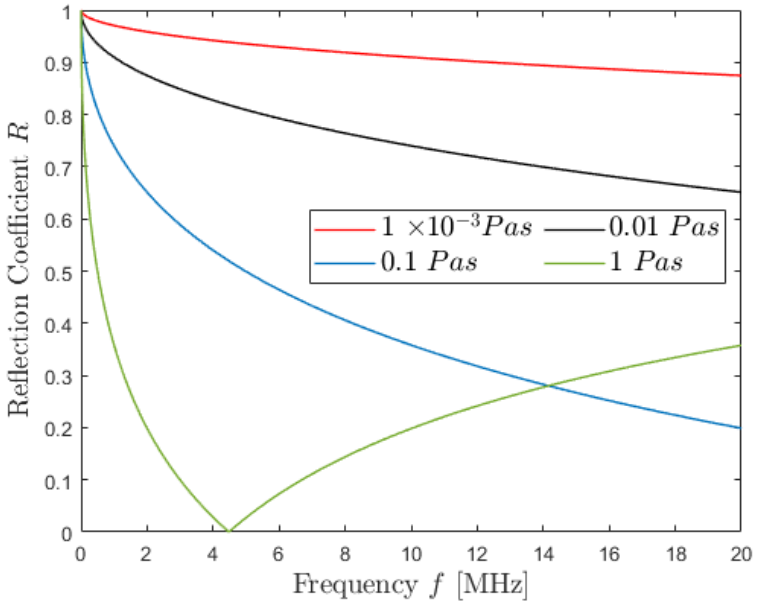

Figure 5.7: A comparison of the minimum reflection coefficient at resonance with respect to frequency for a Newtonian three-layer system, for different viscosity fluids.

The input variables from Table 5.2 were used to produce Figure 5.7 using the MATLAB script shown in Appendix A. Reflection coefficient values across the 1×10^{-3} - $1\ Pas$

viscosity range showed distinguishable trends from 0.5 - 4.5 MHz. A larger frequency range is achieved for viscosity values of 1 $\times 10^{-3}$ - 0.1 Pas, as the 1 Pas fluid impedance goes beyond that of the matching layer, producing higher reflection values. Despite this, the reflection coefficient values were significant enough that it could allow accurate viscosity measurements. Finally, the result could be optimised depending on the viscosity of the fluid under investigation.

5.3 Numerical Study

The previous section uncovered the analytical interaction of ultrasonic pressure at the matching layer-liquid interface, and how it considers the general solution to the wave equation in terms of basic wave parameters (pressure amplitude, frequency, wave length and wave number). By implementing a finite element scheme the wave equation can be modelled directly. Thus providing a simulation with a similar data acquisition method as the actual experiments completed in Chapter 7. Therefore, a simple finite difference method was created in this section, where propagation of ultrasound throughout the entire three-layered system was simulated and studied. There are other numerical methods and tools available, however, this numerical model was capable of capturing the physical phenomenon of viscosity measurement, reasonably. A comparison of the two models was made as a corroborative tool, which in theory should match as the analytical model mathematically originates from the wave equation.

5.3.1 Numerical Model

A similar simple one-dimensional model used by Li, [153], was applied to predict the reflection coefficient due to fluid viscosity at an interface. Once again, a three layered system is considered, Figure 5.1. However a new diagram that better illustrates a numerical approach is shown in Figure 5.8.

As mentioned in Section 5.2.3, the materials utilised to simulate a three layered ultrasonic viscometer consisted of aluminium as layer 1, polyimide as layer 2 (matching layer) and a fluid as layer 3. Each layer is considered a half space material, where the aluminium

and matching layer have defined lengths. The aluminium has a set thickness of 25 mm, which was used in work done by Schirru and Brenchley, [15, 16], and the matching layer was a quarter thickness of the wavelength, again calculated using Equation 3.13. The fluid layer thickness was defined as the penetration depth, Equation 3.12, which is based on the fluids viscosity and the frequency of the propagating wave, as explained in Section 3.3.4. At the end of this fluid layer, the shear wave is completely absorbed, as it would be in a real fluid. The two interfaces are defined as being in complete contact. The numerical model uses speed of sound to distinguish between each layer, thus creating an interface. As an ultrasound wave was excited at point $x = 0$, it propagated towards $x = x_1$ at $c = c_1$. At that location $c_1 = c_2$ for a distance $x = x_2$, until $c_2 = c_3$. For each change in speed of sound a reflection was created. Due to the matching layer thickness, resonance occurs, resulting in one reflection wave.

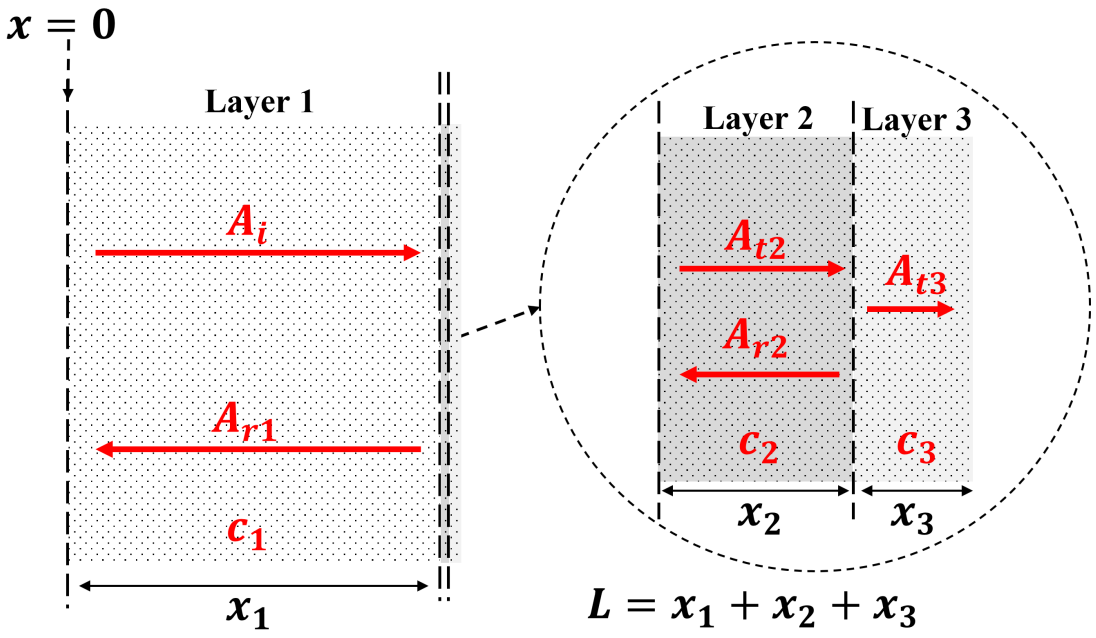

Figure 5.8: Shear numerical diagram illustrating sound propagation specifically for the numerical model. Here pressure, P, is replaced with amplitude, A, layer thicknesses, x, are applied, and speed of sound, c replaces impedance, Z.

5.3.2 Numerical Implementation

To numerically solve the one dimensional wave equation, Equation 5.2, a source β was added to represent a given controlled start point for the wave. This restructures the one dimensional wave equation to become Equation 5.19.

$$\frac{\partial^2 \delta}{\partial t^2} = c^2 \frac{\partial^2 \delta}{\partial x^2} + \beta \tag{5.19}$$

The classic Euler scheme was applied to discretise the wave equation, Equation 5.19, and did so with respect to space and time, for the current, previous and following step. This is illustrated by Figure 5.9, where subscript, i, and superscript, n, denotes the space and time index, respectively.

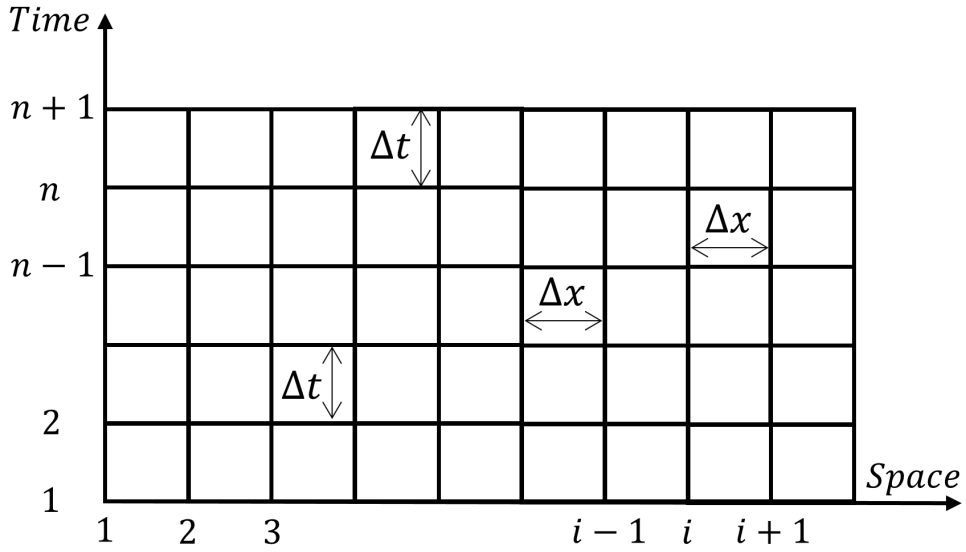

Figure 5.9: Space and time discretisation for a one-dimensional acoustic system.

Equation 5.19 can be discretised as Equation 5.20 and rearranged for easier implementation, as Equation 5.21.

$$\frac{\delta_i^{(n+1)} + 2\delta_i^n + \delta_i^{(n-1)}}{\Delta t^2} = c^2 \frac{\delta_{i+1}^{(n)} + 2\delta_i^n + \delta_{i-1}^{(n)}}{\Delta x^2} + \beta_i^n \tag{5.20}$$

$$\delta_i^{(n+1)} = 2\delta_i^n - \delta_i^{(n-1)} + [c\frac{\Delta t}{\Delta x}]^2 (\delta_{i+1}^{(n)} + 2\delta_i^n + \delta_{i-1}^{(n)}) + \Delta t^2 \beta_i^n \tag{5.21}$$

In Equation 5.21 $c\Delta t/\Delta x$ is called the Courant-Friedrichs-Lewy number (CFL), where Δt is the time increment and Δx is the space increment. This number was chosen to ensure that the numerical speed $\Delta t/\Delta x$ is less than the propagation speed, Equation 5.22. Without this, the numerical simulation would not have been possible.

$$c > \frac{\Delta t}{\Delta x} \tag{5.22}$$

The wave can be modelled to be reflected or absorbed by a boundary. The first case was given by Dirichlet boundary conditions, Equation 5.23. This condition was ideal for the boundary at $x = 0$ where the wave is pulsed from.

$$\delta(x, t) = 0 \tag{5.23}$$

For absorption across the boundary, Mur's discretised absorbing boundary conditions are given by Equation 5.24. This condition was ideal for the boundary at the end of the fluid layer, where $L = x_1 + x_2 + x_3$.

$$\delta_L^{(n+1)} = \delta_{L-1}^n + \frac{CFL - 1}{CFL + 1}[\delta_{L-1}^{(n+1)} + 2\delta_L^n] \tag{5.24}$$

5.3.3 Initial Wave Design

The ultrasonic wave emitted by source β from the boundary at $x = 0$ required defining. Initially a simple harmonic sine wave was applied, however, this type of wave does not truly represent a transducer, which has been deformed to produce a vibration. Therefore a Gaussian distribution was applied, Figure 5.10a, using the Gaussian function in MATLAB, which is shown in Appendix B. Furthermore, to accurately simulate real ultrasonic viscosity measurements, a chirp wave was designed to pulse at a range of frequencies across a specified number of cycles, Figure 5.10b. The length of the chirp is dependent on the number of cycles, resonant frequency and time increment and was produced using Equation 5.25, where A is the voltage amplitude, $f_{ChirpVec}$ is the chirp frequency vector, t_{Vec} is the time vector and Gaussian is the MATLAB function mentioned previously. The chirp frequency vector was created at a desired length using a start frequency which then peaks

in amplitude at the resonant frequency.

$$\delta_{i=0}^{n=1:ChirpLength} = Gaussian[A \times sin[2\pi \times f_{ChirpVec} \times t_{Vec}]] \tag{5.25}$$

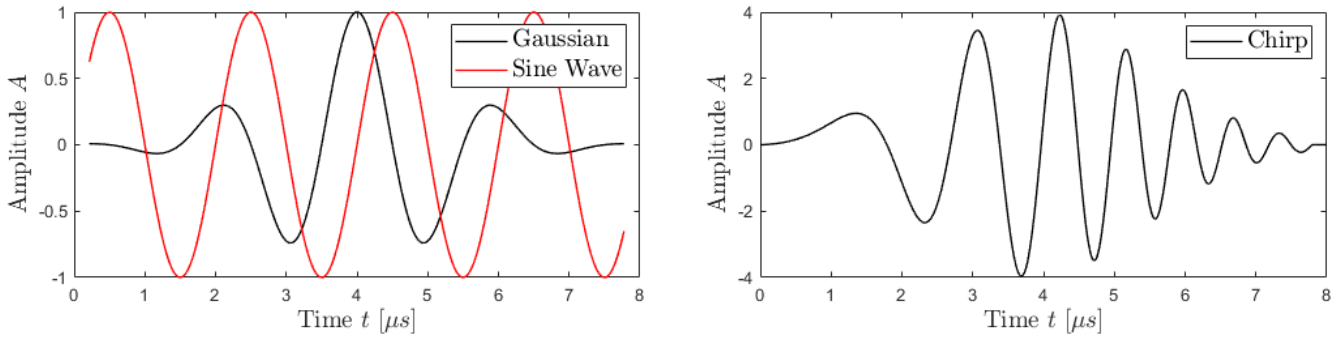

(a) Harmonic sine wave and Gaussian distributed sine wave.

(b) Gaussian distributed chirp wave.

Figure 5.10: Initial wave design showing progression from a harmonic sine wave through to a Gaussian distributed chirp wave.

5.3.4 Numerical Parameters

The numerical model uses speed of sound to distinguish between each layer, creating a boundary and producing a reflection encountering a change in speed of sound. The speed of sound values for aluminium and the matching layer were already available for a shear wave, Table 5.3. However, shear wave speeds in fluids are not well documented due to their short propagation lengths. Therefore, considering a Newtonian fluid, it was necessary to utilise Equation 5.26 to calculate the shear speed of sound in a liquid.

$$c_l = \sqrt{\frac{G}{\rho}} = \sqrt{\frac{iG''}{\rho}} = \sqrt{\frac{i\omega\eta}{\rho}} \tag{5.26}$$

Table 5.3 shows numerical parameters used for the following simulations. The same speed of sound values for the solid layers in the analytical model were reproduced here, along with calculated speed of sounds for fluids with the same viscosities. It is important to note that speed of sound is a material property and therefore it will not change. However, as illustrated by Equation 5.26, the speed of sound in a fluid is dependent on the viscosity and density, hence varied sound speeds with respect to viscosity are shown in Table 5.3.

Also the density used for the oils was kept at 800 kg/m^3. A Gaussian distributed ultrasonic chirp was used with a centre frequency and start frequency comparable with the analytical model resonance at 10 MHz, Figure 5.7. Space and time resolution was setup to clearly observe a wave form and to align with available pulsing instruments. Finally the CFL condition is shown in Table 5.3, which is dependent on the layer speed of sound and the ratio of the time to space resolution. The CFL values vary between fluids as their speed of sound varies.

Table 5.3: Numerical model parameters.

Solid Layers Speed of Sound	
Aluminium	3158 m/s
Matching layer	780 m/s
Fluid Layers Speed of Sound	
1 $\times 10^{-3} Pas$	6.27 m/s
0.01 Pas	19.82 m/s
0.1 Pas	62.67 m/s
1 Pas	198.17 m/s
Ultrasound Parameters	
Resonant frequency	10 MHz
Start frequency	8.5 MHz
Number of cycles	5
Amplitude A	4V
Numerical Set-up Parameters	
Space resolution Δx	9.75 μm
Time resolution Δt	1 ns
CFL Condition	
Aluminium	0.6477
Matching layer	0.16
1 $\times 10^{-3} Pas$	0.18 $\times 10^{2}$
0.01 Pas	0.57 $\times 10^{2}$
0.1 Pas	0.182 $\times 10^{1}$
1 Pas	0.575 $\times 10^{1}$

5.3.5 Numerical Simulation Method

Implementing equations from Section 5.3.2 with the initial wave design and applying parameters listed in Table 5.3 to the MATLAB script, shown in Appendix B, the numerical simulation was executed using the method illustrated by Figure 5.11. The following steps shown in Figure 5.11 were taken:

- Boundary conditions are set for the three layered model using Equation 5.23 for the boundary at x = 0 and Equation 5.24 at x = N, Figure 5.8.
- Numerical parameters are inputted such as material layer properties and ultrasonic wave values. The first fluid speed of sound (dependent on viscosity) was used until the time loop was completed, at which point a new fluid was selected, depending on the number of fluids simulated. The first fluid is always a fully reflected reference of a zero speed of sound value. This is highlighted later in the analysis method.
- The time step loop is conducted using Equation 5.21 where a new space vector was created based on the previous, current and next increment.
  - A chirp wave was created, using Equation 5.25, over a time range equal to that of the length of the chirp.
  - After the chirp has been produced, the source seizes to emit sound and new time increments process the propagation of this chirp wave.
- Simulating how a transducer would detect an ultrasonic signal, a time domain signal was obtained by observing the voltage amplitude at the point in space, x = 0.
- The entire time step computation was then repeated for the next fluid speed of sound and a time domain signal was similarly produced.
- Finally the signal analysis was conducted, which is discussed more in later sections.

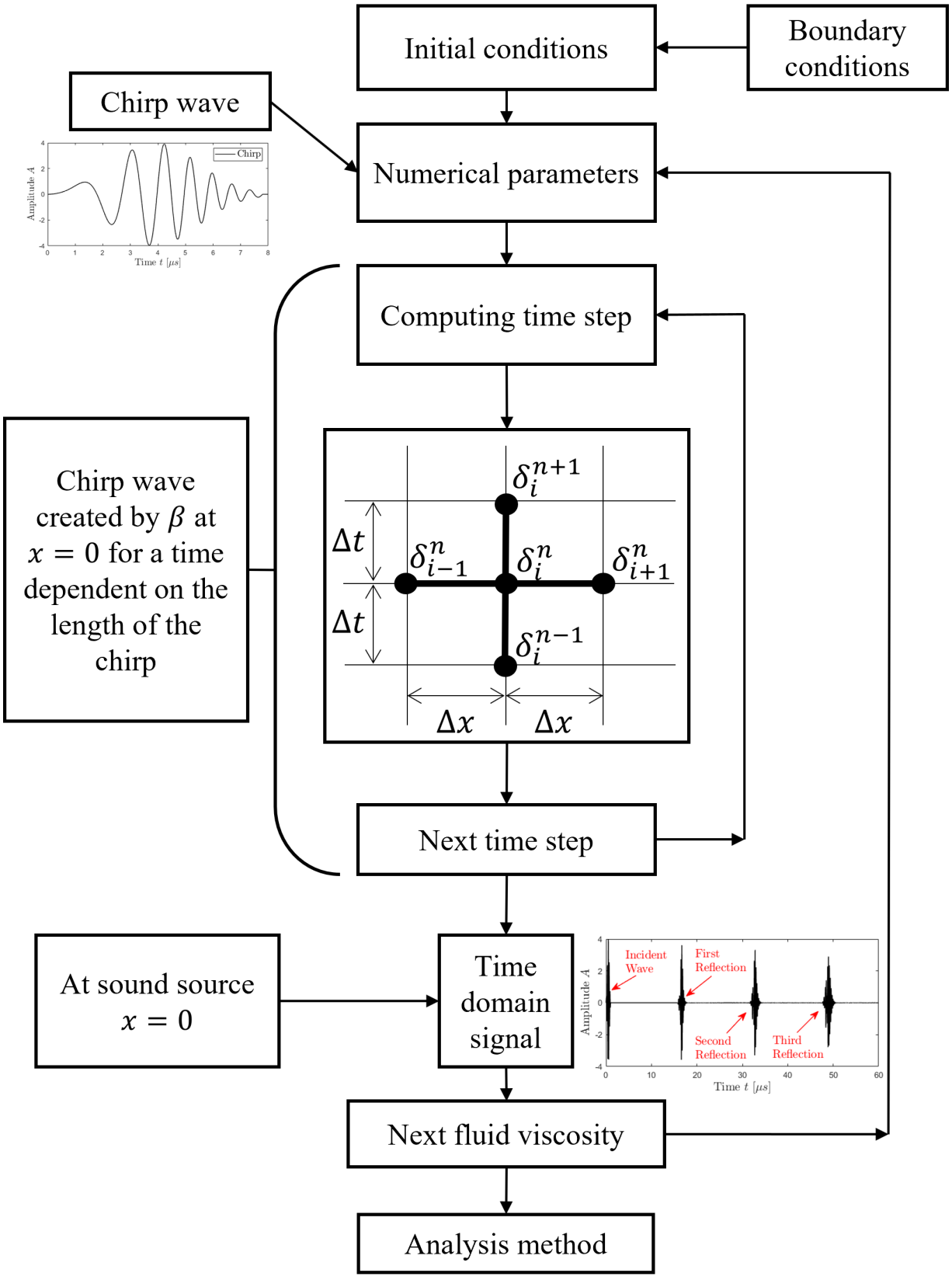

Figure 5.11: Numerical Simulation Method.

5.3.6 Numerical Simulation

Following on from the method in Section 5.3.5 some of the frames at different time intervals are given in Figure 5.13. Figure 5.12 was created to show the location of the layers in the simulation, which would cause a change in speed of sound and therefore create a reflection. The initial ultrasonic wave was created at the source, β, on the left boundary and was propagated towards the matching layer-fluid interface on the right. The fluid in this simulation had a viscosity of 1 Pas. After striking the measurement interface, the waveform was clearly distorted.

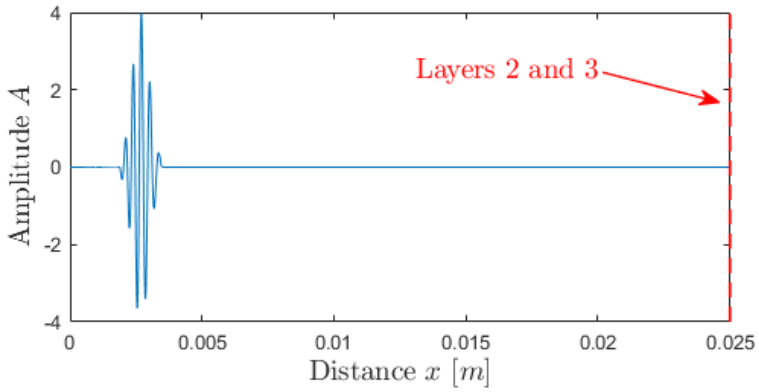

(a) Waveform at point in time, $t = 1.1\mu s$.

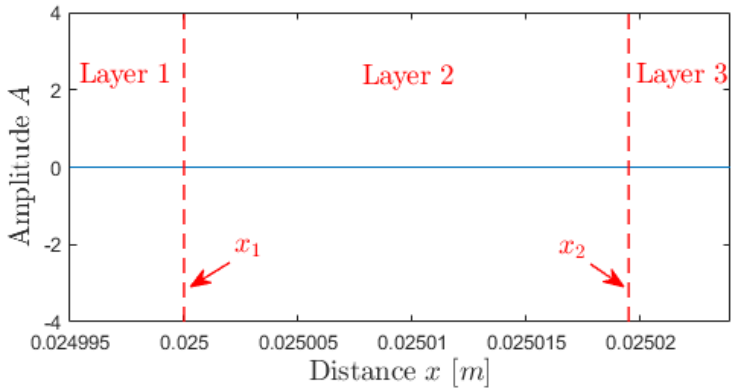

(b) Focused version of Figure 5.12a to clearly illustrate each layer, which aligns with Figure 5.8.

Figure 5.12: Representation of layer locations within the simulation. At each boundary a speed of sound change occurs which creates a reflection.

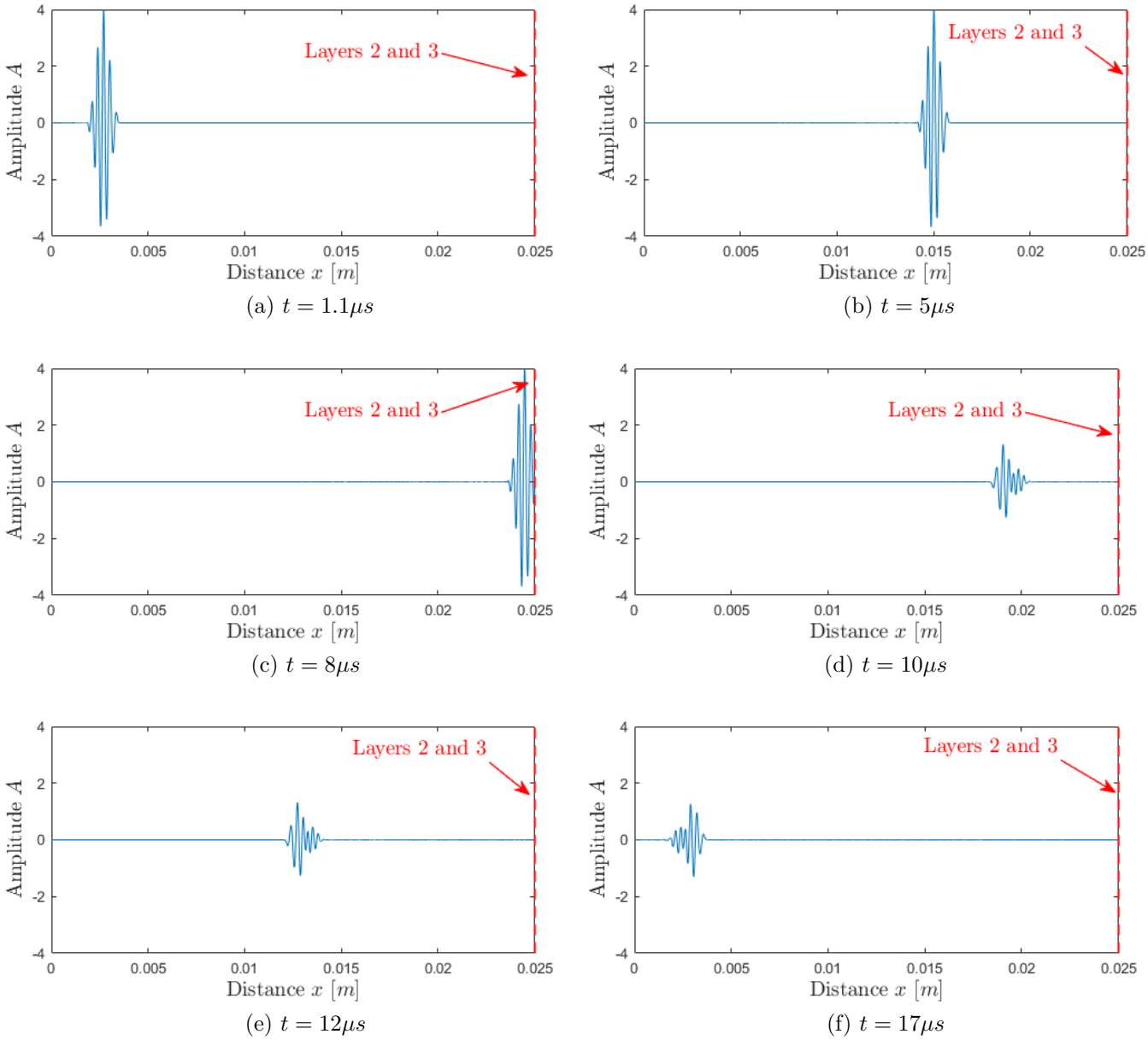

(a) $t = 1.1\mu s$ (b) $t = 5\mu s$

(c) $t = 8\mu s$ (d) $t = 10\mu s$

(e) $t = 12\mu s$ (f) $t = 17\mu s$

Figure 5.13: Numerical solution example of an ultrasonic wave striking a fluid interface in a three layered model.

As the ultrasound source was positioned at $x = 0$, a signal displacement observation with respect to time was made at that same location, Figure 5.14. Compared with the initial waveform, the reflected waveforms were distorted after interaction with the fluid interface.

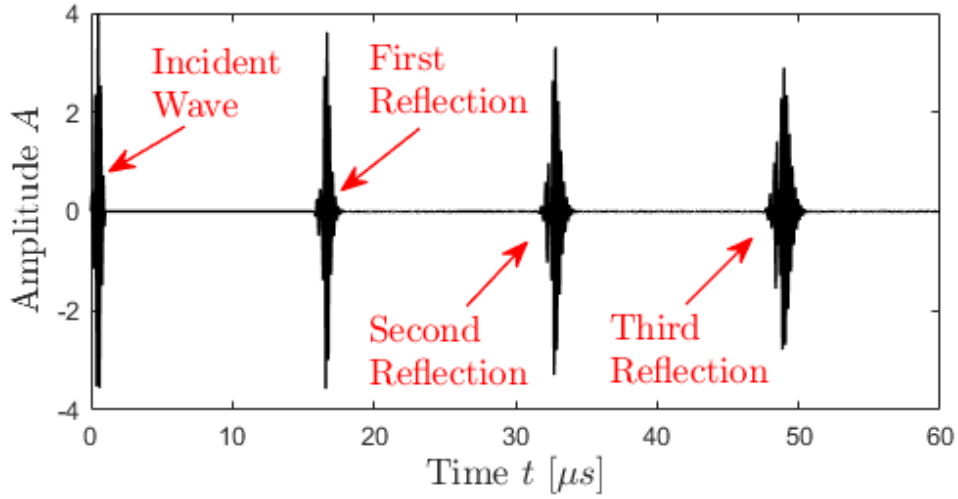

Figure 5.14: Signal voltage amplitude observation with respect to time at $x = 0$

5.3.7 Analysis Method

To obtain the reflection coefficient from the simulation, a number of steps were completed once a signal was produced. It followed the same processing steps as real ultrasonic data, which is clearly outlined in the following chapter. As this followed the same analysis as real data, a reference measurement was required. A reference measurement is a reflected wave from the matching layer-fluid boundary when there is no fluid. Hence, the reference was modelled as a complete reflection using a speed of sound equal to zero.

- Time domain waveform trimming - The full signal, Figure 5.15a, was focused on the first reflection, Figure 5.15b.
- FFT - A Fast Fourier Transform was used to convert the time domain signal into the frequency domain, Figure 5.16a. This showed the energy amplitude of the reflection in terms of its frequency components, which displayed key features, as discussed in Section 3.7.2.

- Reflection coefficient - The reflection coefficient was then found by dividing a fluid FFT signal by the reference FFT signal (full reflection), Figure 5.16b.

5.3.8 Reflection Coefficient From a Newtonian Fluid Layer

Using the numerical parameters from Table 5.3, Figure 5.15 was produced, where Figure 5.15a shows the full time domain signal response, and Figure 5.15b shows the first reflection. It is visually clear that the signal amplitude is reduced as the viscosity of the fluid increases.

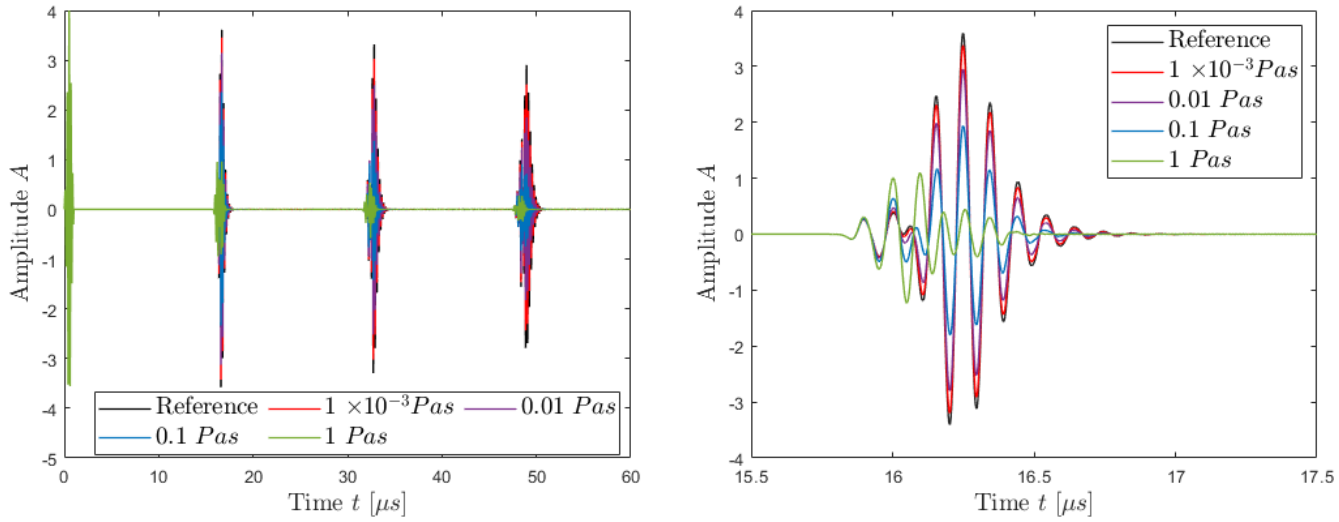

(a) Full time domain signal.

(b) Trimmed first reflection time domain signal.

Figure 5.15: Numerical model time domain response at 10 MHz centre frequency for a range of different viscosity fluids and a reference simulation.

Converting the time data into the frequency domain, Figure 5.16, the signal amplitude is displayed in terms of its frequency components, Figure 5.16a. The FFT shows a much greater differentiation with amplitude in comparison to the reference simulation. Also, as the viscosity increases, a dip in the amplitude becomes more visible at the resonant frequency. The bandwidth of the chirp pulse is also visible in the FFT, spanning from around 8.5 to 11.5 MHz, when considering a -6 dB range. Dividing the fluid FFT data by the reference data produced the reflection coefficient, Figure 5.16b. The result is of a similar format to Figure 5.6 produced by the analytical study, however, the resonant dips

shown here are clearest within the bandwidth of the pulse. This is more realistic to how a real ultrasonic viscometer would work. This response would then by correlated to the viscosity by selecting the lowest reflection coefficient value within the resonant dip.

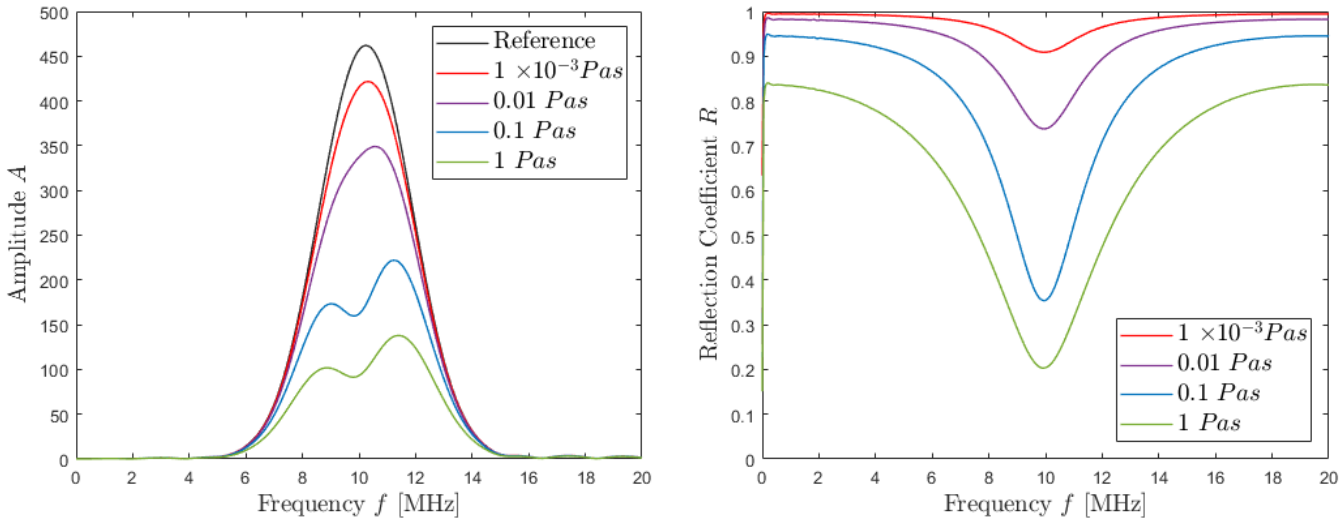

(a) FFT amplitude frequency spectrum.

(b) Reflection coefficient.

Figure 5.16: Numerical model frequency domain response at 10 MHz centre frequency for a range of different viscosity fluids.

5.4 Comparison Between Numerical and Analytical Models

Numerical solutions computed in section 5.3.8 were compared with the analytical result at the same resonant frequency and solid and fluid layer parameters. The result is illustrated in Figure 5.17 and it was noted that numerical result showed good agreement with the analytical solution at the maximum resonant frequency dip. The reflection coefficient from the numerical model revealed similar behaviour as the analytical result, Equation 5.10, when subject to various fluid viscosities. This agreement suggested that both models predict a similar result at the maximum resonant dip frequency. Outside of the resonant dip frequency, differences start to emerge, as the analytical model's reflection coefficient tends to 1 at a much faster rate. This is because the analytical model considers each frequency step as if it was the centre frequency and calculates the reflection based on

the impedance mismatch at the measurement interface (boundary x_2 in Figure 5.1). In contrast, the numerical model produces a waveform within a frequency bandwidth and compares the reflection from an oil with a reference (complete reflection, R = 1). However, some frequencies outside the bandwidth are also excited, and as there is no noise within the simulation, a lower reflection coefficient value is produced for each oil. The following chapters show real data where frequencies outside of the waveform bandwidth are filled with noise. Hence, the numerical model's reflection coefficient values outside of the bandwidth in Figure 5.17 are ignored.

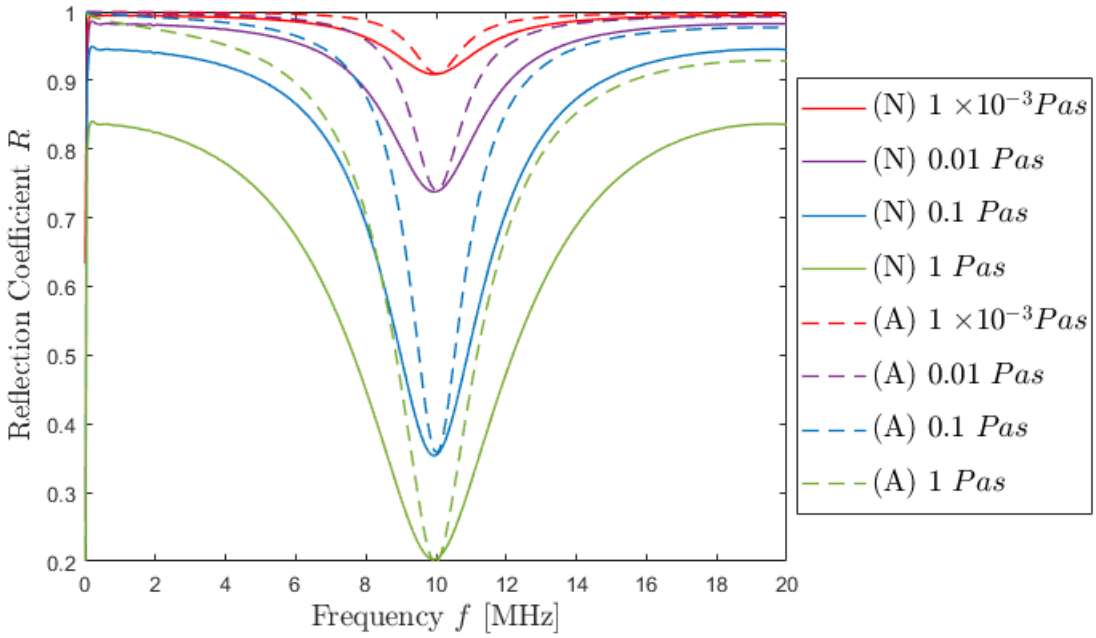

Figure 5.17: Comparison of the reflection coefficient data obtained using both analytical and numerical solutions for a 10 MHz centre frequency. The analytical model uses Equation 5.18.

To further illustrate the agreement between the two models, Figure 5.18 was made. Here the analytical model was used to fit the numerical model data which was selected at the peak resonance (10MHz). Figure 5.18 showed that the analytical model provided a perfect correlation of $R^2 = 1$ for numerical results. Using the analytical model as a fit for the numerical model would allow measured or predicted reflection coefficient values to be converted into a viscosity value.

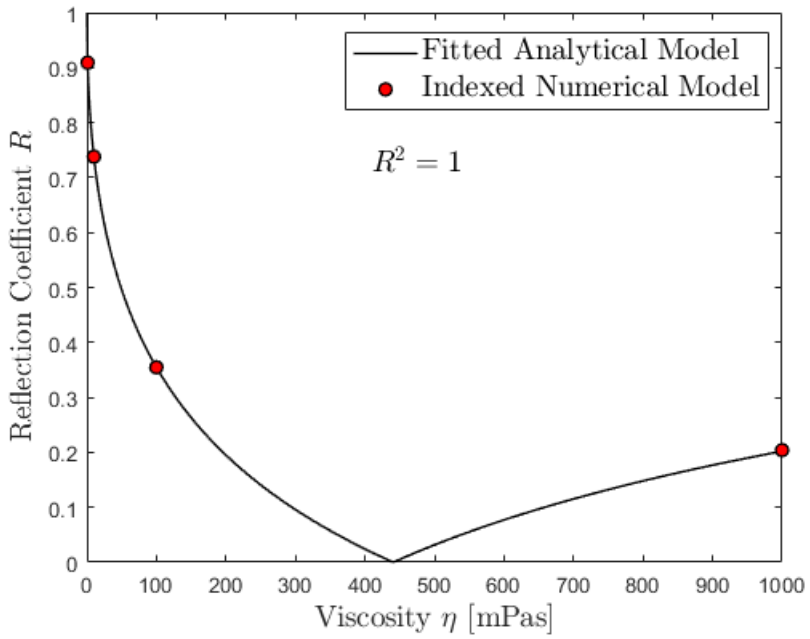

Figure 5.18: Comparison of the reflection coefficient with respect to viscosity. Numerical data points were plotted and fitted with the analytical model, Equation 5.18, which provided a perfect correlation. Results were obtained using a 10 MHz frequency.

5.5 Conclusion

This chapter compared two different approaches to predict the reflection coefficient of varying viscosity fluids using a three layered ultrasonic viscometer. It did so by redeveloping a three layered analytical model and creating a novel numerical model. The following conclusions were made:

- An exact solution to the three layered system was analytically solved in the form of Equation 5.10 and 5.11.
- An estimated solution was conducted using a numerical approach using a discretised one-dimensional wave equation, Equation 5.21. This solution mirrored real ultrasonic data acquisition and was a method to support the analytical approach.
- Both models highlighted that the sensitivity was dependant upon the thickness of the intermediate layer and could be manipulated to increase sensitivity of viscosity measurements.

- They also showed that a higher frequency would produce a lower reflection coefficient value. Depending on the viscosity under investigation, this would similarly increase the sensitive of results, allowing for more accurate measurements.

- The exact solution provided by the analytical model was used to fit the numerical data, and did so with a perfect agreement. Thus illustrating the similarity between each model.

- Both models provided an insight into the physical interaction of an ultrasonic shear wave with varying fluid viscosity in a three layered system. Therefore they are useful tools when understanding the behaviour of real acquired data, which is done in the following chapter.

- Finally, designing an experimental set-up was much easier with the help of these models. Transducer frequencies and material selection could optimised to meet the requirements of the oil under investigation. Also a set-up could be designed with products readily available on the market, without the requirement for bespoke parts.

Chapter 6

Methodology for Ultrasonic Shear Viscometry

This chapter outlines the practical measurement methodology of ultrasonic viscometery that is used to measure viscosity changes due to contamination in a dielectric coolant, which is discussed in Chapter 7. It outlines all experimental hardware, procedures and set-up in order to conduct measurements. It then discusses the calibration process for a range of sensor frequencies and evaluates their results with the analytical and numerical model from Chapter 5.

6.1 Matching Layer Methodology Outline

Up to this point, matching layer theory and the ultrasonic viscometer have been discussed broadly in Chapter 3, however a proper description on the workings of this set-up, which were specific to this research, are discussed here.

Figure 6.1 illustrates the matching layer viscometer set-up, where layer 1 is the metal block, layer 2 is the matching layer and layer 3 is the fluid. Layer 2 was bonded onto the top surface of the metal block using an adhesive. Underneath the metal block a transducer was similarly bonded on, which was then connected to ultrasonic hardware using coaxial cables. The thickness of the metal block was dependent on the application environment of the viscometer, or simply to accommodate for the transducer size and frequency, which would affect the beam spread and near field range. The matching layer had a thickness of a quarter wavelength of the transducer in order to create destructive interference and resonance. It also required an intermediate impedance value compared to the metal block and the test fluid. Both of these design features allowed more energy to be transmitted

into the fluid. The benefits to a matching layer or use of a three layered model were discussed in Section 3.4, where reflection data was compared with a two layered model.

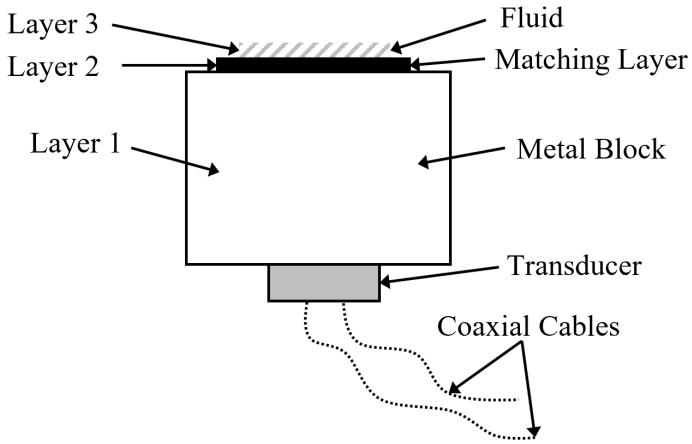

Figure 6.1: Sketch of the ultrasonic viscometer set-up.

When the transducer is excited by an applied voltage, a mechanical wave is produced in a desired format established using ultrasonic pulsing equipment. For example a chirp wave of a desired number of cycles over a range of frequencies. Figure 6.2 illustrates the propagation of a pulsed wave inside a matching layer viscometer.

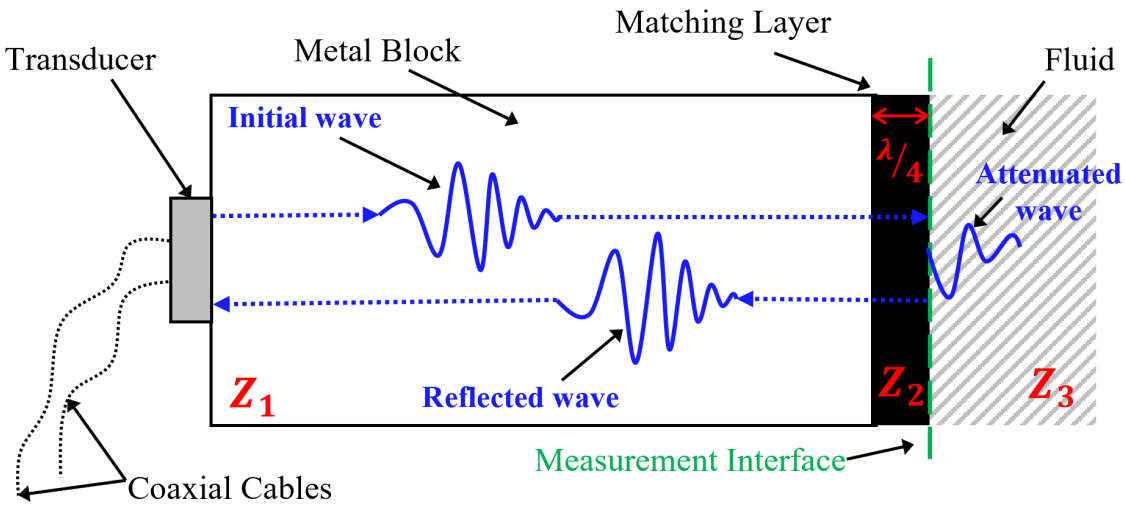

Figure 6.2: Illustration of how a pulsed wave propagates throughout a matching layered viscometer.

The initial wave propagates through the metal until it strikes the first boundary between the metal and matching layer. At this point, some energy is reflected and some

transmitted into the matching layer. Due to the quarter wave length thickness, destructive interference is created, discussed in Section 3.3.5. Therefore energy reflected back at the metal - matching layer interface is cancelled out. Once this is completed, the transferred energy propagates towards the matching layer - fluid interface, where some energy is reflected and some transmitted. The energy transmitted into the fluid is completely attenuated, discussed in Section 3.3.4, whereas the reflected energy propagates back towards the sensor. This energy is then received and converted into a voltage for processing. It is this matching layer - fluid interface that the ultrasonic reflectance method considers, hence this interface is called the measurement interface. Depending on the number of boundaries and the layer materials, multiple reflections will occur from one pulse with respect to time. In order to obtain the reflection coefficient, a waveform reflected from a fluid is compared with a completely reflected waveform from air at the measurement interface. The relationship between reflection coefficient and viscosity is described by the analytical equation, Equation 5.10.

6.2 Apparatus

In the following section, the hardware used to measure the viscosity of fluids using a multiple frequency matching layer viscometer is discussed. An in-depth description of the ultrasonic viscometer and its design is presented. Finally, the instruments utilised to capture data are explained.

6.2.1 Ultrasonic Viscometer Rig

The ultrasonic viscometer, Figure 6.3, was made from a block of 25 mm thick aluminium that had a variety of frequency sensors and matching layers bonded onto it, as used by Brenchley, [16]. The frequencies shown in Figure 6.3 are the resonant frequencies at which a maximum dip in the reflection coefficient will occur due to the thicknesses of the matching layer.

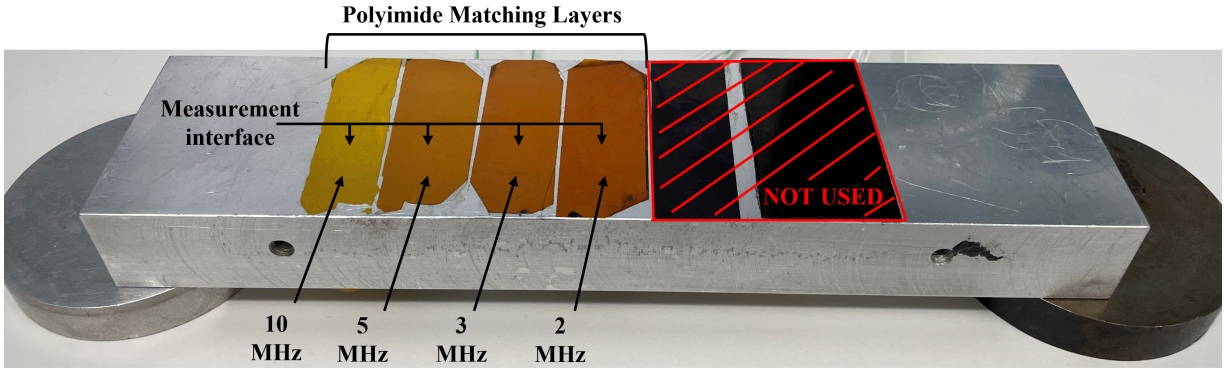

Figure 6.3: Ultrasonic viscometer with a range of matching layers and transducers, where only four of the layers were used. The frequencies shown are the resonant frequencies that relate to the thicknesses of the matching layer.

To better illustrate Figure 6.3, a sketch was created, Figure 6.4, which shows a simplified schematic of the matching layer viscometer. The matching layer resonant frequencies are shown on the top surface and they are partnered with a transducer frequency on the bottom surface of the aluminium block. Each matching layer thickness and transducer centre frequency matches, except for the 5 MHz matching layer and 10 MHz transducer. This was intentional and is discussed in Section 6.2.3.

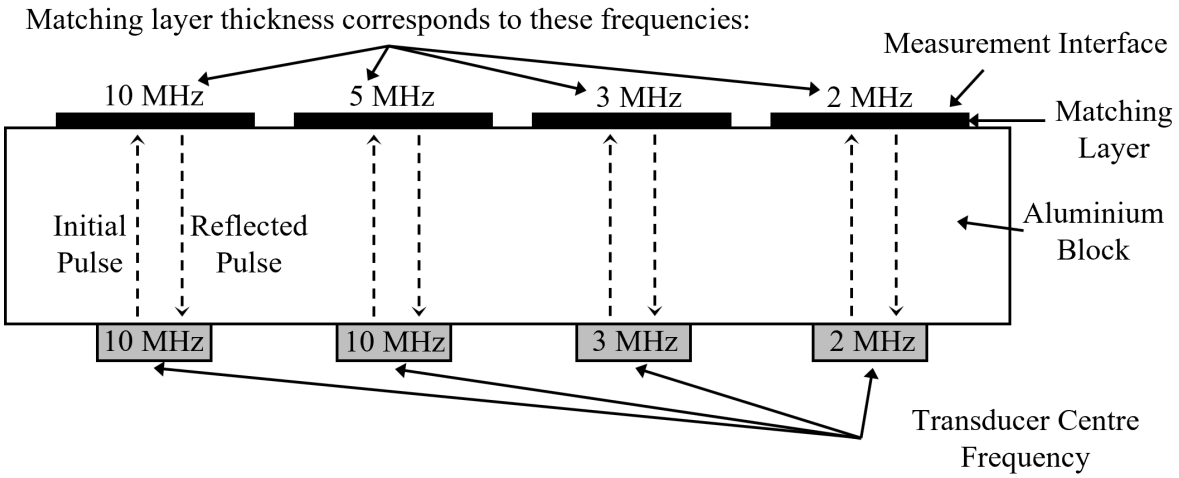

Figure 6.4: Sketch of the ultrasonic viscometer with a range of frequency sensors and corresponding matching layers.

6.2.2 Matching Layers

Selection of a matching layer material was based on successful work done previously by Haller, Thompson, Schirru and finally Brenchley, [154, 155, 15, 14, 16]. Throughout their work they utilised polyimide due to its intermediate acoustic impedance. This made it ideal as an intermediate layer between metal and oil, where sound travels from a very high acoustic impedance into a low one. Figure 6.5a shows an impedance value that was calculated using Equation 5.11 for the aluminium - matching layer - oil set-up. It indicated a suitable shear impedance value of around 1.5 $MRayl$. Thus polyimide was chosen due to it having a longitudinal impedance value of 3.16 $MRayl$, which is typically double the shear impedance. With a density of 1400 kg/m^3, the polyimide therefore has a longitudinal velocity of 2257 m/s and a shear velocity of 1129 m/s. Hence the shear impedance of polyimide is 1.58 $MRayl$, which is similar to that shown in Figure 6.5a. Figure 6.5b shows the viscosity of the oil when the shear impedance of layer 2 and 3 are equal. Other advantages for using polyimide were that it was manufactured in many thicknesses, had high chemical resistance, high temperatures stability, was inexpensive, and could be easily bonded to aluminium using a strain gauge epoxy.

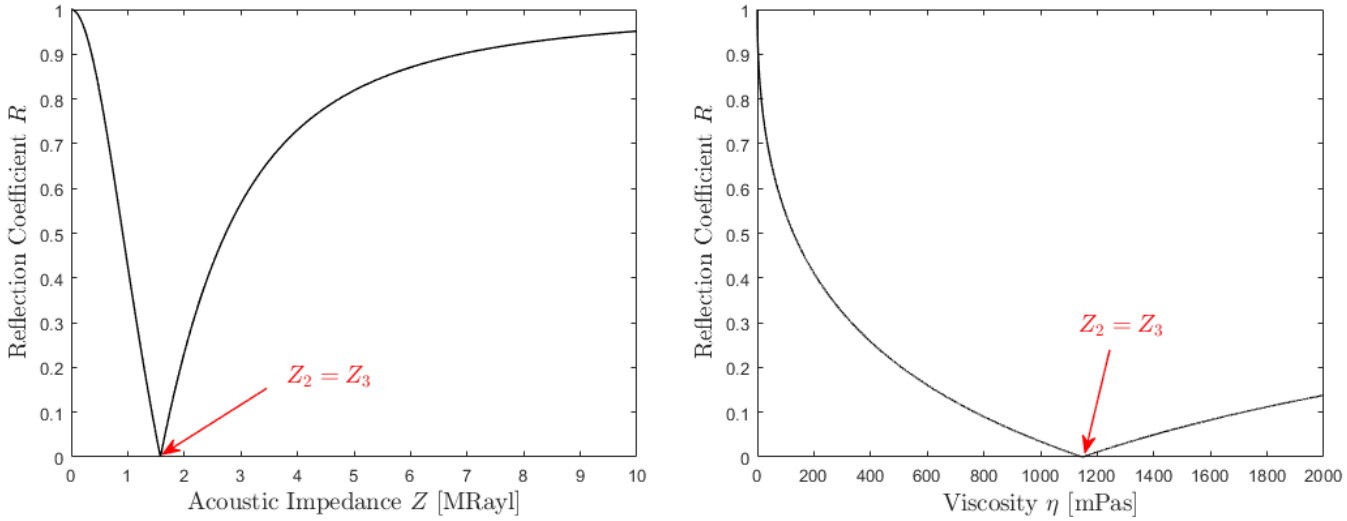

(a) Reflection coefficient changes with shear impedance

(b) Reflection coefficient changes with viscosity

Figure 6.5: Optimum matching layer impedance for intermediate layer between aluminium and a fluid. Modelled using Equation 5.11 for a ultrasonic frequency of 13.86 MHz and, an oil viscosity and density of 1140 $mPas$ and 859 kg/m^3.

6.2.3 Transducers

To measure viscosity at different shear rates, transducer frequencies 2, 3 and 10 MHz were employed with their corresponding matching layers, shown in Figure 6.4. Brenchley, [16], mentions two methods for measuring the viscosity with varied shear rates. The first utilises one sensor with a large bandwidth, enabling the user to excite a liquid over many frequencies. This was completed by Schirru, [15], using a 5 MHz sensor and exciting it at both 5 and 14 MHz (first and second harmonics). The second involves combing the result of many sensors, which pulse at smaller bandwidths around their centre frequency. Throughout this chapter, a mixture of the two methods were used. Table 6.1 shows transducers with set centre frequencies paired with a matching layer thickness that will create resonance at a desired frequency. In Chapter 5 the thickness of the matching layer was calculated using Equation 3.13. However, sourcing a matching layer of an exact thickness that corresponds to a transducer centre frequency was difficult. Instead a matching layer thickness was sourced from a supplier that produced a material near to the calculated thickness. This resulted in a resonant frequency that was slightly skewed from the centre frequency, shown as the actual frequency in Table 6.1. Nevertheless the resonant frequency was within the bandwidth of each transducer. The thicknesses of the material are also shown in Table 6.1 and originate from the supplied data sheet.

Table 6.1: Determining the resonant frequency using different transducer frequencies and corresponding matching layer thicknesses (supplied by polyimide data sheet). Here the actual resonant frequency is created by the polyimide matching layer thickness with the partnered transducer.

Transducer Name	Transducer Centre Frequency (MHz)	Matching Layer Thickness (μm)	Actual Resonant Frequency (MHz)
2 MHz	2	97.5	1.79
3 MHz	3	65	2.98
10 MHz	10	19.5	10.1
14 MHz	10	39	13.86

The 14 MHz transducer, Table 6.1, creates resonance at 13.86 MHz using a 10 MHz centre frequency transducer. This was produced using a similar method to Schirru, [15]. Figure 6.6a shows a simulated reflection coefficient from the analytical model for a match-

ing layer thickness corresponding to 5 MHz. It highlights the first and second resonant dips created by the matching layer. Therefore, a 10 MHz transducer was paired with a matching layer thickness that corresponded to a 5 MHz transducer. By exciting it around the frequency of the second resonant dip a higher frequency measurement at a sensitive dip was obtained. An actual result, shown in Figure 6.6b, illustrates the measured resonant dip using the 14 MHz transducer.

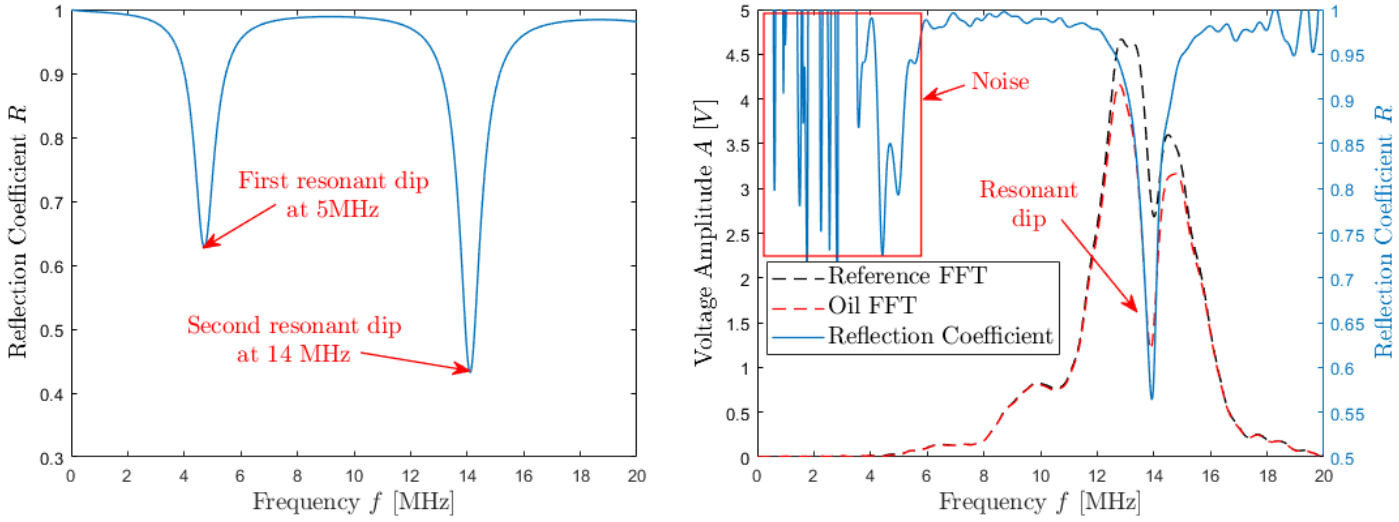

(a) Simulated frequency response

(b) Actual frequency response

Figure 6.6: Simulated and measured data of resonance created at 13.86 MHz using a 10 MHz centre frequency piezoelectric element (14 MHz transducer) paired with a matching layer thickness that corresponded to a 5 MHz transducer.

To conduct experiments using a range of different frequency transducers, bare piezoelectric elements (Figure 3.11) were bonded to the aluminium using a strain gauge adhesive. The benefit of using a bare element was the reduced cost and their capability of being ordered or cut to a required size. The dimensions of the bare piezoelectric elements were $2 \times 5\ mm$. Making transducers this size meant that they were large enough to produce an adequate signal using the Picoscope hardware, and small enough to work in most engineering environments.

The near field range and the beam spread were discussed in Section 3.5.5 and 3.5.6, and are important when designing ultrasonic equipment and/or selecting transducer frequencies. It was desirable but not essential that each transducer produce a fully constructed

waveform before reaching the measurement interface, as illustrated Figure 6.7. They were also required to strike the measurement interface before hitting the side walls, which would result in noise interference. Using Equations 3.21 and 3.22 the values for the two phenomena were calculated with respect to the transducer dimensions and frequency. The results for each frequency are shown in Table 6.2. Although aluminium thickness was set at 25 mm for all experiments, mentioned in Section 6.2.1, the near field range of transducer 4 exceeded that thickness. The effect of this is that the incident wave does not have enough space to properly form before striking the measurement interface. Despite this, it can still obtain viscosity information. Furthermore, the beam spread illustrates that when the lowest frequency transducer propagates a shear wave through the sample it contacts a small area of 21.84° from the centre axis. By striking a small area on the measurement interface, the reflected waves will reach the transducer before hitting the aluminium block sides. Therefore, interference from the metal block walls have little effect on the first reflection. With every subsequent reflection however, the effects of side walls will increase interference and distort the waveform. Nevertheless a large beam spread will result in a larger measurement area.

Table 6.2: Near field and beam spread calculations for each transducer frequency used.

Transducer Name	Near Field (mm)	Beam Spread (°)
2 MHz	4.03	21.84
3 MHz	6.05	14.36
10 MHz	20.16	4.27
14 MHz	27.43	3.13

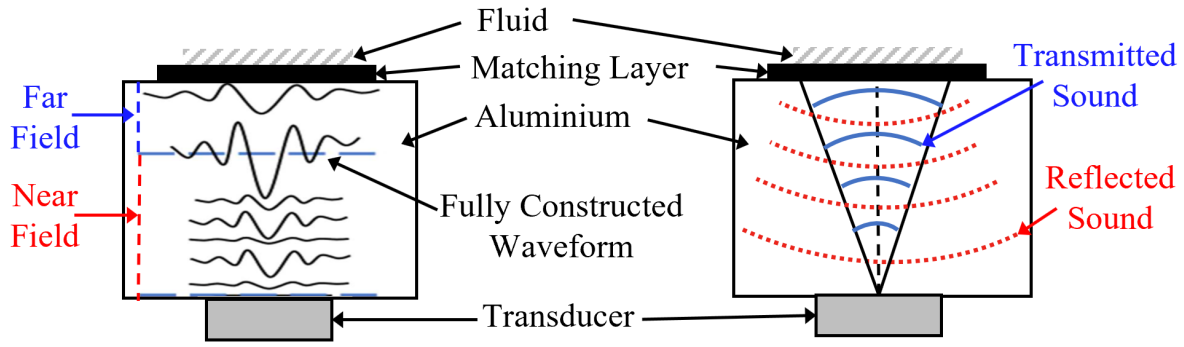

Figure 6.7: Near field range and beam spread of sound waves inside the matching layer viscometer.

To estimate a value for the measurement area that each transducer evaluated, the aluminium block thickness, near field and beam divergence were used. Figure 6.8 illustrates the additional radius created by the beam divergence, which begins after the near field range has been reached. Hence the beam divergence occurred over a distance of the difference between the the total aluminium block thickness and the calculated near field length in Table 6.2. The total measurement diameter for each transducer frequency is shown in Table 6.3, which will be used in the following chapter to understand how ultrasound interacts with mixtures.

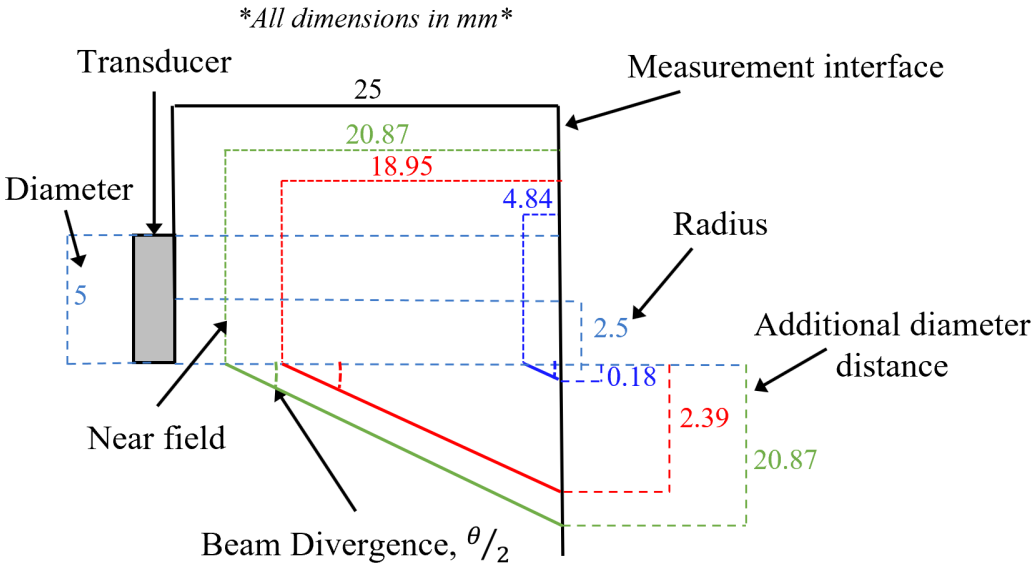

Figure 6.8: Ultrasonic viscometry fluid measurement radius on the solid - liquid interface for each transducer frequency. Based on the near field range and the beam divergence (half of the beam spread), the additional radius measured due to the sensor size and frequency was calculated. Green is for the 2 MHz transducer, red is for 3 MHz transducer, dark blue is for the 10 MHz transducers and the 14 MHz transducer is simply the radius.

Table 6.3: Measurement area for each transducer frequency based on the calculations made in Figure 6.8.

Transducer Name	Estimated Measurement Area (mm^2)
2 MHz	135.61
3 MHz	75.12
10 MHz	22.56
14 MHz	19.63

6.2.4 Instrumentation

The data acquisition (DAQ) instruments are shown in Figure 6.9. The signal acquisition unit was a PicoScope 5000 series, which was used as a dual functionality waveform generator and oscilloscope. Supplied by Pico Technology it offered a superior edge compared with other DAQ instruments due to its low cost, size, adjustable waveform generation and digitiser. To obtain temperature in time with signal captures, a TC-08 thermocouple DAQ was used. Similarly supplied by Pico Technology, it utilised versatile K-type thermocouples both flexible and cheap. Both the PicoScope and TC-08 instruments were capable of being used with only USB power, increasing their portability. However, their most important advantage was the drivers available. These drivers made it possible to work with current LabVIEW software developed at the University of Sheffield, which allowed for input and output settings to be intuitively adjusted. Finally, coaxial cables and connectors were used to link the transducers to the PicoScope, which allowed a voltage to pass from the transducer to the PicoScope, and vice versa.

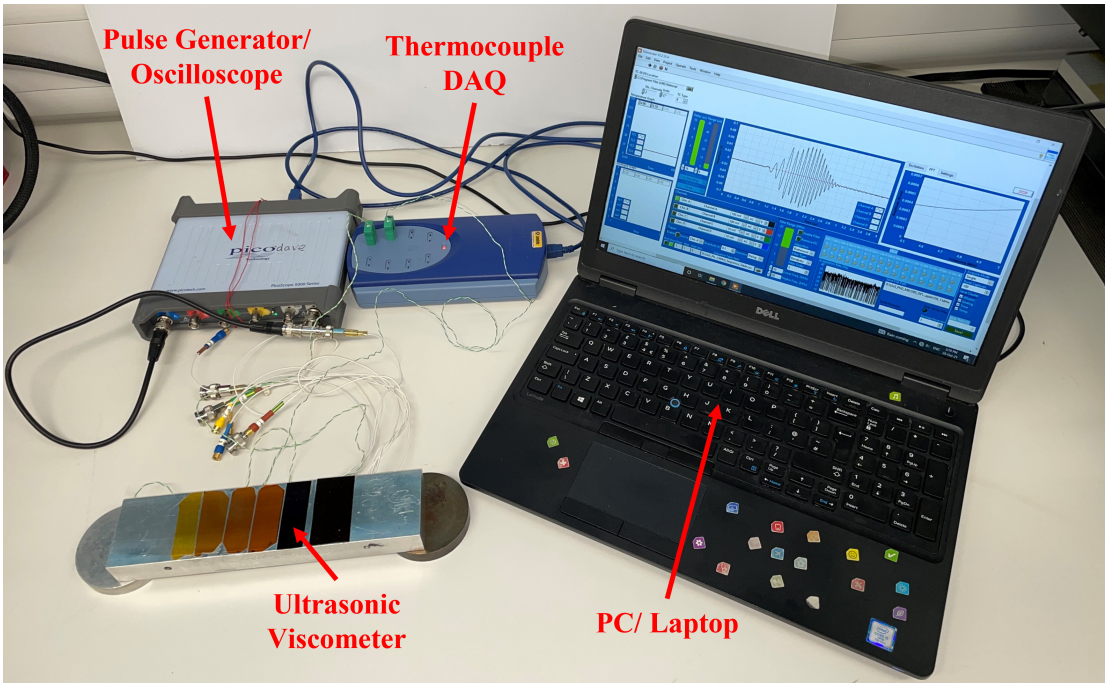

Figure 6.9: Data acquisition instruments consisting of the PicoScope, TC08, coaxial cables, ultrasonic viscometer and the LabVIEW DAQ VI open on the laptop.

6.3 Procedure

Following on from Section 6.2.4, the proceeding steps reveal how these instruments were utilised in this research. To aid this explanation Figure 6.10 shows a simplified block diagram of the complete set-up.

- The signal settings were inputted on a computer using a LabVIEW VI (virtual instrument), which was set up to control the waveform generator via a USB connection.
- The waveform generator uses programmed values from the VI and produces this information in the form of a voltage (electronic signal), displayed as Tx in Figure 6.10.
- The piezoelectric transducer is then excited by this voltage and deformation occurs in its polarised direction. This deformation produces an ultrasonic wave (mechanical wave).
- The ultrasonic wave then travels through the solid and matching layer, where it is then reflected. This reflection contains impedance information about the liquid.
- Then the reflected wave returns to the transducer, where it is converted back from a mechanical wave into an electronic signal, displayed as Rx in Figure 6.10. This is digitised by the oscilloscope part of the PicoScope.
- The digitised data is sent back to the computer, and visually displayed by the LabVIEW VI.
- While the previous steps occurred, temperature data was recorded using the TC-08 DAQ unit. A thermocouple was placed at the pulsing sensor and another at the measurement interface. This enabled the detection of the temperature gradient across the three layered system, which could then be controlled. Temperature control of the sensor and the measurement interface are crucial for reliable viscosity data acquisition.

- The ultrasonic data, with temperature readings, could then be saved and analysed further.

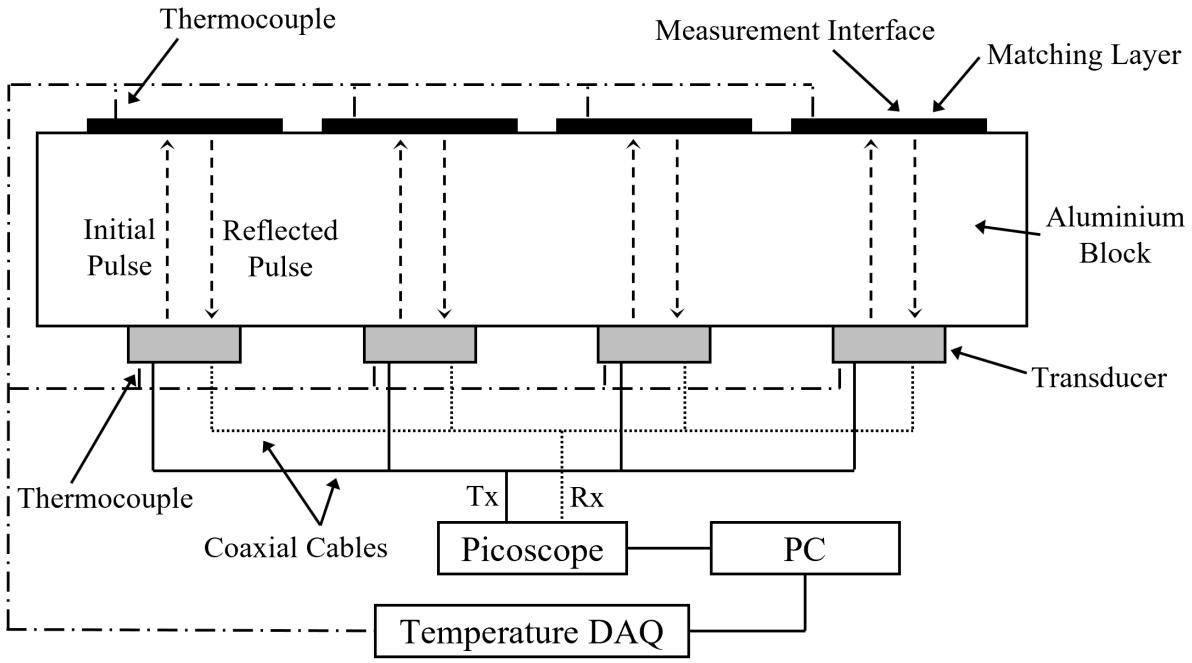

Figure 6.10: Schematic of the experimental configuration, where Tx is the transmitted electronic signal and Rx is the received electronic signal.

6.4 Transducer Excitation Setting

It was explained in Section 6.2.3 how the actual resonant frequency is slightly different to the centre frequency of a transducer. This is due to the supplied thickness of the matching layer. Therefore the most effective pulsing method to excite at the actual resonant frequency is by using a chirp wave. Table 6.4 shows the excitation settings programmed into the LabVIEW VI and executed by the PicoScope. A start and end point were chosen after preliminary data showed where the resonance was actually occurring. The frequency range was selected in order to produce the most energy at the resonant frequency and thus improve signal to noise ratio.

Table 6.4: Chirp excitation settings for each frequency using 5 cycles at 4V peak to peak. Here the actual resonant frequency is created by the polyimide matching layer thickness, which is partnered with a transducer of a certain centre frequency.

Tranducer Name	Transducer Centre Frequency (MHz)	Actual Resonant Frequency (MHz)	Start Frequency (MHz)	End Frequency (MHz)
2 MHz	2	1.79	1	2.5
3 MHz	3	2.98	2.5	3.5
10 MHz	10	10.1	9	11
14 MHz	10	13.86	12.5	15

The more cycles used, the more the electrical energy is transferred by the transducer. When a piezoelectric element is programmed to be excited at a voltage, it does not instantaneously reach the voltage value over 1 cycle. Instead it builds up over each applied cycle until it plateaus at the maximum applied voltage, Figure 6.11a. Despite increased energy levels, a higher number of cycles for longer wavelengths would produce interference with other reflections, causing unreliable results. To justify the cycle number selection, Figure 6.11b is shown. It indicates that the error in the measured reflection coefficient reduces with increased number of cycles. However beyond 5 cycles the reduction in error is negligible. Therefore 5 cycles were chosen as an ideal number as it offered lower measurement error and a cycle count that could be kept constant across all frequencies. Finally, 4 volts were utilised as the maximum peak to peak energy offered by the PicoScope.

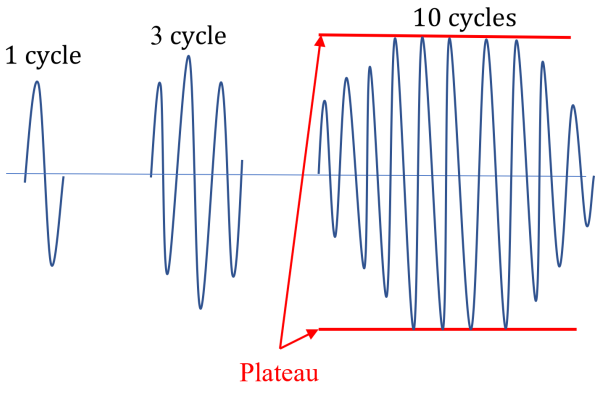

(a) Waveform energy with increased number of cycles.

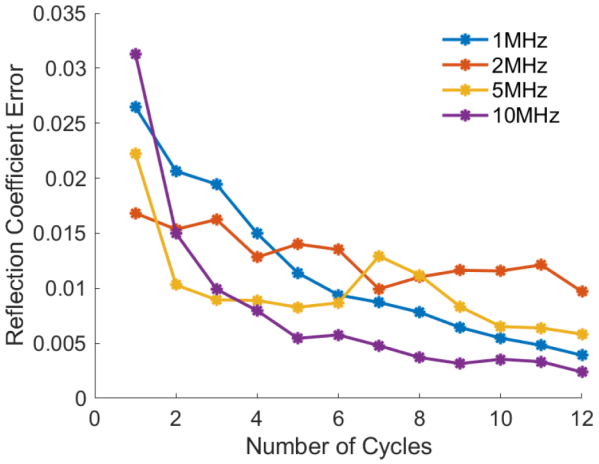

(b) Reflection coefficient error with the waveform number of cycles for 1, 2, 5 and 10 MHz, [16].

Figure 6.11: Selection of the number of cycles for the ultrasonic waveform.

6.5 Signal Processing

Once raw signals were obtained using the PicoScope, a combination of LabVIEW and MATLAB were used to manipulate the data in the following steps. The MATLAB script used to obtain the reflection coefficient from a raw time domain signal can be found in Appendix C.

1. Time domain signal reading - The raw signal data was captured and opened in MATLAB ready for manipulation.
2. Signal averaging - The received ultrasonic signal is shown in Figure 6.12, which illustrates the initial pulse, first and second reflection, and interference. An excess of 100 captures were taken of the signal, which was chosen due to maximising noise reduction, the low memory requirement and the processing times.

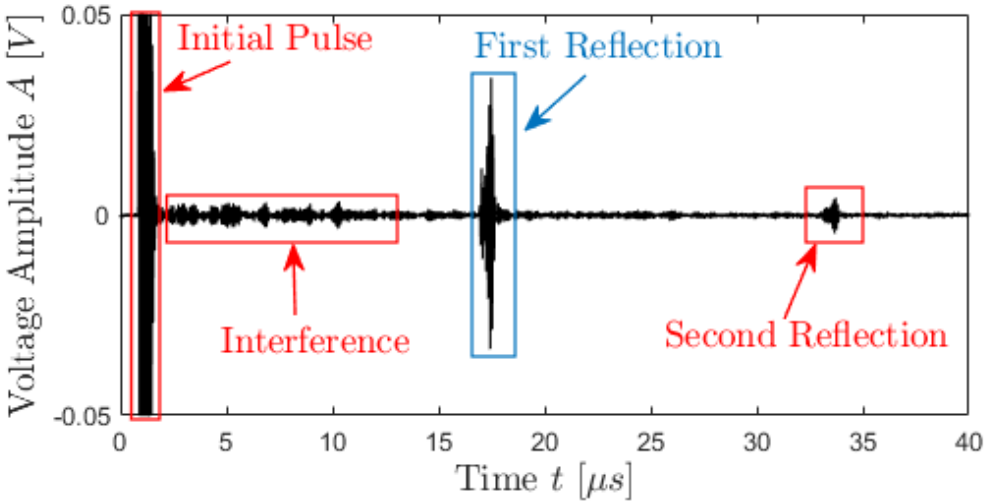

Figure 6.12: Averaged full time domain signal using a 10 MHz sensor on the ultrasonic viscometer.

3. Trim signal - The full time domain signal was then trimmed to focus on the first reflection, Figure 6.13. The first reflection was chosen because it was subject to the least amount of interference. Completing this was necessary to provide frequency components that only correspond to the measurement interface within the signal.

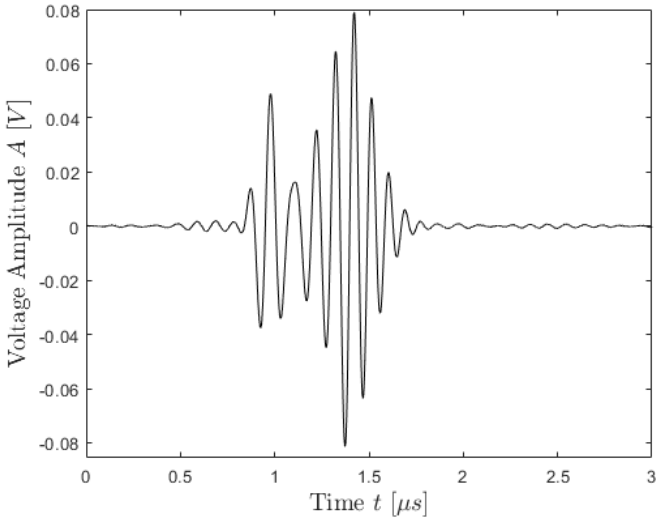

Figure 6.13: The trimmed first reflection from the measurement interface.

4. Zero padding of signal - Zero padding increases the length trimmed signal by adding zero elements, Figure 6.14. Zero padding is a widely used signal processing method, as it makes the length of the time domain equal to the power of two. Thus speeding up processing times and increasing the resolution of the FFT by reducing the spacing of the FFT bins.

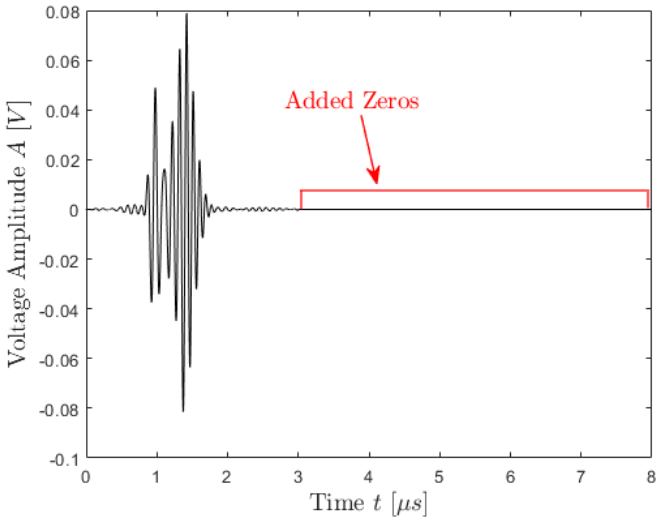

Figure 6.14: Zero padding added to the trimmed first reflection.

5. FFT - A Fast Fourier Transform was used to convert the time domain signal into the frequency domain, Figure 6.15. This showed the energy amplitude of the reflection

in terms of its frequency components, which displayed key features, as discussed in Section 3.7.2.

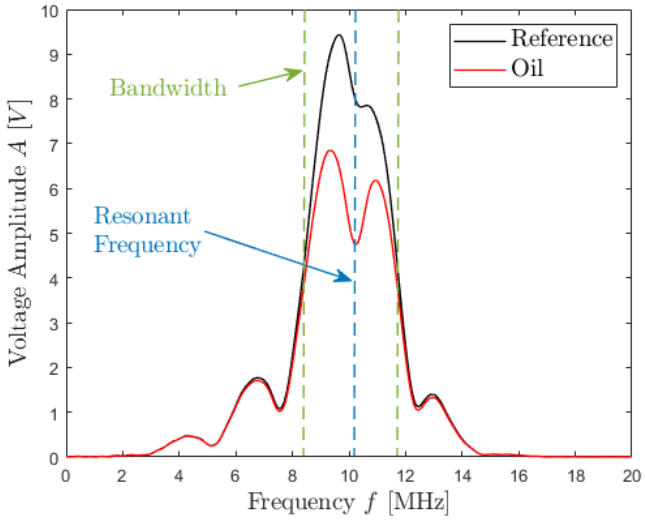

Figure 6.15: Signal FFT amplitude in the frequency domain.

6. Reflection coefficient - To obtain the reflection coefficient, all steps (1-5) up to this point had to be completed with an air reference and an oil measurement. The reflection coefficient was then found by dividing the oil FFT signal by the air reference FFT signal, Figure 6.16.

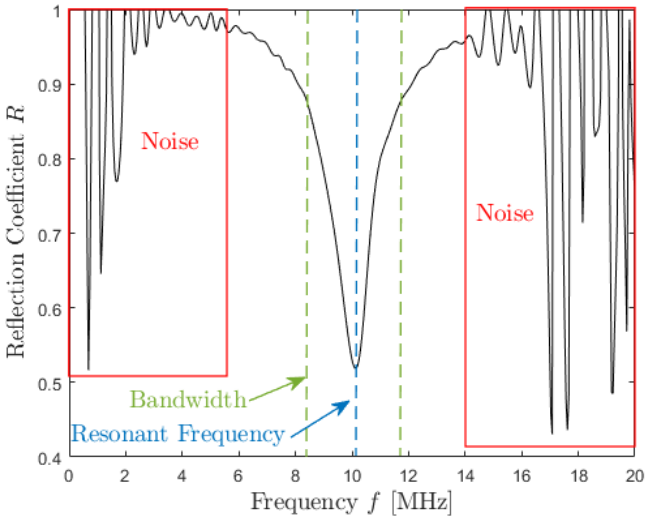

Figure 6.16: Reflection coefficient with respect to the frequency.

Step 6 provides a simple overview for obtaining the reflection coefficient. However once

this step is completed, interpretation of the reflection data requires both Figure 6.15 and 6.16. Within the bandwidth of the transducer, the amplitude energy is high and therefore is not as affected by noise. Hence there is a clearly defined dip at the resonant frequency in Figure 6.16. Energy at frequencies outside the bandwidth are more affected by noise and thus show random, unpredictable fluctuations in the reflection coefficient.

Selecting a frequency for a singular value of the reflection coefficient has been under investigation. Schirru and Brenchley [14, 16] successfully selected reflection coefficient values at the centre frequency of the sensor. The benefit of this was a high signal to noise ratio. However, Franco [156] investigated a further two methods consisting of averaging over a frequency band and integral ratio in a frequency band, where the band was equal to 3 dB. Franco found that the amount of variation in reflection coefficient values decreased as the signal amplitude to noise ratio was improved. Thus indicating that the first method conducted by Schirru and Brenchley was supported further. Throughout this chapter, the reflection coefficient was indexed at the peak resonant frequency of the sensor, which similarly offered a high signal to noise ratio, Figure 6.17. Table 6.5 illustrates the indexed frequencies used for each transducer to obtain the reflection coefficient. It is important to note that this indexed resonant frequency is the actual frequency of each transducer shown in Table 6.4.

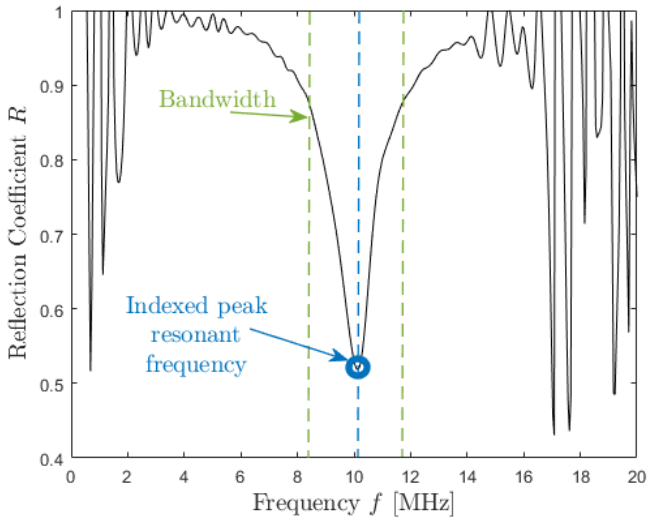

Figure 6.17: Indexed reflection coefficient with respect to the frequency, where the indexed frequency for each transducer is shown in Table 6.5.

Table 6.5: Indexed frequency values to obtain the reflection coefficient for each transducer. The indexed frequency is the same as the resonant frequency shown in Table 6.4.

	Transducer Name			
	2 MHz	3 MHz	10 MHz	14 MHz
Indexed frequency (MHz)	1.79	2.98	10.1	13.86

6.6 Experimental Protocol

Using the ultrasonic viscometer to measure the viscosity of a fluid, the following protocol was used and repeated 5 times for each fluid under investigation. These 5 repeats were to indicate any error in the system, not to reduce signal noise, as that was reduced by taking 100 captures.

- All measurements were taken between 23-23.5$°C$ temperature, as minor fluctuations in temperature can distort results between reference and oil measurements. For extra temperature control, the set-up was placed inside an insulated oven.
- The ultrasonic viscometer was cleaned using Isopropanol, paying particular attention to the measurement interface on the matching layer corresponding to the sensor in use.
- A reference measurement was taken with just air at the interface, which is essential for obtaining the reflection coefficient.
- An oil was then added to the interface using a pipette and allowed to equalise to 23$°C$. If this oil was a mixture, the fluid was mixed using controlled shear rupturing methods at around 1000rpm for 20 seconds. This ensured a smaller droplet size and an evenly distributed emulsion and suspension before applying the sample to the measurement interface.

6.7 Evaluation with Calibration Oils

Preliminary measurements with calibration oils were used to evaluate the ultrasonic models created in Chapter 5. This is a vital step to obtain models for predicting the viscosity as it allows material parameter manipulation which were caused by minute differences in the development of the ultrasonic viscometer. The fluid samples used were all Newtonian hydrocarbon oils, which were certified by the NIST (National Institute of Standards and Technology), Table 6.6. These oils were ideal for validating the models as they are provided with detailed information on their properties; namely the viscosity and density at a large range of temperatures. The following lower viscosity oils were selected as samples that would provide measured data around the viscosity of the coolant under investigation.

Table 6.6: Standard calibration oil data from the data sheet, [157, 158].

Standard Oil Name	Density at $23°C$ (kg/m^3)	Dynamic Viscosity at $23°C$ $(mPas)$
Cannon S3	865	3.58
VWR 70	833	16.52
VWR 92	851	32.5
VWR 82	867	76.76
VWR 98	869	118.1
VWR 71	871	236.46

The analytical model, Equation 5.11, is a mathematical equation used to describe changes in viscosity with reflection coefficient for a three layered system. Therefore, the analytical model was used to fit the measured data using the MATLAB Curve Fitting application. To input this model into the MATLAB application, Equation 5.18 was used with as many defined variables as possible, such as solid impedance and fluid density. This therefore left the matching layer impedance variable, which is an accurate assumption for this set-up due to this layer being bonded between two defined material properties. Equation 5.11 was also used to fit the numerical data where an expected perfect agreement was achieved, $R^2 = 1$. These two models were then plotted, Figure 6.18, with measured data, comparing reflection coefficient with the data sheet viscosity from Table 6.6. Figure 6.18 shows how the analytical and numerical model align with measured data for each

transducer, where their resonant frequencies are shown in Table 6.4. It is evident from Figure 6.18 that the material property values, supplied by the data sheet, for the variable matching layer required adjusting in order to provide a better agreement. However, it was necessary to understand which factors could impact the discrepancy between measured and predicted in such as way, so that appropriate changes could be made.

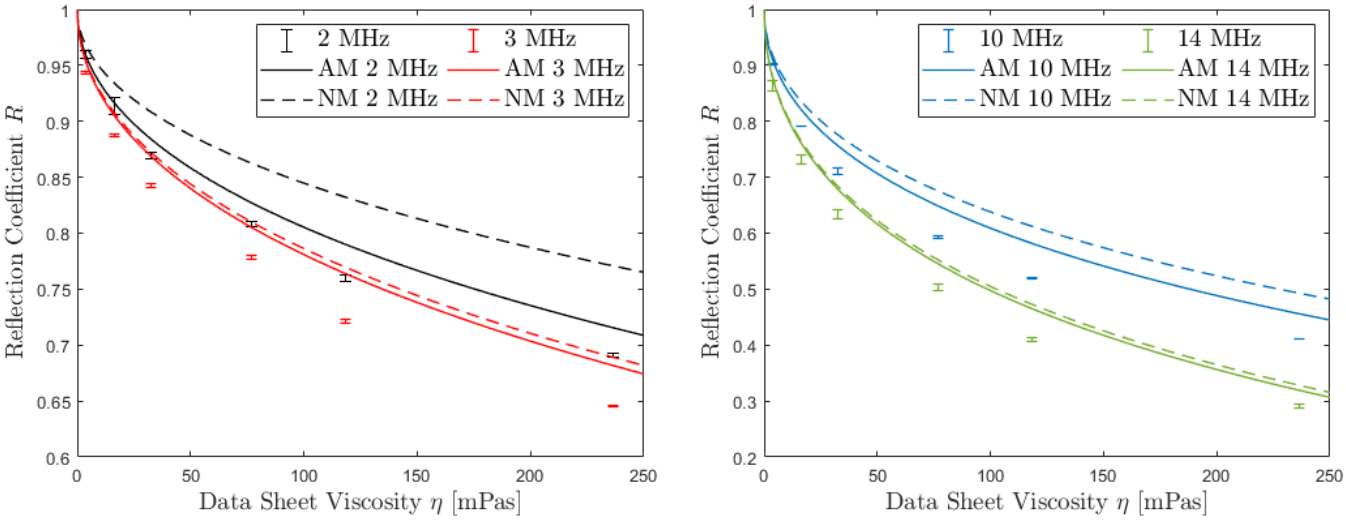

(a) 2 MHz and 3 MHz results for the viscosity models (b) 10 MHz and 14 MHz results for the viscosity models

Figure 6.18: Untuned evaluation of the analytical (Equation 5.18) and numerical viscosity models with measured data from the standard oils shown in Table 6.6.

Manfredi, [17], and Brenchley, [16], highlighted the importance of varying material parameters when evaluating the analytical model with measured data. Furthermore, they reported disparities between measured data and the analytical model which were caused by each individual sensor. These variations arose from instrumentation, for example, using adhesive to bond the matching layer on to the aluminium, which could vary slightly in thickness on each application. This manifested a requirement to optimise current impedance values for the matching layer in order to acquire more accurate model predictions. In Manfredi's and Brenchley's work, they referred to this as tuning.

6.7.1 Model Tuning

Firstly, tuning was required in order to obtain an accurate viscosity value for each reflection coefficient measurement. It does not indicate a lack of agreement between the model and experiments but rather it indicates an unaccountable change between the set-up and model by adding the adhesive. In a practical application, tuning could be considered to be a calibration step in the measurement procedure.

To execute tuning, the reflection coefficient from the analytical and numerical model for a single oil (Cannon S3) was made equal to the measured reflection coefficient data. This was done by manipulating the acoustic impedance of the matching layer for both models until an agreement was reached. The acoustic impedance value for each frequency was noted in Table 6.7. Also, as there was no relationship between viscosity and density, both models assumed that the density was constant for all the fluids. The result of tuning is illustrated in Figure 6.19 where both models provided a better agreement with the measured data. The correlation between each model and the measured data is shown in Table 6.8.

Table 6.7: Analytical and numerical untuned and tuned materials impedance values used to fit the data in Figures 6.18 and 6.19.

Material Parameters	Untuned	Tuned			
		2 MHz	3 MHz	10 MHz	14 MHz
Aluminium acoustic impedance ($MRayl$)	8.37	8.37	8.37	8.37	8.37
Polyimide acoustic impedance ($MRayl$)	1.5	1.45	1.52	1.52	1.42
Oil density (kg/m^3)	859	800	800	800	800

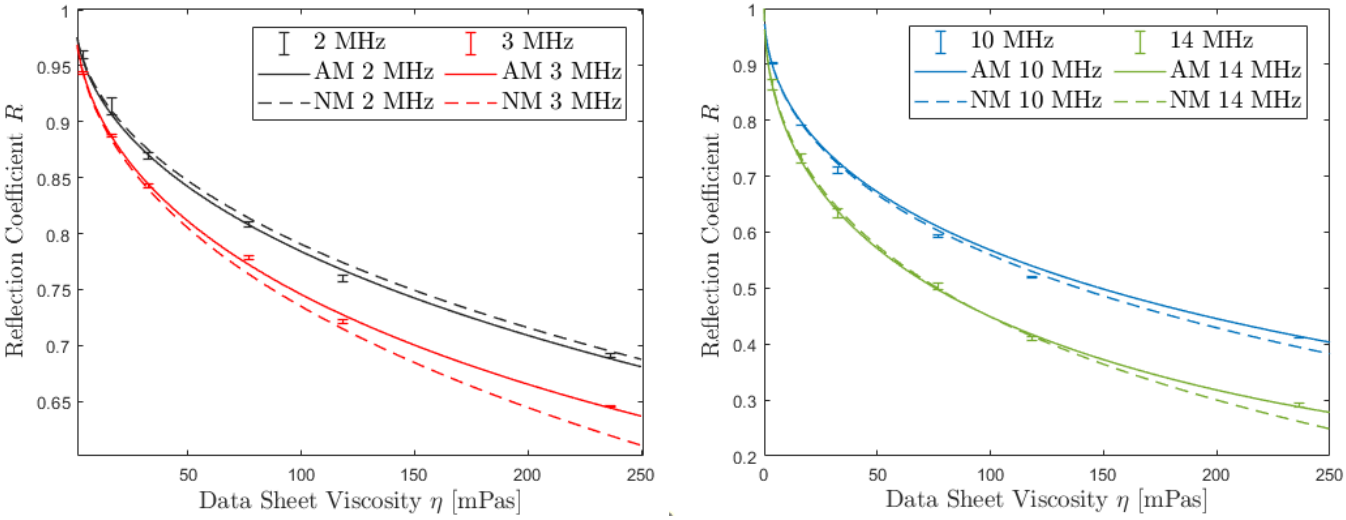

(a) 2 MHz and 3 MHz results for the viscosity models (b) 10 MHz and 14 MHz results for the viscosity models

Figure 6.19: Tuned evaluation of the analytical (Equation 5.18) and numerical viscosity models with measured data from the standard oils shown in Table 6.6.

Table 6.8: Correlation coefficients for both the analytical and numerical model with respect to measured data.

Transducer Name	R^2	
	Analytical	Numerical
2 MHz	0.999	0.997
3 MHz	0.997	0.954
10 MHz	0.999	0.949
14 MHz	0.999	0.955

A good correlation is shown for each transducer between the analytical and numerical model with experimental data. This is confirmed by the R^2 value in Table 6.8. Once tuning was completed the models were set up to predict the value of an unknown viscosity oil. This was done by measuring the reflection coefficient of an unknown viscosity oil and feeding it back into both models to obtain a viscosity value.

6.8 Conclusion

The practical measurement methodology of ultrasonic viscometry was chronologically explained. This methodology will be used to measure the viscosity changes due to contam-

ination in a dielectric coolant in the following chapter. To clarify the signal processing procedure in order to obtain the viscosity of an unknown oil, Figure 6.20 is presented. Finally, to end this chapter, the subsequent conclusions were made:

- An outline of the matching layer viscometer and all the apparatus, including the ultrasonic viscometer, matching layers, transducers and instrumentation, were documented and justified in detail.
- Systematic representation of the test procedure and experimental protocol were created in order to complete measurements.
- For each transducer different signal excitation settings were created that offered the most effective way to produce clear resonance and the actual resonant frequency.
- The signal processing required to obtain the reflection coefficient was explained in chronological stages.
- Calibration oils were utilised in order to evaluate the analytical and numerical model with measured data.
  - For each transducer, both models were tuned to increase the correlation between measured and predicted data.
  - The analytical and numerical model showed an R^2 above 94% for all fits, illustrating good correlation.

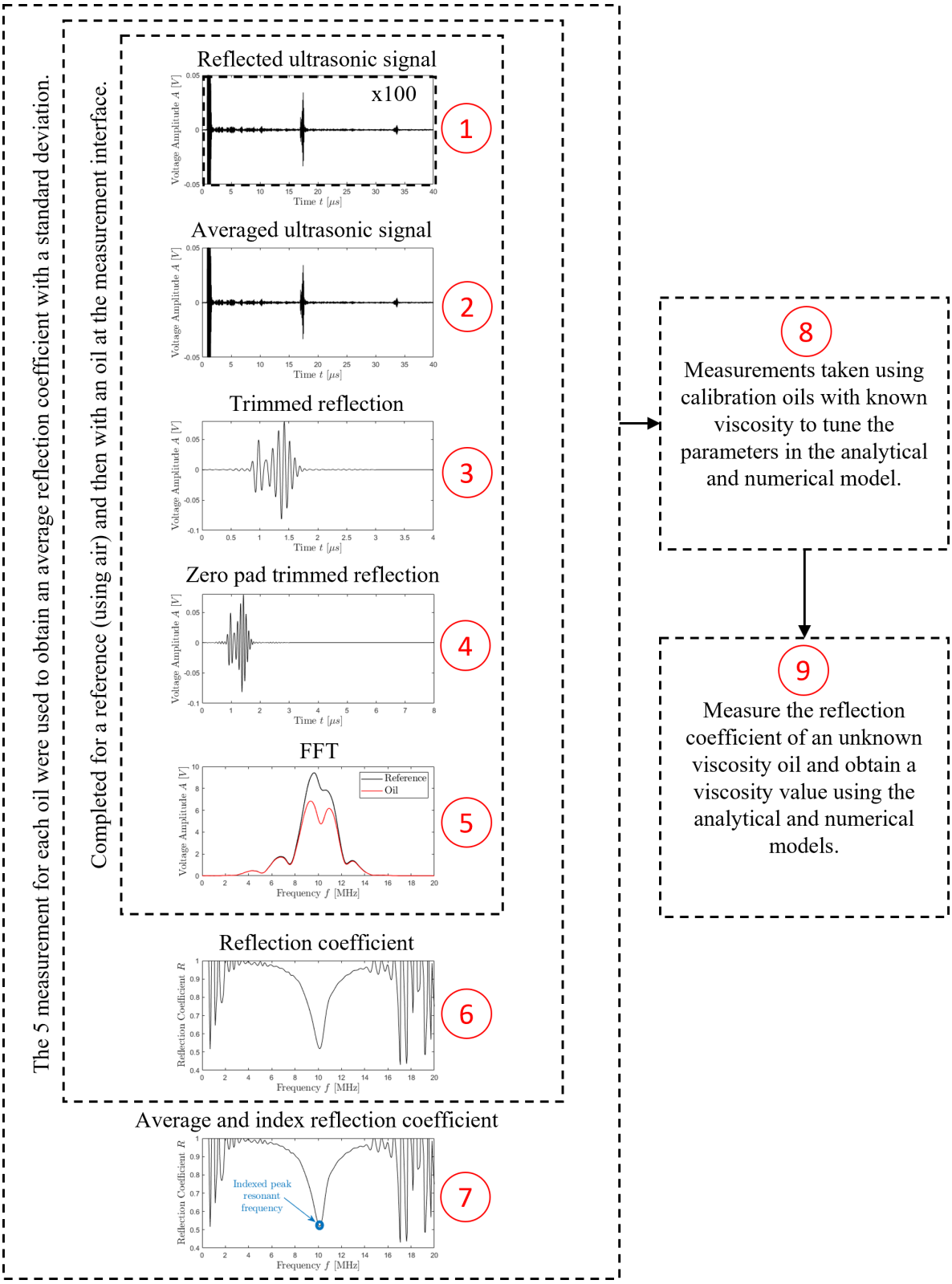

Figure 6.20: Flow chart overview of the signal processing steps required to obtain a functioning ultrasonic viscometer.

Chapter 7

Ultrasonic Shear Viscometry to Detect Contamination

This chapter outlines the practical measurement of ultrasonic viscometry in order to measure viscosity changes caused by contamination in a dielectric coolant. Firstly, the ultrasonic transducers were used to measure the viscosity of the pure coolant fluid and a comparison was made with conventional viscometer tests conducted in Chapter 4. The coolant was then artificially contaminated using distilled water and copper. An evaluation was then made on the measured ultrasonic viscosity and how this compares with viscometer data. Finally the applied shear rate was calculated and the flow behaviour of each fluid was observed in order to determine the negative impact contamination has on their dielectric and cooling properties. As previously discussed, flow behaviour changes, especially as a Newtonian fluids becomes non-Newtonian, can indicate degradation and therefore the dielectric and cooling properties are negatively influenced.

7.1 Introduction

The dielectric fluid samples under investigation in this thesis were highlighted in detail in Chapter 4. The apparent viscosity values measured using conventional shear rotation method, accompanied by the predicted viscosity from Section 4.6, are re-shown in Table 7.1. The coolant mixtures consisted of 3, 10 and 20 % fractions of distilled water droplets, and 0.1, 0.5 and 1 % fractions of copper particles.

For each coolant mixture, measurements were carried out using the method outlined in Chapter 6, which utilised a range of frequency transducers that were indexed at frequencies shown in Table 6.5. For clarification, unless otherwise stated the results shown in this

chapter were all obtained at $23°C$. This temperature was maintained using an insulated oven. To simplify explanations, measured ultrasonic viscosity was referred to as MUV and measured rheometer viscosity was referred to as MRV.

Table 7.1: Low shear rate viscosity of pure coolant with varying fractions of contamination, where the rheometer viscosity was measured in Chapter 4, and the predicted viscosity was calculated using Equation 2.23, 2.25 and 2.24.

Oil		Rheometer Viscosity at $23°C$ $(mPas)$	Predicted Viscosity at $23°C$ $(mPas)$
Pure Coolant		6.01	6.01
Water	3 %	6.78	6.42
	10 %	6.87	7.89
	20 %	7.11	10.95
Copper	0.1 %	5.74	6.03
	0.5 %	6.21	6.09
	1 %	6.6	6.16

7.2 Evaluation of Pure Coolant

In order to evaluate the pure coolant Figure 7.1 was produced. The MUV data was compared with the MRV data to observe any discrepancies between conventional and ultrasonic methods with regards to the mean and percentage deviation.

Figure 7.1a shows the mean values of the MUV for each transducer, using the tuned analytical and numerical model. These values are compared against the pure coolant rheometer viscosity. The same is done in Figure 7.1b, however as the analytical and numerical models had the same percentage deviation, only one bar for each transducer is required.

The pure coolant MUV was in good agreement with the MRV for both 2 and 3 MHz. Although, for higher frequencies such as 10 and 14 MHz, the MUV was lower than the MRV. This indicated that at high ultrasonic frequency oscillations, the coolant was exhibiting shear thinning behaviour. This type of non-Newtonian behaviour at very high frequencies has been shown by Borras, [159], and Franco, [160] and will be outlined in detail in the discussion section. However, as the coolant showed Newtonian behaviour across rheometer measurements found in Chapter 4 and the lower frequency transducers,

the sudden decrease at high frequencies could be a transition zone from one Newtonian plateau to another. Overall there was an insignificant difference between the analytical and numerical models. However the analytical model was favoured as it had a much better correlation across all transducer calibration plots, Figure 6.19.

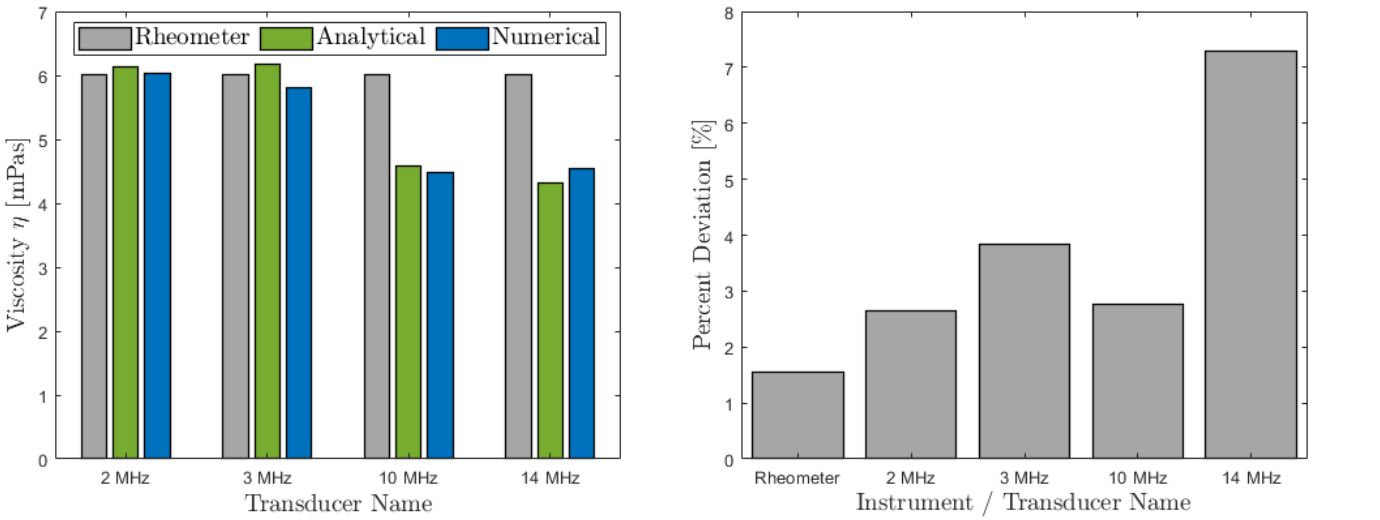

(a) Mean values of the MUV and MRV.

(b) MUV and MRV percentage deviation from the mean.

Figure 7.1: Viscosity mean and percentage deviation values of the pure coolant using conventional and ultrasonic viscometry. Figure 7.1a includes the analytical and numerical models compared with the rheometer data for each transducer name. Figure 7.1b compares the percentage deviation of ultrasound and rheometer measurements, where the deviation of the analytical and numerical models are equal.

With regards to Figure 7.1b, the deviation of the MUV was not as low as the MRV deviation, though it was less than 4 % if the 14 MHz transducer is ignored. The larger deviation of the 14 MHz transducer was due to the method in which the indexed resonant dip is created, discussed in Section 6.2.3 and the near field range. By not creating resonance at the centre frequency and not allowing the wave to properly construct, there is more deviation in the viscosity measurement as the signal to noise ratio is reduced.

7.3 Evaluation of the Effect of Water Contamination

A different approach was considered to evaluate the effects on viscosity with varying degrees of water contamination. Figure 7.2 shows this approach, where the viscosity is

compared with the dispersed phase volume fraction, and the MUV data from the analytical and numerical models are plotted with the MRV for each individual transducer.

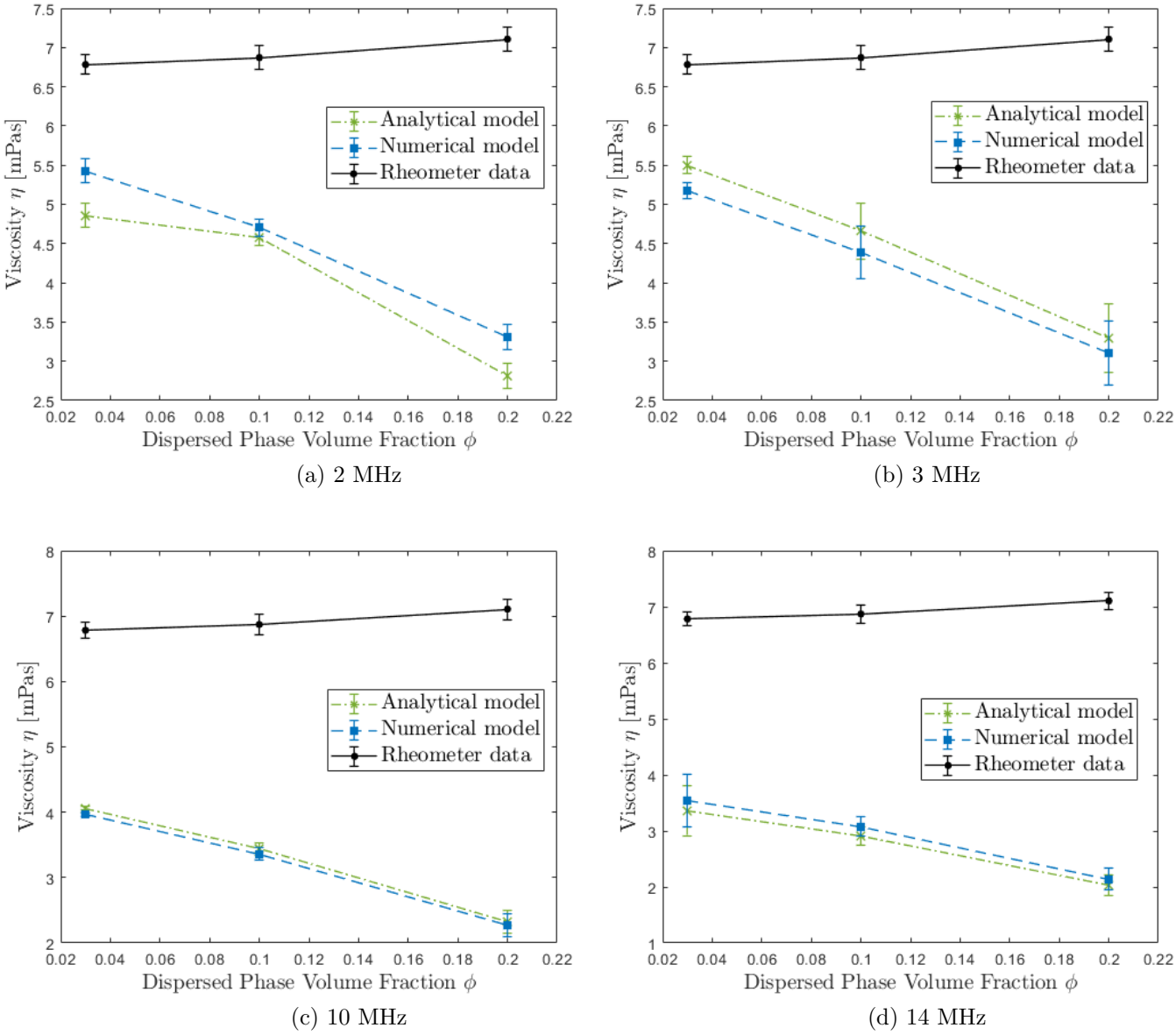

(a) 2 MHz

(b) 3 MHz

(c) 10 MHz

(d) 14 MHz

Figure 7.2: Water contaminated viscosity comparison between conventional and ultrasonic viscometry for each individual transducer. The black coloured plot is the rheometer data, the green plot is the analytical model and the blue plot is the numerical model.

Using Figure 7.2, the MUV of water contaminated mixtures were clearly lower than that recorded in the MRV, for all volume fractions and transducers. The MRV increases with increasing dispersed phase volume, however for MUV it is evident that there is a decrease

with increasing water content. Here MRV remains true to the theory presented in Chapter 2, as with increased water contamination, the viscosity of the complete mixture should also increase. This is the result of distorted flow caused by droplets that hydrodynamically interact with each other as droplets aggregate. However, it was shown in Chapter 4 that increasing water content produced shear thinning behaviour, which was displayed by the n value in Equation 2.13. As the MUV is recorded at higher shear rates, it could be resulting in a lower apparent viscosity. This behaviour was similarly reported by Franco, [160], when measuring the viscosity of presumed Newtonian SAE oils. Franco's conclusions were that the oils were behaving in a non-Newtonian manor, as described by Maxwell's model. There the BP oil testing in this thesis could well be non-Newtonian at higher frequencies.

In contrast, the ultrasonic viscometer measures the fluid mixtures over a small area, Table 6.3, in comparison to the rheometer, which measures an area of 2827.43 mm^2. Thus potential uncertainty around MUV data is raised, especially as higher frequency results for pure coolant also showed a decrease in MUV. This could be overcome by using many ultrasonic transducers, however this was out of the scope of this research.

Identically to the evaluation of pure coolant, the behavioural differences between the analytical and numerical viscosity with dispersed volume fraction were minimal.

7.4 Evaluation of the Effect of Copper Contamination

Similarly to studying the effects of water contamination, the same approach was considered to evaluate the effects on viscosity with varying degrees of copper contamination, Figure 7.3. For 2 and 3 MHz transducers, MUV was consistently greater than MRV, and followed a similar increasing trend with dispersed phase volume fraction, Figures 7.3a and 7.3b. This correlation between MUV and MRV was closer than those seen for water contamination, which could be due to the low quantities of copper contamination. However as seen before for both pure and water contaminated coolant, the higher frequency 10 and 14 MHz transducers presented viscosity values lower than MRV. When considering the amount of deviation for all transducers, the disparity between the amount of contamination was not

clear. However, the MUV data with dispersed phase volume shows an increasing trend that closely follows that of the MRV.

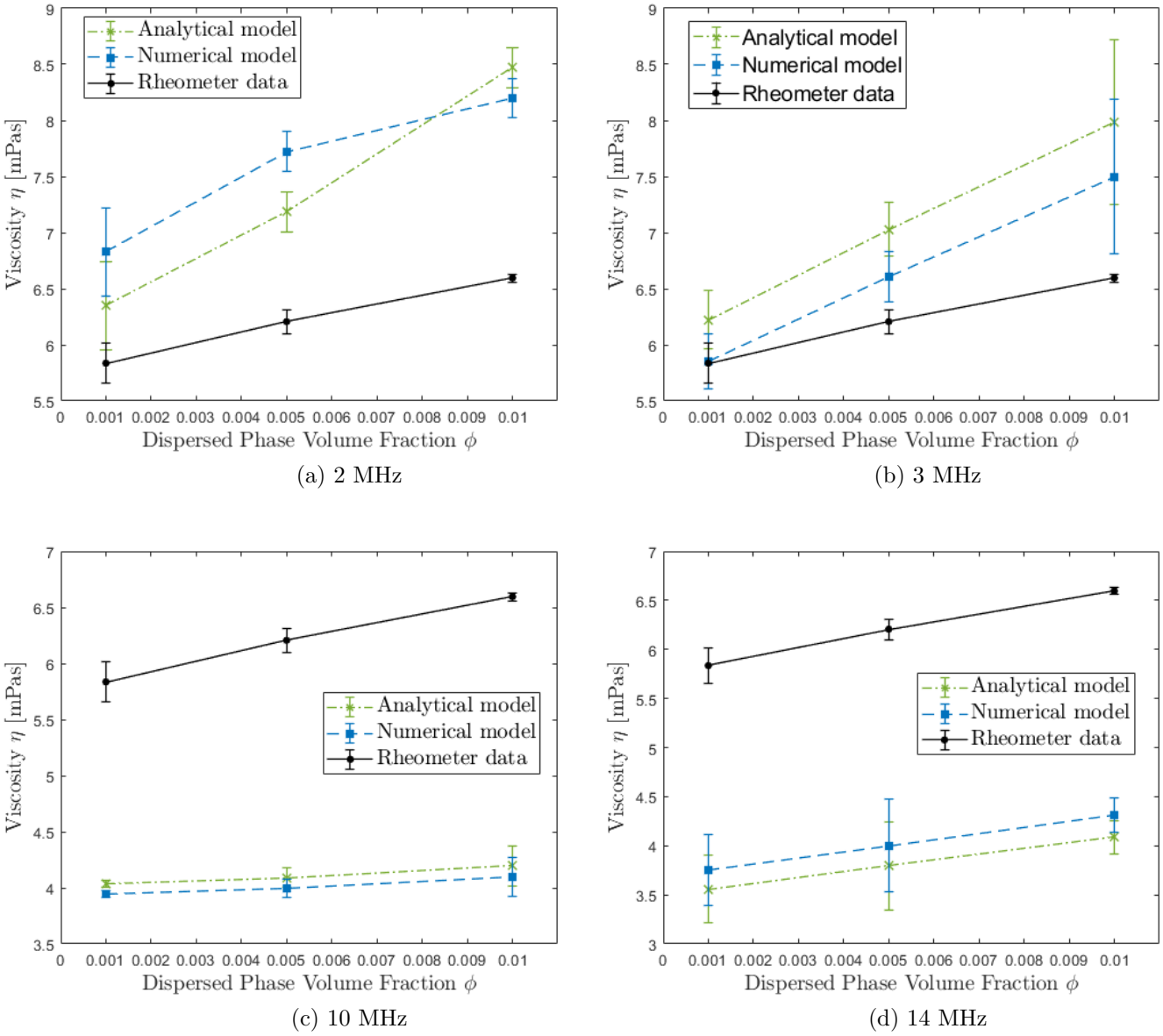

(a) 2 MHz

(b) 3 MHz

(c) 10 MHz

(d) 14 MHz

Figure 7.3: Copper contaminated viscosity comparison between conventional and ultrasonic viscometry for each individual transducer. The black coloured plot is the rheometer data, the green plot is the analytical model and the blue plot is the numerical model.

It is evident that the continuous phase dictates the MUV of the sparsely contaminated copper mixtures, where lower frequencies are similar to MRV and higher frequencies are lower then the MRV.

It was mentioned in Section 7.3 that uncertainty around the ultrasonic viscometer's measurement area size, and whether a true viscosity value regarding the bulk mixture is obtained. This is expanded upon in detail in the discussion part, Section 7.6.

The analytical and numerical models both predicted similar MUV for all the previously discussed fluid samples. Therefore only the analytical model is considered in the following sections, as it provided a better correlation value with the calibration oils, Figure 6.19.

7.5 Shear Rate Effects on the Flow Behaviour

After inspecting Figures 7.1, 7.2 and 7.3, it was suspected that the pure coolant and mixture samples was exhibiting shear thinning behaviour at high shear rates. To properly investigate this, viscosity was graphed against the measured frequency for each sample and is shown in Figure 7.4. The MUV data shown with corresponding frequency further illustrates how distinguishable the effect that contamination content had on the viscosity of each fluid sample tested. For water contamination there is a clearly distinguished decrease in viscosity with increasing dispersed phase volume from a pure coolant, which appears to be decreasing with increasing measurement frequency. For copper contamination there is a similar decreasing viscosity trend with frequency. However, the order at 2 and 3 MHz is completely reversed at 10 and 14 MHz transducer frequencies.

The reason Figure 7.4 maintains the measured transducer frequency and does not display shear rate was due to the invalid nature of the Cox-Merz rule, Equation 2.7, for this type of viscometer. This was explained in Section 3.9.5, hence to illustrate the viscosity in terms of shear rate, further steps are required. As a result it is difficult to draw conclusions around the potential shear thinning behaviour and other flow characteristics.

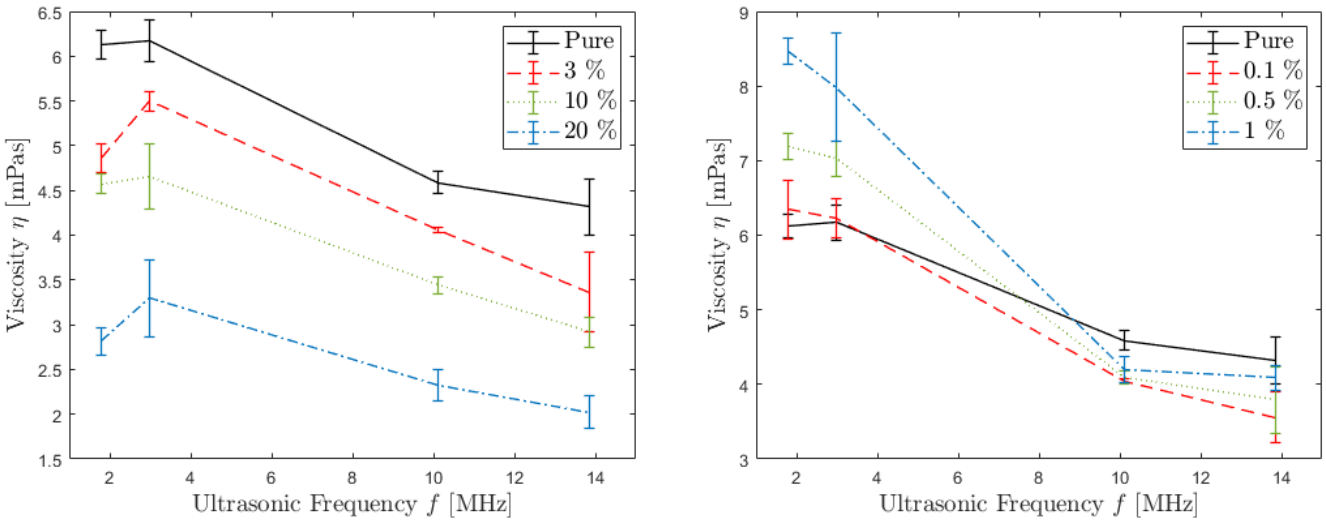

(a) Water contamination.

(b) Copper contamination.

Figure 7.4: Ultrasonic viscosity data with measured frequency for water and copper contaminated mixtures compared with the pure coolant.

7.5.1 Calculating Shear Rate

Measuring the velocity in order to calculate the shear rate applied to a fluid using ultrasonic shear waves was discussed previously in Section 3.9.5. To obtain the true shear rate within the fluid, the relationship shown in Equation 3.24 and 3.25 and are reproduced here for the readers convenience, Equation 7.1 and 7.2. These equations were derived from Stoke's second problem and they are extensively explained in Brenchley, [16].

$$U_t = \frac{Z_1}{Z_3} U_i \left(R + 1\right) \tag{7.1}$$

$$\dot{\gamma} = U_t \sqrt{\frac{\omega}{\nu}} \tag{7.2}$$

Excluding the velocities U_i and U_t, all the variables in Equation 7.1 and 7.2 were already known or had been previously measured, with regards to the coolant and contaminated mixtures:

- The impedance of the incident layer, Z_1, was 8.37 $MRayl$ from Table 6.7.

- The reflection coefficient had been measured.
- Using Equation 5.17, the impedance of the fluid layer, Z_3, was calculated using a known density value (800 kg/m^3 from the tuned material parameters in Table 6.7) and the measured dynamic viscosities.
- The kinematic viscosity, ν, of 8.392 mm^2/s was obtained at 23°C using Equation 2.5 from the values shown in Table 4.1.
- The angular frequency was calculated using the indexed frequencies for each transducer, Table 6.5.

A sketch is shown in Figure 7.5, which highlights the shear wave incident, transmitted and reflected paths. It also shows the incident wave velocity, U_i, and the transmitted wave velocity inside the fluid, U_t. The incident wave velocity occurs inside the incident layer at the very edge of the measurement interface, where it then transmits into the fluid layer.

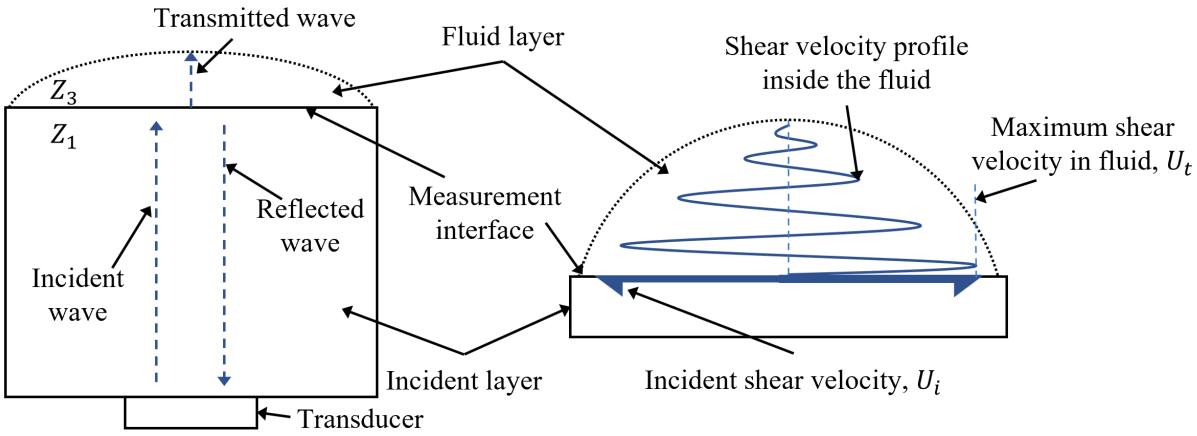

Figure 7.5: Sketch of the ultrasonic wave path and velocity considered by Equation 7.1 and 7.2.

Brenchley, [16], measured the velocity of shear waves at the aluminium interface for 1 and 2 MHz, utilising the same ultrasonic viscometer rig shown in this work. This data was shown previously in Figure 3.32a and is reproduced in Figure 7.6a with an equation for each linear fit, Equation 7.3.

$$U_i^{1MHz} = 4.968e^{-5}x + 1.587e^{-3} \qquad U_i^{2MHz} = 7.728e^{-5}x + 3e^{-3} \tag{7.3}$$

These equations enabled extrapolation to find a value for the incident wave velocity that strikes the measurement interface, U_i, at 4 volts. Thus Figure 7.6b is obtained. Assuming that the behaviour of the incident velocity with frequency is linear, Equation 7.4 was produced that allowed extrapolation to find the incident wave velocity at the frequencies used in this research, Table 6.5.

$$U_i = 1.523e^{-9}x + 2.623e^{-4} \tag{7.4}$$

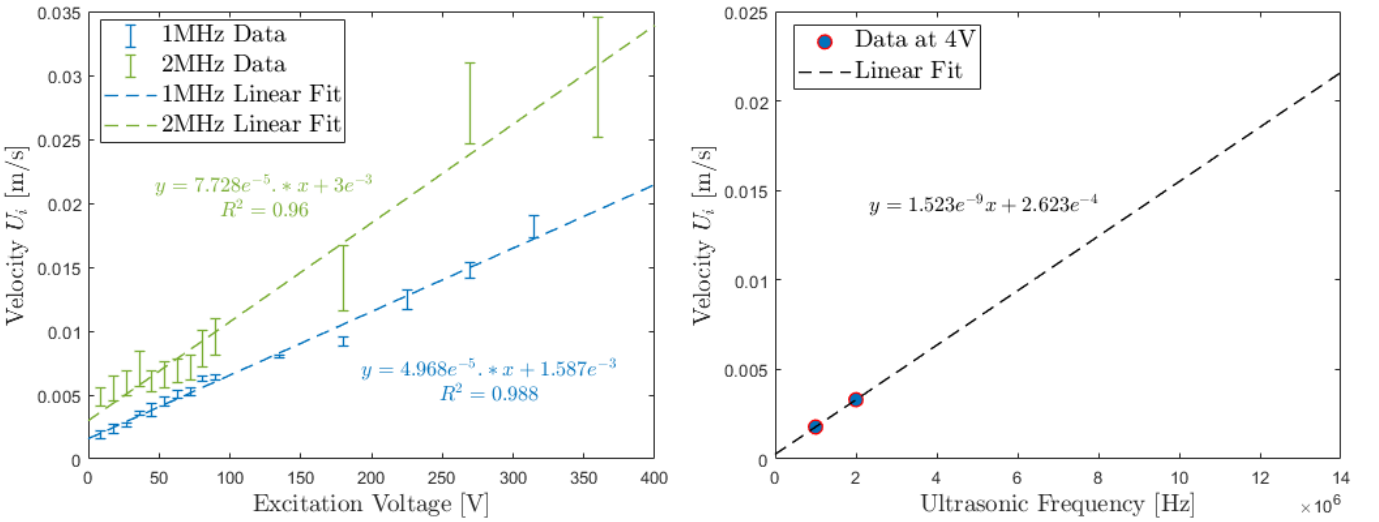

(a) Brenchley's data for 1 and 2 MHz.

(b) Extrapolated velocity with frequency at 4 volts.

Figure 7.6: Extrapolating Branchley's, [16], incident velocity with voltage data to obtain velocity values for the frequencies used in this work.

The transmitted wave velocity, U_t, was then calculated using U_i, which lead to a shear rate value for each tested fluid using a different transducer frequency. The method for calculating the shear rate is summarised as a flow chart in Figure 7.7.

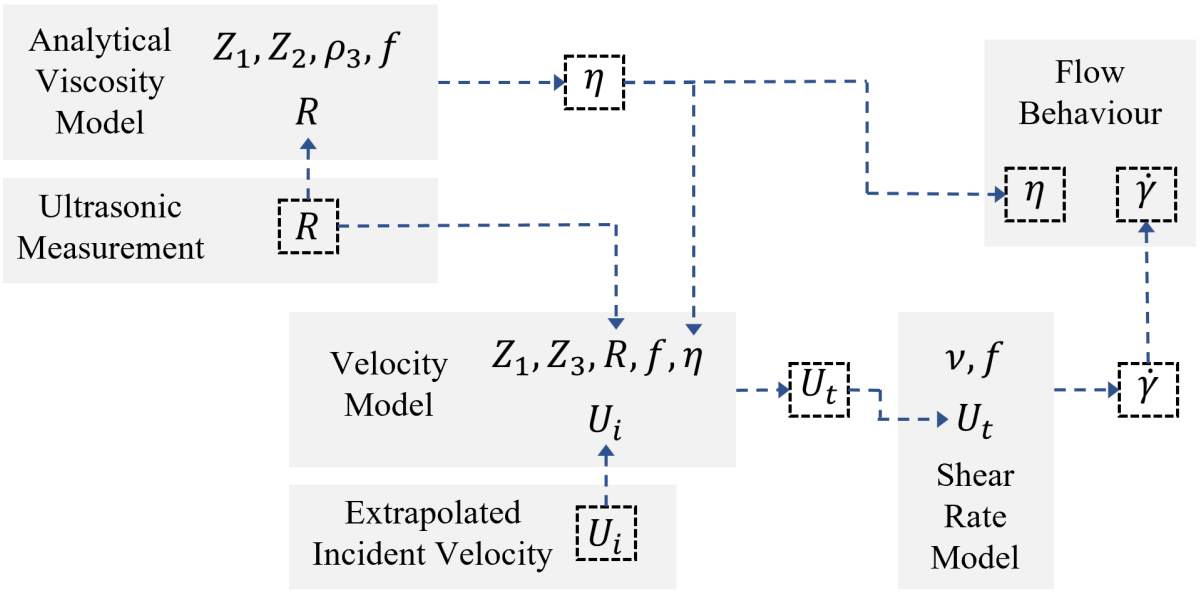

Figure 7.7: Reading from left to right: A flow diagram showing the method for calculating the shear rate. The analytical viscosity model uses Equation 5.11, the velocity model uses Equation 7.1 and the shear rate model uses Equation 7.2.

To illustrate the differences, Figure 7.4 was reproduced in Figure 7.8 to show the measured ultrasonic viscosity with the applied ultrasonic shear rate. Due to the shear rate calculation being dependent on the measured reflection coefficient, viscosity and frequency, the calculated shear rate is therefore different for each transducer and fluid sample. It is evident from Figure 7.8a that the applied shear rate from each transducer increases with increasing dispersed phase volume, whereas in Figure 7.8b, this is reversed. Hence it is obvious that the larger the calculated shear rate, the smaller the MUV. The calculated shear rate, for each fluid sample using each transducer, is shown in Table 7.2.

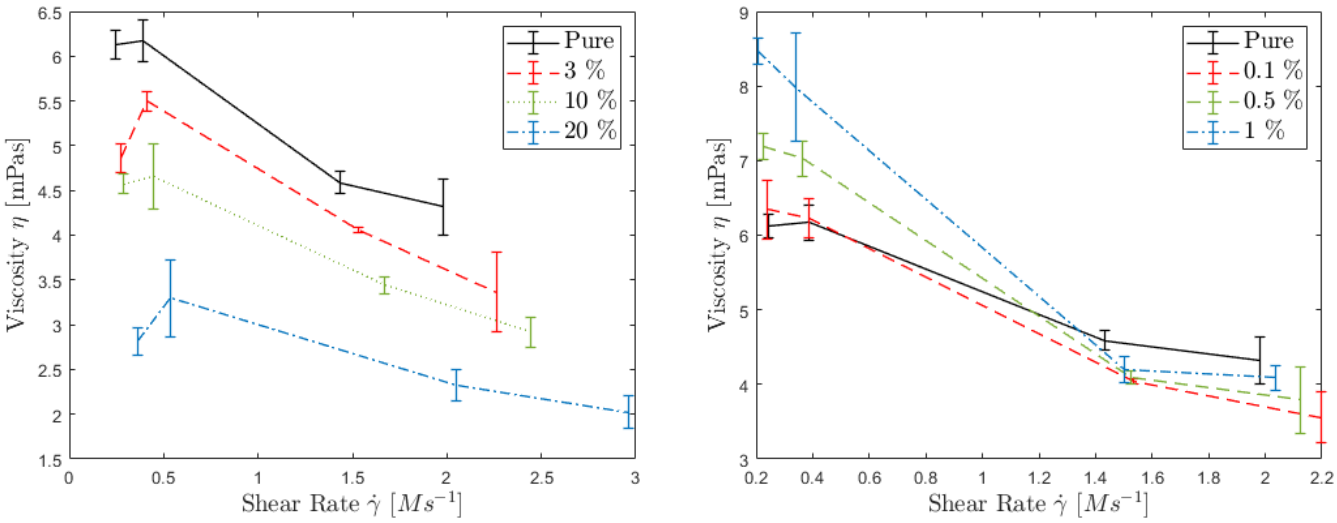

(a) Water contamination.

(b) Copper contamination.

Figure 7.8: Ultrasonic viscosity data with calculated shear rate for water and copper contaminated mixtures compared with the pure coolant.

Table 7.2: Calculated shear rate, in ks^{-1}, for each fluid sample with each transducer.

	Pure	Water Contamination			Copper Contamination		
		3 %	10 %	20 %	0.1 %	0.5 %	1 %
2 MHz	244.8	274.9	283.6	363.8	239.8	224.9	207.2
3 MHz	387.8	411.5	448.3	535.7	385.9	362.4	339.2
10 MHz	1434.1	1529.7	1668.5	2048.9	1534.2	1523.9	1503.5
14 MHz	1980.5	2263.9	2442.1	2961.0	2195.7	2121.9	2038.5

7.5.2 Evaluating the Flow Behaviour

The calculations made to find the shear rate applied to each fluid at different frequencies allows ultrasonic oscillatory shear measurements to be graphed with conventional steady state shear, Figure 7.9. This allows the flow behaviour of each fluid sample to be properly assessed, as previous figures have only compared MUV and MRV values with dispersed phase volume. Nevertheless in previous figures it was suspected that all fluid samples were shear thinning, hence the study in this section should highlight this behaviour. Figure 7.9 shows the relationship between the MUV and shear rate. This was fitted using the Carreau-Yasuda model, Equation 2.14, which was able to describe shear thinning in emulsions and

suspensions, [161]. The constants of the Carreau-Yasuda fit were generated using the MATLAB Curve Fitting application and were noted in Table 7.3 for each fluid sample.

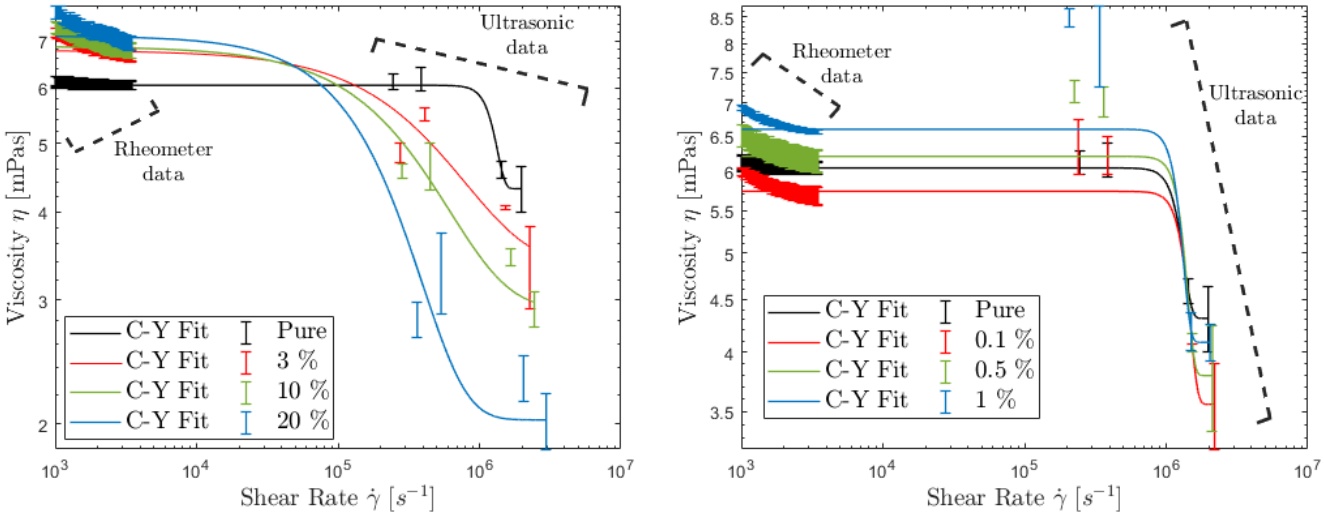

(a) Water contamination.

(b) Copper contamination.

Figure 7.9: Flow behaviour of pure and contaminated fluid samples, where data from conventional methods for obtaining viscosity is plotted with the corresponding ultrasonic viscosity, over the applied shear rate. The Carreau-Yasuda model (Equation 2.14) was used to fit each sample data set and the values for these fits are presented in Table 7.3.

Table 7.3: Carreau-Yasuda model (Equation 2.14) constants used to create fits shown in Figure 7.9.

	Pure	Water Contamination			Copper Contamination		
		3 %	10 %	20 %	0.1 %	0.5 %	1 %
α	1.021	0.837	0.698	1.159	0.886	0.917	1.034
λ	0.2E-6	0.2E-6	0.2E-6	0.2E-6	0.2E-6	0.2E-6	0.2E-6
n	1	0.438	0.994	0.564	0.472	0.759	0.593
η_∞	4.246	3.364	2.915	2.164	3.556	3.781	4.055
η_0	6.05	6.78	6.87	7.11	5.74	6.21	6.6
R^2	0.93	0.91	0.94	0.95	0.9	0.89	0.9

Both Figure 7.9 and Table 7.3 convey a previously observed decrease in viscosity from a low to high shear rate (observing constants η_0 and η_∞). The flow behaviour of the pure coolant, predicted by the Carreau-Yasuda model, appears to be Newtonian up to a shear rate of around 0.7 Ms^{-1}, at which point shear thinning occurs. The high correlation of the Carreau-Yasuda fit indicates this is a shear thinning transition zone between one

Newtonian plateau to another, as reported in Section 2.3.1.5. Furthermore, mixtures containing the coolant as the continuous phase are therefore highly dominated by the pure coolant flow behaviour. This is evident when observing the MUV of water and copper contaminated fluid samples.

Considering Figure 7.9a, the severity of the shear thinning behaviour increased with increasing fractions of contamination. This is indicative of droplet size changes, as discussed in Section 2.8.3. When the water contaminated fluid sample is applied to the measurement interface, droplet flocculation and coalescence begins due to Brownian motion effects. However the less contamination, the longer it takes for Brownian motion to coagulate droplets and create flocs. Hence for lower dispersed phase volume fractions where the particle sizes remain smaller for longer, the amount of movement from a random flow to a more ordered flow is met with a higher resistance. The cause of this resistance is due to the motion of the continuous phase having to do more work to flow in between each individual particle. In addition, once flow lines are properly created, alignment is achieved and the appearance of shear thinning is observed.

With regards to Figure 7.9b, copper particles were all around 50 μm in size and so any resistance to flow alignment due to particle size was not a major impacting factor. Also as the contamination is so low, it is difficult to distinguish between pure coolant and contaminated fluids. At low shear rates measured by the 2 and 3 MHz transducer, an increase in viscosity with dispersed phase volume is apparent. This is most likely the result of a larger measurement area, as there is a higher probability that the ultrasound will be affected by more copper particles in the coolant. At high shear rates the measurement area was smaller and so copper particles could potentially be out of range. Despite these observations, it was evident that the pure coolant continuous phase dictated the behaviour of the copper contaminated mixtures. Hence the sensitivity of the MUV was not significant enough to clearly detect contamination changes, especially at high frequencies where the measurement area was reduced.

7.6 Discussion

The MUV produced distinguishable data for the water contaminated mixtures but found difficulties when measuring the changes with copper contamination. This is potentially the result of a number of impacting factors in the way ultrasound measures viscosity. It was mentioned that this is due to the greater variation in copper and water contamination tested in this thesis, as copper mixtures were all dilute and water mixtures ranged from semi-dilute to concentrated. This is supported by literature such as Mueller, [89]. Similarly supported by literature is the MUV being lower than the MRV. Borras and Franco, [159, 160], both illustrate how different oils, which were assumed to be Newtonian at low shear rates, became non-Newtonian at a higher shear rate. However, only Franco used ultrasound to measure viscosity here. Franco's conclusion was that MUV relies on the reflected energy, which is dominated by the elastic effect, which do not match the MRV. Manfredi, [162], illustrated similar findings but did not elaborate on a cause. Furthermore, the MRV behaviour appeared to conform to findings done in other viscosity research of emulsions, such as Wong, Broboana, Aomari and Farah, [163, 164, 165, 166], although a specific magnitude comparison is difficult to make due to dissimilar oils.

Ultrasonic shear waves at the frequencies tested in this work measure the viscosity over a relatively small area in comparison to conventional rheometry. However, there are other important factors such as the penetration depth and the acoustic wavelength. The sizes of these parameters have an impact on the ability to measure particles or droplets of a set or varying size. Figure 7.10 shows the measurement diameter, penetration depth, wavelength and the sizes of the water and copper particles.

As the ultrasonic frequency increases, the shorter the wavelength and penetration depth become. Therefore shorter wavelength high frequencies are attenuated more easily, as a finer mesh of particles/atoms have a greater diminishing effect on the energy. Hence a shorter penetration depth inside the fluid.

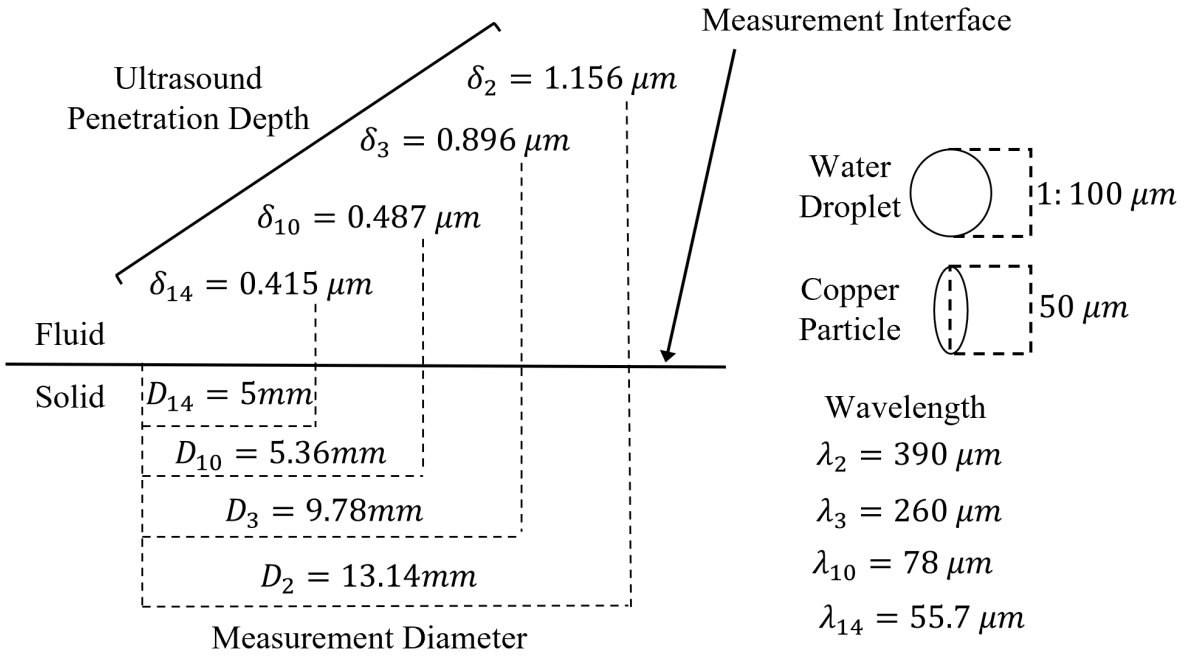

Figure 7.10: Measurement area, wavelength and the propagation depth inside the pure coolant for each transducer indexed frequency, Table 6.5. Subscripts 2, 3, 10 and 14 relate to the frequency of the transducers.

At high the frequency 10 and 14 MHz transducers, where the wavelength (78 and 55.7 μm) is much closer to the sizes of the copper and water, a reduced penetration depth would arise as attenuation increases. However the wavelength of the 2 and 3 MHz transducers (390 and 260 μm) would not have as much of an impact on the penetration depth. While this occurs inside the fluid, it must be highlighted that the measured energy of the reflected ultrasonic waveform is the impedance mismatch between the matching layer and fluid. None of that reflected energy was transferred into the fluid, as the transmitted energy was dissipated over the penetration depth. Therefore, if the contamination was not evenly distributed and droplets were not in contact with the measurement interface, viscosity results would not represent the viscosity of the bulk fluid. Also, this would indicate a viscosity closer to a pure coolant, as shown by the copper suspensions. To illustrate this analogy a sketch of the water droplets and copper particles, with respect to a small section of the measurement area, is shown in Figure 7.11.

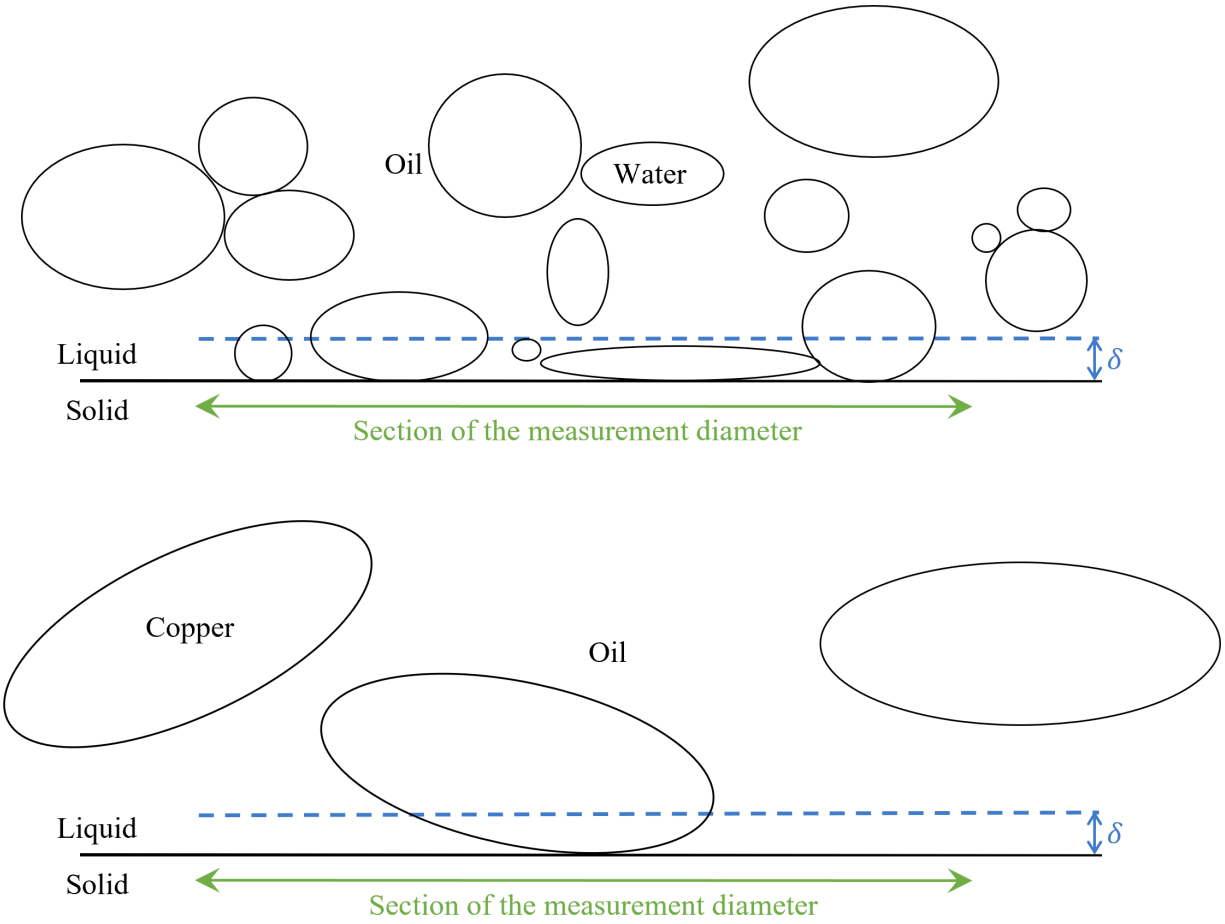

Figure 7.11: Droplets and particles in contact with the measurement interface where the measurement diameter is a small section of the total.

Water flocculation and coalescence created by the breaking of the emulsion could show a viscosity lower than the coolant if the water concentration at the measurement interface was higher than the pure coolant. This would cause local variations in the droplet concentration, which would eventually lead to sedimentation. Although ultrasonic tests were taken over a short time to mitigate the eventual phase separation, there was still uncertainty around the measurement of an evenly distributed fluid mixture. Nevertheless, each water contaminated fluid would behave in a similar manor and attempt to separate to the bottom of the mixture. If ultrasound was only measuring water, the viscosity value would be around 0.9 $mPas$ and the behaviour observed in Figure 7.9a would not be captured.

Uncertainty regarding the Carreau-Yasuda model for water emulsions was also raised. This was due to the MRV similarly showing an increasing shear thinning behaviour with

an increasing dispersed phase volume. This would mean that there would not be a first Newtonian plateau and the viscosity would continually shear thin from the MRV shear rates to the MUV shear rates. However without measuring this behaviour, it cannot be deduced. For MRV this behaviour is also seen for some emulsions in work carried out by Wong and Broboana, [163, 164], however they did not test beyond 1000 s^{-1}.

In a battery cooling system the oil is pumped at a certain velocity, which would result in a more dispersed mixture. This fluid motion could reduce the effects of phase separation. Also at 23°C where the surface tension of water is high, water droplets prefer to reside on surfaces within the cooling system. Therefore using ultrasound to measure the viscosity of a fluid in motion at an increased temperature could result in viscosity value better represented by the effects of contamination.

The rheometers ability to measure the bulk of the fluid would ensure the viscosity is measured by the increased resistance caused by contamination. Hence for the 60 mm plate rheometer a larger sample size is measured with the added mixing effect to stop water and copper particles from aggregating. Some studies have attempted to conduct high shear rate measurements using rheometers such as Bair, Zadorozhnaya and Borras, [167, 168, 159]. However, their findings were similar to that seen in this thesis, with the added complexity of creating a high shear rate rheometer. Despite ultrasound measurements being simple to implement, it was predicted to offer better sensitivity to measure the effects of minute changes throughout a test fluid. However in reality, the sensitivity of the MUV did not appear to be better than conventional viscometers as originally suspected, due to the methods in which the ultrasonic viscometer is calibrated. Firstly, it is calibrated using a wide range of viscosities, where most of the viscosities are much higher than the coolants viscosity. If the calibration oils had viscosities more evenly distributed around that of the coolant, a more accurate measurement could be achieved. Furthermore, the ultrasonic viscometer could be better optimised to measure lower viscosity fluids by increasing the frequency of the sensors or selecting a different matching layer material with an impedance value that better matches lower viscosity fluids, as discussed in Section 6.2.2.

Although MUV changes in such low amounts of copper contamination were not clear, using ultrasonic spectroscopy methods to analyse and the effects of more than 3 % con-

tamination for an emulsion were clearly distinguishable. This behaviour was also true without calculating for the shear rate, which could be questioned in terms of its accuracy.

The shear rate calculation uses Stoke's second problem and extrapolates from measured data obtained by Brenchley, [16]. When extrapolating, there is always degrees of uncertainty, especially using data measured in other work. Furthermore the assumption that there is a linear fit for the incident wave velocity and frequency had to be made as only two values were available. It is also reliant on kinematic viscosity, which in theory would change with increasing contamination. Finally it measures the velocity at the aluminium interface and not the polyimide matching layer, as that was not reflective enough for measurements using the laser vibrometer in Brenchleys work, [16]. Nevertheless a reasonable value was calculated to illustrate the effects of the ultrasonic shear rate, despite it requiring a more in depth investigation before it can be accurately predicted with this method.

It was mentioned previously in this section how measurement area, penetration depth, and wavelength all have an effect on how the fluid is sheared by the ultrasound. However displacement caused by shear motion has not been mentioned, as this is not very well understood in ultrasonic viscometery. The shear displacement amplitude may be equal to or smaller than the particle/droplet size, whereas the displacement produced by conventional shear motion is by orders of magnitude larger than the particle/droplet size. Therefore further research is required to understand more about the displacement caused by ultrasonic shear waves.

7.7 Conclusion

Ultrasonic viscometry was used to measure the viscosity changes due to contamination in a dielectric coolant and the following conclusions were made:

- The viscosity of the pure coolant fluid showed Newtonian behaviour at low ultrasonic frequencies that aligned well with conventional viscometer results. Although at high shear rates the MUV was much lower, indicating shear thinning, which was later confirmed in the flow behaviour study.

- The viscosity changes with the addition of copper had little effect on the viscosity as its flow behaviour followed that of the pure coolant. This was due to such low fractions of contamination. The changes that were seen were more distinguished at lower ultrasonic frequencies, which was because of a larger ultrasonic measurement area.

- Water contamination showed distinguishable viscosity data with increasing dispersed phase volume across all frequencies. Concerns were raised about how evenly dispersed the water was inside the oil at the measurement interface. However the results were indicative of the findings in Chapter 2, where the viscosity appeared to shear thin more drastically with an increasing shear rate.

- For water mixtures, the 10 MHz transducer was by far the greater measurement as it provided clear changes in viscosity, while maintaining a low amount of deviation. Nevertheless, the benefits of ultrasonic spectroscopy allows viscosity to be visualised as its flow behaviour changes.

- A reasonable value for the applied ultrasonic shear rate was calculated to illustrate the effects that high frequency ultrasound had on the fluid sample. Still, the measured ultrasonic shear rate requires more in-depth research for this method to be conducted with less uncertainty.

- The analytical and numerical models provided similar viscosity readings and both were considered good prediction tools. However as the analytical model was used to fit the data directly, the correlation was higher and therefore was considered the more accurate model.

Chapter 8

Conclusion

This research thesis utilised the three layered ultrasonic viscometer, developed by Schirru, [15], in a novel application: to monitor the health of a dielectric battery coolant with regards to the viscosity changes caused by degradation. The key findings of the research conducted in this thesis are presented:

- In an attempt to link theoretical models, calculations were made using Equations 4.3, 4.4, and 4.5. However they did not correlate well with measured data due to their lack of consideration for viscosity varying with shear rate.
- The feasibility of using shear viscosity to measure contamination in a dielectric coolant appeared capable. However, he apparent error illustrated issues with sensitivity when distinguishing between contamination fractions.
- Interpreting measured ultrasonic data is challenging without understanding the physical aspects of acoustic wave motion throughout varying mediums. Therefore an analytical and numerical model were developed in order to link theory with the practical experiment. This allowed predictions of the reflection coefficient with varying viscosity fluids using a three layered ultrasonic viscometer.
- Both models highlighted that the sensitivity was dependant upon the thickness of the intermediate layer and the applied frequency, and could be manipulated to increase sensitivity of viscosity measurements. They also provided an insight into the physical interaction of an ultrasonic shear wave with varying fluid viscosity in a three layered system. The exact solution provided by the analytical model was used as a fitting tool for the numerical model and for the calibration of real acquired data.

- Calibration oils were utilised in order to evaluate the analytical and numerical model with measured data, and showed a good correlation of above 94% for all fits. This allowed the ultrasonic viscometer to measure the viscosity of the coolant mixture samples, with the approval of two theoretical models.

- The measured ultrasonic viscosity of the pure coolant fluid showed Newtonian behaviour at low frequencies that aligned well with conventional viscometer results. However at high frequencies the viscosity was much lower, which appeared as shear thinning behaviour between two Newtonian plateaus. A similar shear thinning behaviour between high and low ultrasonic measurements were also seen in contaminated fluids, which further supported the proposed shear thinning behaviour.

- With the addition of copper there was little effect on the viscosity, which was due to such low fractions of contamination. However, this small amount of copper was indicative of the maximum amount found in actual degraded dielectric coolants.

- Water contamination showed distinguishable viscosity data with increasing dispersed phase volume across all frequencies. The results did not match the conventional rheometer data but they did illustrate shear thinning, which appeared more drastic with an increasing shear rate. However their dispersed phase volumes were higher and represented moisture contamination amounts found in insulation cellulose.

- Based on the ultrasonic viscosity results, shear transducers show the potential to be used to measure the condition of battery coolants similar to the fluid tested in this thesis. A combination of low and high frequencies can provide viscosity results similar to conventional methods and at shear rates potentially within a transition zone.

- Finally, it was a promising investigation as to whether water and copper could be detected in a dielectric oil based on their impact on viscosity. However it is more important to be able to measure the viscosity effects that these contaminants have as catalysts to oxidation and degradation as a whole. As degradation is unique to its environment, it is necessary to utilise the three layered viscometer in-situ.

8.1 Further Directions

The further directions following on from this research are highlighted in the following points. There is a greater focus on the in-situ aspect as it was the final objective of this research work before the unfortunate effects of the COVID-19 pandemic. Therefore the further work regarding in-situ testing is discussed in Section 8.1.1.

- Using the ultrasonic frequencies in this thesis, a new matching layer material could be explored in order to increase the amount of energy transmitted into low viscosity fluids. Alternatively, higher frequencies beyond 13.86 MHz could also be used to achieve a similar result.

- A wider range of ultrasonic frequencies could better highlight the Newtonian plateau seen in the pure coolant. Similarly, lower frequency transducers and higher shear rate rotational viscometers could better illustrate the shear thinning behaviour of emulsions. This could be beneficial to the food industry where the rheology of emulsions and suspensions is important.

- The numerical model could be adapted to provide reflection coefficient values with a closer correlation to measured values. This could be achieved by considering material and transducer geometry constraints, material attenuation effects, the fluids behaviour with an applied shear wave, and extra material layers created using epoxy for bonding.

- Further work is required to measure the true shear rate of different frequency transducers using the three layered viscometer. This will lead to an improved relationship between the shear velocity, frequency, and excitation voltage. Hence a more accurate calculation for the shear rate can be made.

- Research is required to understand how a fluid reacts to an ultrasonic shear wave and whether that energy inside the fluid can be analysed. Furthermore the displacement caused by the shear wave requires further investigation into its magnitude and how that measures against contamination and viscosity modifiers.

- In this research only the Newtonian model was considered, however there are non-Newtonian models. Unfortunately, previous research assumed small relaxation times, [15, 16]. Therefore if relaxation times could be measured for each fluid, there could be a higher potential to measure more accurate data.

- Testing more representative fluids would also be a very good direction. Having access to a, or multiple battery coolant test rigs, or a an electric vehicle dedicated to producing used battery fluids would give the project a stronger case, as to whether the condition could be measured using ultrasound.

- Finally the ultrasonic viscometer discussed in this thesis could help other industries by saving a lot of costs. In the food, chemical and cosmetic industries, viscosity is used for quality control and predicting the behaviour of products for customer usage. Knowing the viscosity, the production process can be optimised effectively to reduce costs. Ultrasonic sensors could be incorporated into this process to monitor the viscosity in-line. As an example, coatings, paints and inks could make use of an in-line viscometer to greatly reduce quality issues.

8.1.1 Ultrasonic Measurement in a Battery Coolant System

Ultrasonic measurement has been previously installed in-situ a journal bearing, [15], and a marine diesel lubricant injector line, [17] with promising results. While this thesis showed similarly promising results ex-situ, a repertoire of consequential data could have been achieved by monitoring viscosity changes on a battery cooling system over an extended period.

There is also the investigation into other battery coolants, as the one tested in this thesis was just one of at least 4 under investigation by BP. Many factors influence the viscosity measurement in-situ such as pressure, temperature, contamination, and degradation due to oxidation. In fact oxidation has been shown to increase the viscosity of the bulk fluid and consequently could be consistently measured by ultrasound. In-situ data acquisition is therefore the first step as a future direction before any other modifications are made.

The development of two ultrasonic viscosity sensor blocks for two different battery cooling systems were produced, where one of the systems was pressurised. An example of the sensor block that would have been installed on a battery cooling test rig is shown in Appendix D. This could potentially be used in future studies to determine the ultrasound's ability to track the condition of electrical cooling fluids.

Bibliography

[1] J. Colato and L. Ice, "Charging into the future: the transition to electric vehicles," Avaliable at: https://www.bls.gov/opub/btn/volume-12/charging-into-the-future-the-transition-to-electric-vehicles.htm#:~:text=Ready%20to%20charge%20into%20the,to%204.6%20percent%20in%202021., (Accessed: 01/03/2023), 2023.

[2] EERE, "Emissions from electric vehicles," Avaliable at: https://afdc.energy.gov/vehicles/electric_emissions.html, (Accessed: 01/03/2023), 2023.

[3] D. W. Sundin and S. Sponholtz, "Thermal management of li-ion batteries with single-phase liquid immersion cooling," Engineering Fluids Whitepaper, 2019.

[4] D. Chen, J. Jiang, G.-H. Kim, C. Yang, and A. Pesaran, "Comparison of different cooling methods for lithium ion battery cells," *Applied Thermal Engineering*, vol. 94, pp. 846–854, 2016.

[5] Energsoft, "Energsoft blog about ai and batteries: Battery prices dropped again," Avaliable at: https://energsoft.com/blog/f/battery-prices-dropped-again, (Accessed: 08/01/2022), 2019.

[6] Midel, "All about ester fluids," Avaliable at: https://www.midel.com/blog/about-esters/, (Accessed: 10/12/2021), 2018.

[7] Future Bridge, "Immersion cooling – potential alternative to traditional battery cooling," Avaliable at: https://www.futurebridge.com/industry/perspectives-mobility/immersion-cooling-potential-alternative-to-traditional-battery-cooling/, (Accessed: 08/01/2022), 2022.

[8] X. Zhu, C. Zhong, and J. Zhe, "Lubricating oil conditioning sensors for online machine health monitoring – A review," *Tribology International*, vol. 109, pp. 473–484, 2017.

[9] J. Zhu, D. He, and E. Bechhoefer, "Survey of Lubrication Oil Condition Monitoring, Diagnostics, and Prognostics Techniques and Systems," *Journal of Chemical Science and Technology*, vol. 2, pp. 100–115, 2013.

[10] A. Agoston, C. Otsch, and B. Jakoby, "Viscosity sensors for engine oil condition monitoring - Application and interpretation of results," *Sensors and Actuators, A: Physical*, vol. 121, no. 2, pp. 327–332, 2005.

[11] Capitol Toyota, "4 things to know about oil life monitors on modern vehicles," Avaliable at: https://www.captoyota.com/service/information/oil-life-monitoring-systems.htm, (Accessed: 01/03/2023), 2021.

[12] The Inside Track, "Oil life monitors – everything you need to know," Avaliable at: https://blog.amsoil.com/oil-life-monitors-everything-you-need-to-know/, (Accessed: 01/03/2023), 2020.

[13] M. Ales, "Oil life monitoring systems: Your car is keeping tabs," Avaliable at: https://columbiatireauto.com/oil-life-monitoring-system-your-car-is-keeping-tabs/#:~:text=Enter%20the%20oil%20life%20monitoring,to%20skip%20an%20oil%20change., (Accessed: 01/03/2023), 2020.

[14] M. Schirru, "Development of an Ultrasonic Sensing Technique to Measure Lubricant Viscosity in Engine Journal Bearing In-Situ," Ph.D. dissertation, Sheffield, UK, 2016.

[15] M. Schirru and R. S. Dwyer-Joyce, "A model for the reflection of shear ultrasonic waves at a thin liquid film and its application to viscometry in a journal bearing," *Journal of Engineering Tribology*, vol. 230, pp. 667–679, 2015.

[16] T. Brenchley, "Viscosity measurements using a multiple frequency matching layer viscometer," Ph.D. dissertation, Sheffield, UK, 2021.

[17] O. Manfredi, "The Development of an Ultrasonic Standing Wave Method to Measure Liquid Viscosity," Ph.D. dissertation, Sheffield, UK, 2019.

[18] G. Tyreas, "Measuring lubricant viscosity at a surface and in a bearing film using shear-horizontal surface acoustic waves," Ph.D. dissertation, Sheffield, UK, 2020.

[19] D. Wooton, "Oxidation - the lubricant's nemesis," Avaliable at: https://www.machinerylubrication.com/Read/1028/oxidation-lubricant, (Accessed: 15/12/2021), 2020.

[20] Fluitec, "Can transformer oils oxidize?" Avaliable at: https://www.fluitec.com/can-transformer-oils-oxidize/, (Accessed: 01/03/2023), 2022.

[21] D. A. Bolliger, "Influence of the Chemical Composition of Dielectric Fluid on Partial Discharge Characteristics for Diagnostic Purposes," Ph.D. dissertation, Connecticut, USA, 2013.

[22] R. Mortier and M. Fox, *Chemistry and Technology of Lubricants*, 3rd ed., S. Orszulik, Ed. London, UK: Springer, 2010.

[23] X. Wang, C. Tang, B. Huang, J. Hao, and G. Chen, "Review of Research Progress on the Electrical Properties and Modification of Mineral Insulating Oils Used in Power Transformers," *Energies*, vol. 11, pp. 2384–2392, 2018.

[24] M. Karthik and N. Narmadhai, "A survey on natural esters based insulating fluid medium for transformer applications," *Elsevier: Materials Today*, 2019.

[25] M. Srivastava, S. K. Goyal, and A. Saraswat, "Ester oil as an alternative to mineral transformer insulating liquid," *Materials Today: Proceedings*, vol. 43, pp. 2850–2854, 2021.

[26] Electrical India, "Transformer oil its evolution," Avaliable at: https://www.electricalindia.in/transformer-oil-its-evolution/, (Accessed: 12/12/2021), 2021.

[27] G. Dombek, P. Goscinski, and Z. Nadolny, "Comparison of mineral oil and esters as cooling liquids in high voltage transformer in aspect of environment protection," *Energy and Fuels*, vol. 14, pp. 2850–2854, 2016.

[28] R. Bartnikas, "The influence of aromatic constituents upon the dielectric losses in oil-impregnated paper insulating systems," *Conference on Electrical Insulation Dielectric Phenomena*, vol. Annual Report 1966, pp. 105–111, 1966.

[29] DSI Ventures Inc, "Dielectric fluids vs mineral oils in electrical cooling applications - part 2: Electrical and fire safety," Avaliable at: https://dsiventures.com/, (Accessed: 12/12/2021), 2017.

[30] G. W. Stachowiak and A. W. Batchelor, *Engineering Tribology*, 3rd ed. New York: Springer, 2005.

[31] Z. D. Wang, A. Darwin, and R. Martin, "Experiences in service with new insulating liquids," *CIGRE*, vol. 436, p. 1–94, 2010.

[32] Noria Corporation, "Lubricant additives - a practical guide," Avaliable at: https://www.machinerylubrication.com/Read/31107/oil-lubricant-additives, (Accessed: 14/12/2021), 2021.

[33] M. C. Bruzzoniti, C. Sarzanini, L. Rivoira, V. Tumiatti, and R. Maina, "Simultaneous determination of five common additives in insulating mineral oils by high-performance liquid chromatography with ultraviolet and coulometric detection," *Separation Science*, vol. 39, p. 2955–2962, 2016.

[34] T. W. Selby, "The Viscosity-Dependent Fuel Efficiency Index for Engine Oils," pp. 13–17, 2002.

[35] Keith Spoonmore, "Dynamic vs. kinematic viscosity: What's the difference?" Avaliable at: https://www.machinerylubrication.com/Read/31591/dynamic-kinematic-viscosity, (Accessed: 08/12/2021), 2021.

[36] ASTM D341-17, "Standard practice for viscosity-temperature charts for liquid petroleum products." Technical report standard, 2017.

[37] H. Vogel, "The law of the relationship between viscosity of liquids and the temperature," *Physikalische Zeitschrift*, vol. 22, pp. 645–646, 1921.

[38] C. Barus, "Isothermals, isopiestics and isometrics relative to viscosity." *American Journal Science*, vol. 45, p. 87–96, 1893.

[39] AntonPaar, "Basics of viscosity and viscometry," Avaliable at: https://wiki.anton-paar.com/uk-en/basic-of-viscometry/, (Accessed: 08/12/2021), 2021.

[40] T. G. Mezger, *Applied Rheology*, 6th ed. Austria: Vincentz Network, 2019.

[41] Malvern Instruments Limited, "A basic introduction to rheology," Whitepaper, 2016.

[42] W. P. Cox and E. H. Merz, "Correlation of dynamic and steady flow viscosities," *Journal of Polymer Science*, vol. 28, p. 619–622, 1958.

[43] M. T. K. Kubo, M. L. Rojas, A. C. Miano, and P. E. D. Augusto, "Chapter 1:Rheological Properties of Tomato Products in Tomato Chemistry, Industrial Processing and Product Development," *Royal Society of Chemistry*, pp. 1–25, 2019.

[44] AntonPaar, "The influence of particles on suspension rheology," Avaliable at: https://wiki.anton-paar.com/uk-en/the-influence-of-particles-on-suspension-rheology/, (Accessed: 20/12/2021), 2021.

[45] ——, "Internal structures of samples and shear-thinning behavior," Avaliable at: https://wiki.anton-paar.com/uk-en/internal-structures-of-samples-and-shear-thinning-behavior/, (Accessed: 20/12/2021), 2021.

[46] R. C. Yasuda, K. Armstrong and R. E. Cohen, "Shear flow properties of concentrated solutions of linear and star branched polystyrenes," *Rheologica Acta*, vol. 20(2), p. 163–178, 1981.

[47] Noria Corporation, "The surface tension test - is it worth resurrecting?" Avaliable at: https://www.machinerylubrication.com/Read/376/surface-tension-test, (Accessed: 15/02/2021), 2021.

[48] Electrical4U, "Transformer oil: Testing, types properties," Avaliable at: https://www.electrical4u.com/transformer-insulating-oil-and-types-of-transformer-oil/, (Accessed: 10/12/2021), 2019.

[49] J. C. Hernandez-Mejia, "Chapter 6: Dissipation factor ($tan\delta$)," Georgia Tech Research Corporation, 2016.

[50] HV Technologies, "Dissipation factor (or power factor) and specific resistivity testing of insulating oils," Avaliable at: https://hvtechnologies.com/dissipation-factor-or-power-factor-and-specific-resistivity-testing-of-insulating-oils/, (Accessed: 11/12/2021), 2019.

[51] ASTM D6304-20, "Standard test method for determination of water in petroleum products, lubricating oils, and additives by coulometric karl fischer titration." Technical report standard, 2021.

[52] D. M. Mehta, P. K. A. Chowdhury, V. K. Lakhiani, and A. S. Jhala, "A Review on Critical Evaluation of Natural Ester vis-a-vis Mineral Oil Insulating Liquid for Use in Transformers: Parts 1 and 2," *IEEE Transactions on Dielectrics and Electrical Insulation*, vol. 23, pp. 873–1712, 2016.

[53] D. S. Viswanath, T. K. Ghosh, D. H. L. Prasad, N. V. K. Dutt, and K. Y. Rani, *Viscosity of Liquids*, 3rd ed. New York: Springer, 2007.

[54] T. A. Instruments, "Hr10 - discovery hybrid rheometer," Avaliable at: https://www.tainstruments.com/hr-10/, (Accessed: 15/10/2021).

[55] T. Chen, "Rheology: Basic theory and applications training," Online training course, 2020.

[56] M. Koch, S. Tenbohlen, J. Blennow, and I. Hoehlein, "Reliability and Improvements of Water Titration by the Karl Fischer Technique," *Chemistry*, vol. 15, pp. 27–32, 2007.

[57] IEC 60156, "Insulating liquids - determination of the breakdown voltage at power frequency - test method," Technical report standard, 2018.

[58] Bennett Fitch - Noria Corporation, "Identifying the stages of oil oxidation," Avaliable at: https://www.machinerylubrication.com/Read/30165/oil-oxidation-stages, (Accessed: 15/12/2021), 2021.

[59] Noria Corporation, "Acid number: A comprehensive guide," Avaliable at: https://www.machinerylubrication.com/Read/1052/acid-number-test, (Accessed: 16/12/2021), 2021.

[60] A. Hamdi, I. Fofana, and M. Djillali, "Stability of mineral oil and oil–ester mixtures under thermal ageing and electrical discharges," *Institution of Engineering and Technology*, vol. 11, pp. 2384–2392, 2017.

[61] Noria Corporation, "How the oxidation rate affects oil change frequency," Avaliable at: https://www.machinerylubrication.com/Read/31454/oil-change-frequency, (Accessed: 15/12/2021), 2021.

[62] ——, "The effects of heat exchangers on oil," Avaliable at: https://www.machinerylubrication.com/Read/29325/heat-exchangers-effects, (Accessed: 16/12/2021), 2021.

[63] Y. Wu, W. Li, M. Zhang, and X. Wang, "Oxidative degradation of synthetic ester and its influence on tribological behavior," *Tribology International*, vol. 64, pp. 16–23, 2013.

[64] D. Clark and E. E. Klaus, "The role of iron and copper in the oxidation degradation of lubricating oils," *Society of Tribologists and Lubrication Engineers*, vol. 39, p. 280–287, 1985.

[65] T. Yao, N. Zhang, M. Zhang, X. She, X. Liao, Y. Shen, and Z. Gan, "Effect of iron and copper on the thermal oxidation stability of synthetic hydrocarbon aviation lubricating oil," *Catalysis Communications*, vol. 161, 2021.

[66] M. Augusta, G. Martins, and A. R. Gomes, "Comparative study of the thermal degradation of synthetic and natural esters and mineral oil: effect of oil type in the thermal degradation of insulating kraft paper," *IEEE Electrical Insulation Magazine*, vol. 28, p. 22–28, 2012.

[67] K. Miners, "Particles and moisture effect on dielectric strength of transformer oil using VDE electrode," *IEEE Transactions on Power Apparatus and System*, vol. 3, pp. 751–756, 1984.

[68] T. V. Oommen and E. M. Petrie, "Particle contamination levels in oilfilled large power transformers," *IEEE Transactions on Power Apparatus and Systems*, vol. 5, pp. 1459–1465, 1983.

[69] L. Lewand, "Understanding Water in Transformer Systems: The Relationship Between Relative Saturation and Parts per Million (ppm)," *Chemist's Perspective*, pp. 1–4, 2002.

[70] J. J. Hahne, H.-P. Liu, C. S. Hearn, E. Schroeder, and J. O'Rarden, "Empirical Data on High Flow Velocity Coolants in Copper Tubing and the Effects on the Coolant's Electrical Resistivity," *IEEE Electromechanics*, pp. 191–196, 2004.

[71] J. E. Castle, "The non-protective oxidation of copper at low temperatures," *Corrosion Science*, p. 165–175, 2002.

[72] R. J. L. Welbourn, C. L. Truscott, M. W. A. Skoda, A. Zarbakhsh, and S. M. Clarke, "Corrosion and inhibition of copper in hydrocarbon solution on a molecular level investigated using neutron reflectometry and XPS," *Corrosion Science*, vol. 115, pp. 68–77, 2017.

[73] A. Akshatha, K. Anjana, D. Ravindra, G. Vishwanath, and J. Rajan, "Study of copper corrosion in transformers due to sulphur in oil using chemical methods," *IEE Annual Report Conference on Electrical Insulation and Dielectric Phenomena*, p. 395–398, 2012.

[74] M. Facciotti, P. S. Amaro, A. F. Holt, R. C. D. Brown, P. L. Lewin, J. A. Pilgrim, G. Wilson, and P. N. Jarman, "Contact-based corrosion mechanism leading to copper sulphide deposition on insulating paper used in oil-immersed electrical power equipment," *Corrosion Science*, vol. 84, p. 172–179, 2014.

[75] H. H. Abou, E. Naga, and A. E. M. Salem, "Effect of worn metals on the oxidation of lubricating oils," *Wear*, vol. 96, pp. 267–283, 1984.

[76] Y. Zhu, H. Gao, W. Liu, L. Zou, and D. J. McClements, "A review of the rheological properties of dilute and concentrated food emulsions," *Texture Studies*, vol. 51, pp. 45–55, 2019.

[77] T. Skodvin, "Dielectric Properties of Flocculated Water-in-Oil Emulsions," Master's thesis, Bergen, Norway, 1995.

[78] S. Laurén, "How emulsions form and break," Avaliable at: https://www.biolinscientific.com/blog/how-emulsions-form-and-break, (Accessed: 01/12/2021), 2020.

[79] D. J. McClements, *Food emulsions: Principles, practice, and techniques.* Boca Raton: CRC Press, 2015.

[80] C. Qu, G. Liu, and Z. Zhang, "Coarsening process driven by surface diffusion and migration," Avaliable at: http://www-personal.umich.edu/~weilu/me574/13/group1/intro.html, (Accessed: 20/12/2021), 2021.

[81] R. Pal, "Rheology of simple and multiple emulsions," *Current Opinion in Colloid Interface Science*, vol. 61, pp. 41–60, 2011.

[82] W. R. Schowalter, C. E. Chaffey, and H. Brenner, "Rheological behavior of a dilute emulsion," *Journal of Colloid and Interface Science*, vol. 26, pp. 152–160, 1968.

[83] A. Fröhlich and R. Sack, "Theory of the rheological properties of dispersions," *Proceedings of the Royal Society A: Mathematical, Physical and Engineering Sciences*, vol. 185, pp. 416–430, 1946.

[84] G. I. Taylor, "The viscosity of a fluid containing small drops of another fluid," *Proceedings of the Royal Society A: Mathematical, Physical and Engineering Sciences*, vol. 138, pp. 41–48, 1932.

[85] T. F. Tadros, "Fundamental principles of emulsion rheology and their applications," *Colloids and Surfaces A: Physicochemical and Engineering Aspects*, vol. 91, pp. 39–55, 1994.

[86] B. C. Tatar, G. Sumnu, and S. Sahin, *Advances in Food Rheology and Its Applications: Chapter 17 - Rheology of Emulsions.* United Kingdom: Woodhead Publishing, 2017.

[87] T. G. Mason, "New fundamental concepts in emulsion rheology," *Current Opinion in Colloid Interface Science*, vol. 4, pp. 231–238, 1999.

[88] H. A. Barnes, "Rheology of emulsions — a review," *Colloids and Surfaces A: Physicochemical and Engineering Aspects*, vol. 91, pp. 89–95, 1987.

[89] S. Mueller, E. W. Llewellin, and H. M. Mader, "The rheology of suspensions of solid particles," *Proceedings of the Royal Society A: Mathematical, Physical and Engineering Sciences*, vol. 466, p. 1201–1228, 1999.

[90] S. Kokal, "Crude-Oil Emulsions: A State-Of-The-Art Review," *Society of Petroleum Engineers*, vol. 20, p. 5–13, 2005.

[91] R. Zolfaghari, A. Fakhru'l-Razi, L. C. Abdullaha, S. H. Elnashaie, and A. Pendashteh, "Demulsification techniques of water-in-oil and oil-in-water emulsions in petroleum industry," *Separation and Purification Technology*, vol. 170, pp. 377–407, 2016.

[92] S. F. Masucci and C. Little, "Emulsion stability basics," Avaliable at: https://www.processingmagazine.com/mixing-blending-size-reduction/article/15586907/emulsion-stability-basics, (Accessed: 10/01/2021), 2017.

[93] S. A. Raya, I. M. Saaid, A. A. Ahmed, and A. A. Umar, "A critical review of development and demulsification mechanisms of crude oil emulsion in the petroleum industry," *Journal of Petroleum Exploration and Production Technology*, vol. 10, p. 1711–1728, 2020.

[94] R. Pal, "Effect of droplet size on the rheology of emulsions," *Materials, Interfaces, and Electrochemical Phenomena*, vol. 42, pp. 3181–3190, 1996.

[95] S. Jafari, E. Assadpoor, Y. He, and B. Bhandari, "Re-coalescence of emulsion droplets during high-energy emulsification," *Food Hydrocolloids*, vol. 22, p. 1191–1202, 2008.

[96] M. N, "Structure and Rheology of Monodisperse and Bimodal Emulsions," Master's thesis, Wellington, New Zealand, 2010.

[97] T. G. Mason and J. Bibette, "Shear Rupturing of Droplets in Complex Fluids," *Journal of Langmuir*, vol. 13, pp. 4600–4613, 1997.

[98] K. Y. Min and W. I. Goldburg, "Nucleation of a binary liquid mixture under steady-state shear," *Physical Review Letters*, vol. 70, p. 469, 1993.

[99] H. A. Barnes, *A handbook of elementary rheology*. Aberystwyth, Wales: Published by The University of Wales Institute of Non-Newtonian Fluid Mechanics, 2000.

[100] K. Batchelor, "The effect of Brownian motion on the bulk stress in a suspension of spherical particles," *Journal of Fluid Mechanics*, vol. 83, p. 97–117, 1977.

[101] I. R. Rutgers, "Relative viscosity of suspensions of rigid spheres in Newtonian liquids," *Journal of Rheology*, vol. 2, p. 202–210, 1962.

[102] D. G. Thomas, "Transport characteristics of suspension: 8. A note on the viscosity of Newtonian suspensions of uniform spherical particles," *Journal of Colloid Science*, vol. 20, p. 267–277, 1965.

[103] J. Happel, "Viscosity of suspensions of uniform spheres," *Journal of Applied Physics*, vol. 28, p. 1288–1292, 1957.

[104] H. Brenner, "Rheology of a dilute suspension of axisymmetric Brownian particles," *International Journal of Multiphase Flow*, vol. 1, p. 195–341, 1974.

[105] H. L. Goldsmith and S. G. Mason, "Particle motions in sheared suspensions XIII. The spin and rotation of disks," *Journal of Fluid Mechanics*, vol. 12, p. 88–96, 1962.

[106] J. Krautkramer and H. Krautkramer, *Applied Ultrasonic Testing of Materials*, 4th ed. New York: Springer, 1990.

[107] S. Pozzi, "High Intensity Focused Ultrasound (HIFU): computing tools for medical applications." Master's thesis, Rome, Italy, 2014.

[108] University of Southampton, "Sound wave - dispersive waves," Avaliable at: https://blog.soton.ac.uk/soundwaves/further-concepts/2-dispersive-waves/, (Accessed: 04/12/2021), 2021.

[109] Centre for Nondestructive Evaluation, Iowa State University, "Nondestructive evaluation techniques: Ultrasonic testing," Avaliable at: https://www.tainstruments.com/hr-10/, (Accessed: 15/11/2021).

[110] Signal Processing, "Technique - acoustic property tables," Avaliable at: https://www.signal-processing.com/table.php, (Accessed: 07/12/2021), 2021.

[111] RSHydro, "Sound speeds in water, liquid and materials," Avaliable at: https://www.rshydro.co.uk/sound-speeds/, (Accessed: 07/12/2021), 2021.

[112] N. David and J. Cheeke, *Fundamentals and Applications of Ultrasonic Waves*, 2002. [Online]. Available: https://books.google.com/books?id=Lnzb4PeTbeYC{&}pgis=1

[113] E. P. S and C. R.R, "The absorption of sound in suspensions and emulsions i. water fog in air." *The Journal of the Acoustical Society of America*, vol. 565, pp. 3–553, 1953.

[114] A. J.R. and H. S.A., "Attenuation of sound in suspensions and emulsions: Theory and experiments." *The Journal of the Acoustical Society of America*, vol. 1564, pp. 51–1545, 1972.

[115] F. Sheng, "Ultrasonic Spectroscopy for in situ Particle Sizing and Crystallization Process Monitoring," Ph.D. dissertation, Leeds, UK, 2012.

[116] L. Kinsler, A. Frey, A. Coppens, and J. Sanders, *Fundamentals of Acoustics*, 4th ed. John Wiler & Sons, Inc, 1999.

[117] V. T. Rathod, "A Review of Acoustic Impedance Matching Techniques for Piezoelectric Sensors and Transducers," *Sensors*, vol. 20, 2020.

[118] M. G. Silk, *Ultrasonic transducers for nondestructive testing.* Accord, MA: Adam Hilger Ltd, jan 1984.

[119] NanoMotion, "The piezoelectric effect," Avaliable at: https://www.nanomotion.com/nanomotion-technology/piezoelectric-effect/, (Accessed: 07/12/2021), 2021.

[120] Physik Instrumente, "Piezoceramic Components and Actuators," Avaliable at: https://www.physikinstrumente.co.uk/en/products/piezoelectric-elements-in-different-shapes/, (Accessed: 11/03/2019), 2019.

[121] Tom Nelligan, "An introduction to ultrasonic transducers for nondestructive testing," Avaliable at: https://www.olympus-ims.com/en/resources/white-papers/intro-ultrasonic-transducers-ndt-testing/, (Accessed: 07/12/2021), 2021.

[122] A. K. Hunter, "Ultrasonic Measurements of the Strip Thickness, Lubricant Film Thickness, Roll Deflection and Roll Stress in the Roll Bite in the Cold Rolling of Steel," Ph.D. dissertation, Sheffield, UK, 2018.

[123] S. Beamish, "Oil Film Thickness Measurements in Journal Bearings Under Normal, Severe and Dynamic Operating Conditions Using Ultrasound," Ph.D. dissertation, Sheffield, UK, 2021.

[124] J. E. Michaels, S. J. Lee, A. J. Croxford, and P. D. Wilcox, "Chirp excitation of ultrasonic guided waves," *Ultrasonics*, vol. 53, p. 265–270, 2013.

[125] ASTM E1065/E1065M, "Standard practice for evaluating characteristics of ultrasonic search units." Technical report standard, 2014.

[126] ISO 5577:2017, "Non-destructive testing ultrasonic testing vocabulary." Technical report standard, 2017.

[127] A. S. Dukhin and P. J. Goetz, "Bulk viscosity and compressibility measurement using acoustic spectroscopy," *Journal of Chemical Physics*, vol. 130, pp. 1–13, 2009.

[128] T. A. Litovitz, T. Lyon, and L. Peselnick, "Ultrasonic Relaxation and Its Relation to Structure in Viscous Liquids," *Acoustical Society of America*, vol. 26, p. 566, 1954.

[129] T. Litovitz and C. Davis, "Structural and Shear Relaxation in Liquids," *Physical Acoustics*, vol. 2, pp. 281–349, 1965.

[130] T. A. Litovitz, "Ultrasonic Spectroscopy in Liquids," vol. 31, pp. 280–285, 2016.

[131] W. P. Mason, W. O. Baker, H. J. Mcskimin, and J. H. Heiss, "Measurement of shear elasticity and viscosity of liquids at ultrasonic frequencies," *Physical Review*, vol. 75, pp. 936–946, 1949.

[132] W. Roth and S. R. Rich, "A new method for continuous viscosity measurement. General theory of the ultra-viscoson," *Journal of Applied Physics*, p. 24:940, 1953.

[133] A. J. Barlow and J. Lamb, "The Visco-Elastic Behaviour of Lubricating Oils under Cyclic Shearing Stress," *Proceedings of the Royal Society A: Mathematical, Physical and Engineering Sciences*, vol. 253, p. 52–69, 1959.

[134] F. Cohen-Tenoudji, W. J. Pardee, B. R. Tittmann, L. A. Ahlberg, and R. K. Elsley, "A Shear Wave Rheology Sensor," *IEEE Transactions on Ultrasonics, Ferroelectrics, and Frequency Control*, vol. 34, p. 263–269, 1987.

[135] I. Alig, D. Lellinger, J. Sulimma, and S.Tadjbakhsch, "Ultrasonic shear wave reflection method for measurements of the viscoelastic properties of polymer films." *Review of Scientific Instruments*, vol. 68, p. 1536–1542, 1997.

[136] M. S. Greenwood and J. A. Bamberger, "Measurement of viscosity and shear wave velocity of a liquid or slurry for on-line process control," *Ultrasonics*, vol. 39, pp. 623–630, 2002.

[137] R. Saggin and J. N. Coupland, "Rheology of xanthan/sucrose mixtures at ultrasonic frequencies," *Journal of Food Engineering*, vol. 65, p. 49–53, 2004.

[138] F. Buiochi, E. E. Franco, R. T. Higuti, and J. C. Adamowski, "Viscosity measuring cell using ultrasonic wave mode conversion," *Ferroelectrics*, vol. 333, pp. 139–149, 2006.

[139] R. Saggin and J. N. Coupland, "Oil viscosity measurement by ultrasonic reflectance," *Journal of the American Oil Chemists' Society*, vol. 78, p. 509–511, 2001.

[140] S. Kasolang and R. S. Dwyer-Joyce, "Viscosity measurement in thin lubricant films using shear ultrasonic reflection," *Proceedings of the Institution of Mechanical Engineers, Part J: Journal of Engineering Tribology*, vol. 222, pp. 423–429, 2008.

[141] S. Kasolang, M. A. Ahmad, and R. S. Dwyer-Joyce, "Measurement of circumferential viscosity profile in stationary journal bearing by shear ultrasonic reflection," *Tribology International*, vol. 44, pp. 1264–1270, 2011.

[142] M. Schirru, R. Dwyer-Joyce, and L. Vergoz, "A new ultrasonic rheometer for space exploration in lander missions," *Rheologica Acta*, 2019.

[143] C. S. Desilets, J. D. Fraser, and G. S. Kino, "The Design of Efficient BroadBand Piezoelectric Transducers." *IEEE Transactions on Sonics and Ultrasonics*, vol. 25, p. 115–125, 1978.

[144] S. W. Xiang and Y. T. Zhang, "Matching layer optimization between ultrasound transducer and human tissues," *Engineering in Medicine and Biology Society*, vol. 1, pp. 623–624, 1995.

[145] M. J. Povey, "Ultrasound particle sizing: A review," *Particuology*, vol. 11, p. 135–147, 2013.

[146] M. Schirru, X. Li, M. Cadeddu, and R. Dwyer-Joyce, "Development of a shear ultrasonic spectroscopy technique for the evaluation of viscoelastic fluid properties: Theory and experimental validation." 2018.

[147] A. Rabani, V. J.Pinfield, and R. E. Challis, "Rate of shear of an ultrasonic oscillating rod viscosity probe," *Ultrasonics*, vol. 65, pp. 18–22, 2016.

[148] T. G. Mezger, *The Rheology Handbook*, 4th ed. Hanover, Germany: Vincentz Network, 2014.

[149] M. T. Johnston and R. H. Ewoldt, "Precision rheometry: Surface tension effects on low-torque measurements in rotational rheometers," *Journal of Rheology*, vol. 57, p. 1515, 2013.

[150] C. W. Macosko, *Rheology Principles, Measurements and Applications*. New York: Wiley-VCH, 1994.

[151] A. Y. Malkin and A. I. Isayev, *Rheology: Concepts, Methods and Applications*. Toronto: ChemTec Publishing, 2006.

[152] Y. Otsubo and R. Prud'homme, "Rheology of oil-in-water emulsions," *Rheologica Acta*, vol. 33, pp. 29–37, 1994.

[153] X. Li, "Measuring Friction at an Interface Using Nonlinear Ultrasonic Response," Ph.D. dissertation, Sheffield, UK, 2018.

[154] M. I. Haller and B. T. Khuri-Yakub, "Composites for ultrasonic air transducers," *IEEE Ultrasonics Symposium*, vol. 1992-October, p. 937–939, 1992.

[155] M. T. L. Thompson, "Multilayer acoustic impedance converter for ultrasonic transducers," 2009.

[156] E. E. Franco and F. Buiochi, "Ultrasonic measurement of viscosity: Signal processing methodologies," *Ultrasonics*, vol. 91, pp. 213–219, 2019.

[157] C. I. Company, "General purpose viscosity standards," Avaliable at: https://cannoninstrument.com/viscosity-flash-point-standards/general-purpose-viscosity-standards.html, (Accessed: 01/04/2023).

[158] V. Avantor, "Vwr viscosity standards," Avaliable at: https://uk.vwr.com/store/catalog/product.jsp?product_id=18545012#, (Accessed: 01/04/2023).

[159] F. Borras, M. de Rooij, and D. Schipper, "Rheological and Wetting Properties of Environmentally Acceptable Lubricants (EALs) for Application in Stern Tube Seals," *Lubricants*, vol. 6, 2018.

[160] E. Franco, J. Adamowski, R. Higuti, and F. Buiochi, "Viscosity measurement of Newtonian liquids using the complex reflection coefficient," *IEEE Transactions on Ultrasonics, Ferroelectrics and Frequency Control*, vol. 55, pp. 2247–2253, 2008.

[161] Z. Imam, "Modeling non-newtonian fluids," Avaliable at: https://blog.rheosense.com/modeling-non-newtonian-fluids, (Accessed: 01/12/2021), 2020.

[162] O. Manfredi, R. Mills, M. Schirru, and R. Dwyer-Joyce, "Non-invasive measurement of lubricating oil viscosity using an ultrasonic continuously repeated chirp shear wave," *Ultrasonics*, vol. 94, pp. 332–339, 2019.

[163] S. Wong, M. Law, Y. Samyudia, and S. Dol, "Rheology Study of Water-in-Crude Oil Emulsions," *Chemical Engineering Transactions*, vol. 45, pp. 1411–1416, 2015.

[164] D. Broboana and C. Balan, "Investigations on the Rheology of Water-in-Crude Oil Emulsions," *Chemical Engineering Transactions*, vol. 69, pp. 35–50, 2007.

[165] N. Aomari, R. Gaudu, F. Cabioc, and A. Omari, "Rheology of water in crude oil emulsions," *Physicochemical and Engineering Aspects*, vol. 139, pp. 13–20, 1998.

[166] M. Farah, R. Oliveira, J. Caldas, and K. Rajagopal, "Viscosity of water-in-oil emulsions: Variation with temperature and water volume fraction," *Journal of Petroleum Science and Engineering*, vol. 48, pp. 169–184, 2005.

[167] S. Bair, "Polymer-Thickened Oil Rheology When There Is No Second Newtonian," *Tribology Letters*, pp. 67–91, 2019.

[168] E. Zadorozhnaya, I. Levanov, and O. Oskina, "Study of HTHS Viscosity of Modern Motor Oils," *Procedia Engineering*, vol. 150, pp. 602–606, 2016.

Appendices

Appendix A

Shear Analytical Model

```
%% Shear Analytical Model
close all;
clear all;
clc;

% Matching layer selection
n = 1;
k = 1;
zl = [1e4 1e5];
cp = 780; rhop = [1400]; % ML SOS and rho 2334
f1w = [2e6 10e6]; %
tm = cp./(4.*f1w(k))

% Fluid properties
rho = 800;
viscom = [1e-3; 1e-2; 5e-1; 1]; %

%**** @23 degrees celcius ****%
% material properties - Al
E=70E9; % young's modulus
nu=0.3; % poisson's ratio
rhoa=2700; % density
G=E/(2*(1+nu));
ca= sqrt(G/rhoa);
Za=rhoa*ca;

%******************************%
%**** Calculations @ 23 degrees ****%
f = 0:0.02e6:12e6;% linspace(0,10e6,83);
w = 2.*pi.*f;
% Material details
lmb = cp./f;
Zm = cp*rhop; Km = (2*pi)./lmb;

% Change these to get a different result
% Zl = zl(n).*ones(1,length(w))
Zl = sqrt(w.*rho.*viscom);

```

```
39
40 %**** Reflection prediction for ****%
41 %**** VWR oils ****%
42 % two layer model Ai and Oil
43 R = abs((Za-Zl)./(Za+Zl));
44 R = R.*ones(1,length(f));
45
46 % Three layer model Ai, matching layer and oil Pressure
       reflection coefficient
47 R1 = abs((((1-(Za./Zl)).*cos(Km.*tm)) + (j.*((Zm./Zl)-(Za./Zm))
       .*sin(Km.*tm))) ...
48       ./ (((1+(Za./Zl)).*cos(Km.*tm)) + (j.*((Zm./Zl)+(Za./Zm)).*
             sin(Km.*tm))));
49
50 R2 = abs((Zm.^2 - (Za.*Zl))./(Zm.^2 + (Za.*Zl)));
51
52 fplot = f./1e6;
53
54 figure;
55 plot(fplot,R(3,:),'-r'); hold on
56 plot(fplot,R1(3,:),'-k');
57 %plot(fplot,R2,'-b');
58 ylabel('Reflection Coefficient $R$','FontSize',14, 'Interpreter'
       ,'latex');
59 xlabel('Frequency $f$ [MHz]','FontSize',14, 'Interpreter','latex
       ');
60 ylim([0,1])
```

Appendix B

Shear Numerical Model

```
%% Shear Numerical Model
clear all
close all
clc

% Signal properties
f1w = 10E6; % Chirp centre frequency

fstart = 9E6; % Chirp start frequency

cycles = 5;

p1w=1./f1w; % period of fundamental wave
amp = 4; %Amplitude

% material properties - Al
E=70E9; % young's modulus
nu=0.3; % poisson's ratio
rhoa=2700; % density
G=E/(2*(1+nu));
ca= sqrt(G/rhoa);
Za=rhoa*ca; % acoustic impedance

% material properties - Polyimide
cp = 780;
rhop = 1400;
Zp = rhop*cp;

lim = 1.55E4:1.85E4;

% Space and time numerical
D1 = 25E-3; D2 = cp/(4*f1w); D3 = sqrt(1./(800*2*pi*f1w))% D3 is
    penetration depth
Lx= D1 + D2 + D3; % length of specimen plus matching layer and
   final space
T= 60E-6; % total time 25E-6
dx= D2/4; % space increment or sampliming increment 4.5E-5 D2/4
dt= 1E-9; % time increment 2E-9  4.5E-9
```

```
nx=round(Lx/dx); % number of space divisions, integer
nt=round(T/dt); % number of time divisions, integer
x = linspace(0, Lx, nx);
AIDivisions = D1/dx; MatchingLayerDivisions = D2/dx;
MLtoL_layer = round(AIDivisions + MatchingLayerDivisions)

% Properties of Fluid at interface of interest
cl = zeros(1,4); %
w = 2*pi*f1w;
T = 23; % Temperature of tests

rho = [0; 800; 800; 800; 800];
viscom = [0; 1e-3; 1e-2; 1e-1; 1];
Zl = sqrt(w.*rho.*viscom);
Cl(1:length(viscom)) =sqrt((w.*viscom)./rho);
Cl([1]) = 0;
%
 frame_no = 0;

for m = 1:length(viscom);

cl = Cl(m);

% Creating the Boundaries
C = ones(nx,1).*ca; D4 = D1+D2;
        for i=1:nx
            if x(i) >= D1 & x(i) <= D4 % thin polyimide layer
               C(i) = cp;
            elseif x(i) > D4
               C(i) = cl;
            end
        end

% stability & wave check
CFL = C.*dt/dx; % cfl condition
js=round(cycles.*p1w./dt+1);
w = gausswin(js);
fchirp = linspace(fstart,f1w,js);
pwchirp = 1./fchirp;

% Field variables
deltan = zeros(nx,1);
deltanm1 = deltan;
deltanp1 = deltan;

```

```
82
83
84 %Time_Space = zeros(nx,nt);
85
86 % Time stopping loop
87         for j=1:nt+1
88         tvec(j)=(j-1)*dt;
89         end
90
91 %clearvars -except nt nx tvec deltan deltanp1 deltanm1 js amp
       f1w t w CFL dx
92         for k = 1:nt
93             t = tvec(:,k);
94
95             % Complete absorption boundary conditions
96             deltanp1(end) = (deltan(end-1) + (((CFL(end)-1)/(CFL
                   (end)+1)) * (deltanp1(end-1) - deltan(end)))) ;
97
98
99             % Reflection boundary conditions
100            %if m == 1;
101              %deltan([1; MLtoL_layer]) = 1;
102            %else
103               deltan([1]) = 1;
104            %end
105            %
106
107            % Time and Space Matix
108                %Time_Space(:,k) = deltan;
109                signal(m,k) = deltan(6);
110            % Solution
111            deltanm1 = deltan;
112            deltan = deltanp1;
113
114            % Source
115            if k <= js
116            f = amp * sin(2 * pi * fchirp(k) * t); % modulated
                   source, apply gaussian window
117            idx = find(tvec == t);
118            deltan(1)= f.* w(idx,:);
119
120            for i = 2 : nx -1
121                    deltanp1(i) = 2*deltan(i) - deltanm1(i)...
122                        + CFL(i)^2 * (deltan(i+1) - 2*deltan(i)
                               + deltan(i-1));
```

```
123             end
124 %                   clf;
125 %                   plot(x, deltan)
126 %                   shg; pause(0.001);
127 %                frame_no = frame_no + 1;
128 %                frame=sprintf('Frame%d.png', frame_no);% saveas(
    gcf, frame);
129 %                disp(frame)
130 %                print (frame, '-dpng', '-r300');
131
132             else
133
134             for i = 2 : nx -1
135                 deltanp1(i) = 2*deltan(i) - deltanm1(i)...
136                     + CFL(i)^2 * (deltan(i+1) - 2*deltan(i) +
                        deltan(i-1));
137             end
138 delta(:,k) = deltan;
139 %          clf;
140 %              plot(x, deltan)
141 %          shg; pause(0.001);
142             end
143
144         end
145
146 t  = tvec(:,1:nt);
147
148 % FFT
149 Fs=1/(dt); % sampling frequency
150 %signal = bandpass(signal,[3E6 7E6],Fs);
151 n1 = 2^(nextpow2(length(t(lim)))); %length of freq vector
152 n1 = n1 + n1*2; % adds zeros the length of the frequency vector
153 freq = Fs/n1.*(0:(n1/2)); % frequency vector = 0:(Fs/n):(Fs/2)
154
155 % Signal FFT of signal limits
156 Y=fft(signal(m,lim),n1); %fft of the signal
157 freq_signal(m,:) = abs(Y(1:end/2+1));
158
159 % Reflection coefficient
160 R(m,:) = freq_signal(m,:) ./ freq_signal(1,:);
161
162 end
163
164 %*****************************%
165
```

```
166 % Axis corrections
167 freqlims = [0 20];
168
169 t = t.*1E6;
170 freqplot = freq.*1e-6;
171
172 m = 2:length(viscom);
173
174 [ d, fidx ] = min( abs( freqplot-f1w.*1e-6)) ;
175 Ridx = R(:,fidx);
176 viscom = viscom'.*1E3;
177
178 R2 = abs((cp.^2 - (ca.*Cl')).^(cp.^2 + (ca.*Cl')));
179
180 R2 = R2 .* ones(1,length(freqplot));
181
182 figure
183 plot(t,signal(1,:),'k')
184 ylabel('Amplitude $A$','FontSize',14, 'Interpreter','latex');
185 xlabel('Time $t$ [$\mu s$]','FontSize',14, 'Interpreter','latex'
    );
186 set(gcf,'units','points','position',[10,10,420,200]); xlim([0
    8]);
187
188 figure
189 plot(t,signal(1:5,:))
190 ylabel('Amplitude $A$','FontSize',14, 'Interpreter','latex');
191 xlabel('Time $t$ [$\mu s$]','FontSize',14, 'Interpreter','latex'
    );
192
193 figure
194 plot(t(lim),signal(1:5,lim))
195 ylabel('Amplitude $A$','FontSize',14, 'Interpreter','latex');
196 xlabel('Time $t$ [$\mu s$]','FontSize',14, 'Interpreter','latex'
    );
197
198 figure;
199 plot(freqplot,freq_signal(1:5,:));
200 ylabel('Amplitude $A$','FontSize',14, 'Interpreter','latex');
201 xlabel('Frequency $f$ [MHz]','FontSize',14, 'Interpreter','latex
    ');
202 xlim(freqlims);
203
204 figure
205 plot(freqplot,R(m,:)); hold on
```

```
206 %plot(freqplot,R2(m,:));
207 ylabel('Reflection Coefficient $R$','FontSize',14, 'Interpreter'
    ,'latex');
208 xlabel('Frequency $f$ [MHz]','FontSize',14, 'Interpreter','latex
    ');
209 xlim(freqlims);
210 ylim([0 1]);
```

Appendix C

Signal Processing

```
%% Time Domain Signal to Frequency Domain
Clear all;
close all;
clc;

folder_name = ('E:\UoS_PhD_MEC095_DF\PhD_Project_MEC095_DFORT\
    Large_pianno_rig_viscosity\')
cd(folder_name);

%**** 1:9 calibration **** 1:7 coolant ****%
for n = 1;
    close all
disp('Select Oil File')
folder_name = uigetdir;
cd(folder_name);
load('DATA.mat')

%******************************%

% 1:5 are Oils
% 6:10 are References
% 1&6 2&7 3&8 4&9 5&10 go together
% 1     2     3     4     5         OIL
% Divided by
% 6     7     8     9     10        REFERENCE

%******************************%

freqlim = 20;
time_step = 0.002;
t = linspace(0,time_step*length(s),length(s));
Signal(n).t{:,1} = t; for k = 1:reflength(end); Signal(n).s{:,k}
    = s(:,k);end
sref = s(:,reflength); soil = s(:,oillength);

%******************************%

figure; plot(t,s(:,reflength(1)),'k'); hold on;
```

```
plot(t,s(:,oillength(1)),'r');
ylabel('Voltage Amplitude $A$ [$V$]','FontSize',14, 'Interpreter','latex');
xlabel('Time $t$ [$\mu s$]','FontSize',14, 'Interpreter','latex');

%******************************%

% FFT
T=diff(t(1:2))/1e6; % sampling period
Fs=1/(T); % sampling frequency
n1 = 2^(nextpow2(length(t))); %length of freq vector
n1 = n1 + n1*2; % adds zeros the length of the frequency vector
freq = Fs/n1.*(0:(n1/2)); % frequency vector
freqplot = freq./1e6;

% Signal FFT of signal limits
for k = oillength
    Yref=fft(sref(:,k),n1);%fft of the signal
        freqFFT(n).ref{:,k} = abs(Yref(1:end/2+1));
        freqFFT(n).refang{:,k} = angle(Yref(1:end/2+1));
    Yoil=fft(soil(:,k),n1);%fft of the signal
        freqFFT(n).oil{:,k} = abs(Yoil(1:end/2+1));
        freqFFT(n).oilang{:,k} = angle(Yoil(1:end/2+1));
end
%

figure; %subplot(2,1,1)
        plot(freqplot,freqFFT(1).ref{1,1},'k-'); hold on
        plot(freqplot,freqFFT(1).oil{1,1},'r-');
xlabel('Frequency $f$ [MHz]','FontSize',14, 'Interpreter','latex');
ylabel('Voltage Amplitude $A$ [$V$]','FontSize',14, 'Interpreter','latex');
        xlim([0  20])

end

%******************************%
%******************************%
% disp('Save')
% folder_name = uigetdir; cd(folder_name);
% save('Time_Frequency_Data','Signal','freqFFT','freqplot','oillength','reflength')
%******************************%
```

```
77 %******************************%
78
79 %% Frequency to Reflection Coefficient
80 % Select folder of the calibration oils
81 % then select folder for the unknown oils
82 clear all;
83 close all
84 clc;
85
86 disp('Calibration - Select Calibration Oil Data')
87 folder_name = uigetdir; cd(folder_name);
88
89 load Time_Frequency_Data.mat
90 for ol = 1:length(freqFFT);
91     for sn = oillength
92     reflection{:,sn} = freqFFT(ol).oil{:,sn}./freqFFT(ol).ref{:,
          sn};
93     end
94     R = cell2mat(reflection);
95     Mean_Rall(ol,:) = mean(R'); STD_Rall(ol,:) = std(R');
96 end
97
98 freqlim = 20;
99
100 %******************************%
101 figure
102 plot(freqplot,Mean_Rall,'k'); hold on
103 xlabel('Frequency $f$ [MHz]','FontSize',14, 'Interpreter','latex
      ');
104 ylabel('Reflection Coefficient $R$','FontSize',14, 'Interpreter'
      ,'latex')
105 xlim([0 15]);ylim([0 1]);
106 %******************************%
107
108 T = 23.2;
109 for ol = 1:length(freqFFT);
110 viscom(:,ol) = Vogel_Equation(T,ol);
111 end
112
113 %******************************%
114
115 for r = 1:length(ResFreq);
116 [ d, fidx(r) ] = min( abs( freqplot-ResFreq(r)) );
117 end
118
```

```
119 Mean_R = Mean_Rall(:,fidx); STD_R = STD_Rall(:,fidx);
120
121 %******************************%
122 %******************************%
123 % disp('Save')
124 % folder_name = uigetdir; cd(folder_name);
125 %save('RC_Calibration_Data','Mean_R','STD_R','viscom','ResFreq')
126 %******************************%
127 %******************************%
```

Appendix D

Sensor Block for a Battery Cooling System

The plan was to originally set up a sensor block on battery cooling rig with one of BP's partners, Figures D.1 and D.2. However the plan changed and a new sensor block was made for the thermal rig at BP, Figure D.3. This would have had interchangeable viscosity sensor plugs with different frequency transducers, Figure D.4

Using the rig, measurements could be made using different coolants. The one used in this thesis was generation 1. There were 1-5 different coolants available to test. The generation 1 coolant could also be contaminated using less than 5% water on the test rig, as the battery was simulated using two metal hot plates. It did not use a battery pack/cell.

Parameters:

- Temperature working range: 10-40 $°C$.
- Mass flow rate: 200 – 800 kg/h.
- Atmospheric pressure.
- Pipe diameter 1 inch – Sensor block uses 0.75 BSP thread connectors.

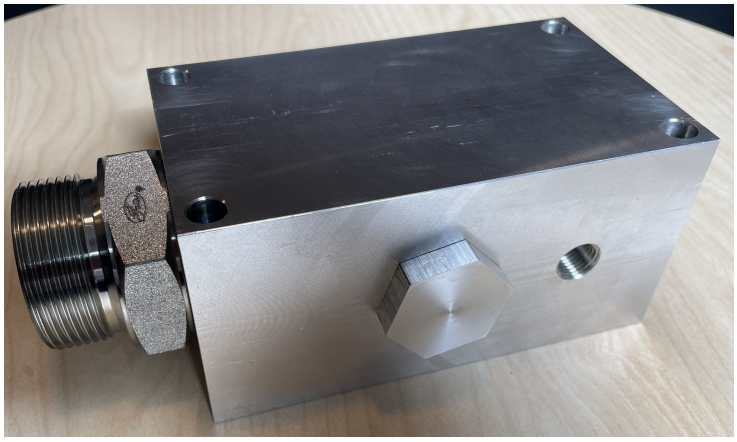

Figure D.1: BP's partner rig sensor block.

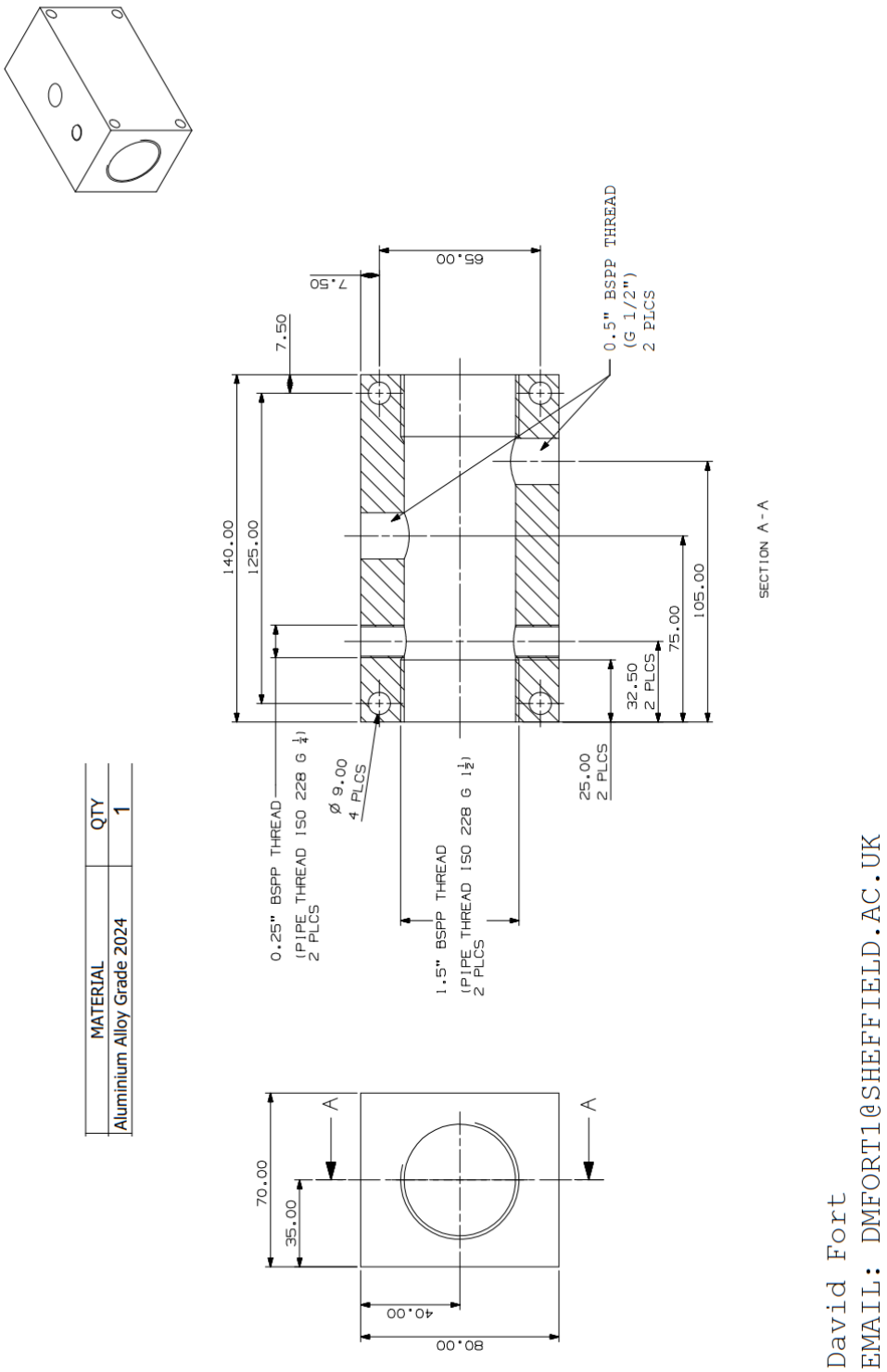

Figure D.2: BP's partner rig sensor block design.

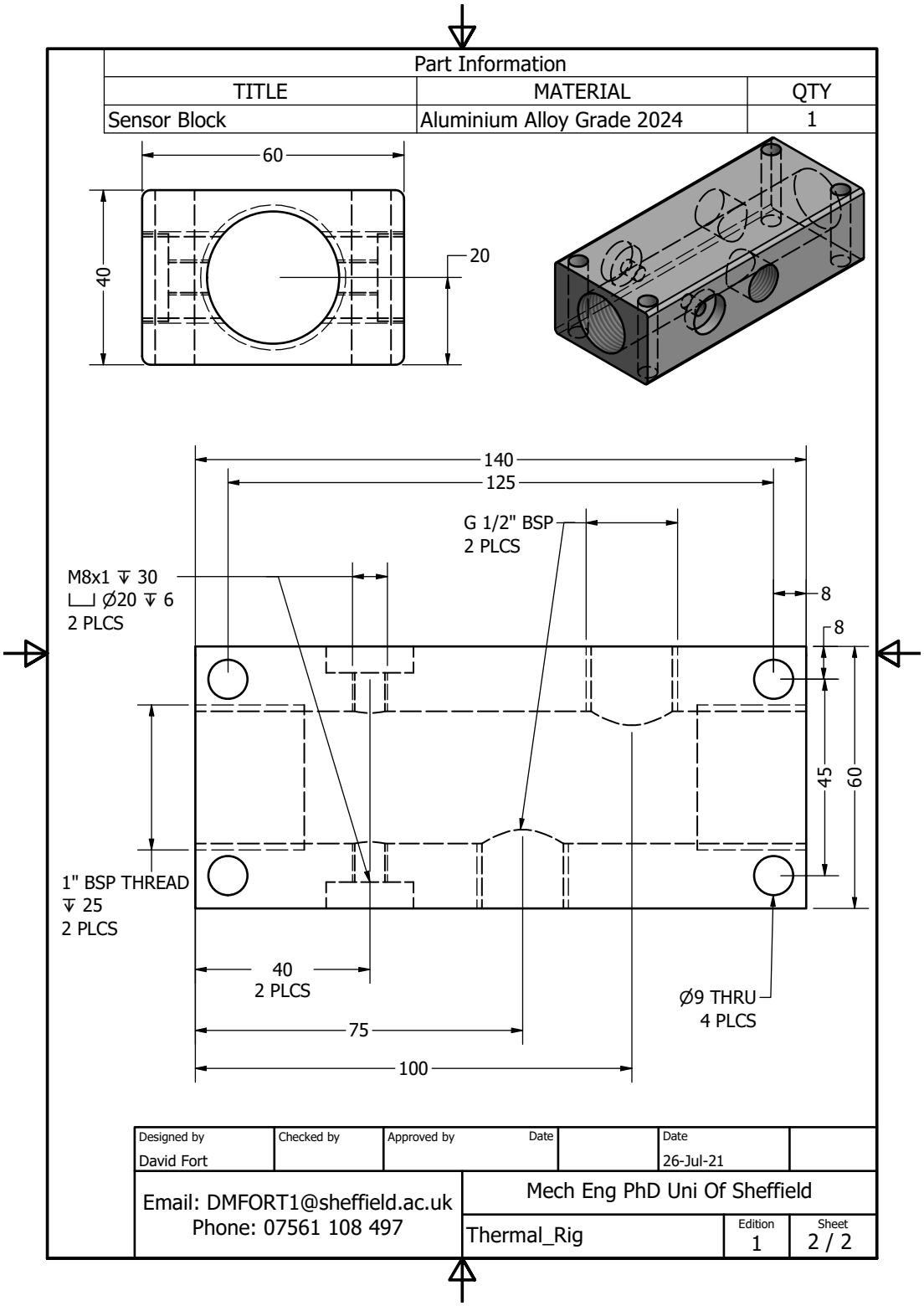

Figure D.3: Thermal rig sensor block design.

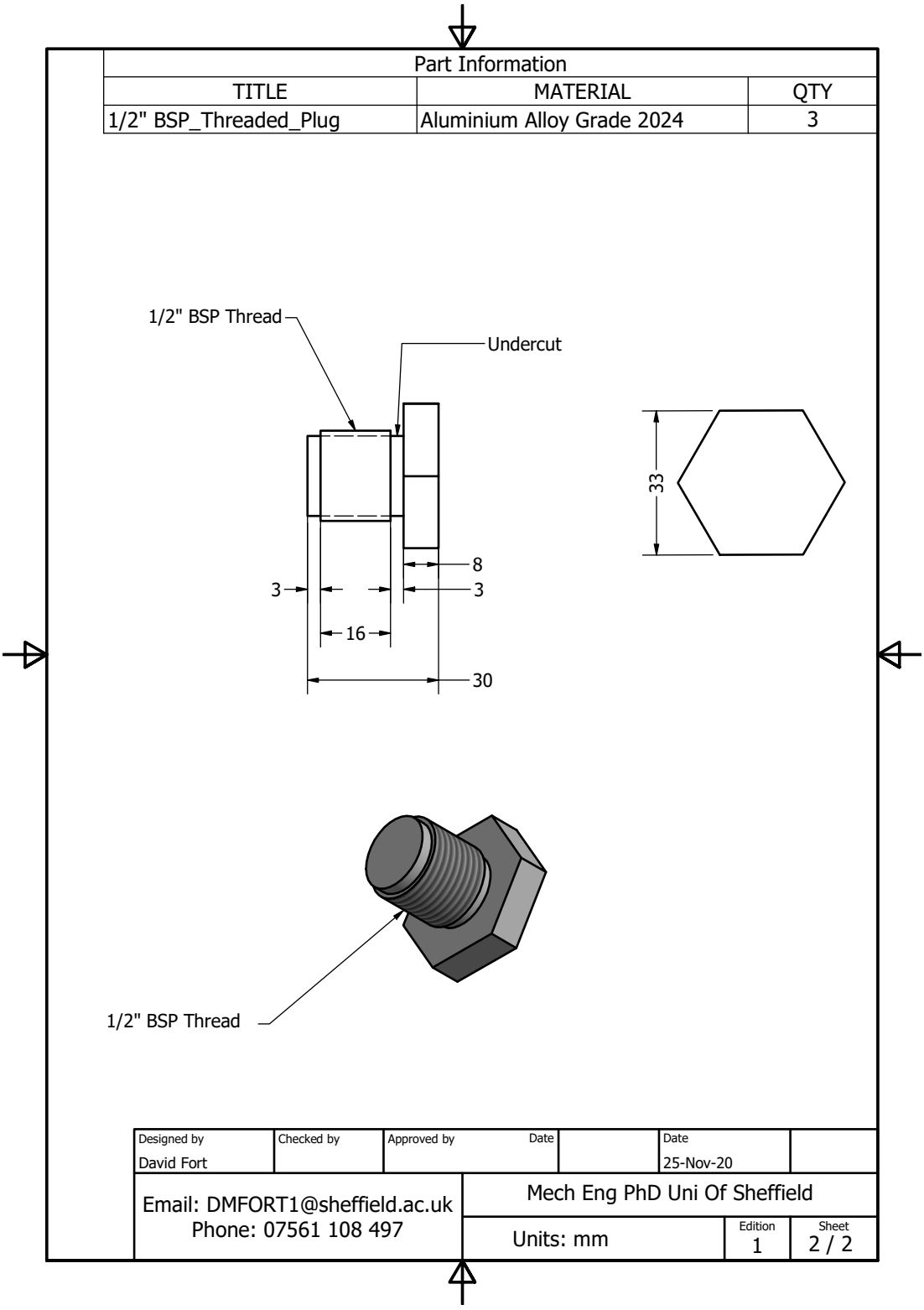

Figure D.4: Shear viscosity sensor plug.